MONASH UNIVERSITY
THESIS ACCEPTED IN SATISFACTION OF THE
REQUIREMENTS FOR THE DEGREE OF
DOCTOR OF PHILOSOPHY
ON..... 9 December 2003 .....
.....[redacted].....
Sec. Research Graduate School Committee

[redacted]

H24/3659

Errata

p 61 para 3, second sentence: "In our model of liquid light, this is evident in Eqs. (2.71) and (2.72)" for "In our model of liquid light, this is evident in Eqs. (2.71) and (2.71)"

p 65 para 2, second last sentence: "Recently Silverman and Mallett considered a neutral self-interacting scalar field with spontaneously brcken symmetry coupled to gravity (Silverman and Mallett 2001a, 2001b and 2002)" for "Recently Silverman and Mallett (2001a) considered a neutral self-interacting scalar field with spontaneously broken symmetry coupled to gravity"

p 213 between the references Silverman and Mallett (2001b) and Sin (1994), insert the reference:

Silverman, M.P. and Mallett, R.L. (2002), *Gen. Rel. Grav.* **34**, 633.

5. Ratification by academic unit

This is to ascertain that the Department / School / Centre / Institute has no objection to the candidate's options regarding access to the Library thesis copy. If so, please sign below and return the completed form to: **Monash Graduate School, Building 3D, Clayton Campus.**

Supervisor's signature:	[redacted]	Date: **29/07/2003**
(please print name)	**Michael J. Morgan**	

Numerical Simulations of Topological Defects in $\mathcal{R}^{2+1}$, $\mathcal{R}^{3+1}$ and $\mathcal{R}^{4+1}$ Spacetime

A THESIS SUBMITTED FOR THE DEGREE OF
DOCTOR OF PHILOSOPHY

By
Rotha P. Yu
B. Sc. (Hons.)

School of Physics and Materials Engineering,
Monash University,
Australia.

July 2003.

Contents

Summary

This thesis investigates the formation and dynamics of topological defects that result from symmetry breaking phase transitions in $\mathcal{R}^{2+1}$, $\mathcal{R}^{3+1}$ and $\mathcal{R}^{4+1}$ spacetime. We examine the behaviour of vortices, cosmic strings, domain walls and monopoles from the perspectives of condensed matter physics and particle cosmology.

Chapter 2 analyzes the evolution of vortex defects in a rotating Bose-Einstein condensate (BEC). Following a phase transition to the BEC state, vortices and anti-vortices form in pairs as a consequence of conservation of topological charge. It is found that a rotating BEC imprints a background phase gradient on the condensate, creating a confining (trap) potential for vortices and expelling anti-vortices. The competition between the confining potential and repulsive inter-vortex interactions causes an initially random vortex configuration to evolve toward a triangular lattice. The behaviour of quantum vortices in a BEC is in marked contrast to vortices in a classical condensate. The latter arises in classical electrodynamics, for example, when light in a cubic-quintic non-linear medium undergoes a "phase transition" to a liquid light condensate (LLC). We show that vortices in a LLC do not experience mutually repulsive interactions; instead they rotate about each other in a stable configuration. The origin of the difference in vortex behaviour is explored by examining the role of viscosity in classical and quantum fluids.

Chapter 3 investigates a self-interacting scalar matter field, which has been postulated to give rise to a weakly interacting degenerate "ether" (WIDGET) in the early Universe. Following a late-time cosmological phase transition these scalar particles can form a BEC, which is considered as a candidate for cold dark matter. The condensate forms a spherical halo around a rotating protogalaxy. Rotation of the dark matter condensate nucleates vortices and imprints a background phase gradient on the condensate, establishing a trapping potential for vortices. Numerical simulations show that the vortex number density, n_v, for an initially Keplerian velocity profile ($n_v \propto r^{-1.5}$), evolves toward a vortex lattice with number density $n_v \propto r^{-1}$. This is consistent with a flat velocity profile for the dark matter condensate, in broad agreement with the observed rotation curves of spiral galaxies. We also investigate gravitational interactions between dark matter and baryonic matter.

Gravitational drag results in baryonic matter adopting the same (flat) velocity profile as the dark matter condensate. This provides a novel explanation for the flat Universal Rotation Curve of spiral galaxies and suggests that vortices in a rotating dark matter (scalar) condensate may play a significant role in the evolution of spiral galaxies.

Chapters 4 and 5 examine topological defects within the context of particle cosmology. Monopole defects are predicted to form in numbers that conflict with observational bounds, based on cosmic magnetic fields and proton decay. Other defects, such as domain walls, are inconsistent with data from the Cosmic Background Explorer (COBE) and the recent Wilkinson Microwave Anisotropy Probe (WMAP). Chapter 4 examines the domain wall problem. We explore the ramifications of symmetry breaking phase transitions, leading to the formation of hybrid defects in which cosmic strings terminate on a domain wall. These so called Dirichlet defects (or D-walls) are stable for a wide range of parameters and when perturbations are imposed on the wall. However, a string connecting two domain walls causes the walls to move toward each other, resulting in collision and annihilation. This process is analogous to the Langacker-Pi mechanism for monopoles, and when invoked in the context of D-walls provides a novel solution to the domain wall problem. Furthermore, monopoles located between domain walls will also collide with the walls and annihilate. In this scenario, both monopoles and domain walls are removed from the early Universe.

The topological defect problem is examined further in Chapter 5, where we extend spacetime to $4+1$ dimensions. We study monopoles in $\mathcal{R}^{4+1}$ spacetime, where they behave like strings. It is found that the intercommutation rate for the string network in $\mathcal{R}^{4+1}$ is very low. The energy density of a long string network is shown to vary as $\rho_\infty \propto t^{-1.5}$, while the energy density of the Universe has $\rho \propto t^{-2}$. This is consistent with Kibble's scaling model and confirms that a string network in $4+1$ dimensions does not have a scaling solution. These results would appear to rule out $\mathcal{R}^{4+1}$ spacetime as a means of avoiding the monopole problem. However, if the extra dimension is compactified, monopoles exist as loops, which collapse and annihilate in a time scale comparable to the size of the compactified dimension. This result is then generalized to topological defects in $\mathcal{R}^{d+1}$ spacetime, with $d-3$ compactified dimensions. It is found that introducing at least one (extra) compactified dimension obviates the topological defect problem in the early Universe.

Finally, in Chapter 6 we comment on the implications of our results and identify directions for future work.

Declaration

This thesis contains no material accepted for the award of any other degree or diploma in this or any other university. To the best of my knowledge, it contains no material published or written by another person, except where due reference is made in the text.

Rotha P. Yu

July 2003.

Acknowledgements

First and foremost I would like to thank my supervisor Associate Professor Michael Morgan. His experience, patience, advice, constructive criticism and financial support helped in the completion of this thesis. His time and commitment is greatly appreciated.

I wish to thank my mum, Jenny Kao, for her support love and care - I would not be who I am without her. I would also like to thank my sisters Mei-Lin and Mei-Len, and my brother Bun-Long for all the support they have given me. I greatly appreciate the patience (only with minimal complaints) they have shown towards my academic endeavors. Further, I would also like to thank Veng-Chay and Chan-Monika for everything they have done for me.

In alphabetical order I would like to acknowledge the following people who provided valuable comments and discussions on physics, computer issues, as well as for their friendship: Dr. Simon Drew, Dr. Yvette Hancock, Steven Homolya, Dr. David Paganin, Dr. Karen Siu, Dr. Imants Svalbe, Dr. Marcus Thatcher and David Zuidema.

Finally, I wish to acknowledge the financial support of an Australian Postgraduate Award, and a Departmental Scholarship provided by my supervisor Associate Professor Michael Morgan.

This thesis was typed in LaTeX2e using the Monash University thesis style format. Numerical simulations were written in Fortran90 using the Microsoft Fortran Power Station v4.0. Codes were compiled and evaluated on the Monash Silicon Graphics Power Challenge R10000 (Hotblack) and under the auspices of the Victorian Partnership for Advanced Computing (VPAC) on the 32 Compaq ES40. Images were generated using Mathematica v4.0 running on a Micro-Pro PC with Microsoft Windows 95 and Mathematica v3.0 running under the IRIX Release 6.3 operating system.

Supporting Publications

Some of the work presented in this thesis has been published, or submitted for publication. Reprints are included at the end of the thesis.

Yu, R.P., Adam, N., Thatcher, M.J., and Morgan M.J., 'Numerical study of the stability of $U(1) \times U(1) \times Z_2$ Dirichlet defects' (2001). *Class. and Quantum Grav.* **18**, L163-L169.

Yu, R.P., and Morgan M.J., 'Vortices in a rotating dark matter condensate' (2002). *Class. and Quantum Grav.* **19**, L157-L166.

Tan, Y-R. E., Paganin, D.M., Yu, R.P., and Morgan, M.J., 'Wavefunction reconstruction of complex fields obeying non-linear parabolic equations' (submitted to Phys. Rev. E, 2003).

Units and Conventions

Unless otherwise specified we employ natural units throughout this thesis, in which

$$c = \hbar = k_B = 1,$$

where the conversion between natural units and SI units uses

$$\text{GeV}^{-1} \approx 1.98 \times 10^{-16}\text{m}$$

$$\text{GeV} \approx 1.79 \times 10^{-27}\text{kg}$$

$$\text{GeV}^{-1} \approx 6.57 \times 10^{-25}\text{s}.$$

Many of the simulations reported in the thesis assume a flat spacetime, in which the Universe has zero curvature ($k = 0$). In flat spacetime we denote a $(d+1)$-dimensional Universe by $\mathcal{R}^{d+1}$, where d is the number of spatial dimensions.

Relativistic models assume a spacetime metric with signature $\text{diag}(+,-,-,-)$ in $\mathcal{R}^{3+1}$, or $\text{diag}(+,-,-,-,-)$ in $\mathcal{R}^{4+1}$. Greek indices are used to label the spacetime coordinates, i.e., $\mu, \nu, ... = 0, 1, 2, 3$ in $\mathcal{R}^{3+1}$ or $\mu, \nu, ... = 0, 1, 2, 3, 4$ in $\mathcal{R}^{4+1}$.

CHAPTER 1

Introduction

This thesis presents numerical simulations of topological defects in $\mathcal{R}^{2+1}$, $\mathcal{R}^{3+1}$ and $\mathcal{R}^{4+1}$ spacetime. We investigate the formation and evolution of vortices, cosmic strings, domain walls and monopoles, and elucidate their role in condensed matter, astrophysics and particle cosmology. Chapter 1 presents an overview of the theoretical models and the underlying physical principles that lead to the formation of topological defects. We start with a general discussion of phase transitions and topological defects in the early Universe.

1.1 Phase transitions and topological defects

The "Big Bang" model conjectures that the Universe came into being from an infinitely dense hot state approximately fourteen billion years ago.[1] According to "Big Bang" cosmology the Universe has been expanding ever since the initial singularity. To understand the very early Universe (i.e., as early as $t = 10^{-36}$ seconds after the Big Bang) requires us to utilize effective field theories of particle physics (referred to as Grand Unified Theories or GUTs), which describe particle symmetries and interactions at very high energies. Further, to ensure that these effective field theories provide a gauge invariant description of particle interactions, they must exploit a mechanism known as symmetry breaking (Goldstone 1961, Goldstone *et al.* 1962 and Higgs 1964). Symmetry breaking occurs when the symmetry of the Lagrangian is higher than that of the ground state of the system. Particle symmetries that are broken at low temperatures are thought to be restored at sufficiently high temperatures. As the Universe expanded and cooled from a dense hot state, it is postulated that it underwent a series of symmetry breaking phase transitions, where the strong, weak and electromagnetic forces became distinguishable.[2] These symmetry

[1] The most recent data from a one-year probe of the Cosmic Microwave Background Radiation (CMBR) by the Wilkinson Microwave Anisotropy Probe (WMAP) reveals that the Universe is 13.7 billion years old (Bennett *et al.* 2003).

[2] The GUT scale phase transition describes the separation of the strong and electroweak forces, which occurred at 10^{16} GeV, or 10^{-36} seconds after the Big Bang. The electroweak phase transition describes the separation of the weak and electromagnetic forces, which occurred at 10^{3} GeV, or 10^{-11} seconds after the Big Bang.

breaking phase transitions (based on field theoretic models) have numerous analogues in condensed matter systems (see e.g., Kirzhnits 1972, Kirzhnits and Linde 1972, Zurek 1996 and Kibble 2002).

Symmetry breaking phase transitions in the early Universe are facilitated by spin-0 Higgs particles (Higgs 1966), described by the Higgs field, Φ. For example, the simplest realistic electroweak symmetry breaking model of Glashow, Salam and Weinberg (Glashow 1961, Salam 1968 and Weinberg 1967) is $SU(2)\times U(1) \rightarrow U(1)$, in which the Higgs field is a complex doublet.[3] Following a phase transition the vacuum expectation value of the Higgs field adopts a non-zero value. Kibble (1976) predicted that topological defects would form when the Universe underwent a phase transition. These cosmic topological defects can be classified as monopoles ('t Hooft 1974 and Polyakov 1974), cosmic strings (Nielsen and Olesen 1973), domain walls (Zel'dovich *et al.* 1975) or textures (Turok 1989), according to the homotopy group, $\pi_n(\mathcal{M})$, of the vacuum manifold[4], $\mathcal{M}$; each homotopy group (and thus each type of defect) is topologically distinct.

Monopoles, cosmic strings and domain walls are characterized by a large energy density. For example, GUT monopoles have an energy density in the order of 10^{64} GeV^4 ($\sim 10^{85}$ kgm^{-3}), GUT cosmic strings have a linear energy density in the order of 10^{32} GeV^2 ($\sim 10^{21}$ kgm^{-1}), and GUT domain walls are characterized by sheets of energy density in the order of 10^{48} GeV^3 ($\sim 10^{53}$ kgm^{-2}). These large densities are attributed to the energy of the "false vacuum" ($\langle\Phi\rangle = 0$). Following a symmetry breaking phase transition an energy "barrier" develops between the false vacuum (at the local maximum of the potential) and the "true vacuum" ($\langle\Phi\rangle \neq 0$) at the minimum of the potential. Topological defects represent regions of false vacuum "trapped" within the true vacuum. The energy density of a defect is given by the energy difference between the symmetric state ($\langle\Phi\rangle = 0$) and the non-symmetric state ($\langle\Phi\rangle \neq 0$). Following the GUT phase transition the appearance of massive topological defects is expected to have observable cosmological consequences. For example, the gravitational effect of cosmic strings should initiate density anisotropy in the early Universe, leading to Large Scale Structure (LSS) (Zeldovich 1980,Vilenkin 1980 and Avelino and Shellard 1995). Defects should also induce anisotropy in the Cosmic

[3]That is $\Phi = \begin{pmatrix} \phi_1 \\ \phi_2 \end{pmatrix}$, where ϕ_1 and ϕ_2 are complex scalar fields.

[4]The homotopy group, $\pi_n(\mathcal{M})$, denotes a topologically distinct mapping between the n-dimensional sphere, S^n, embedded in 3-space, and the vacuum manifold, $\mathcal{M}$. The vacuum manifold represents all possible orientations of the Higgs field in its ground state.

Microwave Background Radiation (CMBR) (Vachaspati 1986, Stebbins 1988 and Bouchet *et al.* 1988). These predictions have led to tremendous interest in the role of topological defects in the early Universe, and in the models that predict their formation.

As we have noted, topological defects (predicted by particle cosmology) are subject to observational constraints, particularly those imposed by LSS formation and the CMBR anisotropy. Other constraints arise from nucleon decay processes in stars. For example, monopole production in the early Universe (Zeldovich and Khlopov 1978 and Preskill 1979) is inconsistent with the rate of nucleon decay via the processes, $p \rightarrow \pi^0 + e^+$ or $n \rightarrow \pi^- + e^+$, which take place in the Sun[5] (Kolb *et al.* 1982, Dimopoulos *et al.* 1982 and Freese *et al.* 1983). Other topological defects, such as domain walls, are inconsistent with the magnitude of the temperature anisotropy observed in the CMBR (Zel'dovich *at al.* 1975, Stebbins and Turner 1989 and Press *et al.* 1989). Therefore, these defects (monopoles and domain walls) either did not form, or formed and then were removed by inflation (Guth 1981), or were annihilated by some mechanism (see e.g., Langacker and Pi 1980 and Dvali *et al.* 1995 and 1998). More encouraging are cosmic strings that exhibit scaling behaviour[6], which means that a network of cosmic strings will not dominate the energy density of the Universe (Kibble 1985, Albrecht and Turok 1989, Allen and Shellard 1990, Bennett and Bouchet 1990 and Martin and Shellard 1996). For this reason, cosmic strings are widely studied in the literature (see e.g., Vilenkin 1985, Vachaspati 1986 and Stebbins 1988).

Although cosmological topological defects have been postulated to form following symmetry breaking phase transitions in the early Universe, there is no observational evidence for their existence. However, topological defects can be produced in condensed matter systems (see e.g., Gill 1998). For example, domain wall defects are observed in ferromagnetic systems (see e.g., Forsbergh 1949, Merz 1952 and Hooton and Merz 1955). A network of string defects has been observed in superfluid helium (see e.g., Zurek 1994 and 1996 and Hendry *et al.* 1994). String defects (or vortex-lines) have also been observed

[5]Monopoles have a baryon-number-violating coupling and therefore can act as a catalysis for nucleon decay processes (Rubakov 1981 and 1982). Since monopoles can be captured by stars, nucleon decay within the Sun sets constraints on the monopole density in the Universe. However, this constraint is inconsistent with the predicted monopole density.

[6]Scaling behaviour refers to the dilution of the energy density of string defects, which occurs at the same rate as the dilution of the energy density of the Universe due to its expansion. A scaling solution is a consequence of the decrease in the energy density of a string network due to the formation of loops, which subsequently collapse.

in other systems, such as in superconductors (Abrikosov 1957), nematic liquid crystals (Chuang *et al.* 1991 and Bowick *et al.* 1994) and Bose-Einstein condensates (Madison *et al.* 2000). A field theoretic description of phase transitions in these latter systems utilizes the Ginzburg-Landau phenomenological model with symmetry breaking facilitated by an order parameter (e.g., a wavefunction Ψ), which is analogous to the Higgs field Φ in a GUT model. Studying phase transitions in condensed matter systems may provide insight into the behaviour of topological defects in the early Universe.

The formation of topological defects following a phase transition in the early Universe exploits the Kibble mechanism (Kibble 1976 and 1980). This mechanism can also be invoked to describe defect formation in condensed matter systems. For example, Chuang *et al.* (1991) and Bowick *et al.* (1994) studied phase transitions in nematic liquid crystals under a rapid temperature quench, which produces topological defects in the form of vortex-lines.[7] Observing the evolution of the vortex-line network shows that the number density of the network dilutes rapidly when strings exchange ends upon crossing (intercommution). This results in the formation of vortex-loops, which collapse due to tension along the loop. The direct observation of intercommutation in nematic liquid crystals confirmed earlier field theoretic simulations of cosmic strings performed by Shellard (1987). The vortex-line networks in condensed matter systems has provided an important testbed for elucidating the behaviour of topological defects in the early Universe.

1.2 Effective field theories of symmetry breaking

To understand how topological defects arise, it is necessary to examine the effective field theories that predict their formation. In this section we discuss several effective field theories of particle physics that exhibit symmetry breaking.

1.2.1 The Mexican hat potential

The simplest symmetry breaking potential is the "Mexican hat" potential[8], given by

$$V(|\Phi|) = \frac{\lambda}{4}\left(|\Phi|^2 - \eta^2\right)^2 . \tag{1.1}$$

[7] Zurek (1985) suggested that vortex-lines could be produced in a rapid pressure quench in liquid helium (rather than a temperature quench). Consequently, the production of topological defects in condensed matter systems via this mechanism is often referred to as the Kibble-Zurek mechanism.

[8] It is so named because the potential when plotted as a function of a two-component (complex) scalar field has the shape of a Mexican hat.

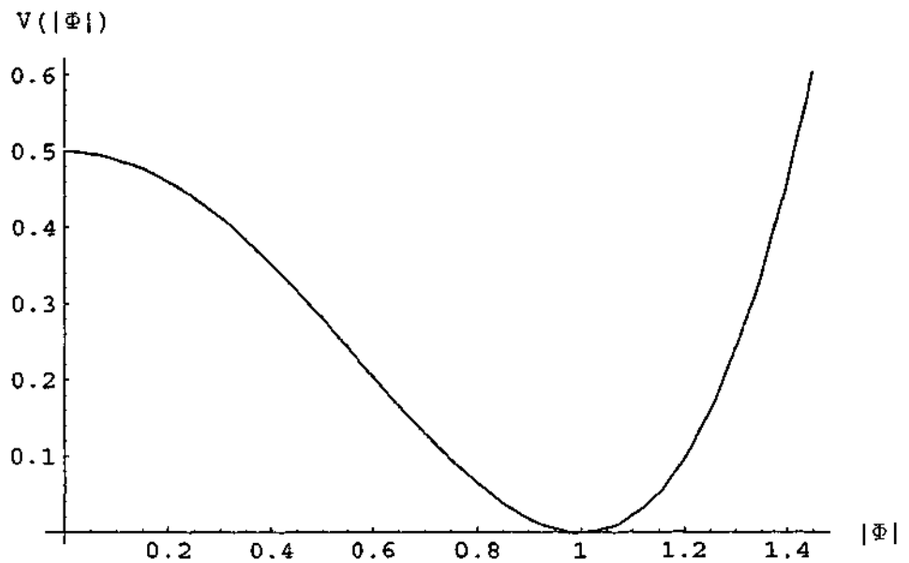

Figure 1.1: A one-dimensional cross-section of the Mexican potential, for $\eta = 1$ and $\lambda = 2$. The VEV of the Φ-field is located at $|\Phi| = \eta$.

In Eq. (1.1) Φ denotes the Higgs field with components Φ_a ($a = 1, 2, ...$), λ is a self-coupling constant, η is the symmetry breaking scale and $|\Phi| = \Phi_a \Phi_a$, where a repeated index a implies a summation over the components (i.e., $\Phi_a \Phi_a = \Phi_1^2 + \Phi_2^2 + ...$).

To show that the potential specified by Eq. (1.1) exhibits a vacuum state with broken symmetry, consider a unitary transformation $\mathcal{U}$ corresponding to a "rotation" group G defined by

$$\mathcal{U} = \exp(i\sigma_a \alpha_a), \tag{1.2}$$

where α_a ($a = 1, 2, ...$) are real scalar functions that describe "rotation" around the corresponding Lie generators σ_a ($a = 1, 2, ...$) of the group G.[9] The "rotation" is given by the unitary transformation

$$\Phi \to \Phi' = \mathcal{U}\Phi, \tag{1.3}$$

where the corresponding transformation of the complex conjugate field is $\bar{\Phi}' = \mathcal{U}^\dagger \bar{\Phi}$. Since $|\Phi'| = |\Phi|$, the model potential (1.1) is invariant under the unitary transformation (1.2).

Figure 1.1 represents a one-dimensional plot of the potential, $V(|\Phi|)$, as a function of the magnitude of the Higgs field, $|\Phi|$. The vacuum expectation value (VEV) of the

[9]For example, the Lie generators of the three-dimensional rotation group $SO(3)$ and its universal covering group $SU(2)$ are the Pauli spin matrices, $\sigma_1 = \begin{pmatrix} 0 & 1 \\ 1 & 0 \end{pmatrix}$, $\sigma_2 = \begin{pmatrix} 0 & -i \\ i & 0 \end{pmatrix}$ and $\sigma_3 = \begin{pmatrix} 1 & 0 \\ 0 & -1 \end{pmatrix}$.

Higgs field is located at the minimum of the potential, which for our one-dimensional plot occurs at $|\Phi| = \eta$. The potential is invariant under the transformation $\Phi \to \mathcal{U}\Phi$, and once a vacuum state of the Higgs field is obtained all the VEVs, $\langle\Phi\rangle$, can be found by using the unitary transformation, i.e.,

$$\langle\Phi\rangle = \mathcal{U}\eta. \tag{1.4}$$

Following a phase transition the Higgs field "chooses" a VEV by fixing $\mathcal{U}$. Once $\mathcal{U}$ is fixed the symmetry of the vacuum state is broken, i.e., the vacuum state is no longer invariant under the transformation (1.2) for arbitrary $\mathcal{U}$.

The number of components of the Higgs field Φ_a ($a = 1, 2, ...$) is dictated by the symmetry breaking model that gives rise to the topological defect. For example, domain walls, cosmic strings, and monopoles are described by models that are invariant under Z_2, $U(1)$, and $SU(2)$ transformations, respectively (see Sec. 1.2.2). These correspond to a Higgs field with one, two, and three components.

1.2.2 Higgs model with symmetry breaking

The simplest Higgs field model describing a domain wall with the Lagrangian

$$\mathcal{L} = \frac{1}{2}\partial_\mu\Phi\partial^\mu\Phi - V(|\Phi|), \tag{1.5}$$

where ∂_μ denotes differentiation with respect to the (flat) spacetime coordinates (t, x, y, z), and $V(|\Phi|)$ is the symmetry breaking potential (1.1) written in terms of a real Higgs field, Φ. The field equation is derived from Eq. (1.5) using the Euler-Lagrange formalism, i.e.,

$$\frac{\partial\mathcal{L}}{\partial\Phi} - \partial^\mu\left(\frac{\partial\mathcal{L}}{\partial(\partial^\mu\Phi)}\right) = 0. \tag{1.6}$$

Substituting Eq. (1.5) into (1.6) we obtain

$$\Box\Phi + \lambda\Phi\left(|\Phi|^2 - \eta^2\right) = 0, \tag{1.7}$$

where $\Box = \partial_\mu\partial^\mu$. Equation (1.7) is a relativistic equation with a self-interaction term $\lambda|\Phi|^2\Phi$. Since the Higgs field only has one component, the Lagrangian (1.5) is characterized by a discrete symmetry group Z_2, i.e., the Lagrangian is invariant under the symmetry transformation

$$\Phi \to \Phi' = -\Phi. \tag{1.8}$$

The vacuum state is $\langle\Phi\rangle = \pm\eta$ and the vacua are invariant under an identity transformation $\Phi \to \Phi$, so that the unbroken group is I. The formation of a domain wall is therefore described by the symmetry breaking scheme $Z_2 \to I$.

The next level of complexity is the abelian-Higgs model describing cosmic strings. In this case the Lagrangian is given by

$$\mathcal{L} = \overline{D_\mu \Phi} D^\mu \Phi - \frac{1}{4} F_{\mu\nu} F^{\mu\nu} - V(|\Phi|), \tag{1.9}$$

where $V(|\Phi|)$ is the symmetry breaking potential (1.1) and Φ is a two component (complex) Higgs field, with $|\Phi|^2 = \Phi_1^2 + \Phi_2^2$. The gauge covariant derivative D_μ and electromagnetic field tensor $F_{\mu\nu}$ are defined by

$$D_\mu = \partial_\mu - ieA_\mu \tag{1.10}$$

$$F_{\mu\nu} = \partial_\mu A_\nu - \partial_\nu A_\mu, \tag{1.11}$$

where A_μ is the electromagnetic 4-vector potential and e is the coupling strength between the Φ-field and A_μ-field. The equations of motion for the Higgs and gauge fields are derived from Eq. (1.9). Utilizing the Euler-Lagrange formalism we obtain

$$D_\mu D^\mu \Phi + \frac{\lambda}{2} \Phi \left(|\Phi|^2 - \eta^2 \right) = 0, \tag{1.12}$$

$$\Box A_\mu + ie \left(\bar{\Phi} D_\mu \Phi - \Phi \bar{D}_\mu \bar{\Phi} \right) = 0. \tag{1.13}$$

The Lagrangian (1.9) is invariant under local $U(1)$ gauge transformations, i.e.,

$$\Phi(x) \to \Phi'(x) = e^{i\theta(x)} \Phi(x), \tag{1.14}$$

$$A_\mu(x) \to A'_\mu(x) = A_\mu - (1/e)\partial_\mu \theta(x). \tag{1.15}$$

Since the VEVs of the Higgs field differ from each other by a rotation $e^{i\theta(x)}$, fixing $\theta(x)$ results in the vacuum being invariant under the identity transformation. The model Lagrangian (1.9) has a $U(1)$ symmetry group, and the symmetry breaking scheme for the formation of a cosmic string is described by $U(1) \to I$.

Finally, we briefly discuss the Higgs field for a monopole. This is formulated in terms of an isospin-conserving Yang-Mills field theory, with a Mexican hat symmetry breaking potential. The Lagrangian is gauge invariant under $SU(2)$ isospin transformations (Polyakov 1974), and is given by (see e.g., Quigg 1983)

$$\mathcal{L} = \frac{1}{2} \mathcal{D}_\mu \Phi_a \mathcal{D}^\mu \Phi_a - \frac{1}{4} F^a_{\mu\nu} F^{a\mu\nu} - V(|\Phi|), \tag{1.16}$$

where $V(|\Phi|)$ is the symmetry breaking potential and Φ now represents a three-component Higgs field, with $|\Phi|^2 = \Phi_1^2+\Phi_2^2+\Phi_3^2$; $\mathcal{D}_\mu$ denotes the non-abelian gauge covariant derivative defined by

$$\mathcal{D}_\mu\Phi_a = \partial_\mu\Phi_a - e\epsilon_{abc}A_\mu^b\Phi_c, \tag{1.17}$$

where e is a coupling constant, ϵ_{abc} is the Levi-Civita completely skew-symmetric tensor, A_μ^a is the a-th component of the gauge field, $A_\mu = A_\mu^a\sigma^a$, and $F_{\mu\nu}^a$ is the Yang-Mills field given by

$$\begin{aligned} F_{\mu\nu}^a &= \mathcal{D}_\mu A_\nu^a - \mathcal{D}_\nu A_\mu^a, \\ &= \partial_\mu A_\nu^a - \partial_\nu A_\mu^a + 2e\epsilon_{abc}A_\mu^b A_\nu^c. \end{aligned} \tag{1.18}$$

The field equations derived from the non-abelian model (1.16) are

$$\mathcal{D}_\mu\mathcal{D}^\mu\Phi_a + \lambda\Phi_a\left(\Phi_b\Phi_b - \eta^2\right) = 0, \tag{1.19}$$

$$\partial_\mu F^{a\mu\nu} - 2e\epsilon_{abc}A_\nu^b F^{c\mu\nu} + 2e\epsilon_{abc}\Phi_b\mathcal{D}_\mu\Phi_c = 0, \tag{1.20}$$

where the four-dimensional Laplacian is defined by

$$\mathcal{D}_\mu\mathcal{D}^\mu\Phi_a = \partial_\mu\mathcal{D}^\mu\Phi_a - e\epsilon_{abc}A_\mu^b\mathcal{D}^\mu\Phi_c. \tag{1.21}$$

The Lagrangian (1.16) is invariant under the local gauge transformations

$$\Phi \rightarrow \Phi' = \mathcal{U}\Phi, \tag{1.22}$$

$$A_\mu \rightarrow A'_\mu = \mathcal{U}A_\mu\mathcal{U}^{-1} - \frac{i}{e}(\partial_\mu\mathcal{U})\mathcal{U}^{-1}, \tag{1.23}$$

where $\mathcal{U}$ is the $SU(2)$ symmetry group. Since the Higgs field is a three-component scalar field, the vacuum manifold of the Higgs field is a sphere, S^2. A vacuum state is obtained by fixing the orientation of the Higgs field on the vacuum manifold. However, choosing an orientation on S^2 still leaves the Higgs field the freedom to rotate in a two-dimensional plane perpendicular to the orientation of the Higgs field. Therefore the vacuum state of a three-component Higgs field is invariant under the $U(1)$ symmetry group. The symmetry breaking scheme is described by $SU(2) \rightarrow U(1)$.

In the absence of a gauge field, the Lagrangians (1.9) and (1.16) are invariant under "global" symmetry transformations, i.e., transformations that do not depend on the spacetime coordinates. Models that are invariant under coordinate-dependent symmetry transformation are referred to as "local". The introduction of a gauge field changes the

nature of the symmetry transformations, and is expected to have significant ramifications for defect interactions. In the next section we discuss how interactions differ in local and global models.

1.2.3 Local and global models

We begin by considering the abelian-Higgs model specified by Eq. (1.9). Goldstone (1961) predicted that symmetry breaking gives rise to massless particles (called Goldstone bosons). To see how Goldstone bosons arise in a symmetry breaking model consider a complex scalar (Higgs) field defined by

$$\Phi(\mathbf{x},t) = f(\mathbf{x},t)e^{i\theta(\mathbf{x},t)}, \tag{1.24}$$

where $\mathbf{x}$ denotes the Cartesian coordinates (x,y,z), $\theta(\mathbf{x},t)$ is the phase angle around the vacuum manifold, $\mathcal{M}$, and $f(\mathbf{x},t)$ is the magnitude of the Higgs field. Since the abelian-Higgs model is invariant under local gauge transformations, the exponential term in Eq. (1.24) can be transformed away via $\Phi(\mathbf{x},t) \rightarrow e^{-i\theta(\mathbf{x},t)}\Phi(\mathbf{x},t)$, leaving only the magnitude. Thus in the unitary gauge, it is possible to write the Higgs field as

$$\Phi(\mathbf{x},t) = f(\mathbf{x},t)\begin{pmatrix} 0 \\ 1 \end{pmatrix}. \tag{1.25}$$

In this gauge, the abelian-Higgs model (1.9) becomes

$$\mathcal{L} = \partial_\mu f \partial^\mu f - \frac{1}{4}F_{\mu\nu}F^{\mu\nu} - e^2 f^2 A_\mu A^\mu - \frac{1}{4}\lambda\left(f^2-\eta^2\right)^2. \tag{1.26}$$

Equation (1.26) describes a massive scalar Higgs field $m_\Phi = \eta\sqrt{\lambda/2}$ and a massive vector boson $m_v = e\eta$. There are no massless Goldstone bosons in the abelian-Higgs model. In the absence of the gauge field the abelian-Higgs model (1.9) reduces to the Goldstone model, i.e.,

$$\mathcal{L} = \overline{\partial_\mu \Phi}\partial^\mu\Phi - \frac{1}{4}\lambda\left(|\Phi|^2-\eta^2\right)^2. \tag{1.27}$$

The Goldstone model (1.27) is invariant under a global $U(1)$ transformation, $\Phi \rightarrow e^{i\theta}\Phi$. In this model, it is not possible to gauge away the exponential term in the Higgs field (1.24), since such a transformation requires the presence of a gauge field. Substituting Eq. (1.24) into Eq. (1.27) we obtain

$$\mathcal{L} = \partial_\mu f \partial^\mu f + f^2\partial_\mu\theta\partial^\mu\theta - \frac{\lambda}{4}\left(f^2-\eta^2\right)^2. \tag{1.28}$$

The Lagrangian (1.28) describes a massive Higgs field and a massless Goldstone boson. By varying Eq. (1.28) with respect to f and θ, the equations of motion are

$$\left[\Box - \left(\partial_\mu\theta\partial^\mu\theta + \frac{\lambda}{2}\eta^2\right)\right] f + \frac{\lambda^3}{2}f^3 = 0, \tag{1.29}$$

$$\Box\theta + \frac{2}{f}\left(\partial_\mu f\right)\left(\partial^\mu\theta\right) = 0. \tag{1.30}$$

Equation (1.29) is the equation of motion for the magnitude of the Higgs field with an effective mass $\sqrt{\eta^2\lambda/2 + \partial_\mu\theta\partial^\mu\theta}$; the second equation (1.30) describes a massless Goldstone boson field, which arises due to the global nature of the symmetry breaking.

Massless Goldstone bosons arise in models with global symmetry, however, there are no massless Goldstone bosons if the system exhibits local symmetry. The Goldstone boson "disappears" when the gauge field is introduced, resulting in a massive gauge field[10] which depends on the symmetry breaking scale η. This is known as the Higgs mechanism, whereby a massless particle acquires mass via interacting with the Higgs field (Higgs 1964).

Since the Goldstone boson is massless, topological defects described by global models are expected to have long-range interactions. For example, two global vortices experience a repulsive interaction, whereas a vortex and an anti-vortex experience an attractive interaction (Perivolaropoulos 1992 and Shellard 1987). However, the gauge field removes the massless Goldstone bosons, and screens the long-range interactions between defects.

1.3 Temperature dependence of the symmetry breaking potential

Although the zero temperature symmetry breaking potential (1.1) provides a simple description of the vacuum state of the Higgs field following the phase transition, it does not describe how the Higgs field interacts with particles in the early Universe, nor does it give any insight into how the phase transition occurred. To describe the symmetry breaking phase transition and to better understand the formation of topological defects requires a temperature-dependent symmetry breaking potential.

Following Jackiw (1974) and Dolan and Jackiw (1974), we write the effective temperature-dependent potential as the sum of a temperature independent part and a temperature-dependent part, i.e.,

$$V(|\Phi|,\beta) = V_0(|\Phi|) + \sum_i V_i(|\Phi|,\beta), \tag{1.31}$$

[10] In colloquial language we say that the gauge field becomes massive by "eating" the massless Goldstone bosons.

where $\beta = 1/T$. The term $V_0(|\Phi|)$ is the contribution to the effective potential in the tree approximation, and $\sum_l V_l(|\Phi|, T)$ is the sum over connected loop diagrams in the higher order perturbation series. In the tree approximation the zero temperature symmetry breaking (Mexican hat) potential is given by Eq. (1.1). Ignoring a constant term this potential is

$$V_0(|\Phi|) = -\frac{\lambda\eta^2}{2}|\Phi|^2 + \frac{\lambda}{4}|\Phi|^4. \tag{1.32}$$

To evaluate the exact temperature dependence would require a summation over all connected loop diagrams. We can obtain a qualitative understanding of the symmetry breaking phase transition by utilizing only the $l = 1$ term in Eq. (1.31). The one-loop correction, $V_1(|\Phi|, \beta)$, has been computed by Jackiw (1974) and Dolan and Jackiw (1974) for the case of a spin-0 scalar field, i.e., neglecting contributions from the vector boson and fermion fields. It is found that the temperature-dependent potential at the one-loop level is given by

$$V_1(|\Phi|, \beta) = -\frac{\pi^2}{90}\beta^{-4} + \frac{m_\Phi^2}{24}\beta^{-2}, \tag{1.33}$$

where m_Φ is the zero temperature Compton mass of the Higgs field defined by

$$m_\Phi^2 = \lambda|\Phi|^2 - \frac{\lambda\eta^2}{2}. \tag{1.34}$$

The temperature-dependent one-loop correction (1.33) is accurate to $\mathcal{O}(\beta^{-1})$. Additional terms are not included in $V_1(|\Phi|, \beta)$ because they are unphysical. For example, the next term in $V_1(|\Phi|, \beta)$ is $m_\Phi^3\beta^{-1}/12\pi$ which can become imaginary when $|\Phi|$ fluctuates about $\eta^2/2$. Successive terms in $V_1(|\Phi|, \beta)$ either do not vanish in the zero temperature limit, or become infinite (Dolan and Jackiw 1974). However, Dolan and Jackiw (1974) suggest that the infinite one-loop terms (at zero temperature) are exactly cancelled by temperature-dependent infinite terms at the two-loop level. Consequently, the temperature-dependent symmetry breaking potential at the one-loop level may be written as

$$V(|\Phi|, \beta) = \frac{\lambda}{4}|\Phi|^4 + \left(\frac{\lambda}{24\beta^2} - \frac{\lambda\eta^2}{2}\right)|\Phi|^2 - \frac{\lambda\eta^2}{48\beta^2} - \frac{\pi^2}{90\beta^4}. \tag{1.35}$$

We will assume that Eq. (1.35) provides a qualitatively correct description of a phase transition in the early Universe. Equation (1.35) corresponds to the Landau-Ginzburg potential, which describes a second order phase transition in a variety of condensed matter systems (see e.g., Zurek 1996).

At zero temperature Eq. (1.35) reduces to the Mexican hat potential (1.1). Since the last two terms in Eq. (1.35) do not couple to the Higgs field, they do not affect the vacuum state. From Eq. (1.35) it can be seen that the temperature dependence of the vacuum state is determined by the term $\lambda|\Phi|^2/24\beta^2$. Since this term is positive, adding it to $-\lambda\eta^2|\Phi|^2/2$ would effectively decrease the magnitude of the Higgs field in the vacuum state. The decrease in the VEV depends upon the temperature T. More specifically the temperature-dependent vacuum state of the Higgs field, $\langle\Phi\rangle$, is determined from

$$\frac{\partial V(|\Phi|,\beta)}{\partial|\Phi|} = 0 \quad (\Phi \neq 0). \tag{1.36}$$

Using the temperature-dependent potential (1.35), we can approximate the VEV of the Higgs field at non-zero temperature as

$$|\Phi|^2 = \eta^2 - \frac{1}{12\beta^2}. \tag{1.37}$$

The critical temperature, T_c, for the phase transition is characterized by a vanishing vacuum expectation, $\langle\Phi\rangle = 0$, whence

$$T_c = \frac{1}{\beta_c} = \sqrt{12}\eta. \tag{1.38}$$

Equation (1.38) indicates that the critical temperature of the phase transition is proportional to the symmetry breaking scale of the Higgs field. It also follows from Eq. (1.34) that the Compton mass of the Higgs field (in the vacuum state) is proportional to the symmetry breaking scale, and therefore the critical temperature is given by

$$T_c = \frac{1}{\beta_c} = \sqrt{\frac{24}{\lambda}}m_\Phi. \tag{1.39}$$

For temperatures $T > T_c$, the coefficient of the $|\Phi|^2$-term in the potential (1.35) is positive, which results in a vanishing VEV. At the critical temperature ($T = T_c$), the coefficient vanishes and the potential is described by a quartic term in the Φ-field. Below the critical temperature the coefficient of the $|\Phi|^2$-term is negative, which results in a non-vanishing VEV for the Higgs field. This results in the symmetry of the vacuum state being broken. The temperature-dependent behaviour of the potential is shown in Fig. 1.2.

As the temperature of the early Universe decreased below a critical temperature a phase transition occurred, leading to non vanishing VEVs of the Higgs field. The broken symmetry phase will manifest itself as different choices of the local vacua in regions which

(a)

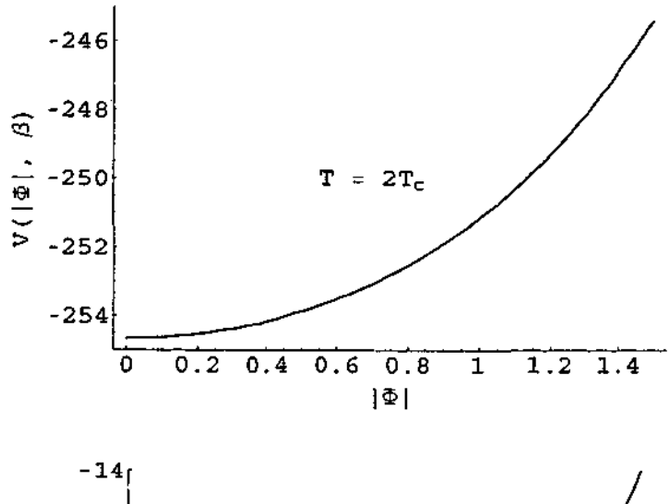

(b)

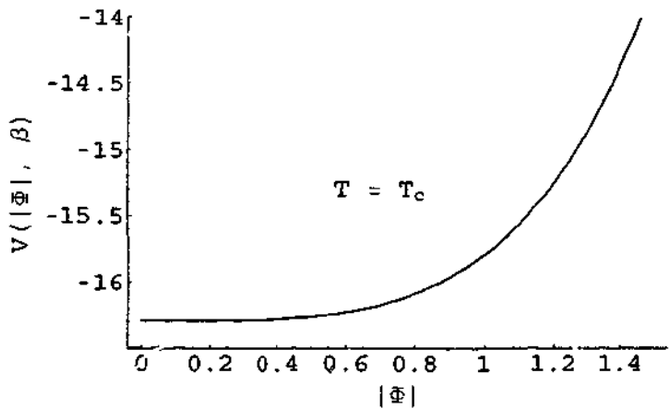

(c)

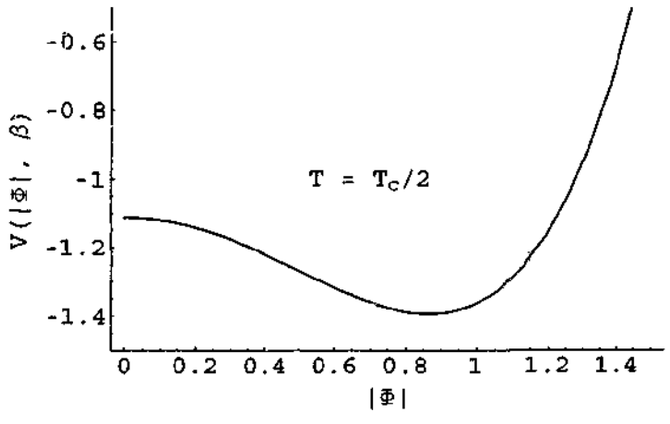

Figure 1.2: Temperature dependence of the symmetry breaking potential given by Eq. (1.35) ($\lambda = 2$, $\eta = 1$). (a) Above the critical temperature, $T_c = \sqrt{12}$, (b) at the critical temperature, and (c) below the critical temperature. This plot shows the characteristic features of a symmetry breaking phase transition. The VEV of the Higgs field vanishes ($\langle\Phi\rangle = 0$) for $T > T_c$ and is non-vanishing ($\langle\Phi\rangle \neq 0$) when the system passes through the critical temperature. This results in the VEV of the Higgs field breaking the symmetry of the Lagrangian.

are space-like separated. Following the phase transition, these disconnected regions, with different VEVs, came into contact with each other. This scenario was first discussed by Kibble (1976) and results in the formation of topological defects, where the defect type is determined by the symmetry breaking scheme.

1.4 Classification and formation of topological defects

In this section we discuss the classification of topological defects and their formation via the Kibble mechanism. The classification of topological defects and the manner in which defects interact is central to the work reported in this thesis.

1.4.1 Classification of topological defects

Topological defects are classified according to the homotopy group of the vacuum manifold, $\pi_n(\mathcal{M})$. For the symmetry breaking scheme $G \to H$, where G is a symmetry group and H is a subgroup, the vacuum manifold of the Higgs field $\mathcal{M}$ describes the space of all possible configurations of the VEV, i.e.,

$$\mathcal{M} = G/H. \tag{1.40}$$

The n-th homotopy group, $\pi_n(\mathcal{M})$, classifies distinct mappings from $\mathcal{M}$ to the n-dimensional sphere $C = S^n$.

Topological defects are constructed from a mapping, f, between the vacuum manifold, $\mathcal{M}$, and the n-dimensional sphere, in physical space, i.e.,

$$f : \mathcal{M} \to C. \tag{1.41}$$

The equations of motion of the Higgs field require that the mapping between $\mathcal{M}$ and C be continuous and differentiable (smooth). Consequently we can only deform the surface C in physical space in such a way that f is continuous and differentiable.

The mapping can be understood by considering a surface $C = S^n$ embedded in a N-dimensional physical space. We start by examining the mapping between the vacuum manifold of a domain wall Z_2 and the surface $C = S^0$ (embedded in one, two and three spatial dimensions). The Higgs field, Φ, of a domain wall has two possible orientations in the vacuum manifold, i.e., $\Phi = \pm\eta$. Figure 1.3 (a) illustrates the orientation of the Higgs field of a domain wall and the surface $C = S^0$ embedded in one spatial dimension. As the surface C is contracted to a point, the orientation of the Higgs field is undefined. To keep

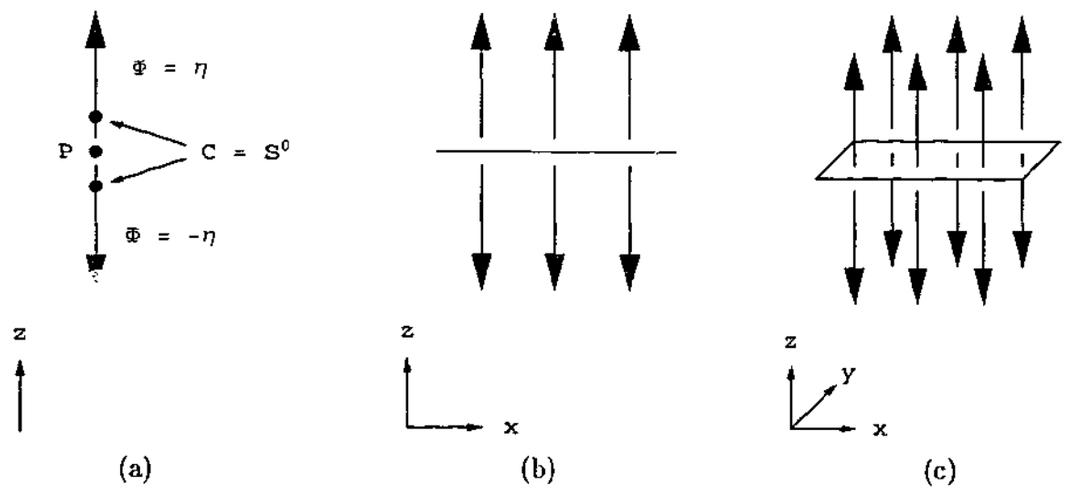

Figure 1.3: Schematic showing the construction of a domain wall in one, two and three spatial dimensions. Arrows indicate the orientation of the Higgs field in the vacuum manifold. (a) As $C = S^0$ shrinks to a point (P) the orientation of the Higgs field is undefined, and departs from the vacuum manifold. To keep the Higgs field in the vacuum manifold, C cannot be contracted to a point. This represents a non-trivial mapping between $\mathcal{M}$ and C, i.e., $\pi_0(\mathcal{M}) \neq I$. In one spatial dimension a domain wall is a point defect, (b) in two spatial dimensions it has a linear extension, and (c) in three spatial dimensions it is a sheet defect.

the Higgs field in its vacuum manifold, the surface C cannot be contracted to a point. This gives rise to a stable domain wall defect. In higher dimensions, the surface C can traverse a path in the additional dimensions and still maintain continuity and differentiability of f. Thus a domain wall is a line defect in two dimensions and a sheet defect in three dimensions (see Figs. 1.3 (b) and (c)).

The Higgs model of a cosmic string is invariant under a $U(1)$ symmetry transformation, and therefore its vacuum manifold is a circle, i.e., $\langle\Phi\rangle = \eta e^{i\theta}$. Figure 1.4 (a) illustrates the orientation of the Higgs field in the vacuum manifold and the embedding of a surface $C = S^1$ in two spatial dimensions. As the loop C is contracted to a point, the orientation of the Higgs field is undefined. To reconcile this undefined orientation, the magnitude of the Higgs field must vanish, i.e., $|\Phi| = 0$, which means that the Higgs field departs from the vacuum manifold. It is not possible to contract the loop C to a point without the Higgs field departing from the vacuum manifold. This gives rise to a stable (cosmic) string defect. In two dimensions this defect is a vortex (i.e., a point defect). In three spatial dimensions the loop C can traverse a path in the additional dimension while still

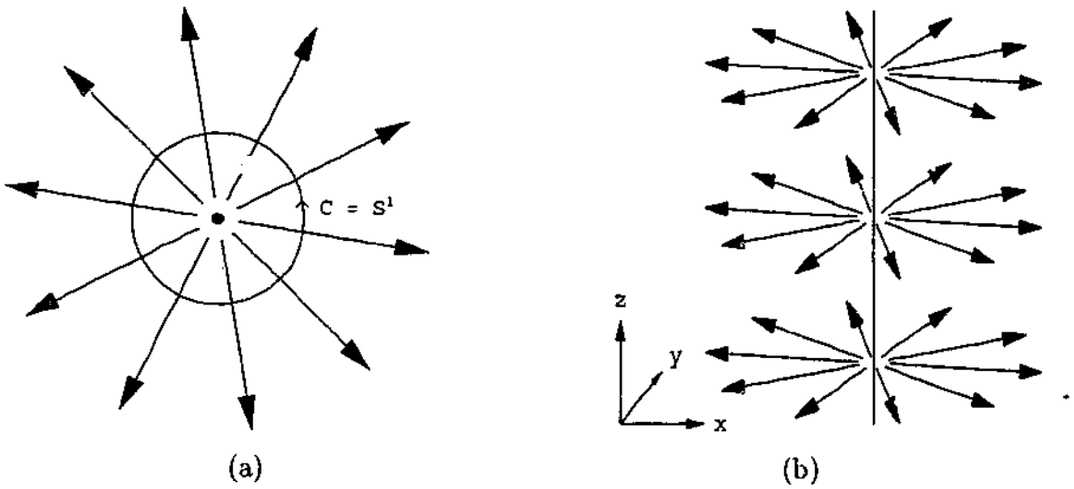

Figure 1.4: Schematic showing the construction of a (cosmic) string in two and three spatial dimensions. Arrows indicate the orientation of the Higgs field in the vacuum manifold. (a) As the loop $C = S^1$ shrinks to a point, the orientation of the Higgs field is undefined. This results in a non-trivial mapping between $\mathcal{M}$ and C, i.e., $\pi_1(\mathcal{M}) \neq I$. In two spatial dimensions this defect is a vortex. (b) In three spatial dimensions the defect has a linear extension and represents a string.

maintaining continuity and differentiability of f; in this case we have a line defect.

The Higgs model of a monopole is invariant under an $SU(2)$ or an $SO(3)$ symmetry transformation, therefore the vacuum manifold is a sphere. The orientation of the Higgs field in the vacuum manifold adopts a "hedgehog" configuration. Figure (1.5) illustrates the "hedgehog" orientation of the Higgs field. For a surface $C = S^2$ embedded in three spatial dimensions it is not possible to contract C to a point while keeping the Higgs field in the vacuum manifold. This gives rise to a stable monopole (point) defect.

To preserve continuity and differentiability of the mapping f, the n-dimensional sphere enclosing the "false vacuum" ($\langle\Phi\rangle = 0$) cannot be contracted to a point. When this situation arises, the homotopy group of the vacuum manifold is said to be non-trivial, i.e., $\pi_n(\mathcal{M}) \neq I$. Domain walls, cosmic strings and monopoles arise when $\pi_0(\mathcal{M}) \neq I$, $\pi_1(\mathcal{M}) \neq I$ and $\pi_2(\mathcal{M}) \neq I$, respectively; whereas textures arise when $\pi_3(\mathcal{M}) \neq I$. The homotopy classification of topological defects is summarized in table 1.1.

The dimensionality of a topological defect depends upon the number of spatial dimensions. In higher spatial dimensions, the non-contractable surface characterizing a defect has the freedom to traverse the additional spatial dimensions. In four dimensions a domain

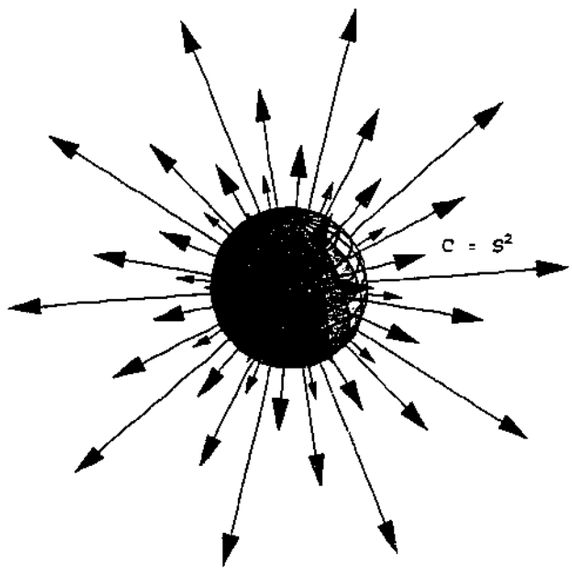

Figure 1.5: Schematic showing the construction of a monopole in three dimensions. Arrows indicate the orientation of the Higgs field in the vacuum manifold. It is not possible to contract the surface $C = S^2$ to a point, and consequently the mapping between $\mathcal{M}$ and C is non-trivial, i.e., $\pi_2(\mathcal{M}) \neq I$. In three spatial dimensions a monopole is a point defect.

wall, cosmic string and monopole become a volume, sheet and line defect, respectively.

1.4.2 Defect formation via the Kibble mechanism

Topological defects form when the scalar field (in three-dimensional space) chooses a VEV for which there is a non-trivial mapping between the vacuum manifold of the Higgs field and a surface embedded in physical space. A topologically non-trivial configuration of the Higgs field can arise in a symmetry breaking phase transition. To see how this occurs consider the formation of string defects.[11] Following a symmetry breaking phase transition the vacua of the scalar field are non-vanishing throughout space.[12] Each point in the vacuum can be parameterized by the phase (or orientation) of the Higgs field, $\theta \in [0, 2\pi]$, where the vacuum at $\theta = 0$ and at 2π are identified. As there is no energy difference between two different vacua, θ can adopt a random value between 0 and 2π. The choice of the vacuum state depends on fluctuations in Φ during the phase transition. The distance

[11] Other topological defects, such as domain walls and monopoles, form in the same way.

[12] For the phase transition to occur simultaneously throughout space, the temperature of the Universe is assumed to be uniform. This assumption is consistent with the homogeneity of the Universe on the largest scale, as confirmed by observations of the CMBR.

Topological defect	Dimension of defect	Homotopy classification
Domain wall	2	$\pi_0(\mathcal{M}) \neq I$
Cosmic string	1	$\pi_1(\mathcal{M}) \neq I$
Monopole	0	$\pi_2(\mathcal{M}) \neq I$
Texture	Not localized	$\pi_3(\mathcal{M}) \neq I$

Table 1.1: The homotopy classification of topological defects. Topological defects arise from a non-contractable mapping of the vacuum manifold $\mathcal{M} = G/H$ into the n-dimensional sphere S^n. The dimensionality refers to the situation when the defect is embedded in three spatial dimensions.

over which Φ fluctuates is given by the correlation length, ξ, which is the order of the inverse Compton mass of the Φ-field (see e.g., Kibble 1976), i.e.,

$$\xi \sim m_{\Phi}^{-1}. \tag{1.42}$$

From Eq. (1.39) we note that $m_{\Phi} \propto T_c$, and hence the correlation length is inversely proportional to the phase transition temperature in the early Universe.[13] For distances larger than the correlation length, the possible orientations of the Higgs field are not expected to be correlated and the Higgs field will adopt random values in regions separated by distances larger than ξ. Kibble (1976) conjectured that immediately after the phase transition the Universe can be divided into different regions, or "domains", with each "domain" being the size of the correlation length. The Φ-field in each "domain" has a random orientation, but Φ is assumed to smoothly vary over the size of the correlation length and it is possible that the vacuum "domain" structure adopts the configuration shown in Fig. 1.6 (a). Figure 1.6 (b) shows that as the "domain" structure expands and boundaries collide, there are regions that cannot be contracted to a point without leaving the vacuum manifold; this results in the formation of topological defects. This mechanism for producing topological defects is known as the Kibble mechanism.

Figure 1.7 shows a numerical simulation of a typical phase transition illustrating the Kibble mechanism. The symmetry breaking scheme is $U(1) \rightarrow I$, leading to the formation of cosmic string defects (which are vortices in two dimensions). The bubbles of new phase expand and collide, segmenting space into "domains" whose size is the correlation length

[13]Following the phase transition the correlation length is constrained by the causal horizon, d_H. The Higgs field in regions separated by a distance larger than d_H is not expected to be correlated.

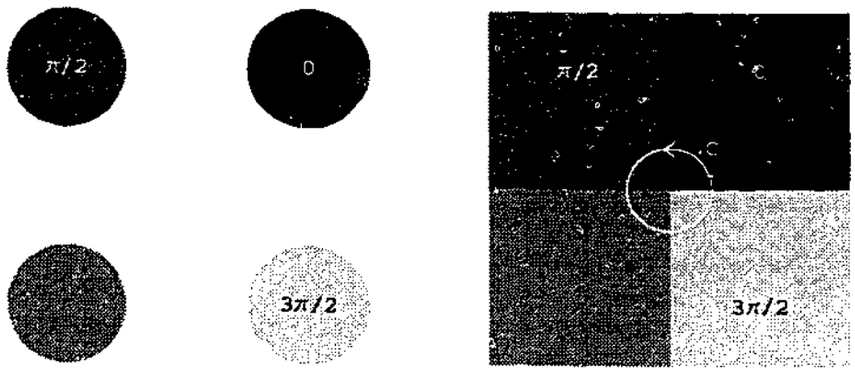

Figure 1.6: Schematic representation of a possible configuration of the Higgs field during a phase transition. (a) Initial configuration, and (b) at the end of the phase transition. The loop C at the center of (b) cannot be contracted to a point without leaving the vacuum manifold. The Φ-field at this point constitutes a topological defect (i.e., a string defect).

ξ (see Fig. 1.7 (c)). Figure 1.7 (d) shows the subsequent formation of string defects.

Once formed, topological defects are characterized by their energy density. The potential energy density of the false vacuum is higher than in the true vacuum, and the false vacuum traps energy inside the defect. The energy density of the defect can be obtained by inspecting the symmetry breaking potential (1.1). Since topological defects are regions with undefined phase (or orientation), the magnitude of the scalar field must vanish at the center of the defect. Setting $|\Phi| = 0$, we obtain the energy density of the defect as

$$\rho = \frac{\lambda}{4}\eta^4 = \frac{m_\Phi^4}{\lambda}. \tag{1.43}$$

The mass, m_Φ, of the Higgs particle is currently unknown. However, experiments from the LEP accelerator at CERN constrain the mass of the Higgs particle to be greater than 115 GeV (McNamara and Wu 2002). A Higgs particle with mass greater than 115 GeV corresponds to a cosmic string width of less than 2×10^{-18} m. Therefore, the size of the topological defect is expected to be only a fraction of the radius of an atomic nucleus; however, the defect is very massive. We can estimate the mass per unit length of a cosmic string from the symmetry breaking scale, η. Using the energy density in Eq. (1.43), and estimating the size of the cosmic string from the correlation length, ξ, we write the mass density as

$$\mu = \pi\xi^2\rho = \frac{\pi}{2}\eta^2 \sim \eta^2. \tag{1.44}$$

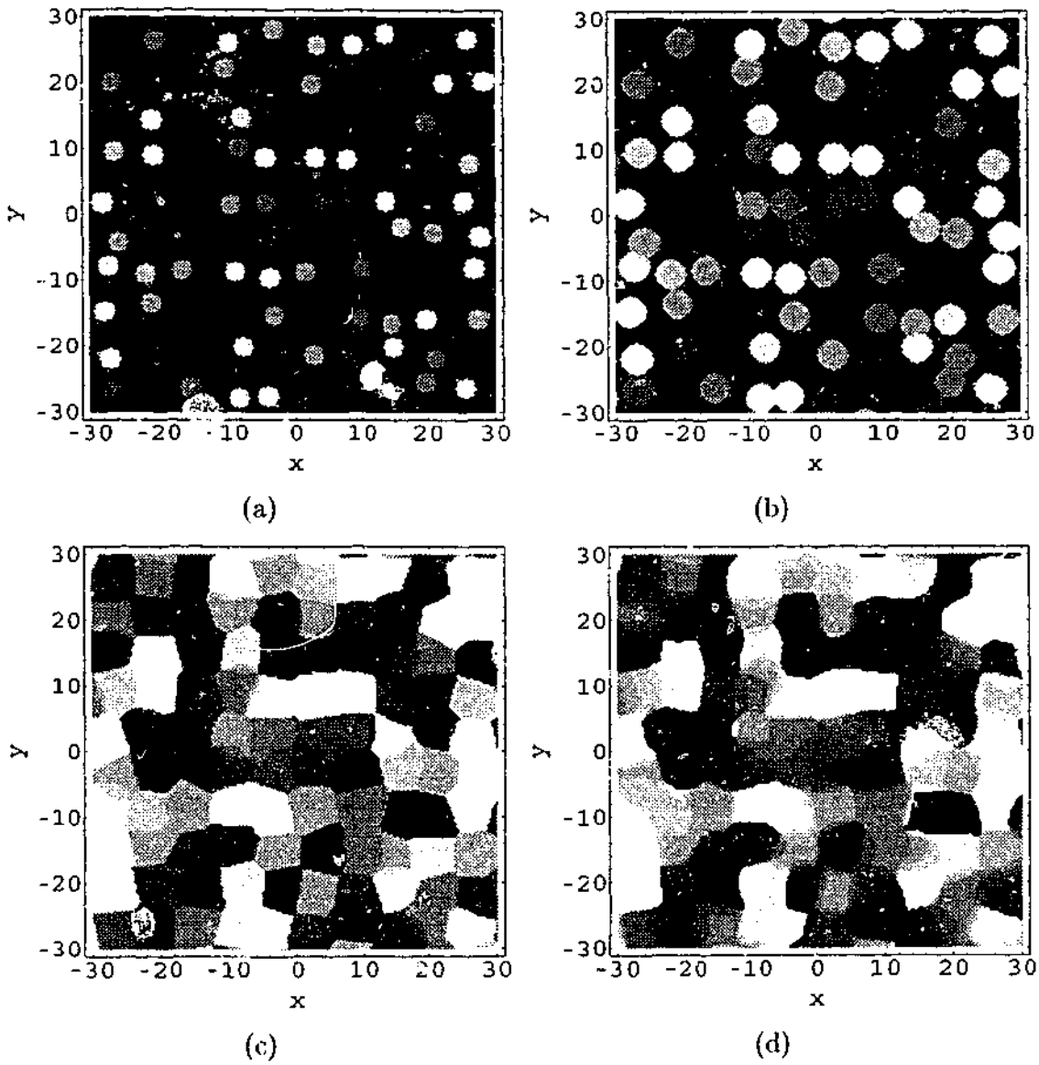

Figure 1.7: Numerical simulation based on the global Higgs model (1.27), with symmetry breaking scheme $U(1) \rightarrow I$. The phase of the Higgs field, Φ, is represented by a grey scale, with black denoting a phase of 0 and white denoting a phase of 2π. The spacetime coordinates are in units of the Compton width of the Higgs field, $1/\eta\sqrt{\lambda/2}$. Figures (a), (b) and (c) show the nucleation, expansion and collision of causally disconnected regions of size ξ. Further evolution at (d) shows that there are regions with 2π phase winding that cannot be contracted to a point. These represent a non-trivial winding around the S^1 vacuum manifold and describe cosmic string defects.

For realistic Grand Unified Theories (GUTs) the symmetry breaking scale is $\eta \sim 10^{16}$ GeV (see e.g., Vilenkin and Shellard 1994).

The large symmetry breaking scale and mass density of primordial topological defects means that they cannot be produced in a terrestrial laboratory. Much of our understanding of the formation and evolution of topological defects in the early Universe is based on numerical simulations. However, since phase transitions are common in condensed matter systems, it is possible to study the formation and evolution of topological defects in analogue models of the early Universe. Despite enormous differences in the length and energy scales, the same general phenomenon of symmetry breaking phase transitions is exhibited by the two systems.

1.5 Symmetry breaking phase transitions in condensed matter systems

In this section we discuss symmetry breaking phase transitions in condensed matter systems. An important parameter in describing the thermodynamical properties of a condensed matter system is the Helmholtz free energy, F. The thermodynamics of the system may be understood by investigating how the free energy of the system changes with respect to the wavefunction, Ψ, of the system. We start by deriving the free energy for a simple symmetry breaking model.

A symmetry breaking phase transition relevant to this thesis is the transition to a Bose condensate (such as superfluid helium or a Bose-Einstein condensate). We follow Ginzburg and Landau (1950) in obtaining an expression for the free energy of the system as a function of the condensate wavefunction Ψ. Since $|\Psi|^2$ is the probability density (or number density) of the condensate, the ground state expectation value of Ψ must be zero above the critical temperature, T_c. Below the critical temperature $|\Psi|^2$ is non-vanishing. For temperatures close to T_c, the free energy may be expanded in a power series. An expression for F accurate for two-body interactions is given by

$$F = a + b|\Psi| + c|\Psi|^2 + d|\Psi|^3 + e|\Psi|^4, \tag{1.45}$$

where the coefficients a, b, c, d and e are temperature-dependent parameters. A property of the free energy is that at equilibrium its value is a minimum, i.e.,

$$\frac{\partial F}{\partial |\Psi|} = b + c|\Psi| + d|\Psi|^2 + e|\Psi|^3 = 0. \tag{1.46}$$

Since $|\Psi| = 0$ above T_c, the equilibrium state of the system requires that $b = 0$. Ignoring a trivial constant term, the free energy becomes

$$F = c|\Psi|^2 + d|\Psi|^3 + e|\Psi|^4. \tag{1.47}$$

The shape of the free energy depends on the parameters c, d and e. For example, when $d \neq 0$ it is possible that the free energy could adopt the form shown in Fig. 1.8. Figure 1.8 shows the free energy at two different temperatures, T_1 and T_2. The free energy at T_1 does not exhibit broken symmetry since the ground state of the system occurs at $|\Psi| = 0$. However, at T_2 the system possesses a local minimum at $|\Psi| = 0$ (a symmetric ground state), a local maximum at P_B, and another local minimum at P_M (a non-symmetric ground state). The non-symmetric ground state has a free energy lower than the symmetric ground state. Above the critical temperature the ground state of the system is symmetric, hence the ground state must change from a symmetric state to a non-symmetric state during the phase transition. Continuity of the wavefunction requires that the system evolving from $|\Psi| = 0$ to P_M must pass through an energy barrier at P_B. The transition from the symmetric state to a non-symmetric state is only possible via quantum fluctuations in the Ψ-field.[14] This implies that the change cannot occur continuously and bubbles of non-symmetric phase nucleate inside the bulk symmetric phase. This is characteristic of a first order phase transition.[15]

For $d = 0$ the free energy may be written as

$$F = c|\Psi|^2 + e|\Psi|^4, \tag{1.48}$$

which has the same form as the zero temperature symmetry breaking potential (1.32). Comparing Φ in Eq. (1.32) with Ψ in Eq. (1.47), we note that the parameters c and e can be identified with $-\lambda\eta^2/2$ and $\lambda/4$, respectively. This suggests that the Helmholtz free energy in condensed matter physics plays the same role as the potential energy (density) in the Higgs model. To pursue the analogy between phase transitions in the early Universe

[14]Quantum fluctuations (in the free energy) are allowed by the uncertainty principle, i.e., $\Delta F \Delta t \sim \hbar$. For a short period of time $\Delta t < \hbar/F_B$ (where F_B is the free energy barrier at P_B), the system in some regions can temporarily have free energy larger than F_B. This allows the wavefunction in these regions to adopt values corresponding to the non-symmetric phase.

[15]The order of a phase transition is commonly characterized by the Ehrenfest scheme, i.e., by a discontinuity in the n-th derivative of the free energy. It is first order ($n = 1$) if the first derivative is discontinuous, and higher order if the discontinuity occurs for $n > 1$. In a continuous (second order) phase transition the system changes smoothly from the symmetric to the non-symmetric state throughout space.

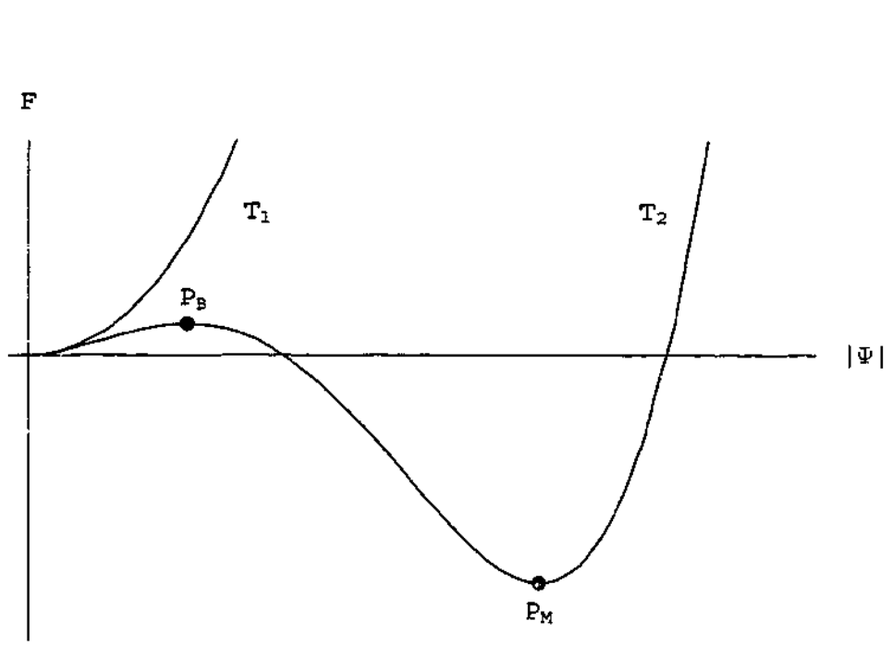

Figure 1.8: The Helmholtz free energy, F, as a function of $|\Psi|$ for two different temperatures T_1 and T_2. At T_1 the free energy corresponds to the system above the phase transition with vanishing ground state, whereas at T_2 the free energy is indicative of a first order phase transition.

and condensed matter systems, consider the simple temperature-dependent model used to characterize a phase transition (see e.g., Gill 1998)

$$F = c_0 (T - T_c) |\Psi|^2 + e|\Psi|^4. \tag{1.49}$$

Ginzburg and Pitaevskii (1958) adopted this form of the free energy to formulate a theory of phase transitions in superfluid helium. Zurek (1985) has also employed Eq. (1.49) to describe a pressure quench of superfluid ^{4}He leading to the formation of vortex-lines. The free energy (1.49) has a simple interpretation. For $T > T_c$ the coefficient of the $|\Psi|^2$-term is positive and the minimum of the free energy occurs at $|\Psi| = 0$ (symmetric ground state). At $T = T_c$ the $|\Psi|^2$-term vanishes and the phase transition occurs. For $T < T_c$ the coefficient of the $|\Psi|^2$-term is negative and the minimum of the free energy occurs at $|\Psi| \neq 0$ (non-symmetric ground state).[16] In the present context the behaviour of the wavefunction (or order parameter) in condensed matter systems is analogous to the

[16]The symmetric state corresponds to the "disordered" state and the non-symmetric state to the "ordered" state. The symmetric state exists at a temperature above the critical temperature, where there are large fluctuations in the Ψ-field. Further, the symmetric state is described by a Ψ-field with phase angle (or orientation) which is not well defined (since the magnitude of the Ψ-field vanishes); whereas the non-symmetric state has a well defined orientation. For this reason the Ψ-field is also known as the order parameter.

behaviour of the Higgs field during a phase transition (see Sec. 1.3).

A kinetic energy term can be added to the free energy (1.48). The total free energy (Lagrangian) of the system can now be written as

$$F = i\hbar\left(\Psi\frac{\partial\bar{\Psi}}{\partial t} - \bar{\Psi}\frac{\partial\Psi}{\partial t}\right) - \frac{\hbar^2}{2m}\nabla\Psi\cdot\nabla\bar{\Psi} + c|\Psi|^2 + e|\Psi|^4. \tag{1.50}$$

The equation of motion of the condensate order parameter follows from the Euler-Lagrange formalism. This results in a non-linear Schrödinger equation with broken symmetry, i.e.,

$$i\hbar\frac{\partial\Psi}{\partial t} = -\frac{\hbar^2}{2m}\nabla^2\Psi + c\Psi + 2e|\Psi|^2\Psi. \tag{1.51}$$

In the absence of coupling to the electromagnetic field, Eq. (1.51) represents a global model, which describes the evolution of the wavefunction of a neutral condensate. The model (1.51) can be generalized to describe a condensate coupled to the electromagnetic field (such as in a superconductor). This can be accomplished by incorporating the 4-vector potential, $(A_0, \mathbf{A})$, using the rule of minimal coupling, i.e., via the replacements $\partial/\partial t \to \partial/\partial t - ieA_0$ and $\nabla \to \nabla - ie\mathbf{A}$.

It can be shown that the parameter $-c$ plays the role of the chemical potential of the system, whilst e is related to the atomic two-body coupling strength (or self-interaction strength). This interpretation will be pursued in Chapter 2. However, to see that $-c$ plays the role of the chemical potential, replace c by $-\mu$ in Eq. (1.48). A phase transition occurs when c is negative, implying that the chemical potential is positive. The negative term, $-\mu|\Psi|^2$, indicates that the Helmholtz free energy is lower for $\mu > 0$. Since a negative energy term corresponds to an attractive inter-particle interaction, positive μ suggests that there is an energy cost in removing a particle from the system, which is consistent with the role of chemical potential.[17]

This interpretation suggests that the chemical potential μ in a condensed matter system can be identified with $\lambda\eta^2/2 - \lambda T^2/24$ in the temperature-dependent Higgs potential (1.35). In both condensed matter systems and in the Higgs model, a symmetry breaking phase transition occurs when the chemical potential changes sign from negative to positive (i.e., when the system passes through its critical temperature).

Since topological defects arise in a symmetry breaking phase transition, as a consequence of the Kibble mechanism (Chuang *et al.* 1991 and Bowick *et al.* 1994), it is possible

[17] It costs energy to remove a particle from a system with attractive inter-particle interactions, since the forces acting on the particle (due to all other particles) will pull the particle back into the system. However, this is not the case for a particle in a system with repulsive interactions.

to use laboratory models to explore the role of topological defects in the early Universe. In later chapters we will examine the formation and evolution of topological defects in various models of particle cosmology and condensed matter.

1.6 Overview of the thesis

This thesis explores topological defects in $\mathcal{R}^{2+1}$, $\mathcal{R}^{3+1}$ and $\mathcal{R}^{4+1}$ spacetime, ranging from vortices in two-dimensional condensates to domain walls, monopoles and strings in the early Universe.

In Chapter 2 we investigate vortex dynamics in a two-dimensional Bose-Einstein condensate (BEC). Rotation of the BEC induces a "fictitious" gauge field, which is equivalent to imprinting a background phase gradient on the condensate. The effect of rotation on vortices is explored by examining how they interact with the background phase gradient. This provides a framework for understanding the origin of inter-vortex forces in a BEC, and the effect of rotation on these vortices. In contrast to vortices in a BEC, classical hydrodynamical vortices orbit each other rather than experiencing mutually repulsive interactions. Chapter 2 also examines vortices in a liquid light condensate (LLC). A LLC arises when an electromagnetic wave enters a cubic-quintic non-linear optical material. This classical condensate provides an unusual arena in which to explore vortex dynamics.

In Chapter 3 we examine the role of vortices in a rotating dark matter condensate. Measurements of the rotation curves of spiral galaxies and recent observations of the CMBR suggest that the Universe is flat, with most of the matter in the form of non-baryonic dark matter (Robinson 1985 and Bahcall *et al.* 1999).[18] We consider a self-interacting scalar field as a model of dark matter. This scalar field may exist in the form of a cosmic BEC. Rotation of the dark matter condensate leads to the nucleation of quantized vortices. To investigate the evolution of these vortices, we numerically solve the scalar field equation of the condensate coupled to gravity in the weak field limit. An interesting prediction of our simulations is that vortices in the condensate evolve toward a configuration with a flat velocity profile. This provides a novel mechanism for explaining the observed flat rotation curves of spiral galaxies.

[18]Tentative evidence for the existence of non-baryonic dark matter within the environs of our solar system may be found in the acceleration of Pioneer 10 and 11 toward the Sun (Anderson *et al.* 2002). More convincing evidence comes from the recent data from a one-year survey of the CMBR by WMAP (Bennett *et al.* 2003). It reveals that the Universe is flat, comprising 4% baryonic matter, 23% dark matter and 73% dark energy.

In Chapter 4 we explore the formation and evolution of topological defects in the early Universe. In particular, we examine the evolution of domain walls. The existence of domain walls is inconsistent with the magnitude of the temperature anisotropy observed in the CMBR (Zel'dovich *at al.* 1975, Stebbins and Turner 1989 and Press *et al.* 1989). However, domain walls are predicted to form as a consequence of symmetry breaking phase transitions in the early Universe. We address the domain wall problem by investigating Dirichlet defects[19] (D-walls), in which domain walls are connected to cosmic strings. We consider a Langacker-Pi mechanism for D-walls, and formulate a plausible model for resolving the domain wall problem; we also consider the implications of this mechanism for monopoles.

In Chapter 5 we examine the formation and evolution of cosmic strings in $\mathcal{R}^{3+1}$ and $\mathcal{R}^{4+1}$ spacetime. A string network in $\mathcal{R}^{3+1}$ exhibits scaling behaviour (Albrecht and Turok 1989, Allen and Shellard 1990, McGraw 1998 and Moore, Shellard and Martins 2001), and we explore whether scaling extends to spacetime with higher dimensions[20]. Although the Hot Big Bang model, based on Einstein's theory of general relativity, considers the Universe as having three spatial dimensions and one temporal dimension, the theory does not say anything about the topology of spacetime, nor the number of spacetime dimensions (Rey and Luminet 1995). In the context of a symmetry breaking phase transition, higher spatial dimensions modify the dimensionality (and behaviour) of topological defects. For example, a cosmic string is a vortex (point) defect in two spatial dimensions, however, it is a line defect in three spatial dimensions. Similarly, monopoles are string-like in four spatial dimensions. This suggests that the behaviour of topological defects in $\mathcal{R}^{4+1}$ may be relevant to the monopole problem. To address the monopole problem we discuss the evolution of monopoles in a compactified extra dimension[21]. It is shown that for a small compactified dimension (of the size of the coherent length of the Higgs field), monopoles form loops around the compactified dimension. When the loops collapse, they annihilate in a time scale comparable to the size of the compactified dimension, thereby avoiding the monopole problem. We briefly discuss the implications of this result for topological

[19]This is hybrid defect in which one defect terminates on another.

[20]Speculation that the Universe may have additional spatial dimensions has attracted widespread attention. For example, the Kaluza-Klein theory extends the theory of general relativity to $\mathcal{R}^{4+1}$ in an attempt to unify electromagnetism with gravity (see e.g., Appelquist *et al.* 1987). Superstring theory speculates that the Universe has 10 spacetime dimensions, whereas M-theory considers 11 dimensional spacetime (see e.g., Kaku 1999).

[21]A compactified dimension is curled up and small compared to the observed three spatial dimensions.

defects in $\mathcal{R}^{d+1}$ spacetime, with $d-3$ compactified dimensions.

Finally in Chapter 6 we conclude with a summary of the major achievements of the thesis and identify directions for future work.

CHAPTER 2

Vortices in Quantum and Classical Condensates

2.1 Introduction

This chapter explores the behaviour of vortices in two-dimensional condensates; in particular we investigate a Bose-Einstein condensate (BEC) and a novel classical condensate comprising liquid light. A BEC is a new state of matter that was first predicted by Bose and Einstein in 1924-1925 (see e.g., Parkins and Walls 1998 and Dalfovo *et al.* 1999). A BEC arises when the thermal de Broglie wavelength of an ideal gas exceeds the mean spacing, a, between atoms, i.e., $\lambda = h/p > a$, where h is Planck's constant and p is the linear momentum of the atom. Under these conditions a phase transition occurs in which all atoms condense into a single quantum state.

To achieve the BEC state an atomic cloud is cooled to very low temperatures (i.e., lower than 10^{-6} K; see e.g., Anglin and Ketterle 2002). To attain such a low temperature involves multiple steps. First the atoms are trapped by optical laser light. This is accomplished by exploiting the Zeeman splitting of the energy levels of the atoms in an applied magnetic field. A selection rule constrains the angular momentum change of the electron to $\Delta F = 1$, $\Delta m_F = 0, \pm 1$. The resultant energy level splitting exhibits a radial dependence, increasing with distance from the center of the trap. Three pairs of counter-propagating laser beams, each with frequency slightly less than the corresponding energy level splitting of the atoms, are then applied to the atomic cloud. Atoms that move away from the center of the trap with velocity $\mathbf{v}$ "see" the frequency of the incoming photons increase by an amount $\mathbf{v} \cdot \mathbf{k}$, where $\mathbf{k}$ is the wavevector of the photons. This results in electronic transitions between the magnetic sub-levels, i.e., $m_F = \pm 1 \rightarrow m_F = 0$. When an atom absorbs a photon, momentum is transferred, which results in the atom being scattered toward the center of the trap. Atoms interact with the applied laser beams in such a way that they experience a net force directed toward the center of the trap. Following optical trapping the atoms are loaded into a magnetic trap for evaporative cooling. This trap is produced by applying a magnetic field which results in a potential energy $U = -\boldsymbol{\mu} \cdot \mathbf{B}$ for the atoms (where $\boldsymbol{\mu}$

is magnetic dipole moment of the atom and **B** is a spatially-dependent external magnetic field). Atoms are cooled by applying radio frequency (rf) energy, which is tuned to ensure that the magnetic dipole moment of the most energetic atoms is switched. This results in hot (energetic) atoms being expelled from the magnetic trap, leaving behind the colder atoms (see Madison *et al.* 2000). These cold atoms undergo a phase transition to the BEC state when the temperature of the atomic cloud is sufficiently low. BECs with 2.5×10^6 ^{87}Rb atoms (at a temperature $\sim$500 nK) have been confined inside an Ioffe-Pritchard magnetic trap (see Madison *et al.* 2000).

The experimental realization of Bose-Einstein condensation in dilute ultracold neutral alkali-metal gases has generated enormous activity in atomic physics (see e.g., Anglin and Ketterle 2002). An area of particular interest is the study of quantized vortices, first observed in a BEC by Madison *et al.* (2000). When the condensate is rotated at an angular frequency greater than a critical frequency, Ω_c, multiple vortices form, which gives rise to a triangular lattice (Abrikosov lattice). A vortex lattice arises because of mutually repulsive interactions between vortices, however, vortex dynamics in a rotating BEC are not well understood.

A vortex is characterized by a non-vanishing circulation, i.e., the line integral of the velocity field around the vortex is non-zero. There are two kinds of vortices - quantum vortices and classical hydrodynamical vortices. Quantum vortices, such as those found in a rotating BEC, are characterized by quantized circulation with repulsive interactions (Shellard 1987). Consequently a multiple vortex configuration is expected to be unstable, and it is not clear how quantum vortices are confined in a rotating BEC. In this chapter we investigate the origin of vortex interactions and provide a simple mechanism to explain how a vortex lattice develops in a rotating BEC.

Classical vortices do not have quantized circulation and interact differently to quantum vortices. A classical hydrodynamical model predicts that vortices will orbit each other (see e.g., Acheson 2000). In Sec. 2.3 we investigate vortex dynamics in a novel classical system; namely a liquid light condensate (LCC), which arises when a high intensity laser beam is self-focused in a non-linear material (Michinel *et al.* 2002). The field theoretic model of a LLC incorporates a symmetry breaking term, which gives rise to classical vortex states. In Sec. 2.4 we compare vortex dynamics in classical and quantum condensates.

2.2 Vortices in a rotating Bose-Einstein condensate

A BEC is described by a mean-field Gross-Pitaevskii (GP) equation which neglects quantum and thermal fluctuations of the condensate wavefunction (Gross 1961 and Pitaevskii 1961). The GP equation is equivalent to the non-linear Schödinger equation with self-interactions. It was originally used to describe superfluid helium (Gross 1961 and Pitaevskii 1961) and subsequently applied to understand BECs (see e.g., Holland and Cooper 1996). A vortex state can be induced in the BEC via axisymmetric rotation of the condensate. This is accounted for in the GP equation by introducing an external potential that rotates with angular frequency Ω about the z-axis (see e.g., Dalfovo *et al.* 1999).

2.2.1 The Gross-Pitaevskii equation

We consider a BEC confined to a magnetic trap, whose strength depends on the frequency, ω, of the external magnetic field and the displacement of the atoms from the center of the trap. The trap can be modeled using a harmonic potential, V_{trap}. For simplicity we assume confinement of the BEC in the z direction. The two-dimensional harmonic trap has the form $V_{trap} = \frac{1}{2}m(\omega_x^2 x^2 + \omega_y^2 y^2)$, where m is the atomic mass. Typical values of ω_x and ω_y are in the order of 10 Hz to 100 Hz, and the size of the atomic cloud is in the order of microns (see e.g., Parkins and Walls 1998). The GP equation describing a BEC with a harmonic trap potential is

$$i\hbar\frac{\partial\Psi}{\partial t} = -\frac{\hbar^2}{2m}\nabla_\perp^2\Psi + \frac{m}{2}\omega^2 r^2\Psi + g|\Psi|^2\Psi, \tag{2.1}$$

where $\nabla_\perp^2 = \partial^2/\partial x^2 + \partial^2/\partial y^2$ is the two-dimensional Laplacian, $\Psi = \Psi(\mathbf{r}, t)$ is the wavefunction of the condensate normalized to the number of atoms in the x-y plane, $g = 4\pi\hbar^2 Na/m$ is related to the s-wave scattering length, a, of a binary collision[1], N is the number of condensate atoms and $r = \sqrt{x^2 + y^2}$. The term $\frac{1}{2}m\omega^2 r^2\Psi$ describes the localization of the condensate atoms due to the harmonic trap potential. The trap is assumed to be isotropic with $\omega_x = \omega_y = \omega$. To understand how the condensate is localized inside the trap, we consider its ground state wavefunction (see e.g., Dalfovo *et al.* 1999)

$$\Psi(\mathbf{r}, t) = e^{-i\mu t/\hbar}\Psi_0(\mathbf{r}), \tag{2.2}$$

[1]The binary atomic scattering length, a, is an "intrinsic" property of neutral atoms. For ^{23}Na, $a = 2.75$ nm, for ^{87}Rb, $a = 5.77$ nm and for ^{7}Li, $a = -1.45$ nm (Abraham *et al.* 1995).

where $\Psi_0(\mathbf{r})$ is the time-independent (stationary) ground state and μ is the chemical potential, which guarantees that the ground state of the BEC exhibits symmetry breaking[2] (see Sec. 1.5). By substituting Eq. (2.2) into Eq. (2.1), the stationary ground state is determined from

$$-\frac{\hbar^2}{2m}\nabla_\perp^2\Psi_0+\frac{m}{2}\omega^2r^2\Psi_0+g|\Psi_0|^2\Psi_0-\mu\Psi_0=0. \tag{2.3}$$

Equation (2.3) characterizes a BEC with a self-interaction potential,

$$V(|\Psi_0|)=\left(\frac{m}{2}\omega^2r^2-\mu\right)|\Psi_0|^2+\frac{g}{2}|\Psi_0|^4. \tag{2.4}$$

The stationary ground state can be obtained by minimizing the potential (2.4) with respect to $|\Psi_0|$. It is found that there are two solutions for the ground state. One solution corresponds to $|\Psi_0|$ vanishing everywhere, whereas the second solution gives the condensate number density as

$$|\Psi_0|^2=\frac{2\mu-m\omega^2r^2}{2g}. \tag{2.5}$$

From Eq. (2.5) it is evident that without the harmonic trap ($\omega=0$), the condensate is delocalized due to repulsive atomic (binary) collisions, i.e., the number density is equal to μ/g everywhere. As ω is increased from zero the condensate number density decreases as a function of radial distance from the origin (center of the trap). For sufficiently large values of the trapping frequency, ω, the condensate becomes localized and "clumps" at the origin, with the size of the condensate depending on the value of the trapping frequency (see Fig. 2.1).

Equation (2.3) is a non-linear equation amenable to numerical analysis. For simplicity this equation is transformed to dimensionless form by:

$$\Psi_0 \rightarrow \sqrt{\frac{\mu}{g}}\Psi_0, \tag{2.6}$$

$$\mathbf{r} \rightarrow \frac{\hbar}{\sqrt{m\mu}}\mathbf{r}, \tag{2.7}$$

$$\omega \rightarrow \omega. \tag{2.8}$$

These transformations eliminate m, $\hbar$, μ and g from Eq. (2.3). The ground state at the origin (where the harmonic potential vanishes) occurs for $|\Psi_0|=1$. We solve Eq. (2.3) in cylindrical coordinates by setting

$$\Psi_0(x,y)=|\Psi_0(x,y)|e^{-in\theta(x,y)}, \tag{2.9}$$

[2]The BEC is a system with broken symmetry, arising when the neutral atomic gas undergoes a phase transition to the condensate state.

where n is the integer winding number[3], $\theta(x,y)$ is the phase angle, and $|\Psi_0(x,y)|$ is the magnitude of the condensate wavefunction. The condensate profile is determined from the radial equation

$$\frac{d^2|\Psi_0|}{dr^2} + \frac{1}{r}\frac{d|\Psi_0|}{dr} - \frac{n^2}{r^2}|\Psi_0| - \omega^2 r^2|\Psi_0| - 2|\Psi_0|(|\Psi_0|^2 - 1) = 0. \tag{2.10}$$

Equation (2.10) is solved numerically by using an iterative fixed point method. This method involves first guessing the wavefunction and then applying a finite difference scheme (see Appendix A) until the difference in the norm of the wavefunction at two successive iterations is small, i.e., $||\Psi_0||_k - ||\Psi_0||_{k-1} < 10^{-10} \ll ||\Psi_0||_k$, where k denotes the iteration number. In the absence of a vortex state ($n = 0$) the iterative scheme starts by assuming that the wavefunction is equal to its ground state (i.e., $|\Psi_0| = 1$). Figure 2.1 shows $|\Psi_0|^2$ for various values of ω (with $n = 0$). As ω increases the condensate becomes localized at the center of the trap.

In the presence of vortex states ($n \neq 0$), the solution to Eq. (2.10) requires a different initial guess for $|\Psi_0(r)|$. A vortex is characterized by non-vanishing circulation with velocity inversely proportional to the radial distance from the vortex core. A cylindrically symmetric vortex located at the origin has a phase angle, $\theta(x,y)$, given by

$$\theta(x,y) = \tan^{-1}\left(\frac{y}{x}\right). \tag{2.11}$$

The velocity of the condensate is discontinuous at the center of the vortex, which gives rise to an undefined phase at the origin (see Eq. (2.11)). As a consequence the magnitude of the condensate must vanish at the vortex core. Since the condensate number density vanishes at $r = 0$, the initial guess for the wavefunction is $|\Psi_0(0)| = 0$ and $|\Psi_0(r \neq 0)| = 1$.

Figure 2.2 shows a static vortex solution. The condensate number density increases rapidly from the origin to a maximum value and then decreases slowly due to localization of the condensate by the confining potential $\frac{1}{2}m\omega^2 r^2|\Psi_0|^2$. There is competition between the atomic confining potential and the angular momentum of the circulating atoms about the vortex center. The confining potential tends to force the condensate atoms into the center of the vortex core, whereas angular momentum tends to expel atoms from the vortex core. Consequently a small displacement of the vortex from the origin results in the vortex moving out of the condensate (Rokhsar 1997), and a vortex state in a non-rotating condensate is unstable.

[3]The circulation is quantized according to $\oint_C \mathbf{v}\cdot d\mathbf{l} = nh/m$, where C is a path enclosing the vortex, $\mathbf{v}$ is the velocity of the condensate and n is the integer winding number.

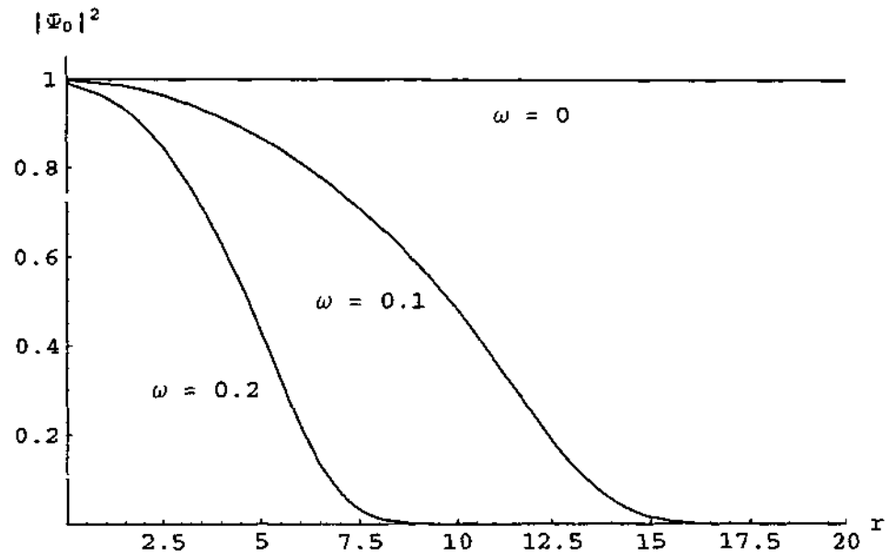

Figure 2.1: The number density $|\Psi_0|^2$ as a function of the radial coordinate for various values of ω. As ω increases, the condensate number density begins to "clump" at the center of the trap. This is indicative of localization of the condensate.

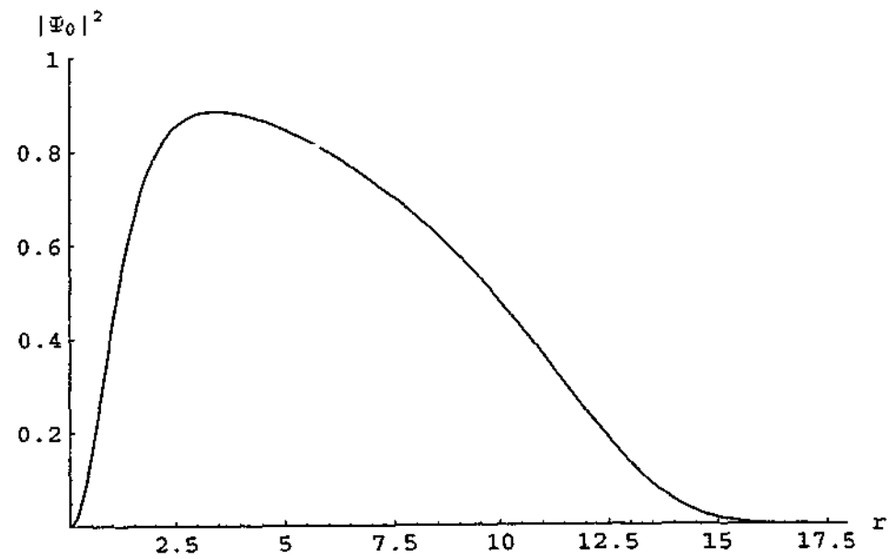

Figure 2.2: A typical static vortex solution ($n = 1$ and $\omega = 0.1$). The condensate number density vanishes at the origin, which is consistent with an undefined phase at the vortex core.

A stable vortex state can be obtained by externally rotating the condensate. A condensate rotated at angular frequency Ω is described by the modified GP equation

$$i\hbar\frac{\partial\Psi}{\partial t} = -\frac{\hbar^2}{2m}\nabla_\perp^2\Psi - \Omega L_z\Psi + \frac{m}{2}\omega^2 r^2\Psi + g|\Psi|^2\Psi, \tag{2.12}$$

where L_z is the z-component of angular momentum

$$L_z \equiv i\hbar\left(y\frac{\partial}{\partial x} - x\frac{\partial}{\partial y}\right). \tag{2.13}$$

The stationary ground state of the condensate, Ψ_0, is obtained by substituting $\Psi = e^{-i\mu t/\hbar}\Psi_0$ into Eq. (2.12), i.e.,

$$-\frac{\hbar^2}{2m}\nabla_\perp^2\Psi_0 - \Omega L_z\Psi_0 + \frac{m}{2}\omega^2 r^2\Psi_0 + g|\Psi_0|^2\Psi_0 - \mu\Psi_0 = 0. \tag{2.14}$$

Since a vortex in a BEC can only have quantized circulation, rotation of the BEC at an angular frequency, Ω, corresponds to $\oint_C \mathbf{v}\cdot d\mathbf{l} = \Omega\oint_C \mathbf{r}\cdot d\mathbf{l} \geq h/m$. To nucleate a vortex in the BEC, the condensate must be rotated with angular frequency equal to, or higher than, a critical value.

2.2.2 Vortex formation

To understand vortex formation in a rotating BEC we consider the velocity profile of the condensate. Utilizing the GP equation (2.1), the velocity profile, $v(r)$, of the condensate is determined from

$$\rho(r)v(r) = \frac{\hbar}{2mi}\left(\bar{\Psi}\nabla_\perp\Psi - \Psi\nabla_\perp\bar{\Psi}\right), \tag{2.15}$$

where $\rho(r) = |\Psi(x,y)|^2$ is the number density of the condensate. For a cylindrically symmetric vortex with unit circulation

$$\Psi(x,y) = |\Psi(x,y)|e^{i\theta(x,y)} = \sqrt{\rho(r)}e^{i\theta(x,y)}. \tag{2.16}$$

The velocity profile is given by

$$v(r) = \frac{\hbar}{m}|\nabla_\perp\theta(x,y)| = \frac{\hbar}{mr}, \tag{2.17}$$

where the last equality follows from Eq. (2.11). Equation (2.17) indicates that the angular velocity (frequency) of the condensate in the vicinity of the vortex is given by

$$\Omega = \frac{\hbar}{mr^2}. \tag{2.18}$$

For a vortex to form, a condensate of radius R must rotate at an angular frequency equal to, or greater than, $\hbar/mR^2$. This defines the critical angular frequency

$$\Omega_c = \hbar/mR^2. \tag{2.19}$$

Equation (2.19) assumes strong repulsive interactions between condensate atoms. Since a vortex core is devoid of condensate atoms, strongly repulsive interactions make it easier for a vortex to enter the trap from the boundary. On the other hand, it is harder for a vortex to enter the trap for the case of weakly repulsive interactions between condensate atoms. In the weak coupling limit it is expected that a vortex can enter the trap at a higher angular frequency, i.e., $\Omega_c > \hbar/mR^2$.

The prediction of Eq. (2.19) can be compared with the experimental value of Ω_c measured by Madison *et al.* (2000) for a BEC composed of ^{87}Rb atoms. In their experiment the condensate was confined to $R \approx 1$ μm. Substituting in the mass of an ^{87}Rb atom (1.456×10^{-25} kg), Eq. (2.19) gives the critical frequency for formation of a vortex as $\Omega_c/2\pi = 115$ Hz. This value is lower than the experimentally measured value 152 ± 7 Hz (see Madison *et al.* 2000). The discrepancy may be due to the assumption of strong coupling in the model.[4]

When the condensate rotates at an angular frequency much higher than the critical frequency, multiple vortices can form. It is energetically favorable for a condensate to have multiple vortices each with unit circulation, rather than one vortex with a larger circulation (Pitaevskii 1961). To understand how this arises, consider N overlapping vortices with $n = 1$. If each vortex is separated by a distance much greater than its core size, the Abrikosov ansatz (Abrikosov 1957) for N vortices is $\Psi = \sqrt{\rho'}e^{i(\theta_1+\theta_2+..+\theta_N)}$, where ρ' is the density profile of the condensate and θ_k is the phase angle of the k-th vortex. Since the circulation about each vortex core is identical, if all N vortices are located at the same position the phase angle of each vortex can be added to give $N\theta$. This implies that a vortex with a large circulation $\Psi = \sqrt{\rho}e^{iN\theta}$ is equivalent to N overlapping vortices each with unit circulation. However, vortices exhibit mutual repulsive interactions, therefore a vortex with $n > 1$ is unstable and will eventually separate into N vortices (each with $n = 1$).

[4]The difference between the theoretical prediction and the experimental value may also be due to the uncertainty in estimating the size of the condensate R. Since the uncertainty can be $\Delta R = 0.2$ μm, this results in the theoretical prediction $\Omega_c/2\pi = 115 \pm 46$ Hz, which is consistent with the experimental value 152 ± 7 Hz.

Figure 2.3 shows a schematic representation of a vortex lattice in a rotating BEC. Vortices are characterized by a discontinuity in the velocity of the condensate at the vortex core. This is evident in a plot of the y-component of the velocity as a function of x (see Fig. 2.4). The dashed line in Fig. 2.4 shows the average rotational velocity of the condensate. The circles with arrows indicate the direction of circulation of each vortex located on the x-axis. If the circulation of each vortex is unrestricted, then weaker circulation is favored and more vortices appear in the condensate. In the limit of an infinite number of vortices, $v_y(x)$ approaches the velocity profile shown by the dashed line in Fig. 2.4. This corresponds to rigid-body rotation.

Before the experimental observation of a vortex lattice in a BEC, Castin and Dum (1999) studied the minimum energy configuration of a rotating condensate. This is achieved by evolving an arbitrary ground state until a minimum energy configuration is obtained. The ground state wavefunction, Ψ_0, is time independent, however, it may be parameterized by a fictitious time parameter τ. The equation of motion is (Castin and Dum 1999)

$$-\hbar\frac{\partial\Psi_0}{\partial\tau} = -\frac{\hbar^2}{2m}\nabla_\perp^2\Psi_0 - \Omega L_z\Psi_0 + \frac{m}{2}\omega^2 r^2\Psi_0 + g|\Psi_0|^2\Psi_0 - \mu\Psi_0. \qquad (2.20)$$

By identifying τ with imaginary time ($\tau = it$), Eq. (2.20) is the non-linear Schödinger equation with a symmetry breaking potential. Evolving the equation of motion in imaginary time is equivalent to the method of steepest descent. This method starts with an arbitrary condensate wavefunction Ψ_0, then evolves it toward the minimum energy configuration. In the limit of large τ the wavefunction attains the minimum energy (equilibrium) configuration, consequently $\partial\Psi_0/\partial\tau = 0$, and Eq. (2.20) describes the stationary ground state of a rotating BEC. From Eq. (2.20) we can show that a triangular vortex lattice is the minimum energy configuration of a rotating condensate.

Although a triangular lattice configuration minimizes the energy of the rotating condensate, it is not understood how rotation give rises to the formation of a stable vortex lattice. Since a vortex defect is characterized by an non-contractable phase winding (see Sec. 1.4), phase is expected to play a significant role in vortex interactions. It has been shown that a vortex with non-uniform phase winding tends to evolve toward a state with uniform phase winding (see Thatcher and Morgan 1997). A vortex with non-uniform phase winding can be considered as a vortex with uniform phase winding "superposed"

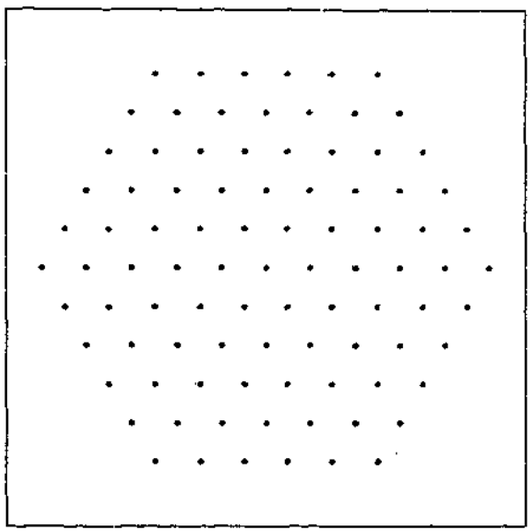

Figure 2.3: Schematic representation of a typical vortex configuration in a rotating BEC. Points represent the center of the vortices. In the limit of large number density the vortex configuration is characterized by rigid-body rotation.

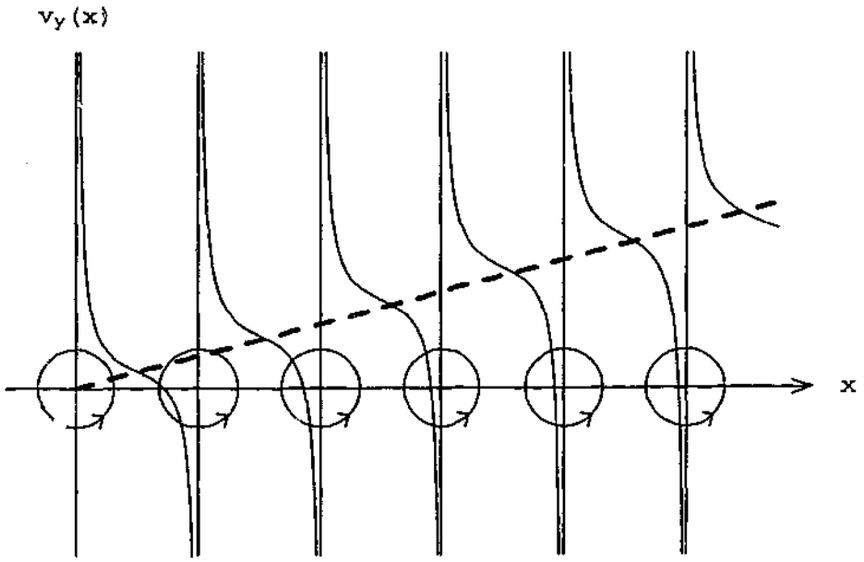

Figure 2.4: The y-component of velocity, as a function of the distance from the origin in the x direction (i.e., $v_y(x) \propto \partial\theta/\partial y$), for the vortex configuration shown in Fig. 2.3. This shows the discontinuity in vortex velocity. Circles and arrows are drawn to illustrate the circulation of vortices. The dashed line illustrates rigid-body rotation of the condensate. The discontinuous velocity profile approaches the rigid-body profile in the limit of large number density.

on a background phase. In what follows we investigate vortex dynamics in a background phase gradient.

2.2.3 A vortex in a background phase gradient

To study the dynamics of a vortex in a background phase gradient we utilize the GP equation (2.1). We write the two-dimensional GP equation (in the absence of rotation) as

$$i\hbar\frac{\partial\Psi}{\partial t} = -\frac{\hbar^2}{2m}\nabla_\perp^2\Psi + \frac{m}{2}\omega_0^2 r^2\Psi + g|\Psi|^2\Psi, \tag{2.21}$$

where ω_0 is the harmonic trapping frequency for the neutral atoms. Consider a time-independent background scalar field, $\psi_B(\mathbf{r})$, superposed on the BEC

$$\psi_B(\mathbf{r}) = e^{i\Theta(\mathbf{r})}, \tag{2.22}$$

where $\mathbf{r} = (x, y)$, $\Theta(\mathbf{r})$ is the phase of the background field and we have set the magnitude of the field to unity. To describe the condensate in the presence of this stationary background field we utilize the Abrikosov ansatz (Abrikosov 1957)

$$\Psi(\mathbf{r}, t) \rightarrow \Psi(\mathbf{r}, t)\psi_B(\mathbf{r}). \tag{2.23}$$

Substituting $\Psi(\mathbf{r}, t)\psi_B(\mathbf{r})$ into Eq. (2.21) we obtain the equation of motion

$$i\hbar\frac{\partial\Psi}{\partial t} = -\frac{\hbar^2}{2m}[\nabla_\perp^2\Psi + 2i\nabla_\perp\Theta\cdot\nabla_\perp\Psi - |\nabla_\perp\Theta|^2\Psi + i\Psi\nabla_\perp^2\Theta] + \frac{m}{2}\omega_0^2 r^2\Psi + g|\Psi|^2\Psi. \tag{2.24}$$

Now consider a background phase gradient of the form

$$\frac{\partial\Theta}{\partial x} = \frac{m}{\hbar}\Omega_x y \quad \text{and} \quad \frac{\partial\Theta}{\partial y} = -\frac{m}{\hbar}\Omega_y x. \tag{2.25}$$

Equation (2.24) reduces to the GP equation (2.12), with $\omega = \sqrt{\Omega^2 + \omega_0^2}$; we have assumed isotropic rotation for which $\Omega_x = \Omega_y = \Omega$. It is evident that our choice of phase gradient is exactly that required to establish the velocity field of a rotating BEC (Dalfovo *et al.* 1999). In the absence of rotation the harmonic trap frequency is ω_0; however, when we introduce a background phase, corresponding to rotation of the condensate, the harmonic trap frequency is modified to $\omega = \sqrt{\omega_0^2 + \Omega^2}$. Since $\omega_0^2 > 0$, ω is always greater than Ω. This accords with the numerical simulations performed by Feder and Clark (2001), and is consistent with the condensate atoms remaining localized if the trapping potential is greater than the angular momentum term.

The effect of rotation can be understood by investigating how vortices interact with the background phase gradient. Consider the Lagrangian of a BEC in the absence of external rotation ($\Omega = 0$), and when the confining potential is set to zero ($\omega = 0$)

$$\mathcal{L} = \frac{i\hbar}{2}\left(\bar{\Psi}\frac{\partial\Psi}{\partial t} - \Psi\frac{\partial\bar{\Psi}}{\partial t}\right) - \frac{\hbar^2}{2m}\nabla_\perp\Psi\cdot\nabla_\perp\bar{\Psi} - \frac{g}{2}|\Psi|^4. \tag{2.26}$$

A vortex embedded in a constant background phase gradient in the y direction can be described by the transformation (see e.g., Eq. (2.23)),

$$\Psi \rightarrow e^{i\alpha ym/\hbar}\Psi. \tag{2.27}$$

Utilizing Eqs. (2.27) and (2.16) we can write the Lagrangian (2.26) in the background phase gradient as

$$\mathcal{L} = \frac{i\hbar}{2}\left(\bar{\Psi}\frac{\partial\Psi}{\partial t} - \Psi\frac{\partial\bar{\Psi}}{\partial t}\right) - \frac{\hbar^2}{2m}\nabla_\perp\Psi\cdot\nabla_\perp\bar{\Psi} + \hbar\alpha|\Psi|^2\frac{\partial\theta}{\partial y} - \frac{m}{2}\alpha^2|\Psi|^2 - \frac{g}{2}|\Psi|^4. \tag{2.28}$$

From Eq. (2.28) we note that the background phase gradient contributes an effective potential to the Lagrangian, i.e.,

$$V_{eff}(|\Psi|) = -\hbar\alpha|\Psi|^2\frac{\partial\theta}{\partial y} + \frac{m}{2}\alpha^2|\Psi|^2. \tag{2.29}$$

For a vortex located at the origin we have $\partial\theta/\partial y = x/r^2$, which enables us to write

$$V_{eff}(|\Psi|) = -\hbar\alpha|\Psi|^2\frac{x}{r^2} + \frac{m}{2}\alpha^2|\Psi|^2. \tag{2.30}$$

The dynamics of a vortex in the background phase gradient are governed by the asymmetric potential $V_A = -\hbar\alpha|\Psi|^2x/r^2$. The near field solution is given by $|\Psi(r)| \approx c'r$, where $c' = 0.58...$ is a constant (see e.g., Shellard 1987); hence the asymmetric potential close to the vortex core has the form $V_A = -\hbar\alpha c'^2x$, with a concomitant force, $\hbar\alpha c'^2$, acting on the vortex in the x direction. Therefore a vortex embedded in a background phase gradient (in the y direction) experiences a force in the x direction and vice versa. An anti-vortex in the same phase gradient experiences a force in the opposite direction.

The dynamics of a vortex is governed by the background phase gradient. Since rotation of the condensate imprints a phase gradient on the condensate given by Eq. (2.25), rotation will provide a trapping potential for vortices and expel anti-vortices. The dynamics of vortices in this background phase gradient can be explored using numerical simulations.

2.2.4 Numerical study of vortex dynamics

Numerical simulations are carried out to explore vortex dynamics in a rotating two-dimensional trap based on Eq. (2.12). We assume $N = 200,000$ condensate atoms and a cylindrically symmetric trap with frequency $\omega/2\pi = 8Hz$. These parameters are consistent with experiments at JILA using ^{87}Rb atoms (see e.g., Feder and Clark 2001). The stationary ground state solution has been discussed previously (see Eq. (2.2)). However, to study vortex dynamics we require the ground state to be time-dependent. The evolution equation can be obtained by using the ansatz

$$\Psi(x,y,t) = e^{-i\mu t/\hbar}\Psi_0(x,y,t), \tag{2.31}$$

where $\Psi_0(x,y,t)$ is the time-dependent ground state of the BEC. Substituting Eq. (2.31) into the GP equation (2.12) we obtain

$$i\hbar\frac{\partial\Psi_0}{\partial t} = -\frac{\hbar^2}{2m}\nabla_\perp^2\Psi_0 - \Omega L_z\Psi_0 + \frac{m}{2}\omega^2 r^2\Psi_0 + g|\Psi_0|^2\Psi_0 - \mu\Psi_0. \tag{2.32}$$

Equation (2.32) is a non-linear Schrödinger equation which is formally identical to Eq. (2.20) with $\tau = it$.

In our numerical simulations it is convenient to rewrite Eq. (2.32) in dimensionless form. This is achieved by the following transformations, which eleminate $\hbar$, m and ω:

$$\Psi_0 \rightarrow \left(\frac{\hbar}{m\omega}\right)^{-3/4}\Psi_0, \tag{2.33}$$

$$\mathbf{r} \rightarrow \left(\frac{\hbar}{m\omega}\right)^{1/2}\mathbf{r}, \tag{2.34}$$

$$t \rightarrow \omega^{-1}t. \tag{2.35}$$

Distance and time are measured in units of $\sqrt{\hbar/m\omega}$ and ω^{-1}, respectively. The chemical potential is given by

$$\mu = \frac{\int d^2r\left[\frac{1}{2}|\nabla_\perp\Psi_0|^2 + \Omega\Psi_0^* L_z\Psi_0 + \frac{1}{2}r^2|\Psi_0|^2 + g|\Psi_0|^4\right]}{\int d^2r|\Psi_0|^2}. \tag{2.36}$$

This definition of chemical potential guarantees that the condensate wavefunction is normalized at each iteration. The transformations (2.33)-(2.34) result in $g = 4\pi Na/\sqrt{\hbar/m\omega} \approx 3458$ ($N = 200,000$, $a = 5.29$ nm and $\sqrt{\hbar/m\omega} = 3.85$ μm).

Before presenting the numerical simulations we discuss the stability of the non-linear Schrödinger equation (2.32). The right hand side of Eq. (2.32) can be obtained by varying

the energy density functional, $E[\Psi_0, \bar{\Psi}_0]$, with respect to $\bar{\Psi}_0$, where

$$E[\Psi_0, \bar{\Psi}_0] = \bar{\Psi}_0 \left(-\frac{\hbar^2}{2m}\nabla_\perp^2 - \Omega L_z + \frac{m}{2}\omega^2 r^2 + \frac{g}{2}|\Psi_0|^2 - \mu \right) \Psi_0. \tag{2.37}$$

Equation (2.32) can be written as

$$i\hbar \frac{\partial \Psi_0}{\partial t} = \frac{\partial E}{\partial \bar{\Psi}_0}[\Psi_0, \bar{\Psi}_0]. \tag{2.38}$$

The evolution of the energy density functional is

$$i\hbar \frac{\partial E}{\partial t}[\Psi_0, \bar{\Psi}_0] = i\hbar \left(\frac{\partial E}{\partial \Psi_0}\frac{\partial \Psi_0}{\partial t} + \frac{\partial E}{\partial \bar{\Psi}_0}\frac{\partial \bar{\Psi}_0}{\partial t} \right) = 2\left| \frac{\partial E}{\partial \Psi_0} \right|^2 > 0. \tag{2.39}$$

If we start with a random wavefunction, Ψ_0, the system does not evolve toward a minimum energy configuration. To remedy this problem we rewrite Eq. (2.38) in the form

$$-\hbar \frac{\partial \Psi_0}{\partial \tau} = \frac{\partial E}{\partial \bar{\Psi}_0}[\Psi_0, \bar{\Psi}_0], \tag{2.40}$$

where $\tau = it$. The evolution of the energy density functional is now

$$\hbar \frac{\partial E}{\partial \tau}[\Psi_0, \bar{\Psi}_0] = \hbar \left(\frac{\partial E}{\partial \Psi_0}\frac{\partial \Psi_0}{\partial \tau} + \frac{\partial E}{\partial \bar{\Psi}_0}\frac{\partial \bar{\Psi}_0}{\partial \tau} \right) = -2\left| \frac{\partial E}{\partial \Psi_0} \right|^2 < 0. \tag{2.41}$$

Starting with a random Ψ_0, the energy density of the system decreases as a function of τ, until a minimum energy configuration is attained.

Equation (2.40) represents the time-dependent Ginzburg-Landau (TDGL) equation. It is widely used to study the superconducting phase transition and has also been used to study the formation of topological defects in a superfluid (see e.g., Zurek 1996 and Gill 1998). The evolution of the GP equation (2.32) in imaginary time (or the TDGL equation (2.40)) may be used to describe vortex dynamics in a BEC.

The equation of motion (2.32) is evolved in imaginary time using Runge-Kutta integration. The numerical scheme utilizes a finite difference approximation to the spatial derivative, which requires the spatial step $\Delta h \leq 1$ and the imaginary time step $\Delta\tau \leq 1$ (see Appendix A). We utilize a spatial step $\Delta h = 0.1$, and an imaginary time step $\Delta\tau = 0.001$, where $\Delta\tau < \Delta h$ guarantees numerical stability. We begin by investigating the dynamics of a single vortex located in a rotating trap. The phase winding of the vortex is determined by

$$\theta(x, y) = \tan^{-1}\left(\frac{y - y_0}{x - x_0} \right), \tag{2.42}$$

where the vortex is located at position (x_0, y_0). To proceed we first calculate the initial ground state wavefunction in the absence of rotation ($\Omega = 0$). This is achieved by utilizing a fixed point iterative scheme (see Sec. 2.2.1), which starts by assigning a constant magnitude to the condensate wavefunction, Ψ_0. The wavefunction is normalized within the area of the simulation frame 60×60, and vanishes on the boundary.[5] The phase of the wavefunction is determined from Eq. (2.42). At each iteration the vortex position is specified by $\Psi_0(x_0, y_0) = 0$. The GP equation (2.32) is evolved in imaginary time τ until the difference in both μ and the norm $||\Psi_0||$ at two successive iterations is smaller than $0.01\Delta\tau$. Once the initial condition has been found, the vortex is then evolved in a rotating condensate ($\Omega \neq 0$) using the equation of motion (2.32). Since $\omega = 1$ and $\Omega \leq \omega$, the simulations were carried out in the range $0 \leq \Omega \leq 1$.

The numerical simulations show that when $\Omega = 0$ the condensate does not support stable vortices (or anti-vortices). The vortex (or anti-vortex) always moves out of the trap for $\Omega = 0$. However, as Ω is increased from zero the vortex moves into the trap with an acceleration that depends on the magnitude of Ω; an anti-vortex is expelled from the trap. There is a critical frequency, Ω_c, that is just able to confine a vortex. The numerical simulations show that $\Omega_c \approx 0.1$. This value is lower than the experimental value $0.32 < \Omega_c < 0.38$ (see Feder and Clark 2001) and lower than the value ($\Omega_c = 0.3$) obtained in the simulations performed by Feder and Clark (2001). This discrepancy may be due to the two-dimensional nature of our simulations, where it is assumed that all the 200,000 condensate atoms are confined to the x-y plane. This means that our condensate will have a larger size than that in the experiments, or in the 3D simulations performed by Feder and Clark (2001). Since the value of the critical angular frequency is inversely proportional to the square of the size of the condensate (see Sec. 2.2.2), a larger condensate results in a smaller critical angular frequency.

Figure 2.5 shows the behavior of a vortex in a rotating trap with $\Omega = 0.2$. The vortex, initially located at the edge of the trap, moves toward the center (at $\tau = 45$). Similarly, an anti-vortex located at the center of the trap is found to move outward (see Fig. 2.6). Further iterations result in an anti-vortex being expelled from the rotating condensate. For $\Omega > 0.3$ it is found that variation of the phase at the boundary of the condensate nucleates vortices that enter the trap, resulting in a multiple vortex configuration. These

[5]The distance from the origin is given by $\Delta h\sqrt{i^2 + j^2}$ ($\Delta h = 0.1$), where i and j are the grid coordinates in the x and y direction, respectively. Thus a simulation frame 60×60 corresponds to a grid size 600×600.

simulations show that rotation of the BEC produces a confining potential for vortices (expelling anti-vortices). Since topological charge is conserved, the formation of vortices will be accompanied by anti-vortices, however, only the latter are expelled from the rotating trap.

It is thought that vortex nucleation involves superfluid turbulence. Since vortices can only be nucleated in pairs they enter the condensate via turbulent superfluid flow at the boundary. This can be achieved by perturbing the condensate using a laser beam (Raman *et al.* 1999), or by introducing an anisotropy in the condensate trapping potential (Madison *et al.* 2000 and Shaeer *et al.* 2001).[6] However, since the BEC forms via a symmetry breaking phase transition, vortices (in a two-dimensional condensate) can also be nucleated locally via the Kibble-Zurek mechanism (see Sec. 1.4). This mechanism predicts that vortices (and anti-vortices) form immediately after a symmetry breaking phase transition.

2.2.5 Vortex nucleation via the Kibble-Zurek mechanism

We have performed numerical simulations to explore the formation of vortices via a phase transition to the BEC state. Immediately following the phase transition the phase of the wavefunction is expected to be uncorrelated at distances larger than the coherence length of the wavefunction (see Sec. 1.4), which is comparable to the size of a vortex core.[7] Since the size of a vortex core is much smaller than the size of the condensate (see Fig. 2.5), the Kibble-Zurek mechanism can be invoked to simulate the nucleation of topological defects in the condensate (see e.g., Kibble 1976 and Zurek 1996). The initial condensate wavefunction is calculated in the absence of rotation. Once the wavefunction has been found, each grid point in the simulation frame is assigned a random phase between 0 and 2π. This has the effect of simulating bubble nucleation during the phase transition to the BEC state. The initial condition of random phases results in large local phase gradients in the wavefunction. Since superfluid flow is proportional to the phase gradient (see Eq. (2.17)), there will be large fluctuations in the superfluid velocity. This implies that our initial condition is consistent with turbulent superfluid flow.

[6] For a three-dimensional system vortices are observed to nucleate instantaneously when the condensate rotates with angular frequency above Ω_c (Madison *et al.* 2000). This suggests that vortices are nucleated locally in the condensate (Dalfovo and Stringari 2001, Feder *et al.* 2001 and Raman *et al.* 2001).

[7] This is only correct immediately following the phase transition. At later times the correlation length of the wavefunction grows, and it is no longer comparable to the size of the vortex core.

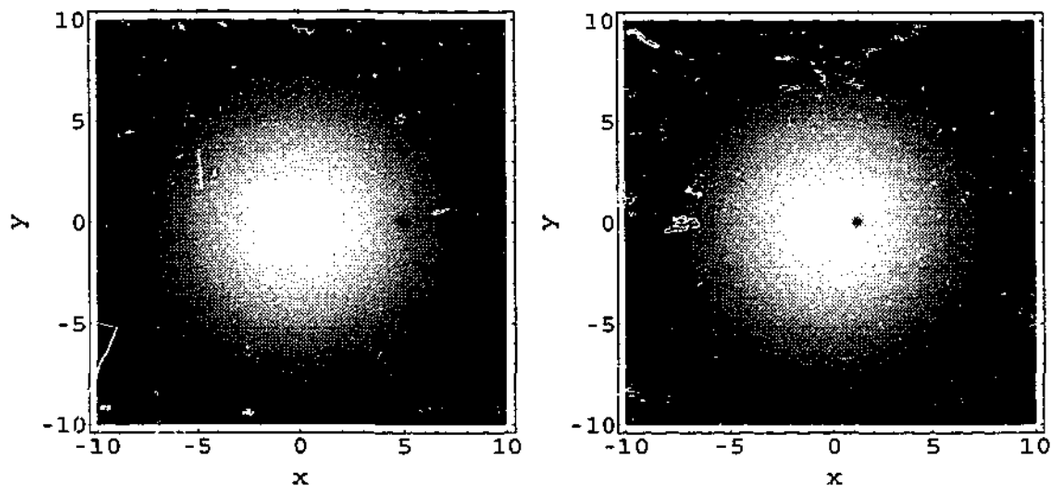

Figure 2.5: The number density, $|\Psi_0(r)|^2$, of a dilute BEC with 200,000 ^{87}Rb atoms showing the behaviour of a vortex inside a rotating BEC ($\Omega = 0.2$). (a) The vortex is initially located at (5,0). (b) At $\tau = 45$ the vortex has moved toward the origin. This shows that rotation of the BEC may be used to confine vortices.

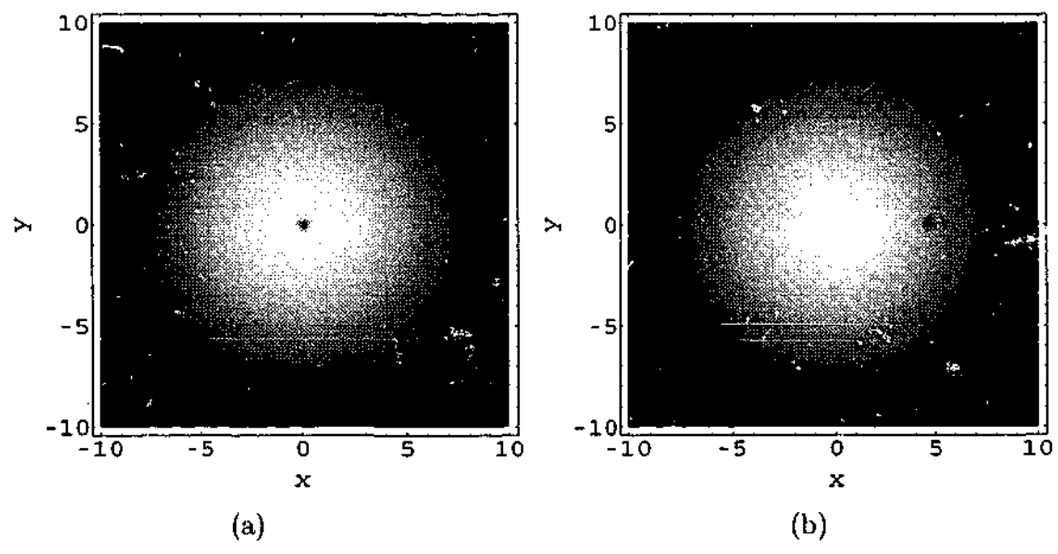

Figure 2.6: Number density, $|\Psi_0(r)|^2$, showing the behaviour of an anti-vortex in a rotating BEC ($\Omega = 0.2$). (a) The anti-vortex is initially located at (0.1,0). (b) At $\tau = 45$ the anti-vortex has moved out toward the edge of the condensate. Rotation of the BEC is found to expel anti-vortices.

Following vortex nucleation, the system is evolved in a rotating trap until an equilibrium vortex configuration is obtained (at $\tau = 100$).[8] A typical simulation of vortex nucleation is shown in Fig. 2.7 with $\Omega = 0.6$. This value of Ω gives rise to multiple vortices in the rotating condensate. Figure 2.7 shows vortex nucleation at random positions in the condensate accompanied by the corresponding anti-vortices. Initially there are equal number of vortices and anti-vortices. Figure 2.7 (b) shows an excess of vortices over anti-vortices. In Fig. 2.7 (c) only vortices are observed, with anti-vortices having been completely expelled from the rotating trap. Despite the initial random positions of the vortices, the system evolves toward a regular lattice. The appearance of a stable vortex configuration is due to two competing forces. The first is a radial trapping force, $F(r) \propto r$, that arises from the background phase gradient imprinted on the rotating BEC. The second is due to inter-vortex forces which exhibit a r^{-1} dependence. This inter-vortex force arises from interactions with the background phase gradient of the other vortices. To understand the origin of inter-vortex forces consider a vortex located at the origin interacting with a second vortex located at position (x, y). The background phase experienced by the second vortex due to the first is $\theta(x, y) = \tan^{-1}(y/x)$. This gives rise to a force on the second vortex, whose component in the x direction is proportional to $\partial\theta/\partial y = x/r^2$; in the y direction the force is proportional to $\partial\theta/\partial x = -y/r^2$. The magnitude of the force is proportional to r^{-1}. The first vortex experiences a force in the opposite direction, and the two vortices exhibit an r^{-1} mutually repulsive force. The background phase gradient in the condensate, established by the vortices, results in a net repulsive force on each vortex. The resultant force on a vortex is zero, since the trapping force due to rotation is exactly balanced by the repulsive inter-vortex forces.

Figure 2.8 shows multiple vortex configurations for $\Omega = 0.2, 0.4, 0.6$ and 0.8. Larger rotational frequencies result in more vortices being confined to the trap. The relationship between n_v and Ω is obtained by considering a rotating condensate with area S and radius R. The circulation, Γ, along the boundary of the condensate is given by

$$\Gamma = \int_S (\nabla \times \mathbf{v}) \cdot \hat{\mathbf{n}} dS \tag{2.43}$$

$$= \oint_{C=\partial S} \mathbf{v} \cdot d\mathbf{l}, \tag{2.44}$$

where $C = \partial S$ denotes a closed path on the boundary of the condensate containing the

[8] Since time is measured in units of ω^{-1}, the dimensionless parameter $\tau = 100$ is approximately equal to one second.

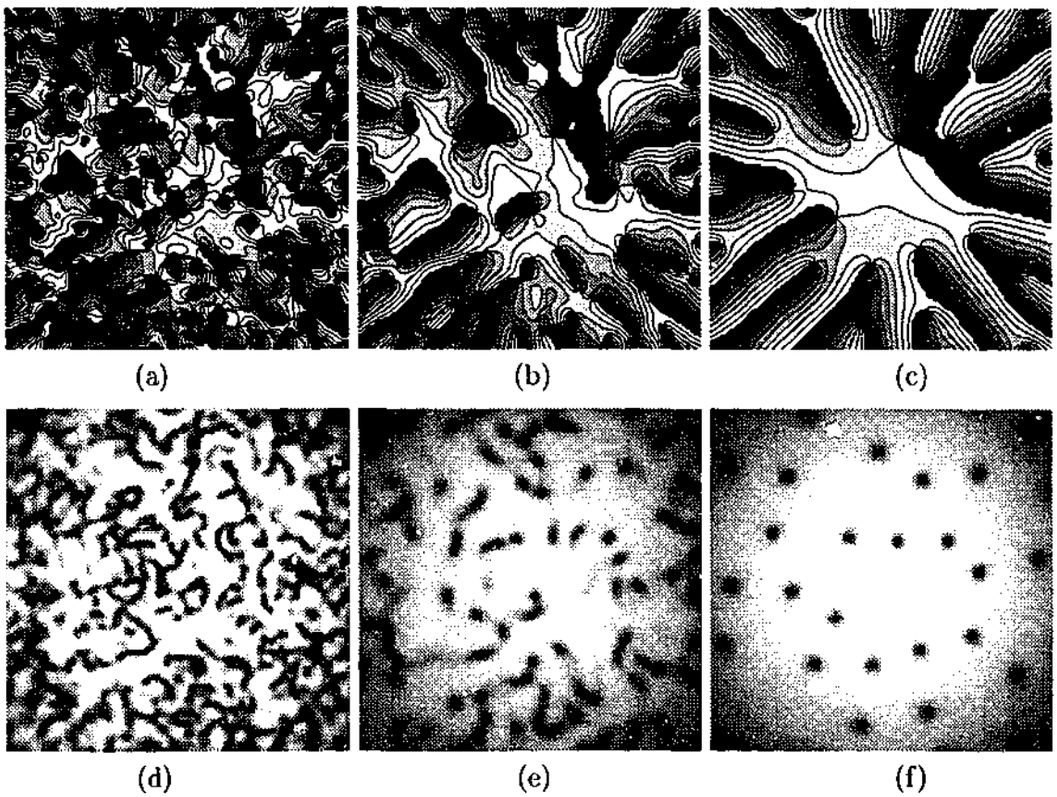

Figure 2.7: Grey scale plots of the phase of a small section (12×12) of the condensate, for $\Omega = 0.6$, at (a) $\tau = 0.05$, (b) $\tau = 0.2$ and (c) $\tau = 2$. The corresponding number density, $|\Psi_0|^2$, is shown in (d), (e) and (f), respectively. Here black denotes a phase of 0 and white denotes a phase of 2π. The initial condition corresponds to a condensate in the absence of rotation with phase randomly assigned to each grid point in the simulation frame. (a) and (d) show the nucleation of vortices accompanied by the corresponding anti-vortices; (b) and (e) show more vortices than anti-vortices, with the rotating trap acting as a confining potential for vortices (expelling anti-vortices). Finally, (c) and (f) show only vortices at random positions. Further evolution of the vortices produces a triangular vortex configuration.

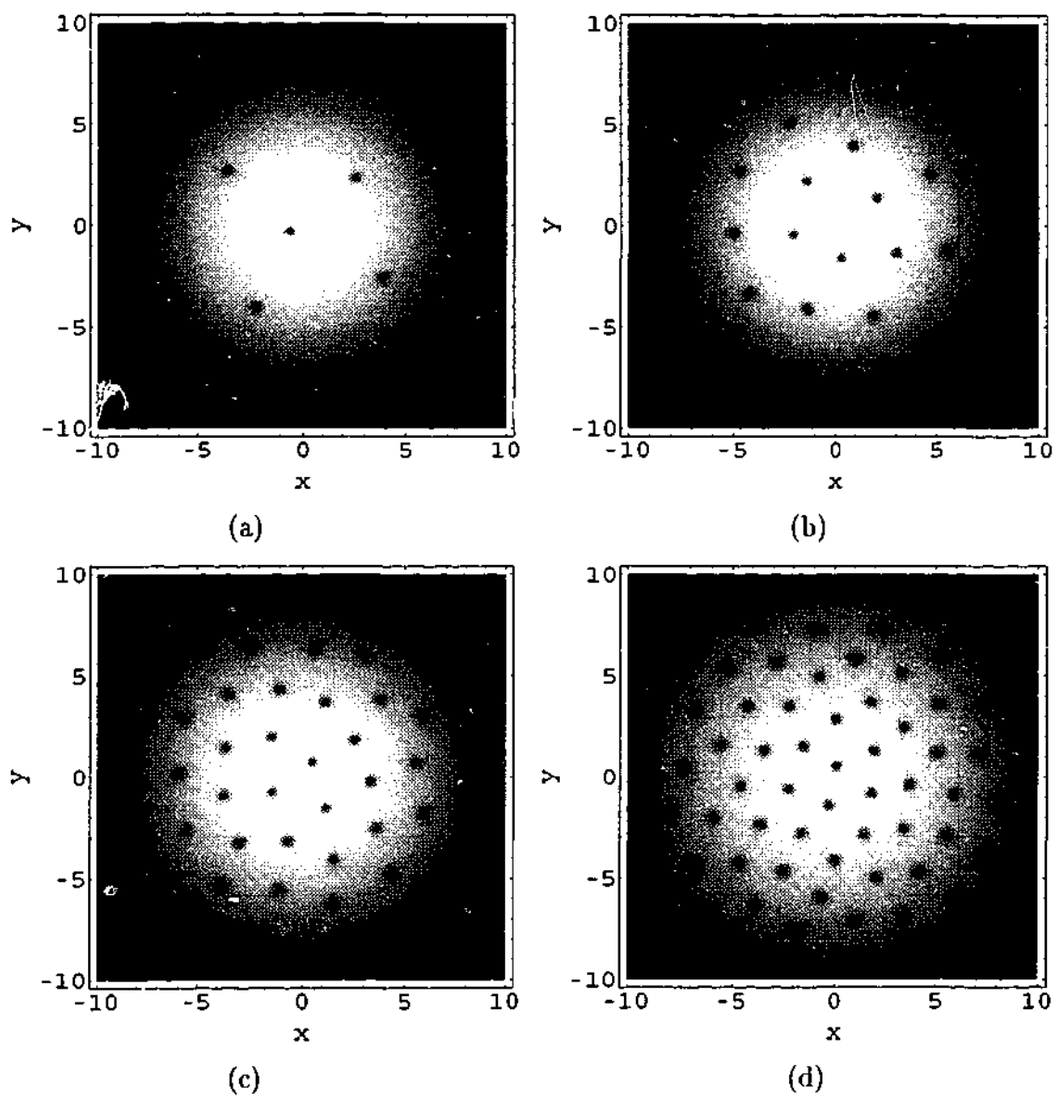

Figure 2.8: The number density, $|\Psi_0|^2$, at $\tau = 100$ with (a) $\Omega = 0.2$, (b) $\Omega = 0.4$, (c) $\Omega = 0.6$ and (d) $\Omega = 0.8$. The initial condition corresponds to the condensate in the absence of rotation, with phase randomly assigned to each lattice point. Vortices form at random positions accompanied by the corresponding anti-vortices as shown in Figs. 2.7 (a) and (d). However, the r^{-1} interactions between vortices produce a triangular lattice whose number density depends on the magnitude of the confining potential, i.e., on Ω.

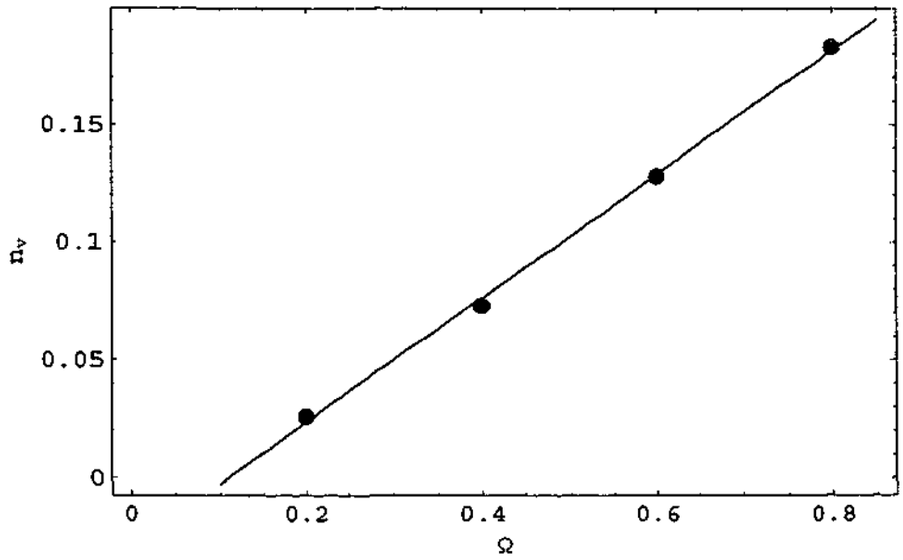

Figure 2.9: Vortex number density, n_v, as a function of angular frequency, Ω. The values of n_v are obtained from Fig. 2.8. The line of best fit shows that $n_v \propto \Omega$. The line does not pass through the origin since there is a critical angular frequency, $\Omega_c \approx 0.1$, for the formation of vortices. The vortex number density vanishes at $\Omega \approx 0.1$.

vortices and $d\mathbf{l}$ is infinitesimal path length along C. Assuming uniform rotation Eq. (2.43) gives

$$\int_S (\nabla \times \mathbf{v}) \cdot \hat{\mathbf{n}} dS = 2\pi R^2 \Omega, \tag{2.45}$$

where we have used $|\nabla \times \mathbf{v}| = 2\Omega$. To evaluate Eq. (2.44) consider the current density, $\mathbf{J}$, defined by

$$\mathbf{J} = \frac{\hbar}{2mi}\left[\bar{\Psi}\nabla\Psi - \Psi\nabla\bar{\Psi}\right] \tag{2.46}$$

$$= \frac{\hbar|\Psi|^2}{m}\nabla\theta, \tag{2.47}$$

where the last equality was obtained by noting that $\Psi = |\Psi|e^{i\theta}$. Since $\mathbf{J} = |\Psi|^2\mathbf{v}$, Eq. (2.47) reduces to

$$\mathbf{v} = \frac{\hbar}{m}\nabla\theta. \tag{2.48}$$

The magnitude of the infinitesimal path length, $d\mathbf{l}$, is given by $Rd\theta$. For N vortices we obtain

$$\oint_{C=\partial S} \mathbf{v} \cdot d\mathbf{l} = \frac{2\pi N\hbar}{m}. \tag{2.49}$$

Equating (2.45) and (2.49) gives

$$\Omega = \frac{h}{2m} n_v. \tag{2.50}$$

The relationship between n_v and Ω can be verified directly by counting the number of vortices in the condensate (see Fig. 2.9). This relationship will be discussed further in Chapter 3 for a relativistic model, where we investigate vortices in a rotating dark matter condensate (see Sec. 3.4).

Repulsive vortex-vortex interactions, in competition with the confining force due to rotation, explain how an equilibrium vortex lattice arises in a rotating BEC. Since a vortex is characterized by non-vanishing circulation, the mutual repulsive interaction between vortices results in them moving in the direction perpendicular to the superfluid flow. This is contrary to our intuitive understanding of vortex dynamics in classical hydrodynamics. When a classical vortex interacts with another vortex, it moves in the circulating fluid of the other vortex. Thus in contrast to quantum vortices, classical hydrodynamical vortices orbit each other (see e.g., Acheson 2000). The difference between vortex interactions in classical hydrodynamics and quantum condensates is puzzling and warrants closer investigation. In the remainder of this chapter we examine vortices in a novel classical system based on the phenomenon of light condensation in a non-linear optical material (Michinel *et al.* 2002).

2.3 Vortices in a liquid light condensate

2.3.1 Liquid light condensate

When a high power laser beam propagates through a non-linear optical material (i.e., a material whose refractive index depends on intensity), self-focusing of the beam occurs inside the material and the beam propagates without spreading. For some non-linear optical materials, such as the chalcogenide glasses (Smektala *et al.* 2000), the refractive index, $n(I)$, can be expanded as a function of light intensity (or irradiance)[9], I, according to (Michinel *et al.* 2002 and Chiao *et al.* 1964)

$$n(I) = n_0 + n_2 I - n_4 I^2 + \mathcal{O}(I^3), \tag{2.51}$$

where n_0, n_2 and n_4 are positive constants that determine the non-linear response of the optical material to the light.[10] For a typical experimental configuration $n_0 = 1.8$, $n_2 \approx 2 \times 10^{-3}$ cm^2/GW, and $n_4 \approx 2 \times 10^{-4}$ cm^4/GW^2, at wavelength $\lambda = 1600$ nm

[9]Light intensity refers to the flow of electromagnetic energy per unit area per unit time. In optics, this is referred to as irradiance.

[10]For light traveling in a homogeneous and isotropic material with velocity v and permitivity ϵ, the intensity I is related to the time average of the electric field via $I = \epsilon v \langle |\mathbf{E}|^2 \rangle$.

(Michinel *et al.* 2002). This suggests that non-linear effects become significant for a laser beam with intensity of the order of GW/cm^2, which is readily achievable. However, at this intensity the higher order terms in Eq. (2.51) are not significant and we neglect terms $\mathcal{O}(I^3)$.

To understand self-focusing consider a laser beam of diameter d propagating inside a non-linear material. Diffraction results in the beam expanding with angular divergence $\theta_{div} \approx 1.22\lambda/n_0 d$, where λ is the wavelength of the light in vacuum. Since the refraction index of the material within the beam is higher than that outside, there is a critical angle where total internal reflection occurs, i.e., at the boundary separating regions with different refraction indices. This angle determines the critical power for self-focusing of the laser beam.

The equation governing a self-focused laser beam can be derived from Maxwell's equations. For a source free[11] non-linear dielectric medium, Maxwell's equations give (in SI units)

$$\mu_0 \frac{\partial^2 \mathbf{D}}{\partial t^2} - \nabla^2 \mathbf{E} = 0, \tag{2.52}$$

where μ_0 is the permeability of free space, $\mathbf{D}$ is the displacement vector and $\mathbf{E}$ is the electric field intensity. In an isotropic medium the displacement vector is given by

$$\mathbf{D} = \epsilon_0 \mathbf{E} + \mathbf{P}, \tag{2.53}$$

where $\mathbf{P}$ is the polarization vector. For an isotropic medium the non-linear polarization vector can also be written as

$$\mathbf{P} = \epsilon_0 \chi_e \mathbf{E} + \epsilon_2 |\mathbf{E}|^2 \mathbf{E} + \epsilon_4 |\mathbf{E}|^4 \mathbf{E}, \tag{2.54}$$

where χ_e is the electric susceptiblity, ϵ_0 is the permittivity of free space, and ϵ_2 and ϵ_4 are constants that determine the non-linear response of the medium. It can be shown that $\epsilon_2 > 0$ and $\epsilon_4 < 0$ (see e.g., Mandel and Wolf 1973).

In general the electric field $\mathbf{E}$ in a medium can be represented by two transverse components and a longitudinal component. The transverse components are orthogonal to the propagation direction of the laser beam, whereas the longitudinal component is parallel to the direction of propagation. In a homogeneous isotropic medium the longitudinal component of $\mathbf{E}$ vanishes. The electric field can be represented by a two-component

[11]The first Maxwell's equation (Gauss's law) is $\nabla \cdot \mathbf{E} = \rho/\epsilon_0$, where ρ is the charge density. In the absence of a charge density (or source) the electric field has zero divergence, i.e., $\nabla \cdot \mathbf{E} = 0$.

vector field. For a laser beam traveling in the z direction the two transverse components are denoted by E_x and E_y. Writing $E = E_x + iE_y$, the vector equation (2.52) reduces to a scalar wave equation, i.e.,

$$\mu_0 \frac{\partial^2 D}{\partial t^2} - \nabla^2 E = 0, \tag{2.55}$$

where

$$D = \epsilon_0(1 + \chi_e)E + \epsilon_2|E|^2 E + \epsilon_4|E|^4 E. \tag{2.56}$$

For a plane wave traveling in the z direction

$$E = \Psi(x, y, z)e^{i(kz-\omega t)}, \tag{2.57}$$

where $\Psi(x, y, z)$ is the (complex) envelope, k is the wavevector and ω is the frequency. Substituting Eq. (2.57) into Eq. (2.55) and assuming that the envelope changes slowly in the z direction, so that $|\partial\Psi/\partial z| \ll k|\Psi|$, we obtain an approximate equation of motion for the envelope:

$$2ik\frac{\partial\Psi}{\partial z} + \nabla_\perp^2\Psi + \omega^2\mu_0\epsilon_2|\Psi|^2\Psi + \omega^2\mu_0\epsilon_4|\Psi|^4\Psi = 0, \tag{2.58}$$

where $\nabla_\perp^2 = \partial^2/\partial x^2 + \partial^2/\partial y^2$ and $k = \frac{\omega}{c}\sqrt{1+\chi_e}$.

Michinel *et al.* (2002) used numerical simulations based on Eq. (2.58) to show that a gas of photons in a cubic-quintic non-linear optical material can "condense" to a state with physical properties analogous to that of a liquid. For example, when a liquid light droplet is incident upon a boundary (i.e., the interface between vacuum and the non-linear material), the collision resembles that of a water droplet impacting on a wall. The phase transition to a liquid light condensate (LLC) state is characterized by a symmetry breaking potential analogous to that of the BEC discussed in Sec. 2.2, i.e.,

$$V(|\Psi|) = -\frac{\omega^2\mu_0\epsilon_2}{2}|\Psi|^4 - \frac{\omega^2\mu_0\epsilon_4}{3}|\Psi|^6. \tag{2.59}$$

To understand the physical significance of the potential (2.59), consider a laser beam with a Gaussian profile propagating in the z direction centered on $r = \sqrt{x^2+y^2} = 0$. For a low intensity beam the material responds linearly and no self-focusing occurs. Increasing the intensity of the laser beam results in non-linear behaviour; in this case the term $-\omega^2\mu_0\epsilon_2|\Psi|^4/2$ becomes significant and the potential decreases with increasing light intensity. For a Gaussian profile the intensity of the beam in the x and y direction is greater closer to the center of the beam. Therefore the potential is lower at the center of

the beam. This results in self-focusing of the beam, with the photon gas becoming unstable to "collapse". As the photon gas "collapses" its number density increases and eventually the term $-\omega^2\mu_0\epsilon_4|\Psi|^6/3$ becomes significant. Since $\epsilon_4 < 0$ the potential increases with increasing light intensity, thus preventing further "collapse".

The interplay between the first and second terms in the potential (2.59) determines the stability of the LLC. The ground state is obtained from $\partial V/\partial|\Psi| = 0$. For $\epsilon_4 < 0$ this is given by

$$|\Psi_0| = \sqrt{-\frac{\epsilon_2}{\epsilon_4}}. \tag{2.60}$$

An immediate consequence of Eq. (2.60) is that since ϵ_2 and ϵ_4 are constants for a non-linear material, a beam with $|\Psi| < |\Psi_0|$ is unstable and experiences strong self-focusing; however, a beam with $|\Psi| > |\Psi_0|$ does not self-focus. For $|\Psi| < |\Psi_0|$ the first term in the potential (2.59) dominates, whereas for $|\Psi| > |\Psi_0|$ the second term dominates.

The potential (2.59) is analogous to that for a BEC. The fourth order term in the potential corresponds to attractive "two-body" interactions, which result in the laser beam collapsing to produce infinite intensity. However, for sufficiently high beam intensity the sixth order term in the potential becomes significant. This latter term corresponds to repulsive "three-body" interactions, which prevent the beam from further collapse. A similar situation arises in a collapsing BEC (see e.g., Kagan *et al.* 1996, Shuryak 1996, Stoof 1997, Ueda and Leggett 1998, Sackett *et al.* 1998 and Kagan *et al.* 1998). To appreciate this analogy consider the stability of the BEC in a confining potential. The BEC exists as a consequence of the interplay between the repulsive two-body interactions and the external harmonic trapping potential. The sign of the two-body scattering length can be changed, by exploiting Feshbach resonances (Inouye *et al.* 1998), from positive (repulsive scattering) to negative (attractive scattering). In this latter case the condensate is unstable to collapse. When the condensate collapses its number density rises. Consequently, the three-body repulsive interactions becomes significant and stop the BEC from further collapse.

The LLC is described by a complex scalar field Ψ and exhibits $U(1)$ symmetry breaking. The existence of a broken symmetry ground state for the LLC suggests that the condensate may support topological defects. As the beam enters the non-linear material, topological defects (e.g., vortices) should form at the interface between vacuum and the medium. For a stationary propagating beam, the equation of motion (2.58) governing Ψ has the same

form as a generalized non-linear Schrödinger equation. However, vortices in a classical system, such as a LLC, are expected to behave differently to quantum vortices in a BEC.

To study vortex dynamics in a LLC we require the condensate to be time dependent. Consider a plane wave traveling in the z direction

$$E = \Psi(x, y, z, t)e^{i(kz-\omega t)}. \tag{2.61}$$

Substituting Eq. (2.61) into Eq. (2.55) and assuming that the envelope changes slowly in the z direction, the equation of motion becomes

$$\begin{aligned} -\frac{(1+\chi_e)}{c^2}\frac{\partial^2\Psi}{\partial t^2} + \frac{2i(1+\chi_e)\omega}{c^2}\frac{\partial\Psi}{\partial t} - \mu_0\left(3\epsilon_2|\Psi|^2 + 5\epsilon_4|\Psi|^4\right)\frac{\partial^2\Psi}{\partial t^2} \\ +i\mu_0\omega\left(6\epsilon_2|\Psi|^2 + 10\epsilon_4|\Psi|^4\right)\frac{\partial\Psi}{\partial t} - \mu_0\left(6\epsilon_2\Psi + 20\epsilon_4|\Psi|^2\Psi\right)\left(\frac{\partial\Psi}{\partial t}\right)^2 \\ +2ik\frac{\partial\Psi}{\partial z} + \nabla_\perp^2\Psi + \omega^2\mu_0\epsilon_2|\Psi|^2\Psi + \omega^2\mu_0\epsilon_4|\Psi|^4\Psi = 0. \end{aligned} \tag{2.62}$$

To simplify Eq. (2.62) we also assume that the envelope changes slowly with time, so that $|\partial\Psi/\partial t| \ll \omega|\Psi|$. In this case we obtain an approximate equation of motion for the envelope:

$$\frac{(1+\chi_e)}{c^2}\frac{\partial^2\Psi}{\partial t^2} - \frac{2i(1+\chi_e)\omega}{c^2}\frac{\partial\Psi}{\partial t} - \nabla_\perp^2\Psi - \omega^2\mu_0\epsilon_2|\Psi|^2\Psi - \omega^2\mu_0\epsilon_4|\Psi|^4\Psi = 0. \tag{2.63}$$

Equation (2.63) neglects the term $2ik\partial\Psi/\partial z$, so that we have a two-dimensional system corresponding to the cross-section of the propagating laser beam. For convenience we rewrite Eq. (2.63) in dimensionless form by employing the transformations:

$$\Psi \rightarrow \left(\sqrt{-\epsilon_4}\epsilon_2\right)^{-1/2}\Psi, \tag{2.64}$$

$$\mathbf{r} \rightarrow c\left(\sqrt{1+\chi_e}\omega\right)^{-1}\mathbf{r}, \tag{2.65}$$

$$t \rightarrow \omega^{-1}t, \tag{2.66}$$

$$\epsilon_2 \rightarrow (1+\chi_e)\epsilon_0\sqrt{-\epsilon_4}\epsilon_2, \tag{2.67}$$

$$\epsilon_4 \rightarrow (1+\chi_e)\epsilon_0\epsilon_2^2\epsilon_4. \tag{2.68}$$

The spatial coordinates are measured in units of $c\left(\sqrt{1+\chi_e}\omega\right)^{-1}$, and time in units of ω^{-1}. With these transformations the equation of motion (2.63) becomes

$$\frac{\partial^2\Psi}{\partial t^2} - 2i\frac{\partial\Psi}{\partial t} - \nabla_\perp^2\Psi - |\Psi|^2\Psi + |\Psi|^4\Psi = 0. \tag{2.69}$$

Equation (2.69) contains both first order and second order time derivatives. To understand the behaviour of Ψ due to these two terms, we decompose the envelope into real and imaginary parts

$$\Psi = \psi_0 + i\psi_1, \tag{2.70}$$

where ψ_0 and ψ_1 are real scalar fields. Substituting Eq. (2.70) into Eq. (2.69), and equating the real and imaginary parts we obtain

$$\frac{\partial^2\psi_0}{\partial t^2} - \nabla_\perp^2\psi_0 + 2\frac{\partial\psi_1}{\partial t} + \psi_0(\psi_0^2+\psi_1^2)\left(\psi_0^2+\psi_1^2-1\right) = 0 \tag{2.71}$$

$$\frac{\partial^2\psi_1}{\partial t^2} - \nabla_\perp^2\psi_1 - 2\frac{\partial\psi_0}{\partial t} + \psi_1(\psi_0^2+\psi_1^2)\left(\psi_0^2+\psi_1^2-1\right) = 0, \tag{2.72}$$

The spatial part of these equations correspond to two non-coupled partial differential equations, which together give rise to a static vortex solution. However, the time-dependent parts of Eqs. (2.71) and (2.72) are coupled-partial differential equations, i.e.,

$$\frac{\partial^2\psi_0}{\partial t^2} + 2\frac{\partial\psi_1}{\partial t} = 0, \tag{2.73}$$

$$\frac{\partial^2\psi_1}{\partial t^2} - 2\frac{\partial\psi_0}{\partial t} = 0, \tag{2.74}$$

which have solutions of the form

$$\psi_0 = \cos 2t \tag{2.75}$$

$$\psi_1 = \sin 2t. \tag{2.76}$$

These solutions satisfy the constraint, $\psi_0^2+\psi_1^2 = 1$, imposed by the potential.

Since Ψ represents orthogonal transverse components of the electric field, the harmonic solutions (2.75) and (2.76) suggest that the electric field exhibits oscillatory behaviour. This solution is different to the non-oscillatory behaviour of the wavefunction in a BEC. This suggests that vortices in a LLC behave differently to quantum vortices, despite the similarities between the model descriptions.

To elucidate vortex dynamics in a LLC we utilize the transformation $\Psi \to e^{i\alpha y}\Psi$. The LLC model (2.69) now becomes

$$\Box\Psi - 2i\frac{\partial\Psi}{\partial t} - 2i\alpha\frac{\partial\Psi}{\partial y} + \alpha^2\Psi - |\Psi|^2\Psi + |\Psi|^4\Psi = 0. \tag{2.77}$$

Writing $\Psi = \Psi(x(t), y(t))$, the time derivative of the scalar field is given by

$$\frac{\partial\Psi}{\partial t} = \frac{\partial\Psi}{\partial x}\frac{\partial x}{\partial t} + \frac{\partial\Psi}{\partial y}\frac{\partial y}{\partial t}, \tag{2.78}$$

where $\partial x/\partial t$ and $\partial y/\partial t$ are the components of the flow velocity in the x and y directions, respectively. For a phase gradient in the y direction the condensate flow is opposite to the phase gradient, i.e., $\partial y/\partial t = -\alpha$. Substituting Eq. (2.78) into Eq. (2.77), the equation of motion now becomes

$$\Box\Psi - 2i\frac{\partial\Psi}{\partial x}\frac{\partial x}{\partial t} + \alpha^2\Psi - |\Psi|^2\Psi + |\Psi|^4\Psi = 0. \tag{2.79}$$

In the LLC a background phase gradient in the y direction exerts a force on a vortex in the y direction (rather than in the x direction, as is the case for a BEC). Vortex dynamics in the LLC is therefore dramatically different to that in the Gross-Pitaevskii model of a BEC. Consider a vortex located at the origin of a LLC interacting with a second vortex located at position $(x, 0)$. The background phase gradients experienced by the second vortex (due to the first) are $\partial\theta/\partial y = x/r^2$ and $\partial\theta/\partial x = 0$. This results in a force on the second vortex in the y direction; similarly the force on the first vortex is in the $-y$ direction. Consequently, the two vortices rotate about each other rather than repelling, as is the case for quantum vortices.

2.3.2 Numerical study of vortex dynamics in a liquid light condensate

A numerical simulation of vortex dynamics in a LLC utilizes the equation of motion (2.69). The initial condition is obtained from a static vortex solution to the field equation (2.69), i.e.,

$$\frac{d^2|\Psi|}{dr^2} + \frac{1}{r}\frac{d|\Psi|}{dr} - \frac{|\Psi|}{r^2} - |\Psi|^3\left(|\Psi|^2 - 1\right) = 0. \tag{2.80}$$

Equation (2.80) is solved by utilizing an iterative fixed point method (see Sec. 2.2). This method requires an initial guess for $|\Psi|$. For large r the field magnitude is expected to approach a constant value; therefore the first, second and third terms on the left hand side of Eq. (2.80) vanish. The asymptotic value[12] is $|\Psi(r \to \infty)| = 1$. Since the condensate field magnitude vanishes at the origin, we set $|\Psi(0)| = 0$ and $|\Psi(r \neq 0)| = 1$. Once the static solution is found (see Fig. 2.10), it is wound onto a two-dimensional Cartesian grid. The initial multi-vortex configuration is constructed using an Abrikosov ansatz (Abrikosov 1957). A leapfrog method is then employed to evolve the field equation (2.69) in real time.

Our numerical simulations used a spatial step $\Delta h = 0.5$ and time step $\Delta t = 0.1$, with $\Delta t < \Delta h$ imposed for numerical stability. The results of a typical simulation with two

[12]This value corresponds to the ground state expectation value of the condensate. Equation (2.69) describes a symmetry breaking potential, $V(|\Psi|) = -|\Psi|^4/2 + |\Psi|^6/3$. Minimization of this potential gives the ground state $|\Psi_0| = 1$.

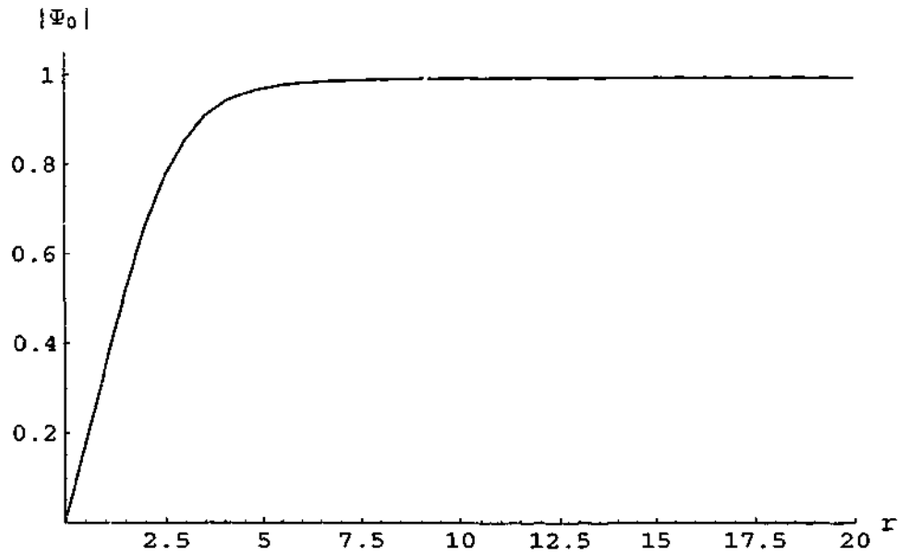

Figure 2.10: Static vortex solution in cylindrical coordinates. The light intensity, $|\Psi|^2$, vanishes at the origin where the phase winding of the vortex is undefined (see Sec. 2.2).

interacting vortices are shown in Fig. 2.11. Figure 2.11 (a) shows the initial condition with two vortices located on the x-axis. Figures 2.11 (b)-(f) show the vortices orbiting each other in the anti-clockwise direction, corresponding to the circulation of each vortex. The direction of rotation reverses for the case of two anti-vortices, i.e., when the sign of the winding number (direction of circulation) is changed. In the case of a vortex and an anti-vortex, the pair move parallel to each other, with the direction reversing when the positions of the pair are interchanged (or equivalently the sign of the winding number is changed). Repulsive interactions are not observed between vortices, or attractive interactions between a vortex and an anti-vortex.

The stability of vortices in a LLC is examined by numerically simulating a multiple vortex configuration. We plot the intensity of light in the condensate, in which vortices appear as dark regions.[13] Figure 2.12 shows a typical simulation with initially random vortex positions. In the LLC vortices rotate about the origin, with vortices within a group also exhibiting local rotation. The long term evolution does not produce a triangular vortex lattice.[14] Since vortices orbit each other, it is tempting to think that the long term

[13]Vortices in the condensate can be imaged directly. A paper detailing how this may be achieved is included at the end of this thesis.

[14]This is in contrast to a BEC, where vortices can nucleate at random positions and then evolve toward a minimum energy configuration.

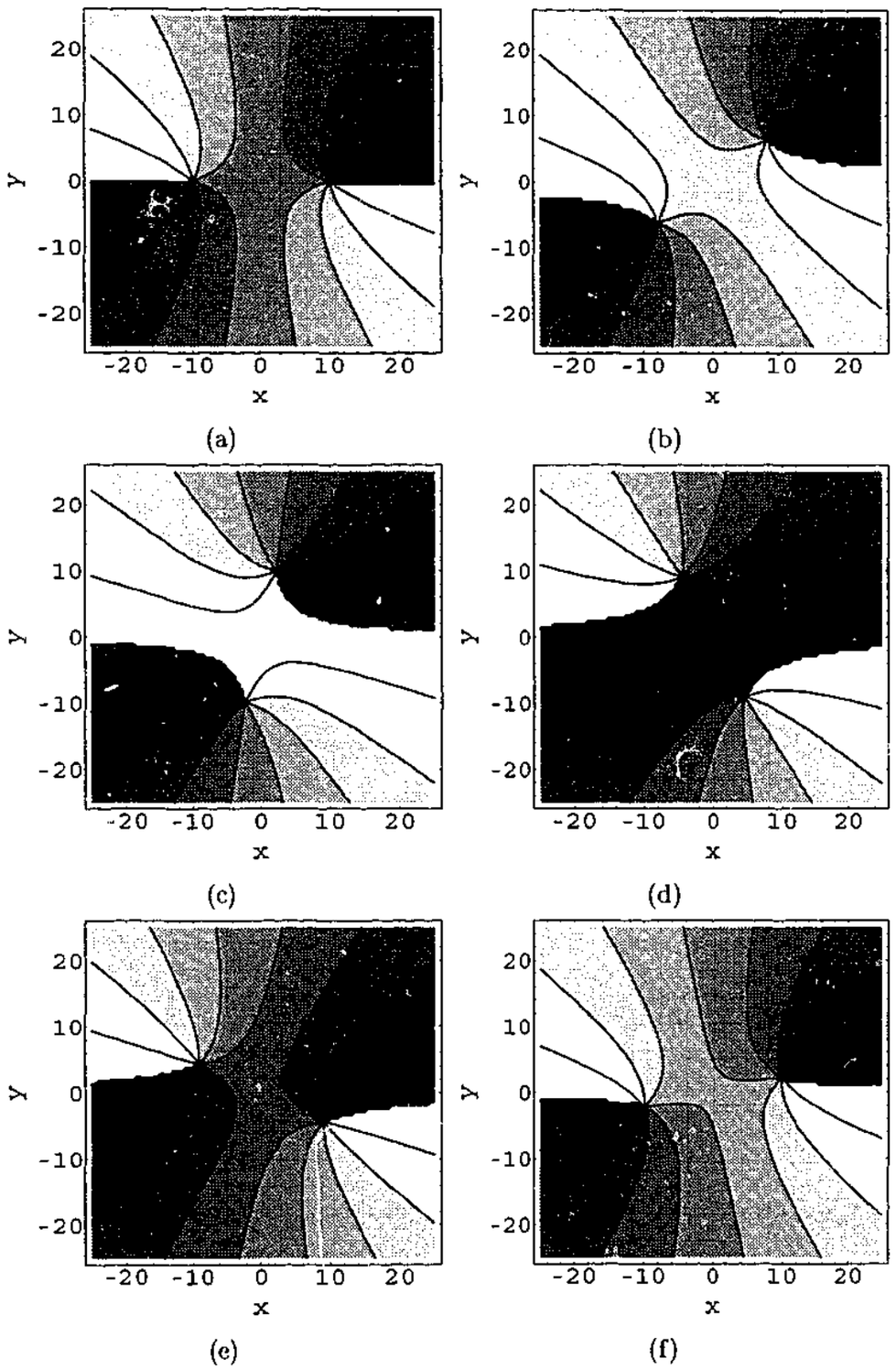

Figure 2.11: Grey scale plot of the phase winding of two vortices. (a) $t = 0$, (b) $t = 140$, (c) $t = 280$, (d) $t = 420$, (e) $t = 560$ and (f) at the end of the simulation, $t = 700$. Black denotes a phase of 0 and white denotes a phase of 2π. These figures show two vortices in the LLC orbiting each other in the anti-clockwise direction. In a classical hydrodynamical model there are no repulsive interactions between vortices.

evolution of a regular vortex lattice is unstable, with any perturbation from the uniform arrangement initiating local rotation, causing the vortex positions to become random. We have carried out simulations to investigate the stability of a rotating triangular vortex configuration. It is found that the entire vortex lattice rotates, with no evidence of peculiar rotation of vortices within the lattice (see Fig. 2.13).

Classical vortices in a LLC do not display mutually repulsive interactions and their structure is different to quantum vortices in a BEC. For example, vortices in the LLC are stable for integer winding numbers $n > 1$. Consider a vortex in the LLC, which is written as

$$\Psi = |\Psi| e^{-in\theta}. \tag{2.81}$$

The continuity equation is derived from Eq. (2.63), i.e.,

$$\frac{1}{\partial t}\left[\bar{\Psi}\Psi - \frac{1}{2i\omega}\left(\bar{\Psi}\frac{\partial \Psi}{\partial t} - \Psi\frac{\partial \bar{\Psi}}{\partial t}\right)\right] + \frac{c^2}{2i\left(1+\chi_e\right)\omega}\nabla_\perp \cdot \left(\bar{\Psi}\nabla_\perp\Psi - \Psi\nabla_\perp\bar{\Psi}\right) = 0, \tag{2.82}$$

where the current density is given by

$$\mathbf{J} = \frac{c^2}{2i\left(1+\chi_e\right)\omega}\left(\bar{\Psi}\nabla_\perp\Psi - \Psi\nabla_\perp\bar{\Psi}\right). \tag{2.83}$$

Substituting Eq. (2.81) into Eq. (2.83) and using $\mathbf{J} = |\Psi|^2\mathbf{v}$, we obtain the velocity profile of a vortex

$$\mathbf{v} = \frac{c^2 n}{\left(1+\chi_e\right)\omega}\nabla_\perp\theta. \tag{2.84}$$

Consequently, the circulation over a closed path is

$$\Gamma = \oint_C \mathbf{v}\cdot d\mathbf{l} = \frac{2\pi c^2 n}{\left(1+\chi_e\right)\omega}. \tag{2.85}$$

Since the frequency, ω, is not necessarily fixed, a vortex in the LLC does not have quantized circulation. Vortices may form in the condensate with any winding number n, however, the lattice adopts a minimum energy configuration in which each vortex has $n = 1$. Once formed, the vortex configuration is stable in the absence of external rotation.

2.4 Vortex dynamics in quantum and classical condensates

A distinctive property of a quantum fluid is that it is frictionless (see e.g., Nozières and Pines 1990). In the absence of viscosity a vortex does not "feel" the background fluid-flow. Consider a quantum fluid with velocity $v_{bg} = \frac{\hbar}{m}\alpha$ in the y direction, where α is the

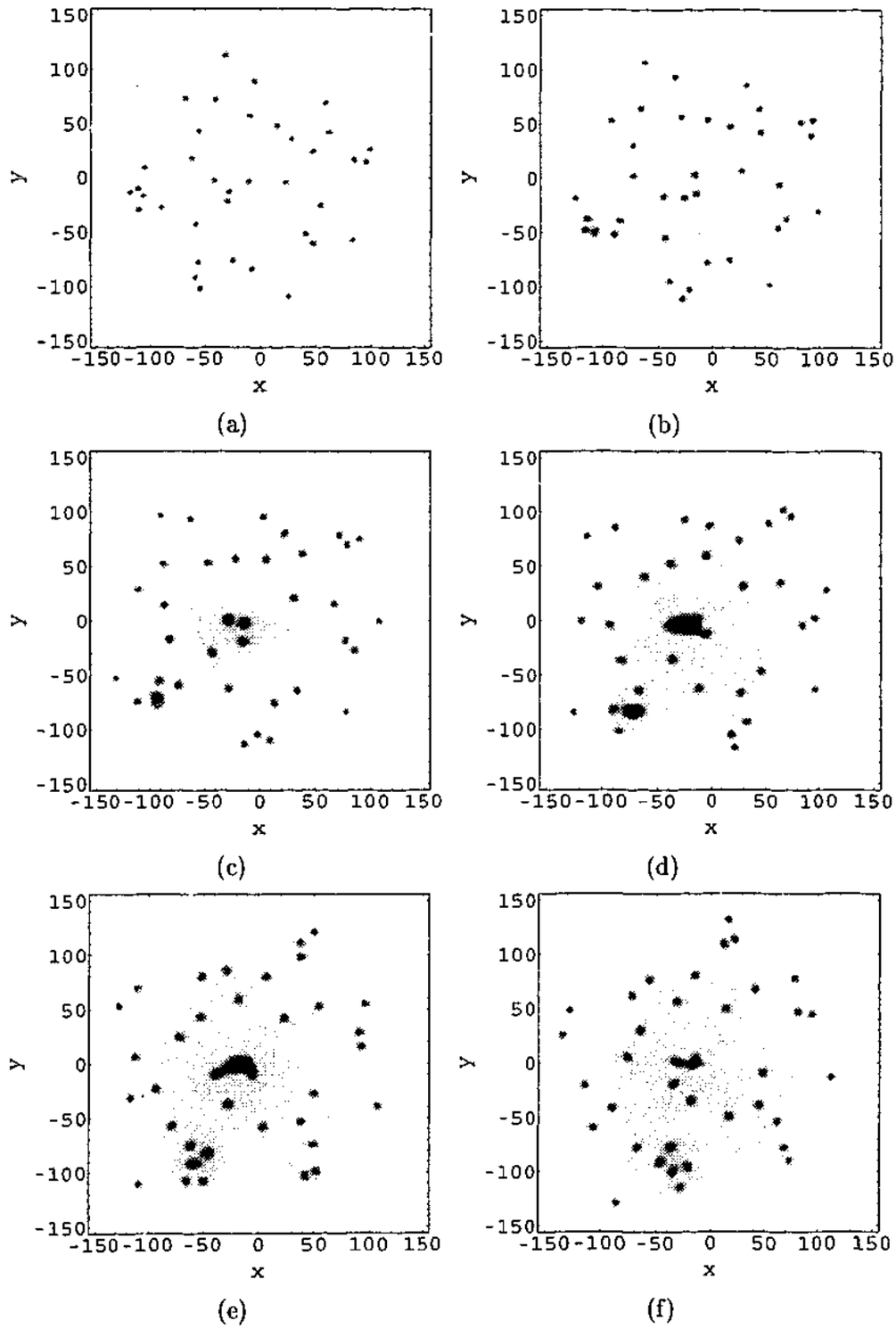

Figure 2.12: Light intensity of a random vortex configuration (black dots) in the LLC. (a) $t = 0$, (b) $t = 120$, (c) $t = 240$, (d) $t = 360$, (e) $t = 480$, and (f) at the end of the simulation, $t = 600$. The vortex configuration rotates anti-clockwise, with individual vortices orbiting each other in the anti-clockwise direction. Since there are no repulsive interactions between vortices the system does not evolve toward a regular lattice.

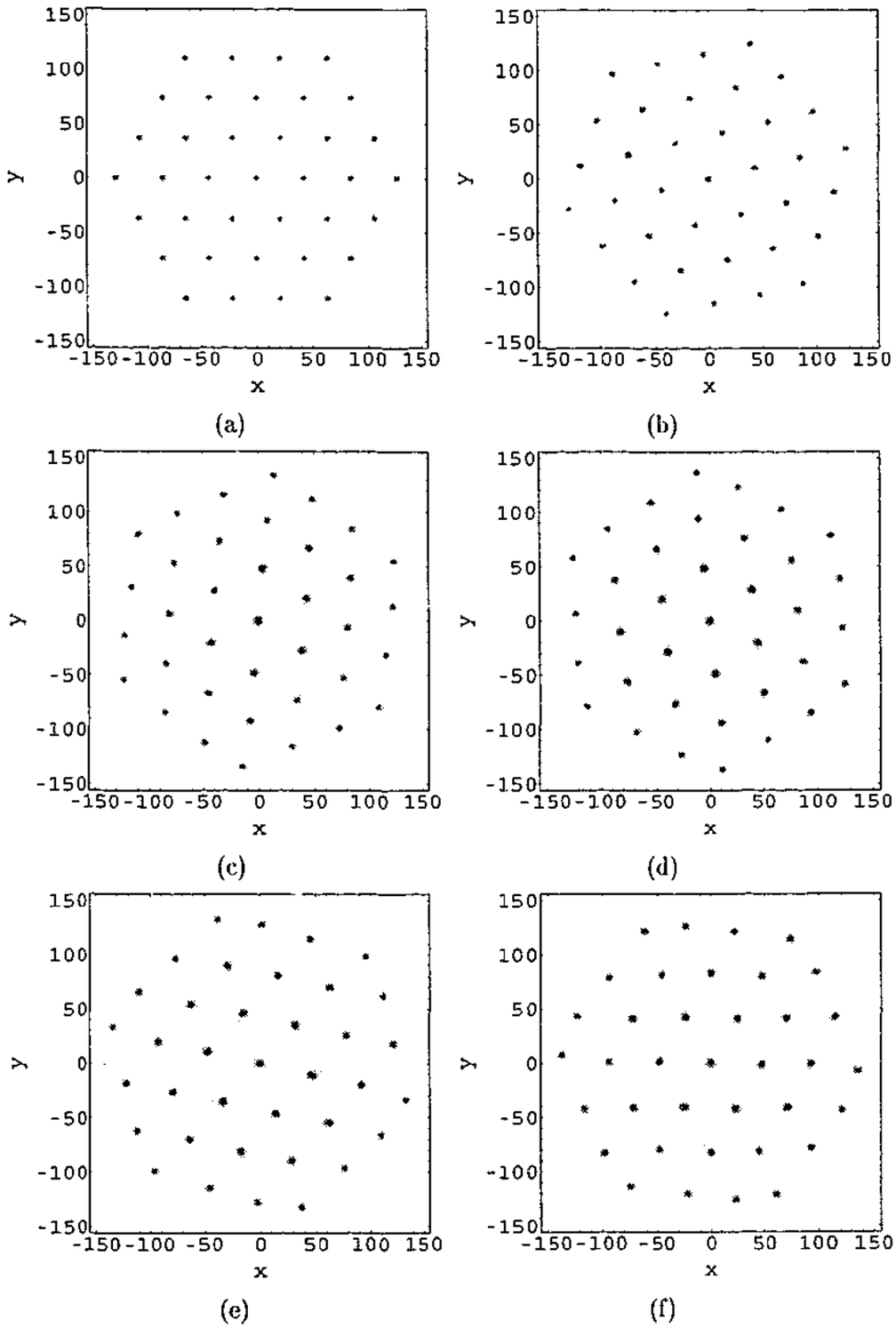

Figure 2.13: Light intensity of a triangular vortex lattice (black dots) in the LLC. (a) $t = 0$, (b) $t = 120$, (c) $t = 240$, (d) $t = 360$, (e) $t = 480$, and (f) at the end of the simulation, $t = 600$. The vortex configuration rotates in the anti-clockwise direction and is stable for the duration of the simulation.

background phase gradient. In the presence of a background phase gradient, the current density (2.47) is modified to

$$\mathbf{J} = \frac{\hbar|\Psi|^2}{m}\nabla\left(\theta + \alpha y\right). \tag{2.86}$$

The non-zero contribution to the current density is in the y direction. For a vortex located at the origin we obtain

$$\mathbf{J}_y = \frac{\hbar|\Psi|^2}{m}\left(\alpha + \frac{x}{x^2+y^2}\right). \tag{2.87}$$

If α is independent of time ($d\mathbf{J}_y/dt = 0$) there is no overall fluid motion in the y direction; consequently, there is no deflection of the vortex in the y direction.

Equation (2.87) suggests that the background fluid-flow modifies the y-component of velocity. The magnitude of the y-component of velocity to the right of the vortex increases by v_{bg}, whereas to the left of the vortex the velocity decreases by v_{bg}. This produces a pressure gradient that causes the entire fluid (including the vortex) to drift to the right (see Fig. 2.14 (a)). The equation of motion of the fluid is governed by (see e.g., Nozières and Pines 1990)

$$\frac{d\mathbf{J}_x}{dt} = -\nabla_x P. \tag{2.88}$$

where $\nabla_x P$ is the pressure gradient from left to the right. Equation (2.88) indicates that a vortex in a quantum fluid deflects in the direction perpendicular to the fluid-flow.

In contrast to a quantum fluid, a classical fluid has viscosity. In our model of liquid light, this is evident in Eqs. (2.71) and (2.71). If we assume that the LLC is in its ground state, for which $\psi_0^2 + \psi_1^2 = 1$, then $\partial\phi_0/\partial t > 0$ corresponds to $\partial\phi_1/\partial t < 0$ (likewise $\partial\phi_0/\partial t < 0$ corresponds to $\partial\phi_1/\partial t > 0$). This means that the real and imaginary components of Ψ are damped, and the LLC exhibits "internal friction" (or "viscosity"). A vortex in this classical fluid "feels" the presence of the background fluid-flow, and moves in the direction of the fluid-flow (see Fig. 2.14 (b)). There is no pressure gradient in the direction perpendicular to the fluid-flow ($\nabla_x P = 0$). This is apparent if we transform to a frame moving with the fluid-flow. In this frame the vortex appears stationary, consequently vortices in a classical fluid do not deflect in the direction perpendicular to the background fluid-flow.

The behaviour of a vortex in a background fluid-flow is dictated by the viscosity of the fluid, with vortices in quantum and classical condensates showing markedly different dynamics. Two vortices in a quantum condensate repel each other (a vortex and anti-vortex attract each other), whereas two vortices in a classical condensate orbit each other

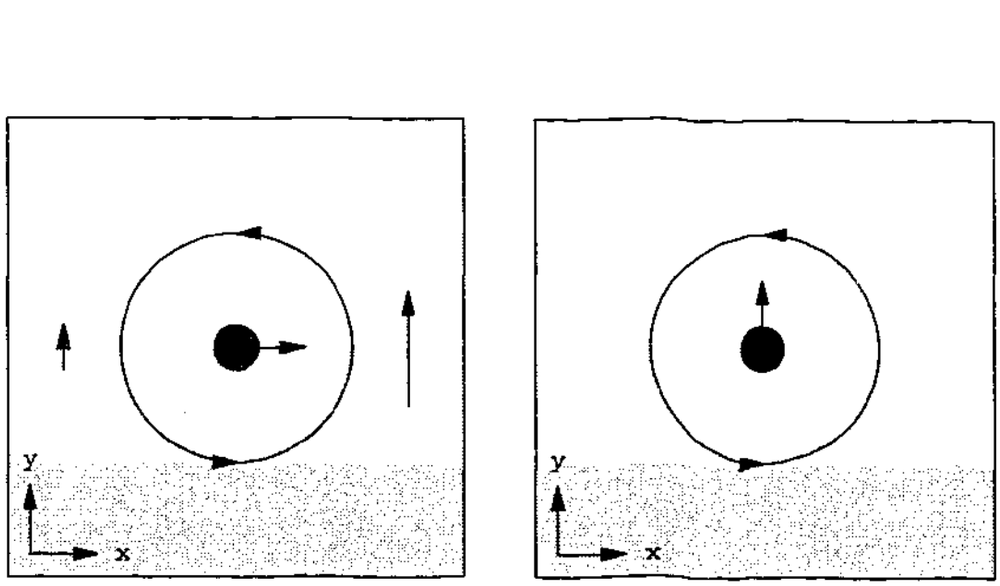

(a) (b)

Figure 2.14: Schematic showing a vortex inside a background phase gradient (in the y direction). The vortex is indicated by a "hole" with surrounding circulation. Arrows on the left and right of the vortex show the direction of the fluid-flow, with the length of the arrow indicating the relative velocity of the fluid. A vortex moves in the direction indicated by the arrow on the vortex. (a) A quantum fluid is frictionless (inviscid), and the vortex moves toward a lower pressure region. (b) A classical fluid is viscous, and the vortex moves in the direction of the background fluid-flow.

(a vortex and anti-vortex move parallel to each other) (see Fig. 2.15).

2.5 Concluding remarks

A vortex lattice in a rotating BEC can be understood in terms of minimizing the energy functional (2.37), however, it is not obvious how vortices evolve to a minimum energy configuration. We have used the GP equation to investigate vortices in a rotating BEC. It is found that rotation of a BEC is equivalent to establishing a background phase gradient in the condensate, which results in a confining potential for vortices (expelling anti-vortices), whose strength depends on the rotational frequency of the trap. As a consequence of conservation of topological charge, vortices and anti-vortices form following the phase transition to the BEC state, however, anti-vortices are expelled from the rotating trap. The competition between mutually repulsive vortex-vortex interactions and the confining potential, due to rotation of the condensate, provides a simple mechanism by which vortices evolve toward a stable (minimum) energy configuration.

In contrast to repulsive interactions between quantum vortices in a BEC, classical

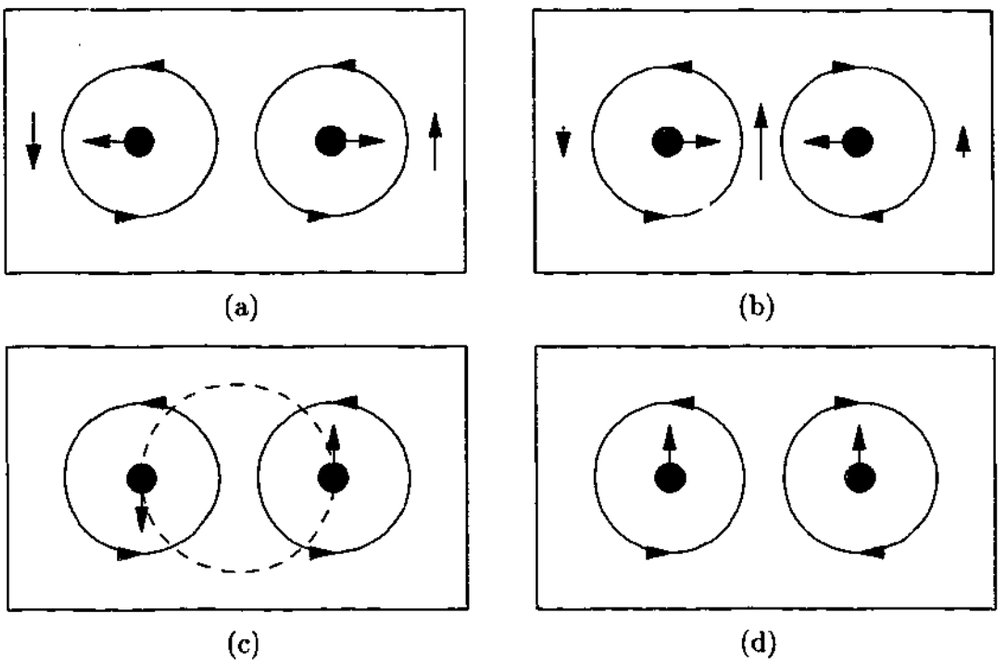

Figure 2.15: Schematic showing vortex dynamics in a quantum condensate (a) and (b), and classical condensate (c) and (d). (a) The velocity field between two vortices is lower than at the left and right of the vortices. This leads to lower pressure at the left and right of the vortices, resulting in the vortices moving away from each other. (b) For a vortex-anti-vortex pair the velocity field is higher (and the pressure lower) between the pair, resulting in the pair moving toward each other. (c) Two vortices in a classical condensate orbit each other, and (d) a vortex-anti-vortex pair moves parallel to each other.

vortices orbit each other. The origin of this difference is due to fluid viscosity. We have examined vortex dynamics in a LLC that highlights the role of dissipation in a novel classical condensate.

The appearance of vortices in disparate systems suggests that a model based on a mean-field approximation can be used to describe vortex dynamics in systems where direct experimental observations are not possible. One such system is considered in the next chapter; namely, vortices in a rotating dark matter condensate.

CHAPTER 3

Vortices in a Rotating Dark Matter Condensate

3.1 Introduction

Observational evidence indicates that over 90% of matter in the Universe is non-baryonic (Robinson 1985 and Bahcall *et al.* 1999). Support for the dark matter hypothesis comes from the flat non-Keplerian behaviour exhibited by the rotation curves of spiral galaxies (see e.g., Persic *et al.* 1996), Large Scale Structure (LSS), and the Cosmic Microwave Background Radiation[1] (CMBR). Numerous models have been proposed to explain the flat velocity profiles of spiral galaxies. One approach is to utilize modified Newtonian dynamics (MOND) (see e.g., Milgrom 2002). MOND modifies Newton's second law by replacing $F = m^*a$ with $F = m^*\mu(a/a_0)a$, where m^* is the mass, $\mu(a/a_0)$ is a dimensionless parameter comprising the acceleration a and an empirical constant $a_0 \sim 2 \times 10^{-10}$ ms^{-2} (see e.g., Kirillov and Turaev 2002). The model assumes that on a galactic scale ($a < a_0$) $\mu = a/a_0$ and for $a > a_0$ we set $\mu = 1$. Based on Newton's law for the gravitational force, $F = G_N M m^*/r^2$, where G_N is the Newtonian gravitational constant and M is the mass of the galaxy, MOND gives asymptotically flat velocity profiles, $v = (G_N M a_0)^{1/4}$, for galactic rotation curves. The dimensionless parameter, μ, modifies the force or the inertial mass. To reproduce the observed flat rotation curve of spiral galaxies, MOND modifies Newtonian gravity by adding terms to the gravitational potential. However, this is an ad hoc procedure which does not have a sound physical basis - it requires a negative cosmological constant term to provide an additional attractive force for matter (Bergström and Goodbar 1999 and Bergström 2000).

Alternative scenarios consider a spherical distribution of dark matter in the galactic halo that acts as a self-attracting sphere of ideal gas at uniform temperature - the isothermal halo model (see e.g., Binney and Tremaine 1987). Other phenomenological models, such as the Navarro-Frenk-White model (Navarro *et al.* 1996) and the "mildly singular"

[1]The most recent data from a one-year probe of the CMBR by the Wilkinson Microwave Anisotropy Probe (WMAP) reveals that the Universe is flat, comprising 4% ordinary (baryonic) matter, 23% dark matter and 73% dark energy (Bennett *et al.* 2003).

models (Kravtsov *et al.* 1998) have been developed to describe the asymptotic behavior of galactic rotation curves (Persic *et al.* 1996 and Bergström 2000). These models are not predicated on any particular dark matter candidate and assume an analytical form for the dark matter distribution, with adjustable parameters chosen to fit the observations.[2]

The nature of non-baryonic dark matter has also been the subject of widespread discussion in the literature (see e.g., Bergström 2000 for a comprehensive review). Candidates for non-baryonic dark matter include neutrinos, axions and neutralinos (see Sec. 3.3). Self-interacting scalar matter fields have also been considered as a possible dark matter candidate (Bergstrom 2000, Guzman and Matos 2000). Following a late-time cosmological phase transition, pseudo Nambu-Goldstone bosons are predicted to form, and under certain conditions may condense as a Bose liquid (Sin 1994). The time of the phase transition can be fine tuned to ensure that the phase transition does not impact adversely on nucleosynthesis. Recently Silverman and Mallett (2001a) considered a neutral self-interacting scalar field with spontaneously broken symmetry coupled to gravity. It is conjectured that these particles constitute a weakly interacting degenerate "ether" (WIDGET), that can form a Bose-Einstein condensate (BEC) about one second after the formation of the Universe (for a detailed discussion of the WIDGET model see Sec. 3.3).

In the present epoch, a cosmic BEC behaves like non-relativistic cold dark matter (CDM), producing a spherical mass distribution which contributes to the gravitational potential. An interesting consequence of galactic rotation is that it can give rise to vortices in the dark matter condensate with quantized circulation. Vortex dynamics in the dark matter condensate lead to a flat velocity profile for the condensate. In what follows we discuss the flat Universal Rotation Curve of spiral galaxies and the need for a dark matter model to explain the observational data.

3.2 The Universal Rotation Curve of spiral galaxies

Consider a galaxy whose mass distribution is $M(r)$, where r is the radial distance from the center of the galaxy. According to Newtonian mechanics the acceleration, a, of a test

[2]The analytical form of the dark matter distribution is expressed as a function of radial distance from the center of the galaxy

$$\rho(r) \propto \frac{\rho_c}{(r/R_0)^{\gamma_0}\left[1+(r/R_0)^{\gamma_1}\right]^{(\gamma_2-\gamma_0)/\gamma_1}}, \tag{3.1}$$

where ρ_c is the critical density of the Universe, R_0 is the core radius of the galaxy, γ_0, γ_1 and γ_2 are model dependent dimensionless parameters. For example, the Navarro-Frenk-White model uses $(\gamma_0,\gamma_1,\gamma_2) = (1,1,3)$, and the mildly singular models use $(\gamma_0,\gamma_1,\gamma_2) = (0.2,2,3)$ and $(\gamma_0,\gamma_1,\gamma_2) = (0.4,2,3)$ (see e.g., Bergström 2000). For the isothermal halo model, $(\gamma_0,\gamma_1,\gamma_2) = (0,2,2)$.

body (e.g., a star) is given by

$$a = \frac{G_N M(r)}{r^2}. \tag{3.2}$$

To remain in orbit the centripetal acceleration, v^2/r, must equal the inward gravitational acceleration of the body, a. As a consequence the velocity of the test body is written as

$$v = \sqrt{\frac{G_N M(r)}{r}}. \tag{3.3}$$

To obtain rigid-body rotation, Eq. (3.3) requires that the mass distribution $M(r) \propto r^3$; whereas for a flat velocity profile the mass distribution $M(r) \propto r$. Since $M(r) = \int \rho(r) 4\pi r^2 dr$, to account for the observed rigid-body rotation at the galactic core and flat rotation outside the galactic center, the required mass density profile must adopt the form

$$\rho(r) = \frac{C_0}{R_0^2 + r^2}. \tag{3.4}$$

Equation (3.4) is identical in form to the isothermal halo model. When $r \ll R_0$ it gives a rigid-body rotation profile, and for $r \gg R_0$ it produces a flat rotation profile. The values of C_0 and R_0 are chosen for each galaxy, however, a value $C_0 = 4.6 \times 10^8\ M_\odot\ \mathrm{kpc}^{-1}$ and $R_0 = 2.8$ kpc gives a parametric fit to the average rotation curve of spiral galaxies.

Not much is known about the visible mass density distribution at the galactic core. Since the gravitational potential of a self-gravitating system rapidly vanishes as we approach the center of the system, a galaxy must have a constant mass density near its center. This is consistent with the observed rigid-body rotation profile at the galactic center. What is surprising is the observation of a flat rotation profile outside the galactic center. Observations indicate that the luminous mass density, $\rho(r)$, varies as $r^{-3.5}$ from the galactic center (see e.g., Carroll and Ostlie 1996). However, this cannot account for the observed flat rotation curves, and leads to the astonishing conclusion that there must be non-luminous matter in the halo that produces the flat velocity profile for spiral galaxies. This non-luminous (dark) matter has been widely discussed in the literature (see e.g., Zwicky 1933, Bubin *et al.* 1980 and Bosma 1981, Persic *et al.* 1996 and Bergström 2000).

3.3 Self-interacting scalar field as a model of dark matter

The existence of dark matter is consistent with the theory of formation and evolution of the Universe in the context of Big-Bang inflationary cosmology (see e.g., Liddle and Lyth 2000). Further support for dark matter comes from observations of LSS (Bahcall 2000) and acoustic peaks in the CMBR (Bernardis *et al.* 2000 and Lange *et al.* 2001).

There is also tentative evidence that the Universe is expanding at an accelerating rate (Riess *et al.* 1998 and Perlmutter *et al.* 1999), suggesting the existence of dark energy (Turner 2000 and 2001), which may be due to a non-vanishing cosmological constant ($\Lambda \neq 0$).[3] The contribution of dark energy to the total mass density of the Universe (Ω_Λ) has been estimated by Turner (1999) to be in the range $0.55 < \Omega_\Lambda < 0.65$. Big-Bang nucleosynthesis (BBN) of light elements (i.e., D, ^{3}He, ^{4}He and ^{7}Li) constrains the baryonic component of the total mass density of the Universe to $\Omega_B = 0.04 \pm 0.01$ (Copi *et al.* 1995 and Burles *et al.* 1999). This implies that the dark matter contribution to the total mass density of the Universe is in the range $0.30 < \Omega_D < 0.42$. The theory of LSS formation favors $\Omega_\Lambda \sim 0.6$, $\Omega_B \sim 0.045$ and $\Omega_D \sim 0.355$ (Ostriker and Steinhardt 1995, Turner 2000, Roszkowski 2000 and Dalal *et al.* 2001).

The possibility of non-baryonic dark matter has been strengthened since the discovery that the neutrino has a small mass (Fukuda *et al.* 1998 and Turner 2000). Experiments to detect atmospheric neutrino oscillations using the Super-Kamiokande detector suggest that the neutrino mass is in the range 0.022 eV - 0.077 eV (Fukuda *et al.* 1998). Although it is unlikely that neutrinos contribute more than about 0.3% to the mass of the Universe (Turner 2000), there are many other possibilities for non-baryonic dark matter. Promising candidates, such as neutralinos and axions, arise from supersymmetry (SUSY). While neutralinos are a natural prediction of SUSY (Roszkowski 2000), axions are an inevitable consequence of solving the strong-CP problem in QCD (Belavin *et al.* 1975, Callan *et al.* 1976, Jackiw and Rebbi 1976 and t' Hooft 1976).[4] The strong-CP problem led Peccei and Quinn (1977) to propose an axion self-interacting scalar field with a broken $U(1)$ symmetry (see e.g., Kim 1987 and Cheng 1988). While the axion may be a viable dark matter candidate, axinos (the fermionic SUSY partner of the axion) have also been considered (Covi *et al.* 1999).

Theoretical modeling of LSS formation suggests that the dominant non-baryonic dark matter component may be a self-interacting scalar field (Spergel and Steinhardt 2000, Riotto and Tkachev 2000, Goodman 2000 and Mcdonald 2002). A self-interacting scalar

[3]The cosmological constant Λ is proportional to the vacuum energy density, ρ_Λ, of the Universe, i.e., $\Lambda = 8\pi G_N \rho_\Lambda / c^2$, where c is the speed of light in vacuum. The cosmological constant governs the rate of expansion of the Universe. A sufficiently large cosmological constant results in the Universe undergoing accelerated expansion.

[4]The violation of CP conservation in the strong interaction leads to a vanishing quark mass (Kolb and Turner 1990).

field may exist in the form of a Bose liquid (Sin 1994). Silverman and Mallett (2001a) consider such a condensate arising from a gravitationally induced symmetry breaking phase transition, which results in a high number density of very low mass WIDGET particles. To incorporate a self-interacting scalar field, Φ, we start with the usual line element

$$ds^2 = g_{\mu\nu}dx^\mu dx^\nu, \qquad (\mu,\nu = 0,1,2,3), \tag{3.5}$$

where $g_{\mu\nu}$ is the metric tensor. In the weak field limit of general relativity the model Lagrangian for the self-interacting scalar field may be written as ($\hbar = c = 1$)

$$\mathcal{L} = g^{\mu\nu}\overline{\partial_\mu\Phi}\partial_\nu\Phi + \frac{\lambda\eta^2}{2}|\Phi|^2 - \frac{\lambda}{4}|\Phi|^4, \tag{3.6}$$

where $\lambda\eta^2$ and λ are positive coupling constants. The vacuum expectation value is $\langle\Phi\rangle = \eta e^{i\theta}$, where θ is the phase angle around the vacuum manifold. By defining the WIDGET scalar field $\tilde{\Phi}$ as

$$\tilde{\Phi} = \Phi - \langle\Phi\rangle, \tag{3.7}$$

the Lagrangian (3.6) can be written as

$$\mathcal{L} = g^{\mu\nu}\overline{\partial_\mu\tilde{\Phi}}\partial_\nu\tilde{\Phi} - \lambda\eta^2|\tilde{\Phi}|^2 - \lambda\eta|\tilde{\Phi}|^3 - \frac{\lambda}{4}|\tilde{\Phi}|^4 + \frac{\lambda\eta^4}{4}. \tag{3.8}$$

The essence of the WIDGET model is to interpret all the terms containing $\tilde{\Phi}$ in Eq. (3.8) as the Lagrangian for the WIDGET, and the term $\lambda\eta^4/4$ as a cosmological constant, Λ, i.e.,

$$\mathcal{L}_{\tilde{\Phi}} = g^{\mu\nu}\overline{\partial_\mu\tilde{\Phi}}\partial_\nu\tilde{\Phi} - \lambda\eta^2|\tilde{\Phi}|^2 - \lambda\eta|\tilde{\Phi}|^3 - \frac{\lambda}{4}|\tilde{\Phi}|^4 \tag{3.9}$$

$$\mathcal{L}_\Lambda = \frac{2\Lambda}{\kappa^2}, \tag{3.10}$$

where κ is the gravitational coupling constant of the scalar field $\tilde{\Phi}$, and the cosmological constant is given by

$$\Lambda = \frac{\kappa^2 m^2\eta^2}{4}, \tag{3.11}$$

where $m^2 = \lambda\eta^2/2$. Equation (3.11) implies that the cosmological constant, Λ, is due to non-vanishing vacuum energy. The constant $\lambda\eta^4/4$ in the Lagrangian (3.8) causes acceleration of the expansion of the Universe. To find the WIDGET mass, Silverman and Mallett (2001a) assume that $\kappa = \eta^{-1}$. With this assumption Eq. (3.11) gives $\Lambda = m^2/4$. Utilizing $\Omega_\Lambda \sim 0.6$ and the critical mass density of the Universe $\rho_c \sim 10^{-26}$ kgm^{-3}, we

can obtain a value for Λ, namely $\Omega_\Lambda 8\pi G_N \rho_c/c^2 \sim 10^{-52}$ m^{-2}. This gives the mass of the WIDGET as $mc^2 \sim 2.5 \times 10^{-32}$ eV. This value for the WIDGET mass is similar to that derived by Silverman and Mallett (2001a); however, in a later paper these authors used data from the rotational curve of the galaxy M31 to estimate the mass of the WIDGET to be much higher[5], i.e., 2×10^{-25} eV/c^2 (see Silverman and Mallett 2001b). Adopting this latter value and utilizing $\rho_c \sim 6 \times 10^9$ eVc^{-2}m^{-3} for the critical energy density of the Universe, the WIDGET number density is $n \sim \rho_c/m = 3 \times 10^{32}$ m^{-3}. The number density is related to the temperature of the phase transition via $T_c \sim 4.6 \times 10^{-3} n^{1/3}$ (Silverman and Mallett 2001a). Using this relationship, the temperature of the phase transition giving rise to these bosons is $T_c \sim 3 \times 10^9$ K. This value for T_c implies that the WIDGET scalar field can exist as a dark matter Bose-Einstein condensate one second after the Big-Bang.

An interesting consequence of a cosmic BEC is the appearance of quantized vortices when the condensate rotates. In subsequent sections we show that these vortices naturally give rise to a flat velocity profile for spiral galaxies.[6] Before proceeding we first discuss the consequences of rotation of the dark matter condensate. In Chapter 2 we discussed rotation in the context of an alkali atom BEC (see Sec. 2.2). We now consider the effect of rotation and vortex dynamics in the context of a dark matter condensate.

3.4 Vortex dynamics and interactions in a rotating condensate

3.4.1 Interaction of a vortex with a background phase gradient

We start by considering the WIDGET model (3.6) for a flat spacetime, i.e., $g_{\mu\nu} = \mathrm{diag}(1,-1,-1,-1)$. In this spacetime Eq. (3.6) reduces to the Goldstone model which may be written as

$$\mathcal{L} = \overline{\partial^\mu \Phi} \partial_\mu \Phi - \frac{\lambda}{4}\left(|\Phi|^2 - \eta^2\right)^2. \tag{3.12}$$

The parameters λ and η determine the Compton mass of the scalar boson, i.e., $m^2 = \lambda\eta^2/2$. The equation of motion derived from Eq. (3.12) is

$$\Box\Phi + \frac{\lambda}{2}\Phi\left(|\Phi|^2 - \eta^2\right) = 0. \tag{3.13}$$

[5]The mass of the WIDGET is an unknown parameter. By relaxing the assumption $\kappa = \eta^{-1}$, the mass of the WIDGET can be varied. If the mass of the WIDGET has a different value, then so too does the WIDGET number density and the temperature of the phase transition.

[6]Although the existence of dark matter may account for the "missing mass", it only solves the problem of flat rotation curves by assuming that the matter density falls off as r^{-2} away from the galactic center (see e.g., Eq. (3.4)).

An axisymmetric static solution to Eq. (3.13), for a string oriented along the z-axis, is given by the Nielsen-Olesen vortex of the form

$$\phi(r) = f(r)e^{in\theta}, \tag{3.14}$$

where $f(r)$ is the magnitude of the field configuration, $r = \sqrt{x^2+y^2}$, $\theta = \theta(x,y)$ is the phase of the field and n is the winding number around the degenerate vacuum manifold, S^1. It can be shown that a vortex with $n > 1$ is unstable and always decays into multiple vortices with $n = 1$. In what follows we set $n = 1$.[7] For a vortex located at the origin, the phase of the scalar field is given by $\theta(x,y) = \tan^{-1}(y/x)$. The magnitude of the field, $f(r)$, is obtained by numerically finding the static solution to Eq. (3.13) in cylindrical coordinates.

We consider a vortex embedded in a background scalar field, ϕ_0. Since we are only interested in investigating how vortices interact with a background phase gradient, the magnitude of the background field is assumed to be unity (see Sec. 2.2). Utilizing a Taylor series expansion we can write the background phase Θ to first order as

$$\Theta = \Theta_0 + \nabla\Theta \cdot \mathbf{r}, \tag{3.15}$$

where $\mathbf{r}$ is the displacement vector from the origin ($\mathbf{r} = 0$), and Θ_0 is the phase at the origin. The phase of the background scalar field varies according to $\nabla\Theta \cdot \mathbf{r}$. For simplicity we assume that the phase gradient is a constant vector in the y direction, in which case we can write ϕ_0 as

$$\phi_0(y) = e^{i\alpha y}, \tag{3.16}$$

where $\alpha = \partial\Theta/\partial y$ is a constant. To describe a vortex in a background phase gradient we use the Abrikosov ansatz (Abrikosov 1957)

$$\Phi(t,x,y) \to \Phi(t,x,y)\phi_0(y). \tag{3.17}$$

At sufficiently large distances from the vortex core, the field configuration of a vortex is approximately constant, with magnitude η (or 1 after re-scaling). A vortex in a background phase is equivalent to overlapping two vortices that are separated by a large distance. Substituting Eq. (3.17) into the Lagrangian (3.12) we obtain

$$\mathcal{L} = \overline{\partial^\mu\Phi}\partial_\mu\Phi + \Phi\bar{\phi}_0\frac{\partial\bar{\Phi}}{\partial y}\frac{\partial\phi_0}{\partial y} + \bar{\Phi}\phi_0\frac{\partial\Phi}{\partial y}\frac{\partial\bar{\phi}_0}{\partial y} + |\Phi|^2\frac{\partial\phi_0}{\partial y}\frac{\partial\bar{\phi}_0}{\partial y} - \frac{\lambda}{4}\left(|\Phi|^2 - \eta^2\right)^2, \tag{3.18}$$

[7] Vortices with $n = 1$ have been discussed in Chapter 2 within the context of an atomic BEC model.

where only derivatives of ϕ_0 with respect to y survive. The latter are given by

$$\frac{\partial \phi_0}{\partial y} = i\alpha\phi_0 \tag{3.19}$$

$$\frac{\partial \bar{\phi}_0}{\partial y} = -i\alpha\bar{\phi}_0. \tag{3.20}$$

By direct substitution of Eqs. (3.19) and (3.20) into Eq. (3.18), we obtain

$$\mathcal{L} = \overline{\partial^\mu \Phi}\partial_\mu \Phi + i\alpha\left(\Phi\frac{\partial\bar{\Phi}}{\partial y} - \bar{\Phi}\frac{\partial\Phi}{\partial y}\right) - \alpha^2|\Phi|^2 - \frac{\lambda}{4}\left(|\Phi|^2 - \eta^2\right)^2. \tag{3.21}$$

Utilizing

$$\begin{aligned}\Phi\frac{\partial\bar{\Phi}}{\partial y} - \bar{\Phi}\frac{\partial\Phi}{\partial y} &= \Phi\frac{\partial}{\partial y}fe^{-i\theta} - \bar{\Phi}\frac{\partial}{\partial y}fe^{i\theta}, \\ &= -2if^2\frac{\partial\theta}{\partial y},\end{aligned} \tag{3.22}$$

where $|\Phi|^2 = f^2$, the Lagrangian (3.21) becomes

$$\mathcal{L} = \overline{\partial^\mu \Phi}\partial_\mu \Phi + 2\alpha f^2\frac{\partial\theta}{\partial y} - \alpha^2 f^2 - \frac{\lambda}{4}\left(f^2 - \eta^2\right)^2. \tag{3.23}$$

Thus the potential may be written as

$$V(f) = -2\alpha f^2\frac{\partial\theta}{\partial y} + \alpha^2 f^2 + \frac{\lambda}{4}\left(f^2 - \eta^2\right)^2. \tag{3.24}$$

For a vortex with uniform phase winding located at the origin, the phase of the scalar field is given by $\theta(x,y) = \tan^{-1}(y/x)$ so that

$$\frac{\partial\theta}{\partial y} = \frac{x}{x^2+y^2}. \tag{3.25}$$

The potential is now written as

$$V(f) = \frac{\lambda}{4}\left(f^2 - \eta^2\right)^2 + \alpha^2 f^2 - 2\alpha f^2\frac{x}{x^2+y^2}. \tag{3.26}$$

The first term in the potential (3.26) is a symmetry breaking term that gives rise to a vortex. Since α is a constant and f is cylindrically symmetric, the second term in the potential (3.26) is symmetric. Therefore the resultant force acting on the vortex due to this term vanishes. However, the third term represents an asymmetric potential, i.e.,

$$V_A = -2\alpha f^2\frac{x}{r^2}. \tag{3.27}$$

The form of V_A is determined from the numerical solution to the static vortex. The asymptotic vortex solution approaches the vacuum expectation value (VEV), for which $f(r \to \infty) = \eta$. However, the near field solution is given by

$$f(r \to 0) \approx c_0 r, \tag{3.28}$$

where c_0 is a constant[8], whence we write

$$V_A = -2\alpha c_0^2 x. \tag{3.29}$$

The resulting force on the vortex is therefore $\mathcal{F}_x = 2\alpha c_0^2$, whence a vortex embedded in a phase gradient (in the y direction) experiences a force in the x direction that is proportional to the magnitude of the phase gradient α. A vortex $\Phi = fe^{i\theta}$ embedded in the background field $\phi_0 = e^{i\alpha y}$ results in an overall field configuration with phase winding $\Theta = \tan^{-1}(y/x) + \alpha y$. This corresponds to a vortex with non-uniform phase winding. Such a configuration is not in equilibrium, since there is a force acting on the vortex. To attain equilibrium the vortex evolves toward a configuration with uniform phase winding.

Numerical simulations were performed to confirm that a vortex embedded in a phase gradient (in the y direction) experiences a force in the x direction. The equation of motion follows from the Lagrangian (3.21)

$$\Box\Phi - 2i\alpha\frac{\partial\Phi}{\partial y} + \alpha^2\Phi + \frac{\lambda}{2}\Phi\left(|\Phi|^2 - \eta^2\right) = 0. \tag{3.30}$$

Equation (3.30) can be recast in dimensionless form by using the transformations:

$$x_\mu \;\to\; (\eta^2\lambda/2)^{-1/2}x_\mu, \quad (\mu = t, x, y), \tag{3.31}$$

$$\Phi \;\to\; \eta\Phi. \tag{3.32}$$

With the transformations (3.31) and (3.32), space and time are now measured in units of the Compton length $1/\eta\sqrt{\lambda/2}$. The numerical simulation uses a second order leapfrog difference scheme.[9] The initial conditions invoke a cylindrically symmetric vortex (see Fig. 3.1), analogous to the vortex solution for the liquid light condensate (see Sec. 2.3).

To complete the simulations in a reasonable time, our numerical scheme uses a time step $\Delta t = 0.01$ and spatial step $\Delta h = 0.1$, where $\Delta t < \Delta h$ guarantees numerical stability. The simulation frame is 140×140, corresponding to a grid size of 1400×1400 (see Sec.

[8] A numerical solution to $f(r)$ in cylindrical coordinates gives $c_0 = 0.58$ (for $\lambda = 2$ and $\eta = 1$).

[9] See Appendix A for a detailed discussion of the numerical scheme and stability criterion.

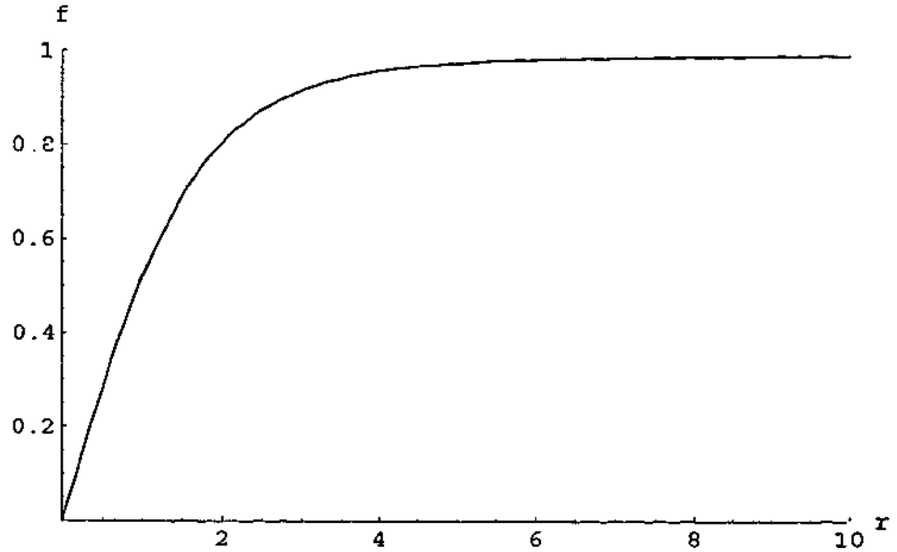

Figure 3.1: Static vortex solution in cylindrical coordinates. The field magnitude, f, vanishes at the origin where the phase winding of the vortex is undefined.

2.2). However, only a subset of the simulation frame (20×20) was chosen for the purpose of visualization.

Free boundary conditions are employed, in which the spatial derivative of the scalar field vanishes on the boundary. Imposing boundary conditions can induce numerical noise in the scalar field. Free boundary conditions allow the scalar field the freedom to "oscillate" on the boundary, however, the derivative of the field on the boundary is only accurate to second order in the spatial step (see Appendix A). This results in noise propagating into the visualization frame. To obviate this problem simulations were evolved for 6000 time steps, in which case noise does not have sufficient time to propagate into the visualization frame.

Figures 3.3 (a) and 3.4 (a) show the energy density of a vortex in a uniform background phase gradient at $t = 0$, and at the end of the simulation, $t = 60$. Figures 3.3 (b) and 3.4 (b) are the corresponding phase plots. The vortex, initially at rest, experiences an acceleration in the x direction whose magnitude depends on α. As the sign of α is changed the acceleration of the vortex reverses. At the end of each simulation the phase winding of the vortex reveals that the lines of constant phase are curved. This is a result of the vortex trying to accommodate the background phase gradient. The long-term evolution

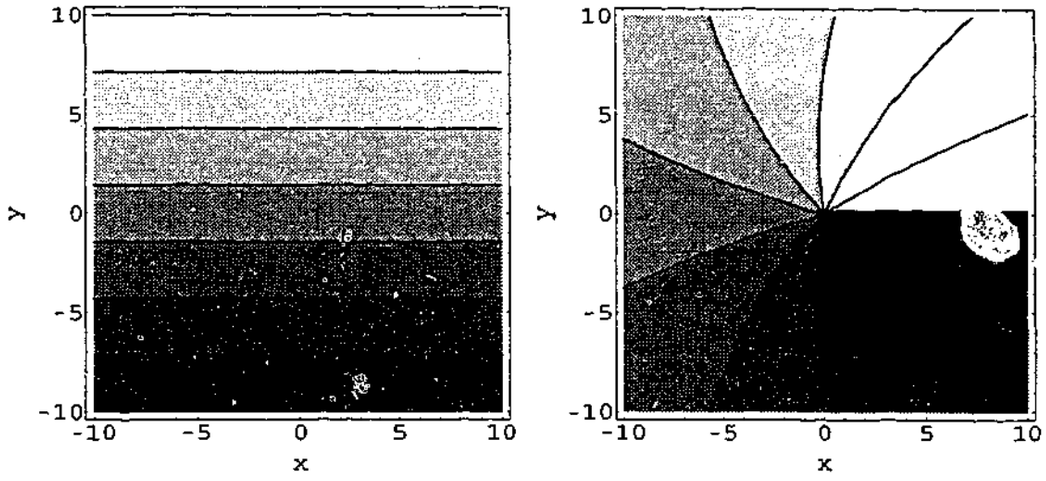

Figure 3.2: (a) A grey scale plot of a typical background phase αy ($\alpha = 0.01$), and (b) the overlapping phase $\tan^{-1}(y/x) + \alpha y$. In (a) the grey level denotes a phase in the range $[-0.1, 0.1]$, whereas in (b) black denotes 0 and white denotes a phase of 2π. The phase in (b) is indicative of a vortex with non-uniform phase winding.

of the vortex in the background phase gradient is toward a state of constant velocity. When "coupled" to the background phase, the vortex can be regarded as having a non-uniform phase winding. This non-uniform phase winding gives rise to a self-force[10], which attempts to restore the uniform phase winding (Thatcher and Morgan 1997). Once the uniform phase winding has been restored, the vortex stops accelerating and moves at a constant velocity.

The consistency of the model is confirmed by deriving the well known $1/r$ vortex-vortex interaction (Shellard 1987). Consider a vortex located at the origin, interacting with a second vortex located at position (x, y) (see Sec. 2.2.5). The background phase experienced by the second vortex, due to the first vortex, is $\theta(x, y) = \tan^{-1}(y/x)$. This gives rise to a force on the second vortex whose components in the x and y directions are

$$\mathcal{F}_x \propto \frac{\partial\theta(x,y)}{\partial y} = \frac{x}{r^2} \tag{3.33}$$

$$\mathcal{F}_y \propto \frac{\partial\theta(x,y)}{\partial x} = -\frac{y}{r^2}, \tag{3.34}$$

where the magnitude of the force is $\mathcal{F} = \sqrt{\mathcal{F}_x^2 + \mathcal{F}_y^2} \propto 1/r$. The two vortices exhibit a

[10] A vortex self-force was postulated by Thatcher and Morgan (1997) to arise as a consequence of the vortex interacting with its surrounding phase field. This self-force was introduced to explain the scattering of critically coupled vortices in the abelian-Higgs model.

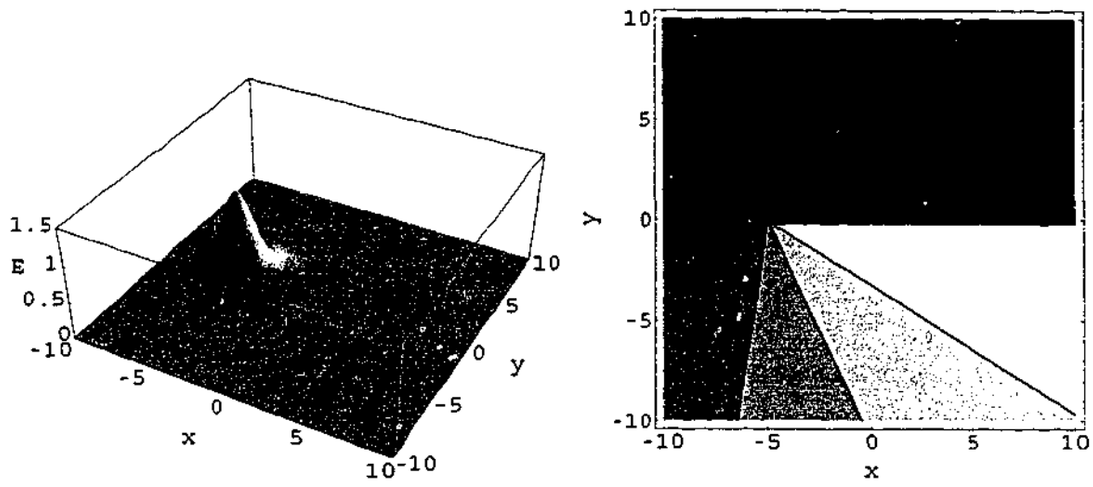

(a) (b)

Figure 3.3: (a) The energy density, and (b) phase winding of a vortex initially located at position $(-5, 0)$ in a constant background phase gradient ($\alpha = 0.01$). The phase winding of the vortex is anti-clockwise with black denoting 0 and white denoting 2π.

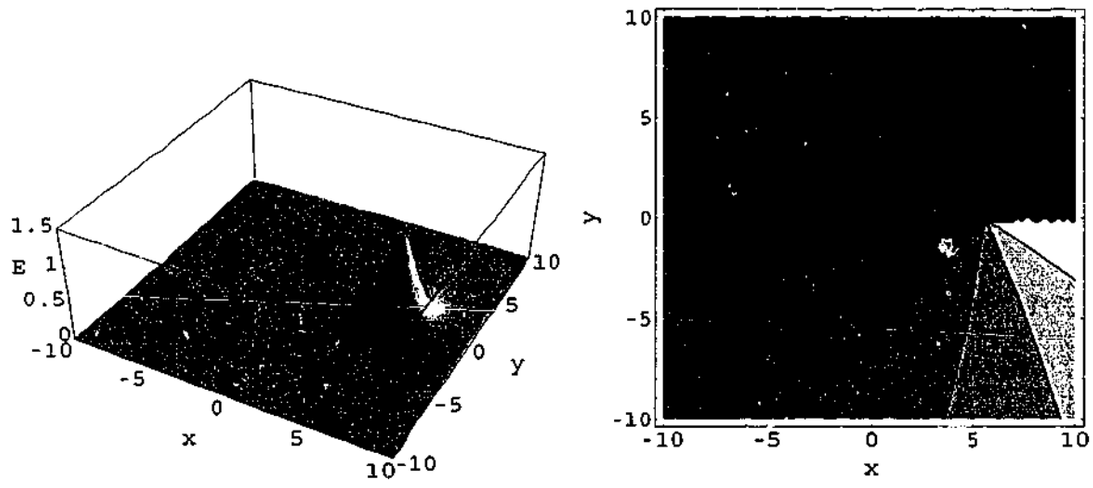

(a) (b)

Figure 3.4: (a) The energy density, and (b) phase winding of a vortex at $t = 60$. The vortex has moved from its initial position (Fig. 3.3) as a consequence of interacting with the background phase.

$1/r$ mutually repulsive force. This interaction will be shown to play a significant role in determining the distribution of vortices in a rotating dark matter condensate.

A vortex embedded in a dark matter condensate is analogous to a vortex in a BEC. In a BEC it is possible to engineer the background phase gradient to produce a confining potential - trapping vortices and expelling anti-vortices (see Sec. 2.2). The simplest way to produce such a background phase gradient is to rotate the condensate. In what follows we explore vortex dynamics in a rotating dark matter condensate.

3.4.2 Vortices in a rotating condensate

The background phase gradient that provides a harmonic trap potential for vortices (see Sec. 2.2) has components

$$\frac{\partial\Theta}{\partial x} = -\frac{1}{2}\Omega_x y \tag{3.35}$$

$$\frac{\partial\Theta}{\partial y} = \frac{1}{2}\Omega_y x. \tag{3.36}$$

The strength of the trap is dictated by the values of Ω_x and Ω_y. For simplicity we assume an isotropic trap with axisymmetric rotation,[11] for which $\Omega_x = \Omega_y = \Omega$. With this background phase gradient the Lagrangian (3.12) becomes

$$\begin{aligned}\mathcal{L} = {} & \overline{\partial^\mu\Phi}\partial_\mu\Phi + i\frac{\Omega}{2}\left[y\left(\bar{\Phi}\frac{\partial\Phi}{\partial x} - \Phi\frac{\partial\bar{\Phi}}{\partial x}\right) - x\left(\bar{\Phi}\frac{\partial\Phi}{\partial y} - \Phi\frac{\partial\bar{\Phi}}{\partial y}\right)\right] \\ & -\frac{1}{4}\Omega^2 r^2|\Phi|^2 - \frac{\lambda}{4}\left(|\Phi|^2 - \eta^2\right)^2.\end{aligned} \tag{3.37}$$

As with the case of an alkali atom BEC, where the background phase modifies the atomic trapping potential (see Sec. 2.2), the background phase of the dark matter condensate introduces a WIDGET trapping potential of the form $\frac{1}{4}\Omega^2 r^2$. The second term (in square brackets) in the Lagrangian (3.37) describes the harmonic potential due to the background phase gradient. The strength of the harmonic potential is proportional to Ωx in the x direction and to Ωy in the y direction. The equation of motion derived from this Lagrangian is

$$\Box\Phi + \frac{\lambda}{2}\Phi\left(|\Phi|^2 - 1\right) - \Omega L_z\Phi + \frac{1}{4}\Omega^2 r^2\Phi = 0, \tag{3.38}$$

where

$$L_z \equiv i\left(y\frac{\partial}{\partial x} - x\frac{\partial}{\partial y}\right) \tag{3.39}$$

[11] In the context of a dark matter condensate there is no evidence to suggest that the galactic halo exhibits non-axisymmetric rotation.

is the angular momentum component, and Ω is interpreted as an angular frequency. The last term in Eq. (3.38) represents a harmonic trap potential for the condensate. Equation (3.38) is the relativistic version of the mean-field Gross-Pitaevskii equation, describing vortices in a rotating BEC (see Chapter 2). The phase gradient in Eqs. (3.35) and (3.36) can be written as $\Omega\hat{\mathbf{e}}_z \times \mathbf{r}$. Rotation imprints a background phase gradient on the condensate, which is equivalent to performing a global $U(1)$ transformation on the wavefunction. The effect of rotation can be eliminated by transforming to a frame rotating with the condensate. This is accomplished by introducing a fictitious gauge field and performing a gauge transformation (see Eqs. (1.14) and (1.15)). A background phase gradient, $\Omega\hat{\mathbf{e}}_z \times \mathbf{r}$, imprinted on the condensate is equivalent to introducing an effective gauge field, $(\Omega\hat{\mathbf{e}}_z \times \mathbf{r})/Q^*$, where Q^* is the bosonic "charge".

The effect of rotation is to produce a confining potential for the vortices. This is confirmed via numerical simulations based on the field equation (3.38). To perform the numerical simulations we first solve Eq. (3.38) for a static vortex in cylindrical coordinates in the absence of rotation ($\Omega = 0$), and then wind the static vortex onto a Cartesian grid. The initial multiple vortex configuration is constructed by overlapping vortices using the Abrikosov ansatz. The numerical solution to the equation of motion (3.38) employs a finite difference scheme. Before proceeding we make a simplification to the model. The velocity of the rotating dark matter condensate ($v = \Omega r$) is of the order 10^{-2} (in natural units, $c = 1$). In what follows we neglect the contribution from the term $\frac{1}{4}\Omega^2 r^2$. Further, to implement the simulations in a reasonable time frame and for a manageable grid size, the numerical scheme was evolved up to $t = 900$, with a spatial step $\Delta h = 1.0$ and time step $\Delta t = 0.1$.

In analogy with vortices in a rotating BEC comprised of alkali atoms, it is expected that an equilibrium vortex lattice will form. We utilized an initial configuration with randomly distributed vortices (see Fig. 3.5 (a)). Since the initial vortex position is random, the separation of vortices can be small, and the Abrikosov ansatz is expected to generate numerical noise as the simulation evolves. To remedy this we introduce a damping term, $b\partial\Phi/\partial t$, into Eq. (3.38), where b is a small positive constant ($b = 0.5\Delta t$). Typical simulations are displayed in Figs. 3.5 (a) and (b). Figure 3.5 (a) shows the initial condition with vortices distributed randomly and Fig. 3.5 (b) shows that a regular ("triangular") vortex lattice develops at the end of the simulation. A plot of the number of vortices as a

function of radial distance from the origin is shown in Fig. 3.6. The corresponding number of vortices, N_v, for an ideal triangular vortex lattice, based on rigid body rotation, is

$$N_v = 3R(R+1)+1, \tag{3.40}$$

where $R = 0, 1, 2, ...$ denotes each "shell" of the ideal vortex arrangement, with $R = 0$ referring to the vortex at the origin. N_v is plotted in Fig. 3.6 as the solid line. The number of vortices based on an ideal triangular lattice (3.40) is slightly higher than the number obtained in our simulation. This discrepancy between the theoretical prediction and the numerical simulation is not well understood (see e.g., Feder and Clark 2001).

It is readily demonstrated that the vortex number density, n_v, is proportional to Ω, when Ω is a constant. Using numerical simulations, we have verified that this relationship is also valid when Ω has a radial dependence. Figure 3.7 shows an example for which $\Omega \propto r^{-1}$. Vortices that are randomly distributed evolve toward an approximately regular lattice. Figure 3.8 is a plot of vortex number as a function of radial distance based on Fig. 3.7 (b). The line of best fit shows that the total number of vortices, $N_v \propto r$, giving a vortex number density $n_v(r) = \pi^{-1} N_v r^{-2} \propto r^{-1}$, which implies that $n_v(r) \propto \Omega(r)$. This allows us to investigate vortices in a rotating dark matter condensate (galactic halo) for which Ω has a radial dependence.

3.4.3 Analytical perspective

Following a similar argument to that invoked for an alkali atom BEC (see Sec. 2.2.5), we obtain the relationship between n_v and Ω. Consider a large rotating surface, S, with radius r. The circulation is given by

$$\Gamma = \oint_{C=\partial S} \mathbf{v} \cdot d\mathbf{l} \tag{3.41}$$

$$= 2\pi r^2 \Omega. \tag{3.42}$$

To proceed we calculate the current density, $\mathbf{J}$, based on Eq. (3.38) for the dark matter condensate. The current density is given by

$$\mathbf{J} = \frac{\hbar}{mi}\left[\bar{\Phi}\nabla\Phi - \nabla\bar{\Phi}\Phi\right] \tag{3.43}$$

$$= \frac{2\hbar}{m} f^2 \nabla\theta. \tag{3.44}$$

Since $\mathbf{J} = f^2\mathbf{v}$, Eq. (3.44) gives

$$\mathbf{v} = \frac{2\hbar}{m}\nabla\theta. \tag{3.45}$$

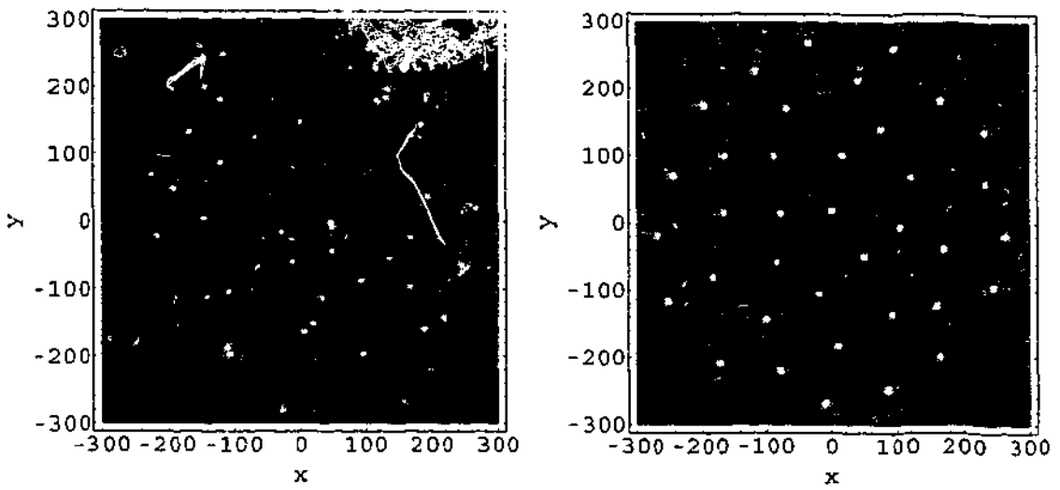

Figure 3.5: Grey scale plot of the energy density based on a typical simulation, showing (a) a random vortex configuration (white dots) at $t = 0$, and (b) the vortex configuration at the end of the simulation ($t = 900$). A minimum energy "triangular" vortex lattice develops as a result of competition between the repulsive inter-vortex forces and the confining potential due to rotation of the condensate.

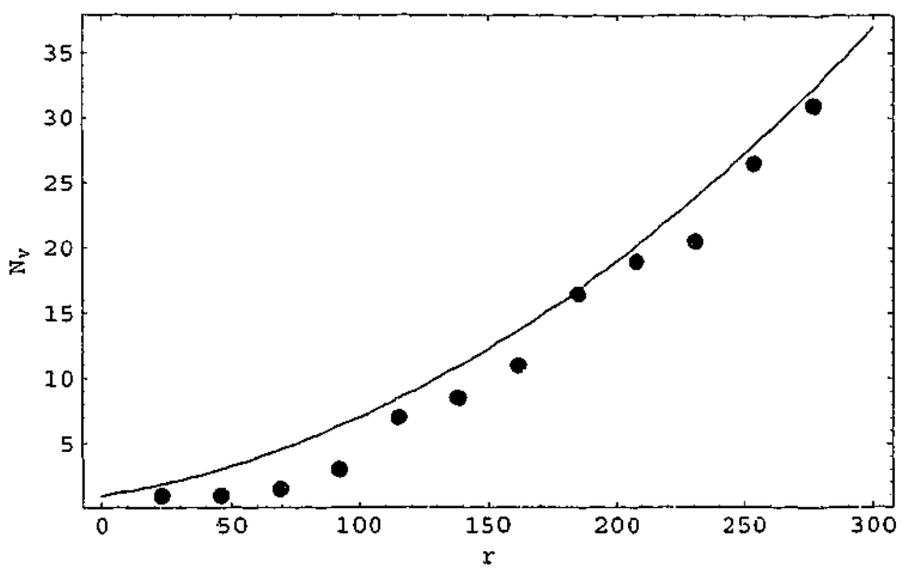

Figure 3.6: Number of vortices as a function of radial distance. The solid line is the prediction based on an ideal triangular vortex lattice.

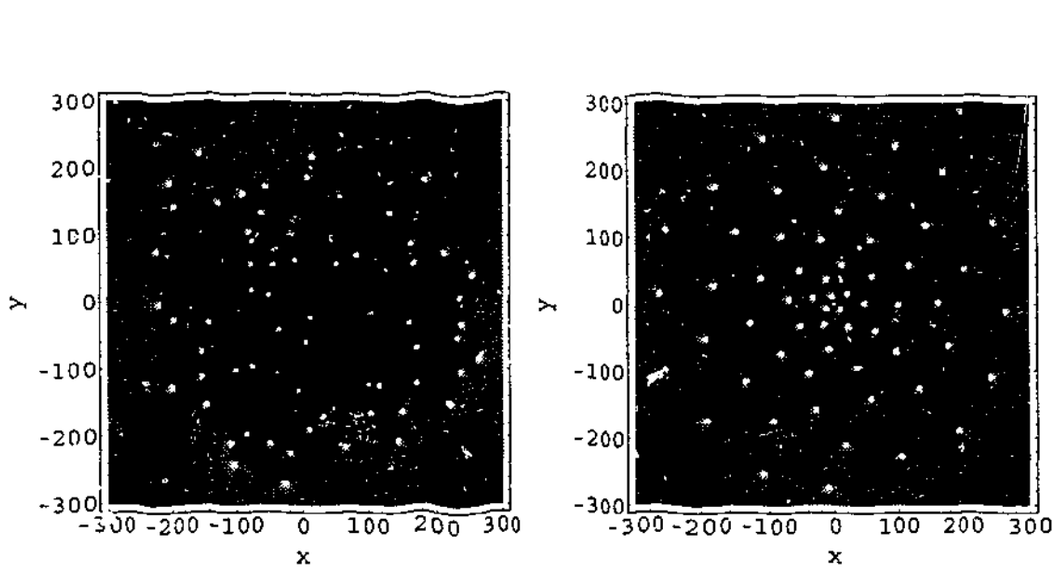

Figure 3.7: Grey scale plot of the energy density, showing (a) a random vortex configuration (white dots) at $t = 0$, and (b) the vortex configuration at the end of the simulation ($t = 900$). The equilibrium vortex lattice has $n_v \propto r^{-1}$.

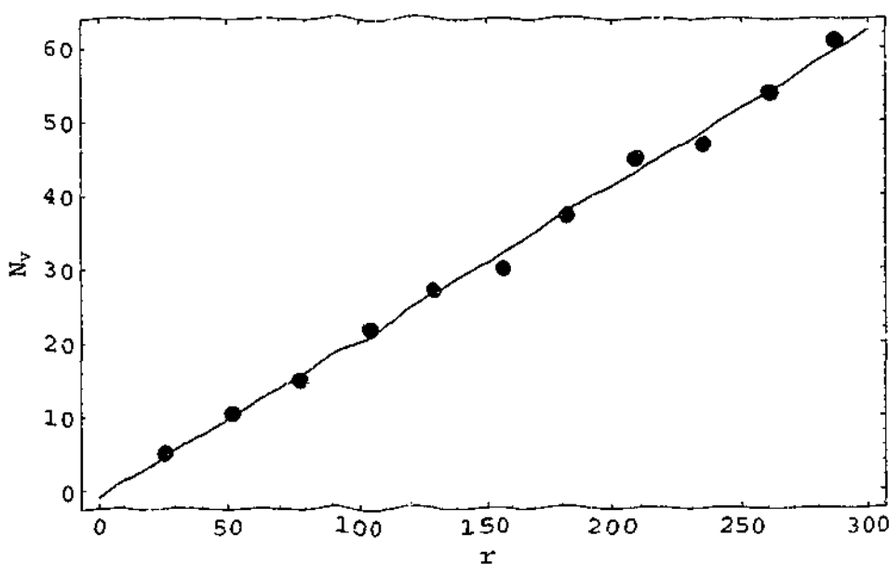

Figure 3.8: Number of vortices as a function of radial distance. The line of best fit indicates that N_v is proportional to the radial distance, in which case $n_v \propto r^{-1}$ (see text).

Substituting $dl = rd\theta$ and $|\nabla\theta| = 1/r$ into the equation for the circulation (3.41), we obtain

$$\oint_C \mathbf{v} \cdot d\mathbf{l} = \frac{4\pi N\hbar}{m}. \tag{3.46}$$

Finally, equating (3.42) with (3.46) gives

$$\Omega = \frac{h}{m} n_v. \tag{3.47}$$

For a rotating condensate, Eq. (3.47) predicts that vortices form with number density proportional to the rotational angular frequency. Our numerical simulations show that the linear relationship between n_v and Ω also holds when the angular rotation has a radial dependence (see Sec. 3.4.2). A galaxy does not rotate with constant Ω (outside its galactic core), and vortices are expected to form (in the galactic dark matter halo) with a radially-dependent number density. In the remainder of this chapter we investigate the implications of this conjecture for the rotation curves of spiral galaxies.

The rotation curve of a typical spiral galaxy is composed of two parts. Up to a few kiloparsecs from its core, the galaxy exhibits rigid-body rotation, where the rotational velocity rises rapidly from zero to a large value (e.g., $v \sim 250$ km s^{-1} for the Milky Way galaxy). The velocity profile in this region is approximately given by $v \propto r$, where r is the radial distance from the galactic center. This implies that the angular frequency, Ω, is constant and matter within the rigid-body region has the same orbital period. The second region corresponds to distances up to the visible edge of the galaxy, i.e., up to about 50 kpc - 100 kpc for most spiral galaxies. In this region we observe a flat velocity profile with oscillatory fine structure superposed on the rotation curve. To understand how a non-Keplerian velocity profile arises, we consider a self-gravitating dark matter condensate, consisting of ultra-low mass scalar bosons that arise during a late-time cosmological phase transition (see Sec. 3.3).

3.5 Vortices in a rotating dark matter condensate

3.5.1 Self-gravitating scalar field

Since galaxies are composed mainly of dark matter, we neglect the contribution from baryonic matter to galactic dynamics.[12] The Lagrangian for a gravitationally coupled self-interacting complex scalar field, with a $|\Phi|^4$ potential is given by (see e.g., Schunck

[12]Sec. 3.6 considers the role of baryonic matter.

and Mielke 1998)

$$\mathcal{L} = \frac{\sqrt{-g}}{2\kappa}\left\{R + \kappa\left[g^{\mu\nu}\overline{\partial_\mu\Phi}\partial_\nu\Phi - \frac{\lambda}{4}|\Phi|^4\right]\right\}, \tag{3.48}$$

where κ is the gravitational coupling constant, g is the determinant of the metric tensor $g_{\mu\nu}$ and R is the curvature scalar. Variation of Eq. (3.48) with respect to $\bar{\Phi}$ and $g_{\mu\nu}$ gives the coupled Einstein non-linear Klein-Gordon equations

$$G_{\mu\nu} = \kappa T_{\mu\nu}(\Phi) \tag{3.49}$$

$$\Box\Phi + \frac{\lambda}{2}|\Phi|^2\Phi = 0, \tag{3.50}$$

where $G_{\mu\nu} = R_{\mu\nu} - \frac{1}{2}g_{\mu\nu}R$ is the Einstein tensor and $T_{\mu\nu}(\Phi)$ is the energy-momentum tensor. In curved spacetime, the energy-momentum tensor and d'Alembertian are given by

$$T_{\mu\nu}(\Phi) = \frac{1}{2}\left[\partial_\mu\Phi\overline{\partial_\nu\Phi} + \overline{\partial_\mu\Phi}\partial_\nu\Phi\right] - \frac{g_{\mu\nu}\mathcal{L}}{\sqrt{-g}} \tag{3.51}$$

$$\Box = \frac{\partial_\mu\left(\sqrt{-g}g^{\mu\nu}\partial_\nu\right)}{\sqrt{-g}}. \tag{3.52}$$

In the weak field limit the metric tensor has the form (see e.g., D'Inverno 1996)

$$g_{\mu\nu} = \mathrm{diag}(1 + 2V(x,y,z), -1, -1, -1), \tag{3.53}$$

where $V(x,y,z)$ is the static gravitational potential. Using Eq. (3.53) the d'Alembertian is approximated by

$$\Box \approx \partial_\mu\partial^\mu\Phi = \frac{1}{1+2V}\ddot{\Phi} - \nabla^2\Phi, \tag{3.54}$$

where a dot denotes a time derivative. In arriving at Eq. (3.54) we have set $\partial_\mu g^{\mu\nu} = 0$, and assumed that the gravitational potential and scalar field is a slowly varying spatial function, so that the cross-term, $\nabla V \cdot \nabla\Phi$, can be neglected.

The self-interacting complex scalar field in the Lagrangian (3.48) does not break the global $U(1)$ symmetry. To obtain stable vortices we require the potential (in the Lagrangian (3.48)) to exhibit symmetry breaking, which is induced by introducing a chemical potential, μ, via the stationarity ansatz

$$\Phi(t,x,y,z) = e^{-i\mu t}\phi(x,y,z). \tag{3.55}$$

Substituting Eq.(3.55) into Eq. (3.50) we obtain the non-linear equation for the stationary state

$$-\nabla^2\phi + \frac{\lambda}{2}\left(|\phi|^2 - \frac{\eta^2}{1+2V}\right)\phi = 0, \tag{3.56}$$

where $\eta^2 = 2\mu^2/\lambda$. It is apparent from Eq. (3.56) that the symmetry breaking potential, in the presence of gravity, is $\lambda\left(|\Phi|^2 - \eta^2/(1+2V)\right)^2/4$. To obtain stable vortices we replace the $|\Phi|^4$ potential in Eq. (3.48) with $\lambda\left(|\Phi|^2 - \eta^2/(1+2V)\right)^2/4$. The equation of motion for the scalar field is now given by

$$\frac{1}{1+2V}\ddot{\Phi} - \nabla^2\Phi + \frac{\lambda}{2}\left(|\Phi|^2 - \frac{\eta^2}{1+2V}\right)\Phi - \Omega L_z\Phi = 0, \tag{3.57}$$

where we have explicitly included the angular momentum term, $\Omega L_z\Phi$. This term arises from the transformation $\Phi \rightarrow \Phi e^{i\nabla\Theta\cdot\mathbf{r}}$, which accounts for axisymmetric rotation of the dark matter condensate as discussed in Sec. 3.4. Such a transformation results in a trap potential for the dark matter condensate, i.e., $\frac{1}{4}\Omega^2 r^2$ (see Eq. (3.38)). This trap potential has been omitted from Eq. (3.57), since $\Omega r \approx 10^{-3}$ for a typical disk galaxy[13] and the condensate is confined via gravitational interactions.

Clumping of the dark matter condensate arises because of the gravitational potential $\eta^2/(1+2V)$ in Eq. (3.57). Since particle number is conserved there will be an increase in the field magnitude at the center of the condensate. However, for convenience we set $\Phi = \eta$ at $r = 0$. For $V \ll 1$ we approach the flat space limit for which $(1+2V)^{-1} \simeq 1-2V$; in this situation the gravitational potential in Eq. (3.57) enters via a term of the form $\eta^2\lambda V\Phi$.

The equation governing the gravitational potential V is obtained from Einstein's field equation (3.49), with the source term specified by the energy-momentum tensor (3.51). Assuming a spherically symmetric dark matter halo, the line element is given by

$$ds^2 = (1+2V)dt^2 - dr^2 - r^2\left(\sin^2\vartheta d\varphi^2 + d\vartheta^2\right). \tag{3.58}$$

Using Eq. (3.58) it is found that the time component of the Einstein tensor vanishes, i.e., $G_{00} = 0$. For a static spherically symmetric scalar field, $|\phi| = f(r)$, the T_{00}-component of the energy-momentum tensor is given by

$$\mathcal{T}_{00} = \frac{\lambda}{8}f^4(r)\,(1+2V) + \frac{1+2V}{2}f'(r)^2 - \frac{2V'}{\kappa r} + \frac{V'^2}{\kappa(1+2V)} - \frac{V''}{\kappa}, \tag{3.59}$$

where a dash denotes differentiation with respect to r. Setting $G_{00} = \kappa T_{00}$, the equation governing the gravitational potential (in the weak field limit) reduces to

$$V'' + \frac{2}{r}V' = \frac{\kappa}{2}\,(1+2V)\,\frac{\lambda}{4}f^4(r). \tag{3.60}$$

[13]For example, the rotation curves of 131 spiral galaxies listed in Persic *et al.* (1996) have velocities in the range 55 kms^{-1} to 320 kms^{-1}, which corresponds to a value of Ωr in the range 1.8×10^{-4} to 1.1×10^{-3}.

In arriving at Eq. (3.60) we have assumed a weak gravitational field, for which the gravitational potential varies slowly in space. This allows us to omit the term V'^2 from T_{00}. The term $f'(r)^2$ is also neglected in deriving Eq. (3.60), since a slowly varying gravitational potential results in the dark matter condensate density slowly decreasing from the center of the galaxy. In the Newtonian limit the equation governing the gravitational potential (3.60) reduces to the well known Poisson equation.

Equations (3.57) and (3.60) indicate that the gravitational coupling constant κ determines the gravitational potential and dark matter (condensate) distribution. Since the numerical value of κ is unknown (see Sec. 3.3), various gravitational potentials and dark matter distributions are obtained for different values of κ. A numerical value of κ must be chosen to ensure that the gravitational potential is consistent with the weak field assumption, and that the dark matter distribution agrees with the generic profile adopted in the literature.

The coupled equations (3.57) and (3.60) are solved numerically using an iterative method (see Appendix A). The parameters in the coupled equations are rendered dimensionless by the following transformations, which eliminate η and λ:

$$x_\mu \rightarrow \left(\eta\sqrt{\lambda/2}\right)^{-1} x_\mu, \tag{3.61}$$

$$\Phi \rightarrow \eta^{-1}\Phi, \tag{3.62}$$

$$\Omega \rightarrow \frac{\eta^2\lambda}{2}\Omega, \tag{3.63}$$

$$\kappa \rightarrow \eta^{-2}\kappa. \tag{3.64}$$

To perform numerical simulations we first look for a static solution to the dark matter distribution, i.e., the gravitationally-coupled scalar field. Numerical solutions for the condensate distribution can be obtained from Eqs. (3.56) and (3.60) by employing a combination of an iterative leap-frog method and a fixed point finite difference scheme. The iteration scheme first solves for the gravitational potential (3.60) using a leap-frog scheme with V and V' set to zero at the origin. The leap-frog scheme starts by computing the gravitational potential with an initial guess for the scalar field magnitude (e.g., $f = 1$). Once the gravitational potential has been obtained, we solve for the magnitude of the scalar field f using a fixed point method (see Sec. 2.3). After the magnitude of the scalar field is obtained, we repeat the iteration scheme by using the newly found magnitude of the scalar field to find the gravitational potential. The iteration scheme proceeds until

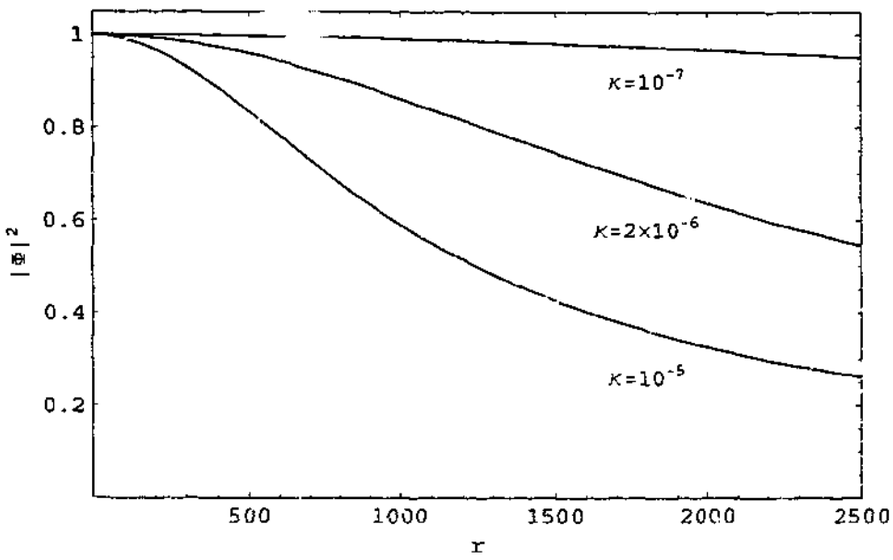

Figure 3.9: Radial plot of the WIDGET number density, $|\Phi|^2$, using the gravitational potential shown in Fig. 3.10. The distribution of the WIDGET number density is dependent on the coupling constant κ. As κ increases, $|\Phi|^2$ changes from an approximately uniform number density to one where the dark matter condensate begins to "clump" at the center of the "protogalaxy".

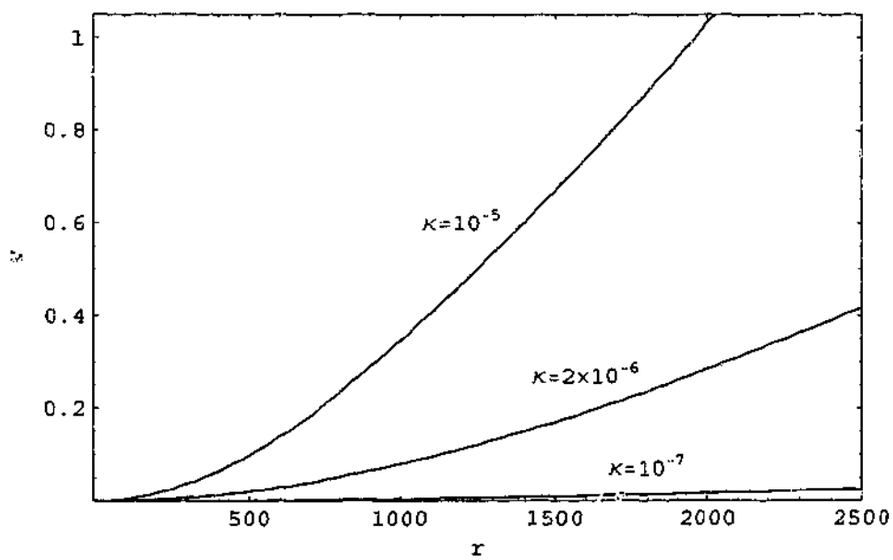

Figure 3.10: Radial plot of the gravitational potential, V, based on the WIDGET number density, $|\Phi|^2$, shown in Fig. 3.9. The strength of the gravitational potential is dependent on κ. Larger values of κ result in a larger gravitational potential.

changes in the gravitational potential and the magnitude of the scalar field at successive iterations are small (typically $\sim 10^{-10}$).[14]

The WIDGET number density, $|\Phi|^2$, and the gravitational potential, V, are plotted in Figs. 3.9 and 3.10 for different values of κ. Figure 3.9 shows that $|\Phi|^2$ decreases from its peak value ($|\Phi|^2 = 1$) at the origin, indicating clumping of the dark matter condensate. The degree of clumping depends on the value of κ, with larger gravitational coupling leading to enhanced clumping of the condensate at the origin, i.e., the WIDGET number density falls off faster for larger values of κ. Since a galaxy exhibits rigid body rotation at its center ($v \propto \sqrt{M/r}$), the dark matter condensate number density has a constant value at the origin. In Fig. 3.10 we note that larger values of κ lead to an increase in the gravitational potential despite the decrease in the WIDGET number density. This is because WIDGETs induce the gravitational potential, which in turn causes clumping of the condensate.

Figure 3.9 shows a radial plot of the WIDGET number density for $\kappa \approx 2 \times 10^{-6}$, which is consistent with the generic dark matter profile adopted in the literature (see e.g., Bergstrom 2000). The value $\kappa \approx 2 \times 10^{-6}$ also produces a gravitational potential consistent with the weak field limit for the metric tensor (3.53). Subsequent numerical simulations of the rotating dark matter condensate adopt this value for the gravitational coupling constant.

3.5.2 Vortex formation via rotation

Vortices form in a rotating dark matter BEC when the angular frequency exceeds a critical value, Ω_c. Immediately after formation we conjecture that a disk protogalaxy has a Keplerian velocity profile outside its nucleus ($r > R_0$), whereas for $r \leq R_0$ the protogalaxy exhibits rigid body motion (Binney and Tremaine 1987). Rotation establishes a background phase gradient in the dark matter BEC, which is determined by the initial angular frequency profile, $\Omega(r)$, of the protogalaxy. When $\Omega(r) > \Omega_c$, vortices are nucleated in the condensate. The background phase gradient produces a harmonic trap for the vortices (expelling anti-vortices), with the trapping force exhibiting a radial dependence, whose magnitude in the Keplerian regime ($r > R_0$) is given by

$$\mathcal{F}(r) \propto r\Omega(r) = \frac{\sqrt{GM_D(r)}}{r^{1/2}}, \tag{3.65}$$

[14] The combination of an iterative leap-frog method and a fixed point finite difference scheme was used by Ruffini and Bonazzola (1969) to solve for a gravitationally-coupled non-self interacting scalar field.

where $M_D(r)$ is the mass of dark matter within radius r from the galactic center. Each vortex has a quantized circulation, h/m, and a vortex lattice forms with number density, $n_v(r)$, proportional to the angular frequency $\Omega(r)$ (see Eq. (3.47)). Numerical simulations indicate that to confine vortices within $r \leq R_0$, it is necessary to increase the strength of the vortex trap. This is achieved by including a parameter β in Eq. (3.47) to modify the trapping potential, thus we write

$$\Omega(r) = \frac{\beta h}{m} n_v(r). \tag{3.66}$$

For $\beta = 1$ Eq. (3.66) reduces to Eq. (3.47). Higher values of β result in a stronger trapping potential for vortices. This implies that a vortex configuration is more stable when β is greater than unity. Numerical simulations are carried out in Sec. 3.5.3 to explore how the strength of the vortex trap depends on β.

According to Eq. (3.65) the trapping force on a vortex (due to the rotation of the protogalaxy) has a $r^{-1/2}$ dependence. However, inter-vortex forces also establish a background phase gradient in the dark matter BEC, with each vortex experiencing a $r^{-1/2}$ repulsive force within its causal horizon ξ_H. Initially ξ_H is of the order of the coherence length of the BEC (following the formation of the condensate). The resultant force on a vortex is zero, since the trapping force due to rotation is balanced by the net repulsive force from all other vortices. In the long term evolution of the dark matter condensate, the scalar field becomes correlated over larger distances and ξ_H increases.[15] As ξ_H increases, each vortex interacts with a larger number of vortices; consequently, a vortex experiences a non-zero force that causes it to move out in the radial direction. This results in an equilibrium vortex configuration with $n_v \propto r^{-1}$, which implies a flat velocity profile for the dark matter condensate (outside the galactic nucleus). In the vicinity of the nucleus, rigid body rotation produces a uniform vortex density with a concomitant zero net radial force on each vortex.

3.5.3 Numerical simulations

To confirm the conjecture that $n_v \propto r^{-1}$ we have studied vortex dynamics in a harmonic trap using numerical simulations. We assume a spherically symmetric distribution of dark

[15] The scalar field exhibits correlations due to drift and/or diffusion of WIDGETs. Drift arises from a temperature gradient, whereas diffusion is due to a gradient in the WIDGET number density. The latter process is a consequence of repulsive interactions between WIDGETs and random (Brownian) motion of WIDGETs.

matter (in the galactic halo), and consider vortices in the two-dimensional transverse plane $r = (x, y)$. The evolution of the scalar field is given by Eqs. (3.57) and (3.60), with the initial vortex configuration, Φ_0, obtained by overlapping the static gravitationally coupled scalar field, according to the Abrikosov ansatz, i.e.,

$$\Phi_0(r) = \prod_{k=0}^{n} \phi_k(r), \tag{3.67}$$

where ϕ_0 is the gravitationally coupled static scalar field with magnitude shown in Fig. 3.9, and ϕ_k $(k \neq 0)$ is the vortex solution obtained by solving Eq. (3.56) in cylindrical coordinates for $V = 0$. Once the initial condition has been constructed, a leap frog discretization method is employed to evolve the equation of motion (3.57). For each time step we reconstruct the WIDGET number density and solve for the gravitational potential V using Eq. (3.60).

To obtain the initial condition for the scalar field, $\Phi_0(r)$, we consider the relationship between the radial velocity distribution, $v(r)$, and vortex number density, $n_v(r)$. The vortex number density is given by $(\hbar = m = 1)$

$$n_v(r) = \frac{v(r)}{2\pi\beta r}. \tag{3.68}$$

To mimic galactic rotation, the velocity profile, $v(r)$, is divided into two parts. The first part represents rigid-body rotation, where $v \propto r$ (for $r \leq R_0$), and the second part represents Keplerian rotation, where $v \propto \sqrt{M(r)/r}$ (for $r > R_0$). Rigid-rotation of the galaxy corresponds to setting the vortex number density

$$n_v(r) = c_0 \qquad (r \leq R_0), \tag{3.69}$$

where c_0 is a constant. The spherical mass distribution within radius r (i.e., $M(r)$) increases in the radial direction. For rigid-body rotation $M(r) \propto r^3$, whereas the flat velocity profile gives $M(r) \propto r$. The mass density (of luminous matter) decreases much faster than the observed flat velocity profile, with the mass distribution specified by $M(r) \propto r^\gamma$ $(0 \leq \gamma \leq 1)$; for a flat velocity profile $\gamma = 1$. Since we anticipate the vortex number density evolving toward a flat velocity profile (i.e., $\gamma \to 1$) we start with $\gamma = 0$, i.e., $v \propto \sqrt{M(r)/r} \propto r^{-1/2}$. From Eq. (3.68) we obtain

$$n_v(r) = c_1 r^{-3/2} \qquad (r > R_0), \tag{3.70}$$

where c_1 is a constant.

To obtain an initial vortex configuration we solve for c_0 and c_1 for a fixed number of vortices. Details of the calculation of the initial vortex configuration are given in Appendix B. The actual number of vortices is determined by the rotational velocity (angular frequency) of the galaxy. For example, the galaxy M31 has an angular frequency of $\Omega \sim 5\times10^{-17}$ rad s^{-1} at 150 kpc from its center (see e.g., Silverman and Mallett 2001b). Using a WIDGET mass $m = 2 \times 10^{-23}$ eV/c^2, Eq. (3.66) gives the number of vortices as $N_v = 181$. This is the minimum number of vortices expected to form within the M31 halo, since higher angular frequencies (at distances less than 150 kpc) produce a larger number of vortices. Silverman and Mallett (2001b) calculate that approximately 340 vortices are expected to form within the M31 halo. The number of vortices is therefore expected to be of order of several hundred for a typical spiral galaxy.

Our simulations use 500 vortices on a grid of size 4600×4600, with all vortices initially placed within a radius $R_1 = 1800$; the rigid body regime is specified by a variable parameter, R_0. The grid size is sufficiently large to ensure that, at the end of the simulation ($t = 500$), noise from the boundary does not propagate into the visualization frame (3300×3300). For these simulations we set the spatial step $\Delta h = 1$ and time step $\Delta t = 0.2$. Although the initial vortex configuration is prescribed radially, its angular distribution is random. A pseudo-random number generator is used to establish the angular distribution (see Fig. 3.15). Since the initial separation of vortices can be small, the Abrikosov ansatz is expected to generate numerical noise as the simulation evolves. To remedy this we introduce a damping term $b\partial\Phi/\partial t$ into Eq. (3.57), where b is a small positive constant ($b = 0.1\Delta t$). The radial dependence of the vortex number density is calculated from the number of vortices inside an annular region ($\Delta r = 2$). To find the number of vortices within the annular region we need to detect the vortex positions at each iteration.

A vortex can be located by detecting the phase winding at each lattice point. However, since the position of a vortex is well defined at the beginning of the simulation we can readily track vortices by identifying the minimum in the magnitude of the scalar field, $|\Phi|$. The vortex position at the current iteration may correspond to the position at the previous iteration, or to the position of one of its nearest neighbors. This provides a simple and efficient method for finding the vortex position which uses a small number of lattice points and minimal computation. It only fails if there is excessive noise[16], or when

[16] Any other vortex detection method will also fail in the presence of excessive noise.

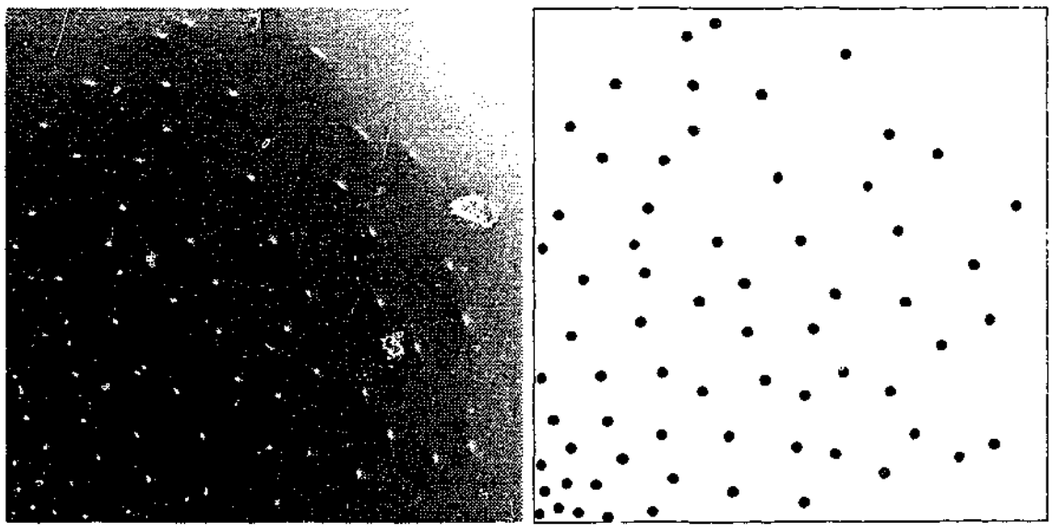

(a) (b)

Figure 3.11: (a) A typical energy density plot in the range $x = [0, 1000]$ and $y = [0, 1000]$ showing the vortex positions as white dots. (b) Vortex positions obtained using the vortex detection method described in the text. The vortex positions in (a) match exactly those in (b).

vortex collisions occur during the simulation.[17] The accuracy of the detection scheme is demonstrated in Fig. 3.11, where vortex positions match exactly those predicted by the vortex detection scheme.

Since the vortex number density is calculated using a small annular region, this approach leads to large variations in the vortex number density, i.e., there are some annular regions where the vortex number density is very high and other regions where the number density vanishes. To ameliorate this problem we smooth the vortex number density using a low-pass spatial filter. The smoothed vortex number density, $n_v^{(s)}(r_0)$, centered on radial position r_0 is given by

$$n_v^{(s)}(r_0) = \frac{\sum_r w(r_0 - r) n_v(r)}{\sum_r w(r)}, \tag{3.71}$$

where $w(r)$ is the filter (window) function. For simplicity we employ a Gaussian filter of the form

$$w(r) = \frac{1}{\sqrt{2\pi}s} e^{-0.5 s^2 r^2}, \tag{3.72}$$

where s is the standard deviation ("smoothing" parameter). The value of s defines the

[17] Vortex positions are stored in an array. When two vortices (e.g., vortex-one and vortex-two) overlap during a collision, two entries in the array register identical positions. The numerical detection scheme fails to distinguish which of the two entries correspond to the position of vortex-one and vortex-two.

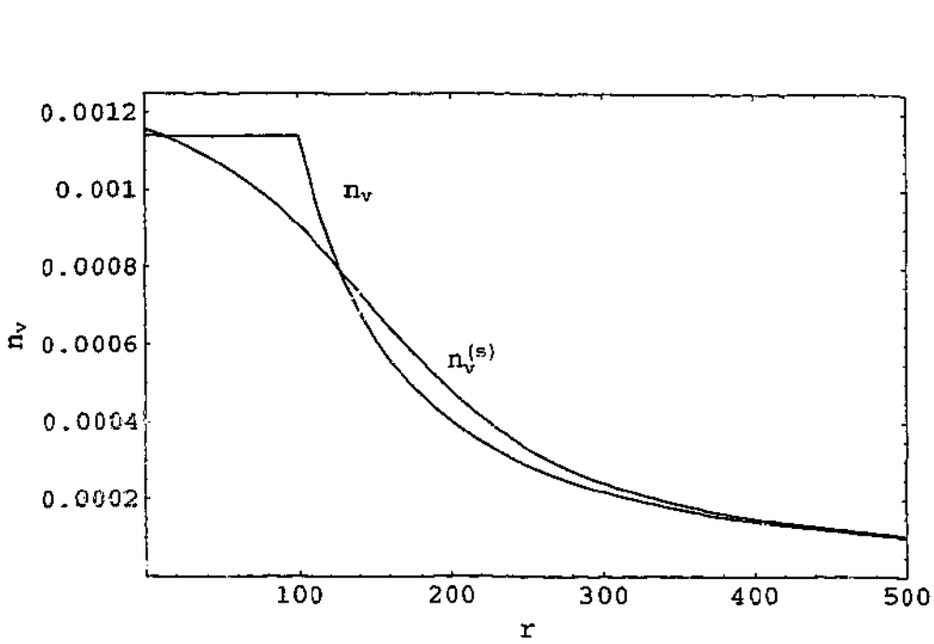

Figure 3.12: Comparison of the original vortex number density prior to smoothing, n_v, with the smoothed number density, $n_v^{(s)}$. The smoothing parameter, $s = 4\sqrt{\ln 4}/3R_0$ ($R_0 = 100$) corresponds to a full width at half maximum of $3R_0/2$.

length scale over which smoothing occurs. A reasonable scale is the size of the rigid-body region, R_0, and the smoothing parameter is given in terms of R_0. Although the vortex number density has been smoothed, this procedure does not modify the positions of vortices in the lattice. Figure 3.12 shows the smoothed vortex number density obtained using

$$s = \frac{4\sqrt{\ln 4}}{3R_0}. \tag{3.73}$$

This corresponds to a convolution kernel with a full width at half maximum of $3R_0/2$.

A comparison between $n_v^{(s)}$ and n_v in Fig. 3.12 shows that $n_v^{(s)}$ is higher than n_v at $r = 0$, lower at $r \approx R_0$ and higher for $r \gg R_0$; however, $n_v^{(s)}(r \to \infty) \to n_v(r \to \infty)$. Since the vortex confining potential depends on the vortex number density, the confining potential after smoothing is stronger at $r \approx 0$ and weaker at $r \approx R_0$. This implies that setting $\beta = 1$ in Eq. (3.66) results in a weak confining potential for vortices at $r \approx R_0$. As a consequence vortices around R_0 move out, while vortices close to $r = 0$ are confined. To maintain rigid-body rotation for $r \lesssim R_0$ it is necessary to "fine tune" the strength of the confining potential by varying the value of β. Vortex dynamics for various values of β are discussed in the next section.

3.5.4 Results and discussion

To explore vortex dynamics and the consequent rotational velocity profile of the dark matter condensate, simulations were performed for various values of β and R_0 in the range $1.3 \leq \beta \leq 1.5$ and $80 \leq R_0 \leq 120$ (see Figs. 3.13 and 3.14). It is found that varying β affects the strength of the vortex trapping force (since β modifies the confining potential). Figure 3.13 shows a plot of the rotational velocities for different values of β. Higher values of β lead to a larger trapping force. This results in more vortices being trapped within the rigid-body region, and consequently to a higher rotational velocity around $r = R_0$. A value of $\beta = 1.4$ gives an approximately "flat" velocity profile outside the rigid-body region.

The parameter R_0 defines the "boundary" between rigid-body rotation and the flat velocity profile. It also defines the scale for smoothing the vortex number density (see Eq. (3.73)). Since the rotational velocity is obtained from the angular frequency (i.e., $v(r) = r\Omega(r)$, where $\Omega(r)$ is proportional to the vortex number density), the rotation curve is expected to show more oscillations for smaller values of R_0. The effect of varying R_0 on the rotation curves is shown in Fig. 3.14 for $R_0 = 80, 100$ and 120, with $\beta = 1.4$. All rotation curves show rigid-body rotation within R_0 and a "flat" velocity profile for $r > R_0$.

Figures 3.15 and 3.16 show the evolution of a vortex configuration using the values $\beta = 1.4$ and $R_0 = 100$. It is observed that the initial vortex configuration evolves toward a regular lattice, whose number density (outside the galactic nucleus, R_0) falls off as r^{-1}; this characterizes a flat velocity profile for the rotating dark matter condensate (see Fig. 3.17). The velocity profile shown in Fig. 3.17 has been scaled to facilitate comparison with the rotation curve of the Milky Way galaxy. Data on the rotation curve of the Milky Way galaxy were obtained from Clemens (1985). Figure 3.17 shows that the rotation curve, based on our simulations, is broadly consistent with the profile for the Milky Way galaxy. Close to the galactic center the velocity profile exhibits rigid body rotation; however, a flat (non-Keplerian) velocity profile is observed out to large distances from the galactic center.

In summary, our simulations show that vortices in a dark matter condensate (with an initially Keplerian profile) evolve toward a configuration that characterizes a flat velocity profile. To account for the observed flat velocity profile for baryonic matter we assume

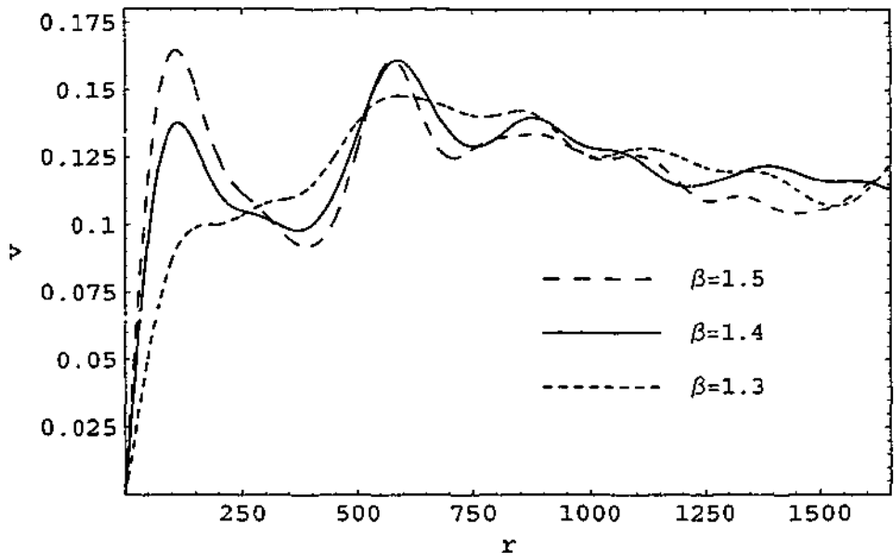

Figure 3.13: Rotational velocities obtained for three values of β, with $R_0 = 100$ and $\kappa = 2 \times 10^{-6}$. The simulations show strong trapping around R_0 for $\beta = 1.5$ and weak trapping around R_0 for $\beta = 1.3$.

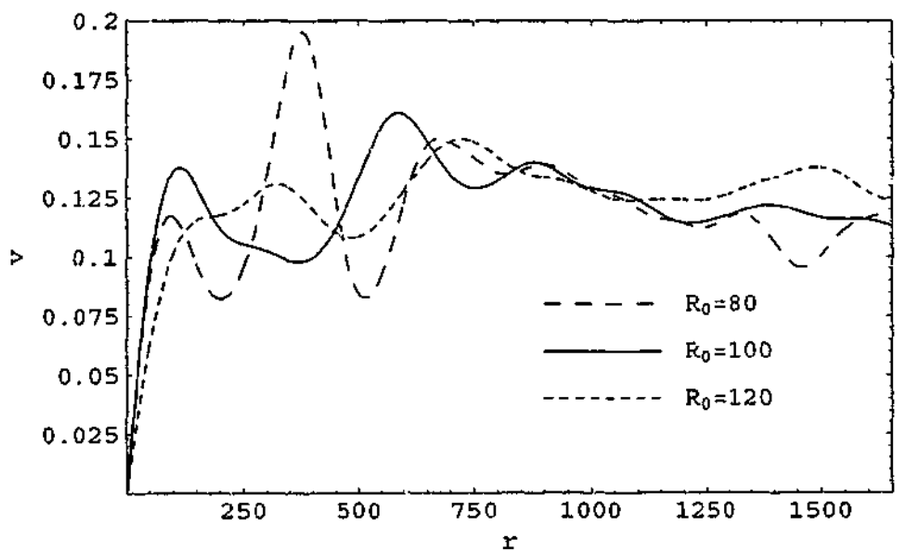

Figure 3.14: Rotational velocities obtained for three values of R_0, with $\beta = 1.4$ and $\kappa = 2 \times 10^{-6}$. The simulations show significant oscillations for $R_0 = 80$, and smaller oscillations for $R_0 = 120$.

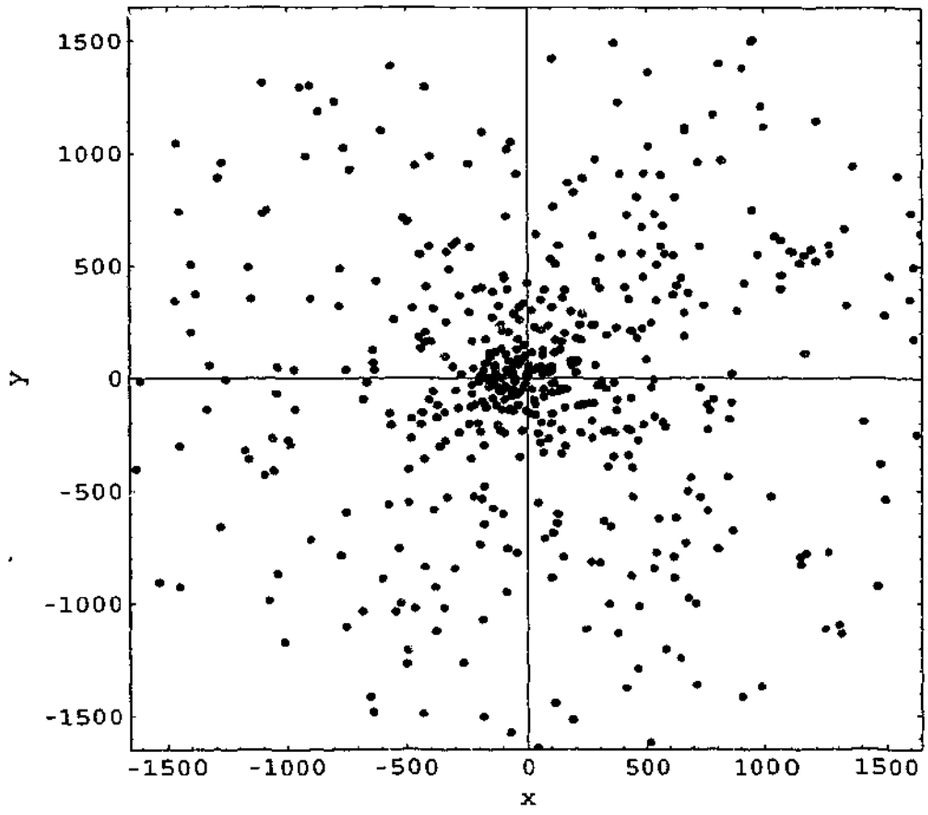

Figure 3.15: Initial configuration of 500 vortices located within $R_1 = 1800$, with $c = 2 \times 10^{-6}$ and trap parameter $\beta = 1.4$ (see text). The angular distribution of vortices is random. The vortex number density, $n_v(r)$, is constant for $r \leq R_0$ ($R_0 = 100$), characterizing rigid body rotation. For $r > R_0$ the initial vortex configuration exhibits a Keplerian velocity profile, for which $\Omega(r) \propto r^{-1.5}$.

that luminous matter adopts the same velocity as the dark matter condensate. In Sec. 3.6 we examine this assumption.

3.6 Gravitational drag between dark matter and baryonic matter

For luminous matter to adopt the same velocity profile as the dark matter condensate we need a mechanism to couple it to dark matter. Since the scalar bosons (which constitute the cosmic BEC) are uncharged they do not participate in electroweak interactions. If we neglect mutual friction between dark matter and baryonic matter, the only interaction between the two components is gravity. Dark matter can couple to baryonic matter via gravitational "drag". This effectively results in both baryonic and dark matter adopting the same velocity profile. To confirm this conjecture we have performed a small N-body

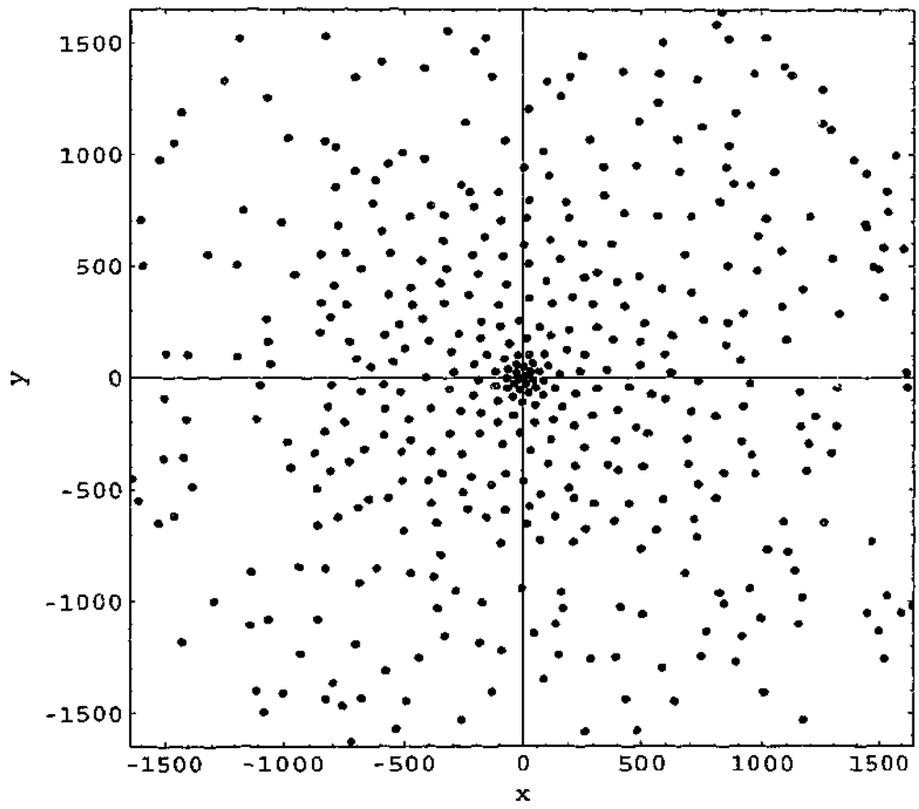

Figure 3.16: Final configuration obtained by evolving the vortices in Fig. 3.15. At the end of the simulation ($t = 500$) the vortex configuration (with 442 vortices remaining within the visualization frame) is characterized by a non-Keplerian profile ($r > R_0$), with $\Omega(r) \propto r^{-1}$.

simulation.

The simplest model for an N-body numerical simulation is the naive particle-particle model with interactions based on the Newtonian potential.[18] For a simulation containing N particles, the force $\mathbf{F}_i$ on the i-th particle is the sum of the forces due to the remaining $N-1$ particles, i.e.,

$$\mathbf{F}_i = \sum_{j \neq i}^{N} \frac{G_N m^2 (\mathbf{x}_j - \mathbf{x}_i)}{|\mathbf{x}_j - \mathbf{x}_i|^3}, \tag{3.74}$$

where $\mathbf{x}_i$ is the position vector of the i-th particle and m is the mass of the particle (assuming each particle has the same mass). Once the force acting on the i-th particle has

[18]Einstein's theory of general relativity gives a better description of gravitational interactions than Newtonian gravity. However, Newtonian gravity is commonly used in N-body simulations because it is simpler to implement than Einstein's formalism. Since mass density is low on a galactic scale, gravitational interactions can be modeled accurately by a Newtonian potential.

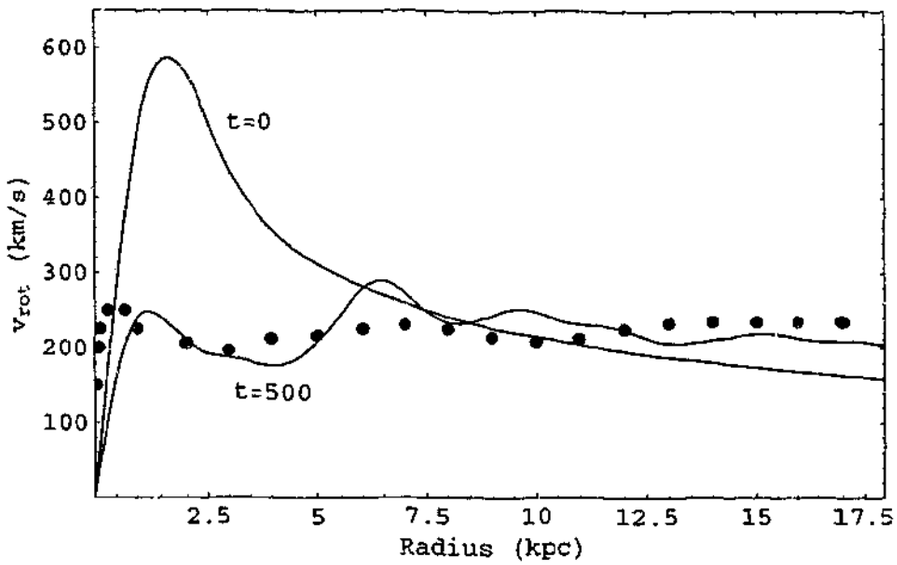

Figure 3.17: Velocity profiles based on the simulations shown in Figs. 3.15 and 3.16, compared with the rotation curve for the Milky Way galaxy. Initially, the dark matter condensate has a Keplerian profile for $r > R_0$. At the end of the simulation ($t = 500$) we obtain a flat velocity profile, with oscillatory structure due to local variations in the vortex number density. The filled circles represent the rotation profile for the Milky Way galaxy (data obtained from Clemens 1985). Our simulated rotation curve has been scaled to facilitate comparison with data for the Milky Way.

been computed, the next position of the particle can be obtained using a finite difference scheme based on $\mathbf{F}_i = md^2\mathbf{x}_i/dt^2$. Although this method for simulating an N-body system is time consuming, it is well suited for small N-body simulations (e.g., with $N < 50,000$). To implement a small N-body simulation using Eq. (3.74) we regard each particle as a small sphere of radius r_s. We replace $|\mathbf{x}_j - \mathbf{x}_i|$ in Eq. (3.74) by r_s, when the interparticle separation is less than r_s, so that $\mathbf{F}_i \to 0$ for $|\mathbf{x}_j - \mathbf{x}_i| \to 0$.[19]

We assume that all the particles are located in the x-y plane at $z = 0$, so that the simulations are conducted in two dimensions. We set $G_N = m = r_s = 1$ for simplicity. Our N-body calculations use 10^4 particles with periodic boundary conditions on a simulation frame $32,000 \times 32,000$. The simulations were run for 100,000 iterations (with time step $\Delta t = 0.1$) corresponding to $t = 10,000$ at the end of each simulation. Although the size of the simulation, the time scale and total mass can be chosen arbitrarily, they are related to

[19]This can be seen by replacing m^2 in Eq. (3.74) by $m\rho(4\pi|\mathbf{x}_j - \mathbf{x}_i|^3/3)$ for $|\mathbf{x}_j - \mathbf{x}_i| < r_s$, where $\rho = m/(4\pi r_s^3/3)$ is the mass density of the sphere.

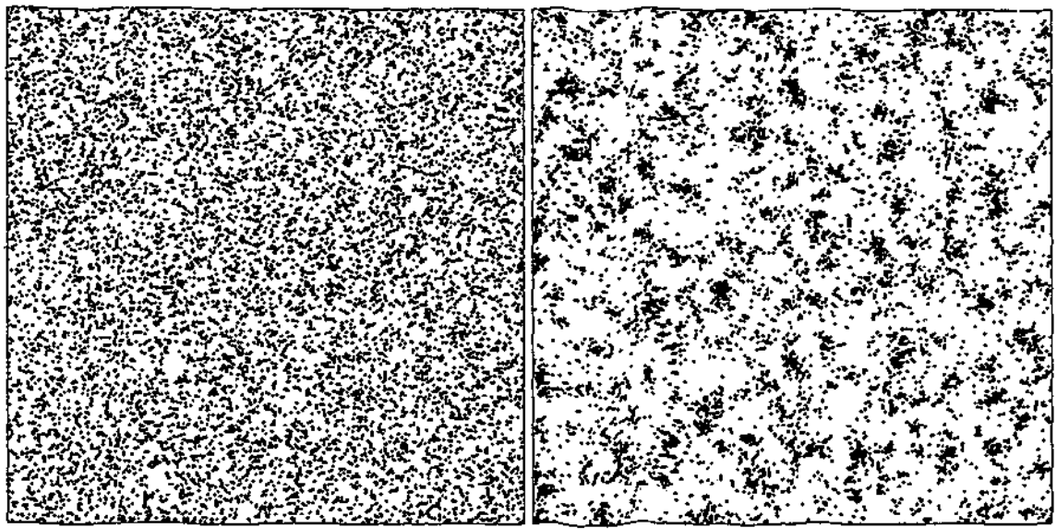

(a) (b)

Figure 3.18: (a) Dark and baryonic matter distribution at the beginning of a simulation, and (b) at the end of the simulation, for the case where the initial dark matter velocity is $v_x = 0.2$. The initial velocity of baryonic matter is zero. The simulation frame is $32,000 \times 32,000$ and the simulation was run for 100,000 iterations. The total number of particles is 10,000, with 10% corresponding to baryonic matter and 90% to dark matter. Both dark matter and baryonic matter eventually adopt the same velocity profile.

each other. For example, if the simulation frame $32,000 \times 32,000$ corresponds to a cross-sectional area of $(32 \text{ kpc})^2$ and 10^4 particles contribute to the mass in this cross-sectional area (i.e., $\sim 10^{10} M_\odot$), then the time scale of the simulation would be of the order of 10^7 years.[20]

To illustrate the effect of gravitational drag on baryonic matter we randomly distribute particles in the simulation frame, with 90% of the particles corresponding to dark matter and 10% to baryonic matter. For simplicity we assume that the dark matter component has a uniform velocity in the x direction ($v_y = 0$), while the initial velocity of the baryonic matter is set to zero. The results of our simulations are shown in Figs. 3.18 and 3.19.

Figure 3.18 (a) shows the initial random distribution of dark matter and baryonic matter. At the end of the simulation (see Fig. 3.18 (b)) clumping is observed in the

[20]The dimensionless velocity of particles in our simulations is of the order of 0.1 (see Fig. 3.19). Since the rotational velocity of a typical galaxy is of the order of 100 kms^{-1}, the velocity in our simulations is measured in units of $1,000$ kms^{-1}. By setting the length scale to parsec, our simulations correspond to a cross-sectional area of $(32 \text{ kpc})^2$, which gives the total mass as $10^{10} M_\odot$. Since $1,000$ kms^{-1} is the unit of velocity, one second corresponds to 10^6 m. The duration of the simulation $t = 10,000$ is of the order of ten million years.

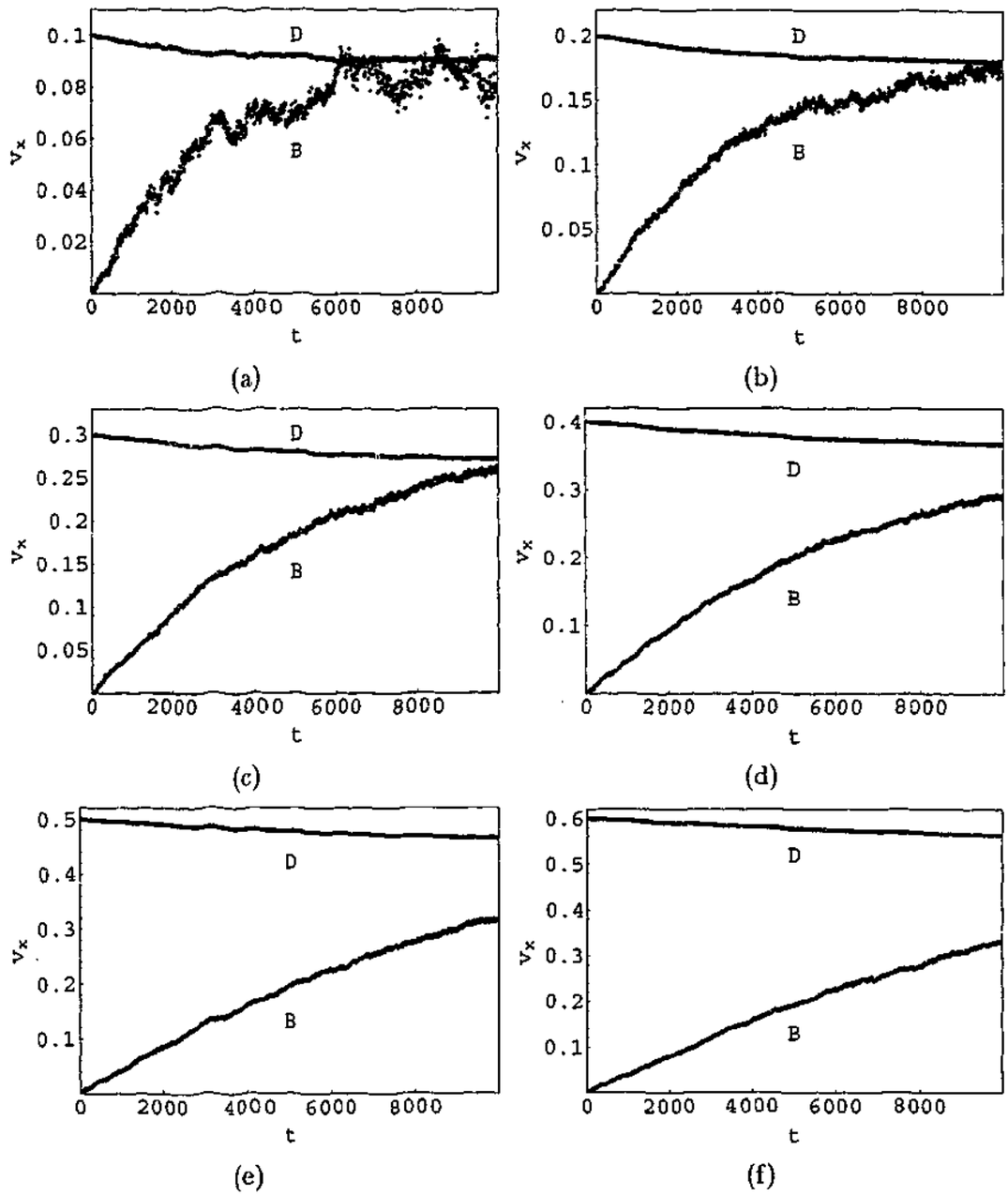

Figure 3.19: Gravitational drag between dark matter (D) and baryonic matter (B). Initially the velocity of the baryonic matter was set to zero, while the x-component of velocity of dark matter was set to: (a) $v_x = 0.1$, (b) $v_x = 0.2$, (c) $v_x = 0.3$, (d) $v_x = 0.4$, (e) $v_x = 0.5$ and (f) $v_x = 0.6$. As the simulations evolve, baryonic matter attains a non-zero velocity due to gravitational drag. For a larger (dark matter) velocity it takes longer for baryonic matter to adopt the velocity profile of the dark matter condensate.

distribution of baryonic and dark matter. Figure 3.19 shows plots of the average velocity, v_x, as a function of t for both dark matter and baryonic matter ($0.1 \leq v_x \leq 0.6$). As the simulation evolves, baryonic matter gains velocity in the x direction until eventually it adopts the same velocity profile as the dark matter condensate (see Figs. 3.19 (a)-(c)). The baryonic matter component in Fig. 3.19 (a) adopts the same velocity profile as the dark matter condensate at $t \sim 6,000$, corresponding to a time of the order of six million years. In Figs. 3.19 (b) and (c) baryonic matter adopts the same velocity profile as dark matter at $t \sim 10,000$, corresponding to a time of the order of ten million years. For a larger initial velocity (see Figs. 3.19 (d)-(f)), baryonic matter adopts the same velocity profile as the dark matter component after a longer time. Baryonic matter also exerts gravitational drag on dark matter, which results in the velocity of the dark matter condensate decreasing slightly from its initial value.

Our simulations show that for a velocity difference (between dark matter and baryonic matter) of the order of 0.1 - 0.3, which corresponds to a velocity of the order of 100 kms^{-1} - 300 kms^{-1}, baryonic matter adopts the same velocity as dark matter in approximately ten million years. Since galactic evolution is of the order of one billion years, this implies that luminous (baryonic) matter quickly adopts the same velocity profile as the dark matter condensate.

3.7 Concluding remarks

Scalar particles arising in a late-time cosmological phase may be a major component of dark matter, and under certain circumstances it is possible for these scalar particles to form a degenerate superfluid (BEC). Rotation of a self-gravitating dark matter condensate gives rise to quantized vortices, which evolve toward a vortex lattice whose number density, $n_v \propto r^{-1}$. This suggests that a rotating dark matter condensate will have a flat velocity profile.

In the absence of strong or electroweak interactions, dark matter can only interact with baryonic matter via gravity. It is found that gravitational "drag" between dark matter and baryonic matter results in luminous (baryonic) matter adopting the same velocity as the dark matter condensate. However, to provide a detailed quantitative understanding of hierarchical clustering and gravitational instabilities will require a large N-body simulation of structure formation, including a three-dimensional model of vortex dynamics.

Nevertheless, the current model has demonstrated a hitherto unexpected role for vortex dynamics in the evolution of disk galaxies.

Chapter 4

Stability of $U(1) \times U(1) \times Z_2$ Dirichlet Defects

4.1 Introduction

Grand unified theories (GUTs), which attempt to unify the electroweak[1] and strong nuclear forces, suggest the Universe underwent a series of symmetry breaking phase transitions $\sim 10^{-36}$ seconds after the Big Bang; before this time the strong nuclear force and electroweak force were indistinguishable. These phase transitions result in the formation of topological defects, such as cosmic strings, domain walls and monopoles.

Domain walls induce anisotropy in the CMBR whose magnitude is inconsistent with observations (Zel'dovich *at al.* 1975, Stebbins and Turner 1989 and Press *et al.* 1989). Similarly monopoles are predicted to form in numbers inconsistent with constraints imposed by proton decay processes in the Sun (Zeldovich and Khlopov 1978, Preskill 1979, Kolb *et al.* 1982, Dimopoulos *et al.* 1982 and Freese *et al.* 1983).

In addition to these canonical topological defects it is possible to form hybrid defects, in which a defect can serve as a boundary to another defect. For example, a string can terminate on a domain wall, or on a monopole. The formation and evolution of hybrid defects in the early Universe has been considered previously in the literature (see e.g., Langacker and Pi 1980 and Dvali *et al.* 1998).

An interesting consequence of hybrid defects is that the evolution of one type of defect can lead to the destruction of the boundary defect, or to the destruction of both defects. For example, a string terminated by two monopoles pulls the monopoles together resulting in the annihilation of the hybrid defect. This mechanism (referred to as the Langacker-Pi mechanism) was suggested as a way of avoiding the monopole problem in the early Universe (see Langacker and Pi 1980).

In the case of strings terminating on a domain wall it is known that the wall is unstable

[1]The electroweak force comprises the electromagnetic and weak nuclear forces (Glashow 1961, Salam 1968 and Weinberg 1967). In a cosmological context the underlying electroweak symmetry is restored at very high temperatures (i.e., $T \sim 10^3$ GeV), corresponding to the state of the Universe at $\sim 10^{-11}$ seconds after the Big Bang (see e.g., Kirzhnits 1972 and Kirzhnits and Linde 1972).

to the nucleation of holes bounded by string loops (Kibble *et al.* 1982). Such holes can result in the eventual decay of the wall defect; however, the time scale involved in hole formation is thought to be extraordinarily large (Kibble *et al.* 1982), which would seem to exclude hybrid topological defects as a way of obviating problems with a domain wall dominated Universe.

Hybrid defects can also arise in supersymmetric Yang-Mills theories (see e.g., Witten 1997). A broken (discrete) chiral symmetry gives rise to distinct vacua separated by domain walls. QCD strings can terminate on these walls. Carroll and Trodden (1998) suggested that hybrid topological defects also form in the early Universe. This chapter discusses the stability of $U(1)\times U(1)\times Z_2$ Dirichlet defects[2] (D-walls). We consider various configurations - in particular two strings terminating on a wall, a single string terminating on a wall and a string segment bounded by two walls. The latter D-wall is analogous to the Langacker-Pi configuration, and the evolution of this hybrid defect results in the destruction of the walls and string segment. Finally, we examine an extended Dirichlet defect model based on $SU(2)\times SU(2)\times U(1)\times U(1)\times Z_2$. This model allows for the formation of monopoles bounded by domain walls, which in turn are connected by cosmic strings. We examine the implications of this Dirichlet defect within the context of the monopole problem.

4.2 Domain walls

The formation of domain walls is associated with the breaking of a discrete symmetry, Z_2, i.e., $H\times Z_2\rightarrow H$. In the simplest symmetry breaking scheme H is the identity group I. For models with Z_2 symmetry the Higgs field that is responsible for the broken symmetry is a real scalar field, ϕ, whence the symmetry breaking potential is written as

$$V(\phi)=\frac{\lambda}{4}\left(\phi^2-\eta^2\right)^2. \tag{4.1}$$

Equation (4.1) describes a field configuration with vacuum expectation value (VEV) η or $-\eta$. When the symmetry is broken the field adopts one of the two VEVs. The region separating the two vacua represents the domain wall, whose thickness, δ, is given by

$$\delta\sim\frac{1}{\sqrt{\lambda}\eta}. \tag{4.2}$$

[2]In general, Dirichlet topological defects arise when one type of defect terminates on another defect. These defects can have the same, or different, dimensionality, e.g., a string (one-dimensional object) can terminate on a string, or a string can terminate on a wall (two-dimensional object).

The energy density of the wall is determined by the energy density difference between the center of the wall ($\phi = 0$) and the vacuum, $\phi = \langle\phi\rangle = \pm\eta$. The energy density at the center of the wall is $\rho \sim \lambda\eta^4$, and vanishes in the vacuum, therefore the energy density of the wall is $\rho \sim \lambda\eta^4$. The surface energy density, σ, of the wall is

$$\sigma \sim \rho\delta \sim \sqrt{\lambda}\eta^3. \tag{4.3}$$

The evolution of a domain wall in a flat (non-expanding) Universe is described by the Lagrangian

$$\mathcal{L} = \partial_\mu\phi\partial^\mu\phi - V(\phi). \tag{4.4}$$

The corresponding field equation governing the dynamics of the wall is

$$\Box\phi + \frac{\lambda}{2}\phi\left(\phi^2 - \eta^2\right) = 0. \tag{4.5}$$

Equation (4.5) can be recast in dimensionless form using the following transformations:

$$\phi \to \eta\phi \quad \text{and} \quad x_\mu \to \left(\eta\sqrt{\lambda/2}\right)^{-1} x_\mu. \tag{4.6}$$

For a wall at $z = 0$, oriented in the z direction, the static solution is (Zeldovich *et al.* 1975)

$$\varphi(z) = \tanh(z). \tag{4.7}$$

Figure 4.1 plots the static solution (4.7), which shows $\phi \to \pm 1$ for $z \to \pm\infty$, with the ϕ-field smoothly varying from 1 (for $z > 0$) to -1 (for $z < 0$). A plot of the energy density as a function of z shows that the potential energy density is a maximum at the center of the domain wall (see Fig. 4.2).

4.2.1 Domain wall formation

Domain walls are conjectured to have formed in the early Universe in a manner analogous to the formation of cosmic strings and monopoles (see Sec. 1.4). The formation of domain walls via the Kibble mechanism, and their subsequent evolution is studied using numerical simulations based on a discretized version of the field equation (4.5) (see e.g., Harvey *et al.* 1982 and Vachaspati and Vilenkin 1984). To emulate the Kibble mechanism, the initial condition is obtained by assigning a random value between -1 and 1 to ϕ at each lattice (grid) point. Since ϕ is random, noise is generated during the simulation, however, the equation of motion (4.5) conserves energy and noise is not damped. To suppress noise we

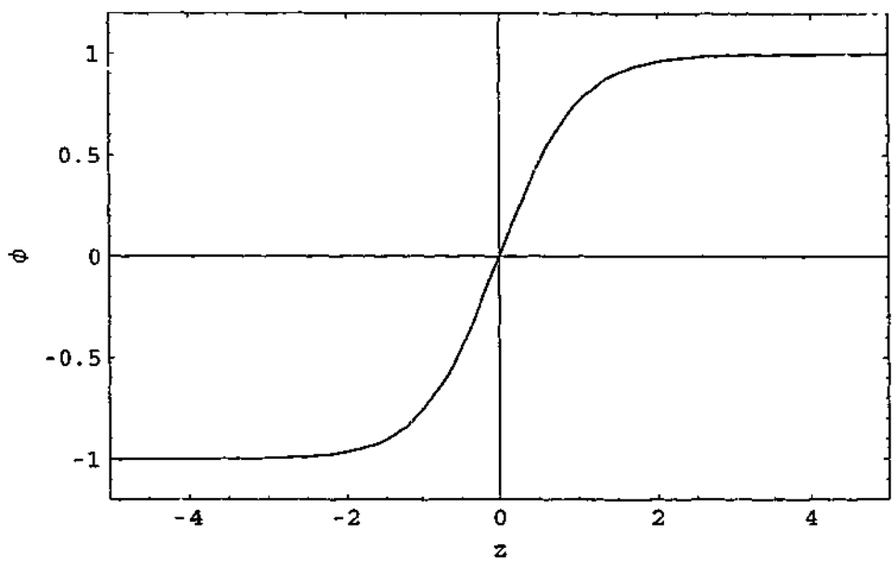

Figure 4.1: Magnitude of the Higgs field as a function of z for a wall located at $z = 0$. As $z \to \pm\infty$, $\phi \to \pm 1$.

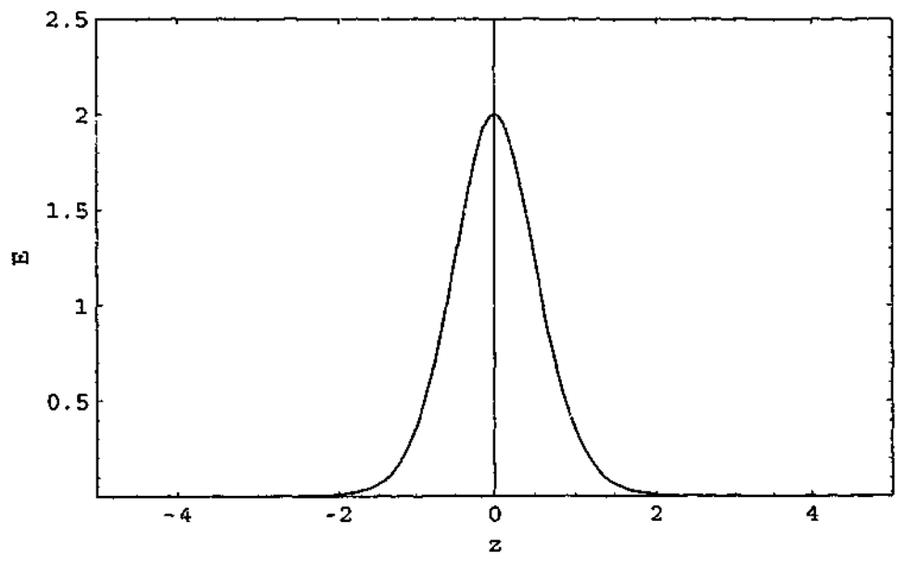

Figure 4.2: Potential energy density as a function of z for the wall in Fig. 4.1. The energy density is a maximum at $z = 0$.

have added a damping term, $b\partial\phi/\partial t$, to the field equation (4.5), where b is a damping constant. Numerical simulations were performed with various values of b. It is found that for $b \gg \Delta t$ (where Δt is the time step) the effect of damping is so large that a wall network does not have enough time to form. On the other hand for $b \ll \Delta t$ there is no significant reduction in noise. As a compromise we set $b = \Delta t$ in our simulations.

The size of a typical lattice is 100^3 with spatial step[3] $\Delta h = 0.5$. The time step $\Delta t = 0.1$ is chosen to guarantee stability of the numerical integration scheme. The simulation was run for 500 iterations. A damping term (with $b = 0.1$) precludes noise from the boundary entering the visualization volume. Figure 4.3 shows the formation and evolution of a wall network at four different times. In Fig. 4.3 (b) small scale structure is evident on the domain walls. This suggests that immediately after formation, domain walls are dominated by small scale structure. Figure 4.3 (b) also shows that some of the wall "segments" are not connected to larger walls; these wall "segments" are in fact closed walls.[4] As the simulation evolves, closed walls collapse and small scale structure disappears due to the large wall tension (see Figs. 4.3 (c) and (d)).

4.2.2 Evolution of domain walls

The evolution of a domain wall is determined by the surface tension σ (Vilenkin 1981), which causes the wall to oscillate and gain velocity (perpendicular to the wall). Consequently, a closed wall will shrink and eventually collapse. The force per unit area acting on the wall, due to its surface tension, is $\mathcal{F} \sim \sigma/R$, where R is the mean radius of curvature of the wall.

The Abrikosov ansatz can be invoked to show that two parallel walls always exist in the form of a wall and an anti-wall.[5] Since a domain wall model exhibits discrete symmetry breaking, the model does not generate a Goldstone boson. Consequently, two stationary walls do not interact with each other (in the absence of gravitational interactions) and will remain stationary. This conclusion has been confirmed by our numerical simulations

[3]With $\Delta h = 0.5$ the grid size 100^3 corresponds to a simulation volume of $100^3\Delta h^3 = 50^3$ (see Sec. 2.2).

[4]The definition of a closed wall (or an infinite wall) only makes sense in an expanding Universe, where the rate of expansion is governed by the scale factor, $a(t)$. Due to expansion an observer can only hope to see objects located within her horizon (or Hubble distance) $d_H = a/\dot{a}$. In an expanding spacetime the wall is considered to be infinite if it extends beyond the horizon, otherwise it is referred to as a closed wall.

[5]Two overlapping walls, described by $\Phi = \phi_1\phi_2$, exist in the form of a wall and an anti-wall. This follows from continuity of the scalar field, Φ. If wall-one is described by a field configuration $\Phi < 0$ for $z < -z_0$, and $\Phi > 0$ for $-z_0 < z \leq 0$, then continuity of the Φ-field at $z = 0$ implies that wall-two is described by a field configuration $\Phi > 0$ for $0 \leq z < z_0$ and $\Phi < 0$ for $z > z_0$.

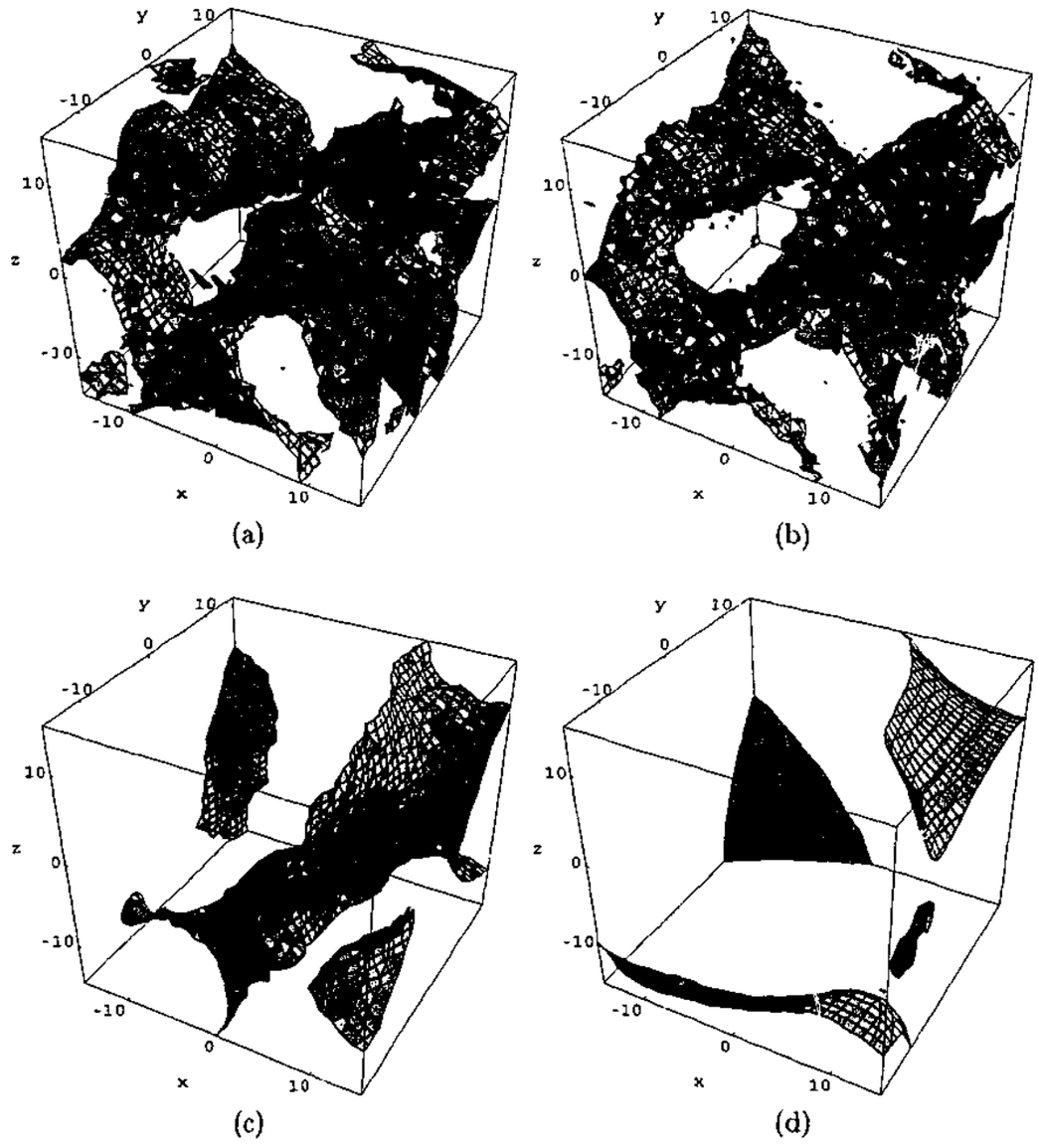

Figure 4.3: Isocontour plots ($\phi = 0$) illustrating the formation and evolution of domain walls (in a visualization volume 30^3) at four different times. (a) $t = 10$, (b) $t = 12.5$, (c) $t = 25$, and (d) at the end of the simulation ($t = 50$). These figures show that small scale structure on the walls is stretched as the walls evolve. Closed walls collapse and annihilate due to wall tension.

based on the field equation (4.5).

GUT scale walls in the early Universe are expected to have a large mass density, in which case wall interactions will be determined by gravity (Lazarides *et al.* 1982). To understand the nature of these gravitational interactions, consider a static wall located at $z = 0$ in the x-y plane. The symmetric energy-momentum tensor is given by

$$T_{\mu\nu} = \partial_\mu\phi\partial_\nu\phi - g_{\mu\nu}\mathcal{L}, \tag{4.8}$$

where $g_{\mu\nu}$ is the metric tensor. The only non-vanishing derivative of the ϕ-field is $\partial_3\phi$. From Eq. (4.4) and the flat space metric tensor $g_{\mu\nu} = \mathrm{diag}(1,-1,-1,-1)$ we obtain

$$T_0^0 = \frac{1}{2}\partial_3\phi\partial_3\phi + V(\phi) \tag{4.9}$$

$$T_1^1 = T_0^0 \tag{4.10}$$

$$T_2^2 = T_0^0 \tag{4.11}$$

$$T_3^3 = -\frac{1}{2}\partial_3\phi\partial_3\phi + V(\phi), \tag{4.12}$$

where $V(\phi)$ is the potential specified by Eq. (4.1).

The gravitational potential in the Newtonian limit, for a static distribution of matter, is governed by Poisson's equation

$$\nabla^2 V_G = 4\pi G_N(T_0^0 - T_i^i), \tag{4.13}$$

where G_N is the Newtonian gravitational constant and $T_i^i = T_1^1 + T_2^2 + T_3^3$. Using Eqs. (4.9) - (4.12), Poisson's equation reduces to

$$\nabla^2 V_G = -8\pi G_N V(\phi). \tag{4.14}$$

In dimensionless form $V(\phi) = \frac{1}{2}(\phi^2-1)^2$ and $\phi = \tanh(z)$. Since a domain wall is invariant under coordinate transformations in the x-y plane we have $\partial^2 V_G/\partial x^2 = \partial^2 V_G/\partial y^2 = 0$. Equation (4.14) has the solution

$$V_G = -\frac{2}{3}\pi G_N\left[4\ln(\cosh z) - \mathrm{sech}^2 z\right] \tag{4.15}$$

A plot of the gravitational potential of a domain wall and the force acting on a test object located at z is plotted in Fig. 4.4. This figure shows that a domain wall gives rise to a repulsive gravitational force. In a region with uniform mass density the domain wall

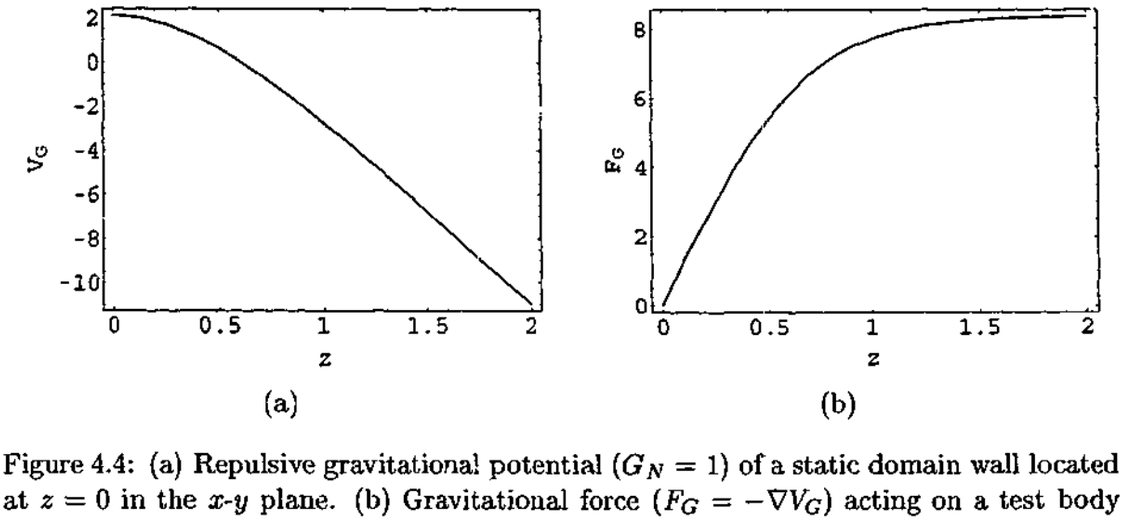

Figure 4.4: (a) Repulsive gravitational potential ($G_N = 1$) of a static domain wall located at $z = 0$ in the x-y plane. (b) Gravitational force ($F_G = -\nabla V_G$) acting on a test body at z due to the wall. The magnitude of the force approaches a constant value at spatial infinity. A test body in the vicinity of the wall will be repelled from the wall in the z direction.

produces a two-dimensional under-density in the matter distribution.[6] As a consequence domain walls do not generate a scale invariant spectrum of fluctuations in the matter distribution (Harrison 1970 and Zel'dovich 1972). Since a scale invariant spectrum is consistent with the observations of COBE (Smoot *et al.* 1992), domain walls would appear to be ruled out on observational grounds.

Small scale structure[7] on the wall is also expected to induce a temperature anisotropy in the CMBR. An analysis based on percolation theory (Stauffer 1979) indicates that a wall network will evolve toward a single infinite wall[8] (Vilenkin 1985). As the Universe expands, wall structure which is comparable to the horizon grows. The density fluctuations corresponding to this wall structure is of the order $10^{60}\eta/m_p$ (Vilenkin 1985), where m_p is the Planck mass. These fluctuations induce a large temperature anisotropy in the CMBR. Since the temperature anisotropy in the CMBR is less than 10^{-4}, this constrains the symmetry breaking scale to be less than 10^{-2} GeV, which is inconsistent with GUT models. The small temperature anisotropy in the CMBR poses significant problems for any model that predicts stable domain walls. However, domain walls are an unavoidable consequence

[6] A single domain wall inside our Hubble horizon will expel matter from the visible Universe. This is inconsistent with the observed large scale structure.

[7] This structure is smaller than, or comparable to, the Hubble horizon.

[8] Since domain walls are two-dimensional objects (in $\mathcal{R}^{3+1}$), two non-parallel infinite walls will intersect in four-dimensional spacetime.

of models with a Z_2 symmetry, and the domain wall problem must be addressed in realistic scenarios of symmetry breaking.

4.2.3 Solutions to the domain wall problem

The accepted paradigm for avoiding the domain wall problem is inflation (Guth 1981). It is conjectured that within a fraction of a second after the Big Bang the Universe experienced a short period of rapid expansion driven by vacuum energy Λ. In the inflationary scenario the scale factor $a(t) \propto e^{\sqrt{\Lambda/3}t}$. The source of the vacuum energy is postulated to arise from a scalar field (i.e., the inflaton field). Inflation occurs via a phase transition, facilitated by the negative pressure of the inflaton field. To avoid domain walls in the early Universe, the inflationary phase transition must have occurred after the GUT phase transition. Prior to inflation, domain walls are within the Hubble horizon, however, following exponential expansion of the Universe the walls lie outside the horizon. Consequently primordial domain walls will not impact on the anisotropy of the CMBR. Another way of avoiding the domain wall problem, without invoking inflation, is to allow the energy density on one side of the wall to be different from that on the other side (Zeldovich *et al.* 1975 and Kibble 1976). The imbalance in the energy density between the two sides of the wall results in a force acting on the wall, which is of the order of the energy density difference, ε. This force causes the side of the wall with the higher energy density to shrink, whilst the other side expands, resulting in the wall moving toward the region of higher energy density. In this scenario the wall moves outside our horizon, thereby obviating a domain wall dominated Universe. In the remainder of this chapter we discuss an alternative solution to the domain wall problem, based on a model of D-wall topological defects.

4.3 $U(1) \times U(1) \times Z_2$ Dirichlet defects

4.3.1 D-wall model

D-wall topological defects are described by a $U(1) \times U(1) \times Z_2$ symmetry breaking model (Carroll and Trodden 1998). In this model the spontaneously broken Higgs fields consist of a real scalar field, ϕ, for the domain wall defect and two complex scalar fields, ψ_1 and ψ_2, for the string defects. There is no gauge field associated with the ϕ-field; however, a gauge field can be associated with the ψ_1- and ψ_2-fields. A characteristic of ψ_1 and ψ_2 is that when ψ_1 has a non-vanishing VEV, the magnitude of ψ_2 vanishes and vice versa. This implies that there is little interaction between the ψ_1- and ψ_2-fields. Therefore, the

presence (or absence) of a gauge field is not expected to significantly affect the stability of the D-wall. For simplicity we consider a global model where there are no gauge fields associated with the ψ_1- and ψ_2-fields. The model is defined by the Lagrangian

$$\mathcal{L} = \partial_\mu \phi \partial^\mu \phi + \overline{\partial_\mu \psi_1} \partial^\mu \psi_1 + \overline{\partial_\mu \psi_2} \partial^\mu \psi_2 - V(\phi, \psi_1, \psi_2), \tag{4.16}$$

where $V(\phi, \psi_1, \psi_2)$ is a symmetry breaking potential given by

$$\begin{aligned} V(\phi, \psi_1, \psi_2) &= \lambda_\phi \left(\phi^2 - \widetilde{v}^2\right)^2 + \lambda_\psi \left[|\psi_1|^2 + |\psi_2|^2 - \widetilde{w}^2 + g\left(\phi^2 - \widetilde{v}^2\right)\right]^2 \\ &\quad + h|\psi_1|^2|\psi_2|^2 - \mu\phi\left(|\psi_1|^2 - |\psi_2|^2\right). \end{aligned} \tag{4.17}$$

The form of the potential is governed by the coupling parameters λ_ϕ, λ_ψ, g, h and μ. If the parameter μ is zero, i.e., the interaction between the different fields vanishes, then there are four degenerate vacuum expectation values (VEVs) which minimize the potential, namely

$$\langle \phi \rangle = \pm \widetilde{v}, \quad \langle |\psi_1| \rangle = \widetilde{w}, \quad \langle |\psi_2| \rangle = 0 \tag{4.18}$$

and

$$\langle \phi \rangle = \pm \widetilde{v}, \quad \langle |\psi_1| \rangle = 0, \quad \langle |\psi_2| \rangle = \widetilde{w}. \tag{4.19}$$

As pointed out by Carroll and Trodden (1998), once the value of μ is increased from zero this degeneracy is removed. In this case there remain only two sets of VEVs given by

$$\langle \phi \rangle = v, \quad \langle |\psi_1| \rangle = w, \quad \langle |\psi_2| \rangle = 0 \tag{4.20}$$

and

$$\langle \phi \rangle = -v, \quad \langle |\psi_1| \rangle = 0, \quad \langle |\psi_2| \rangle = w. \tag{4.21}$$

A wall located at $z = 0$ is obtained by setting $\phi = v$ for $z > 0$, $\phi = 0$ for $z = 0$ and $\phi = -v$ for $z < 0$. The ψ_1-field terminates on the wall from "above" where $\phi = v$, whereas the ψ_2-field terminates on the wall from "below" where $\phi = -v$. We refer to the string characterized by the ψ_1-field as string-one, and the string characterized by the ψ_2-field as string-two (see Fig. 4.5).

The potential (4.17) has been studied previously by Carroll and Trodden (1998) who utilized the parameters $\lambda_\phi = 108$, $\widetilde{v}^2 = 1/24$, $\lambda_\psi = 1/24$, $\widetilde{w}^2 = -3$ $g = 0$, $h = -1/12$ and $\mu = 6$. This choice of parameters gives $v = 1$. Figure 4.6 (a) shows that for $\phi = -v$, the VEV of the ψ_1-field vanishes, and the potential does not display symmetry breaking as

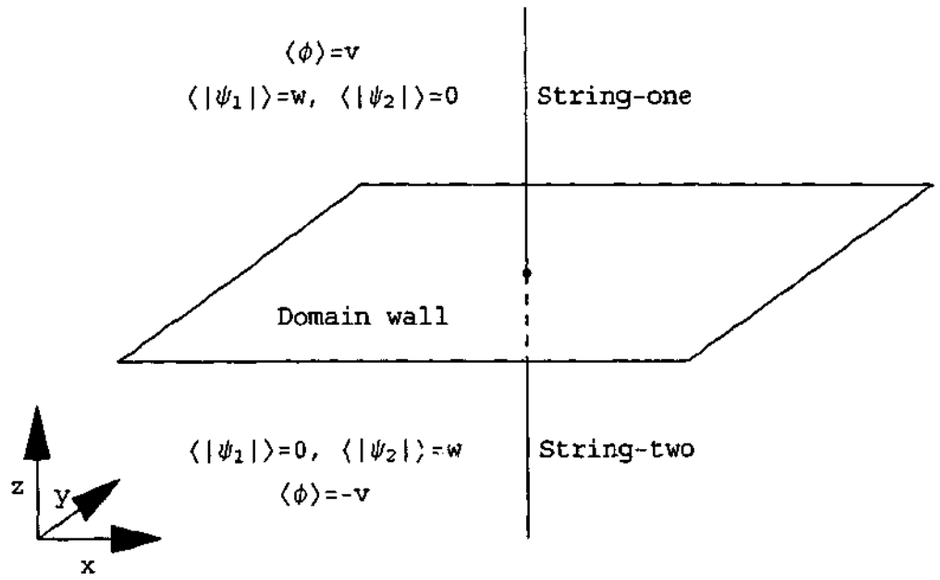

Figure 4.5: Schematic representation of a D-wall. The domain wall is oriented in the z direction, with string-one located above the wall and string-two located below the wall.

a function of $Re(\psi_1)$. However, $V(\phi, \psi_1, \psi_2)$ exhibits symmetry breaking as a function of $Re(\psi_2)$, with minima at $Re(\psi_2) = \pm w$. Figure 4.6 (b) shows that for $\phi = 0$, both the VEVs of the ψ_1- and ψ_2-fields vanish since the potential is a minimum at $Re(\psi_1) = Re(\psi_2) = 0$. Figure 4.6 (c) shows that for $\phi = v$, the VEV of the ψ_2-field vanishes, and the potential does not display symmetry breaking as a function of $Re(\psi_2)$. However, $V(\phi, \psi_1, \psi_2)$ exhibits symmetry breaking as a function of $Re(\psi_1)$, with minima at $Re(\psi_1) = \pm w$. The center of the wall has $\phi = 0$, whereas the two distinct vacua, separated by the wall, have $\phi = \pm v$.

Figure 4.6 (d) shows the potential, $V(\phi, \psi_1, \psi_2)$, as a function of ϕ and $Re(\psi_1)$ for $\psi_2 = 0$. At $Re(\psi_1) = 0$ the minimum of the potential occurs for $\phi = \tilde{v} = 1/\sqrt{24}$. As $Re(\psi_1)$ increases toward the VEV w, the ϕ-field also increases toward the VEV, v. This implies that the magnitude of the ϕ-field is smaller at the center of the string, and the energy density of the wall is lower where the string terminates.

Although the potential energy density in Figs. 4.6 (a), (b) and (c) can adopt negative values, this should not be interpreted as the D-wall having negative energy density. A negative energy density can be avoided by adding a constant positive term to the potential; this does not change the VEVs of the scalar field, and therefore does not change the dynamics or the stability of the D-wall. The formation and dynamics of the D-wall is

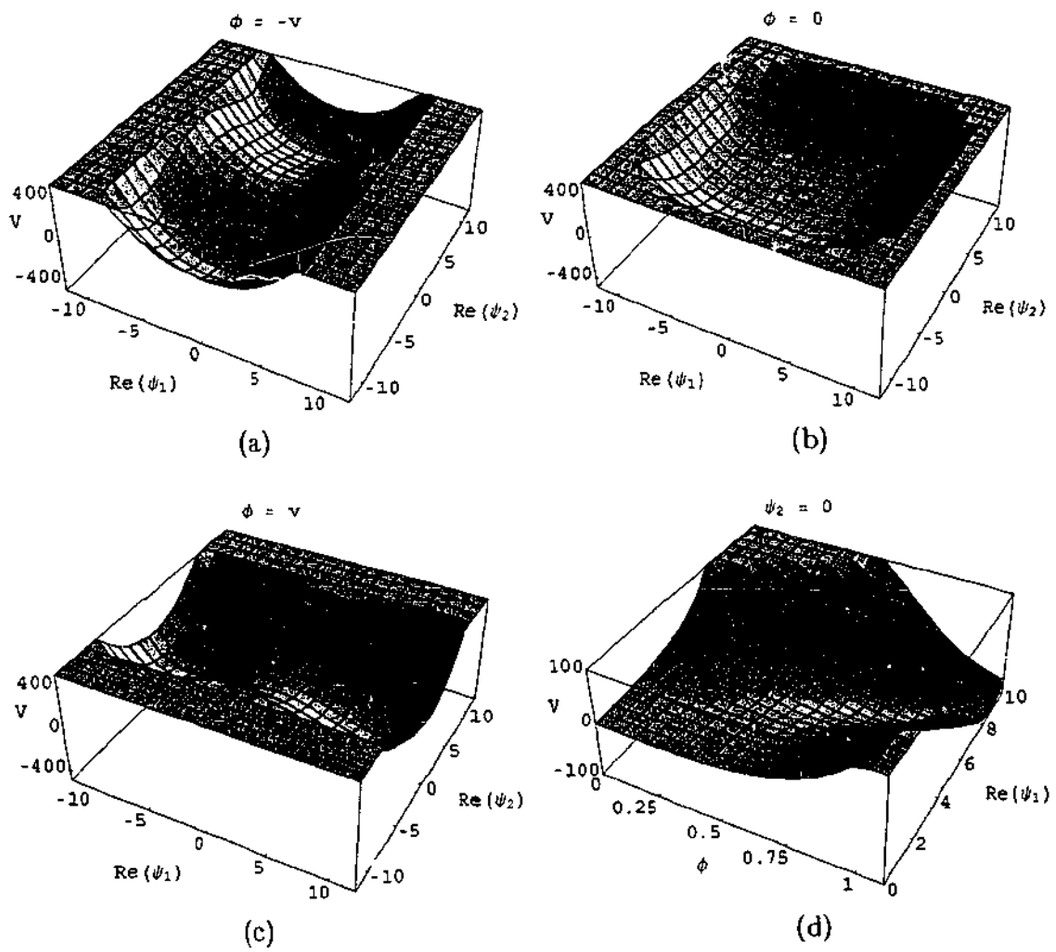

Figure 4.6: Potential energy density, $V(\phi, \psi_1, \psi_2)$, as a function of $Re(\psi_1)$ and $Re(\psi_2)$. (a) $\phi = -v$, (b) $\phi = 0$, and (c) $\phi = v$. In (d) the potential is plotted as function of $Re(\psi_1)$ and ϕ for $\psi_2 = 0$. The parameters are $\lambda_\phi = 108$, $\tilde{v}^2 = 1/24$, $\lambda_\psi = 1/24$, $\tilde{w}^2 = -3$ $g = 0$, $h = -1/12$ and $\mu = 6$.

determined by the energy density difference between the true vacuum and the false vacuum.

The stability of the D-wall depends on how the strings are attached to the wall. When either of the ψ-fields terminate on the wall the corresponding VEV vanishes. In this case the hybrid defect resembles a free wall, which is expected to be stable, since the Higgs field corresponding to a Z_2 domain wall is stable due to conservation of topological charge (see the numerical simulation shown in Fig. 4.3 for Z_2 domain walls). However, to establish the stability of the D-wall it is necessary to show that the wall is stable for a wide range of coupling parameters and when perturbations are imposed on the wall.

4.3.2 Stability of the D-wall

The shape of the potential is governed by a multi-dimensional parameter space. We can gain insight into the parameters that govern the stability of the D-wall by examining the minima of the potential (4.17), which occur at $|\phi| = v$ and $|\psi| = w$, i.e.,

$$4\lambda_\phi v\left(v^2 - \widetilde{v}^2\right) + 2g\mu v^2 - \mu w^2 = 0 \tag{4.22}$$

$$2\lambda_\psi\left(w^2 - \widetilde{w}^2 + g\left(v^2 - \widetilde{v}^2\right)\right) - \mu v = 0. \tag{4.23}$$

These equations indicate that the VEVs of the ϕ- and ψ-fields do not depend on the parameter h, which governs the interaction between the two ψ-fields. Furthermore, since ψ_1 terminates on the wall from "above" (i.e., $|\psi_1|$ vanishes "below" the wall), and ψ_2 terminates on the same wall from "below" (i.e., $|\psi_2|$ vanishes "above" the wall), the term $h|\psi_1|^2|\psi_2|^2$ in the D-wall potential (4.17) will be approximately equal to zero everywhere.[9] Because the equations governing the vacuum states of the D-wall do not depend on the parameter h, and the term $h|\psi_1|^2|\psi_2|^2$ is approximately zero (see Fig. 4.7), the parameter h is not expected to significantly affect the dynamics of the D-wall.

Using Eqs. (4.22) and (4.23) we seek to establish constraints on the other parameters in the potential, i.e.,

$$\lambda_\psi = \frac{\mu^2 v^3}{\beta\mu - \alpha} \tag{4.24}$$

$$g = \frac{1}{v^2 - \widetilde{v}^2}\left[\frac{\mu v}{2\lambda_\psi} + \widetilde{w}^2 - w^2\right], \tag{4.25}$$

where α and β are defined by

$$\alpha \equiv 4\lambda_\phi v\left(v^2 - \widetilde{v}^2\right)^2 \tag{4.26}$$

$$\beta \equiv 2\left(w^2 - \widetilde{w}^2\right)v^2 + \left(v^2 - \widetilde{v}^2\right)w^2. \tag{4.27}$$

[9] At the position where $|\psi_1| \neq 0$, $|\psi_2|$ vanishes and vice versa.

Equation (4.24) determines the conditions under which a D-wall forms. The stability of the wall is dictated by the sign of λ_ψ in the potential (4.17). We note that $\lambda_\psi \to \pm\infty$ if $\mu \to \alpha/\beta$, with $\mu = \alpha/\beta$ representing an unstable configuration. If $\lambda_\psi > 0$ we have a Mexican hat potential which characterizes a symmetry breaking phase transition. However, for $\lambda_\psi < 0$ the potential has local maxima at $\psi_1 = \pm w$ for $z > 0$ and $\psi_2 = \pm w$ for $z < 0$. Since the potential does not have vacuum minima with non-vanishing ψ_1- and ψ_2-fields, this implies that it does not exhibit symmetry breaking, and therefore no topological defects exist in the ψ_1 and ψ_2-field. Thus a D-wall is precluded from forming unless we constrain the parameter μ (which couples the strings to the wall) to $\mu > \alpha/\beta$. We know that a single domain wall is stable, therefore varying the self-coupling, λ_ϕ, is unlikely to cause an instability in the D-wall; consequently, we fix the value of λ_ϕ in our numerical simulations. To facilitate comparison with the work of Carroll and Tkodden (1998), we set $\tilde{v}^2 = \frac{1}{24}$, $\tilde{w}^2 = -3$, $v^2 = 1$, $w^2 = 69$, $\lambda_\phi = 108$ and $h = -1/12$. For this choice of symmetry breaking scale Eqs. (4.24) and (4.25) become

$$\lambda_\psi = \frac{8\mu^2}{1681\mu - 3174} \tag{4.28}$$

$$g = \frac{12}{23}\left(\frac{\mu}{\lambda_\psi} - 144\right), \tag{4.29}$$

which constrains $\mu > \mu_c$, where $\mu_c = 3174/1681 \approx 1.89$. Equations (4.28) and (4.29) show that the parameters λ_ψ and g are completely determined for a given value of μ. In our numerical simulations the string-wall coupling parameter, μ, is the only independent parameter, and the stability of the D-wall is explored by varying μ.

Although our analysis shows that a D-wall forms for $\mu > \mu_c$, negative values of μ should also be possible since the potential given by Eq. (4.17) is symmetric in μ. However, the transformation $\mu \to -\mu$ is identical to the transformation $\psi_1 \to \psi_2$. This is equivalent to swapping the ψ_1- and ψ_2-fields. Therefore we only explore the stability of the D-wall for $\mu > \mu_c$.

4.3.3 Field equations for the D-wall

The equations of motion of the D-wall are determined from the Lagrangian (4.16), i.e.,

$$\Box\chi = -\frac{1}{2}\frac{\partial V}{\partial \overline{\chi}}, \qquad (\chi = \phi,\, \psi_1,\, \psi_2). \tag{4.30}$$

Equation (4.30) is solved numerically by using a second order leapfrog difference scheme (see Appendix A). To obtain a complete picture of the D-wall, numerical simulations were

carried out for one and two strings terminating on the wall. The initial conditions employ a static D-wall solution of the field equation (4.30) in cylindrical coordinates.

4.3.4 Static D-wall solution

Consider a D-wall in three dimensions, with the domain wall located at $z = 0$; the strings are oriented along the z-axis and terminate at the origin ($r = \sqrt{x^2 + y^2} = 0$). The static D-wall solution of the field equation (4.30) is obtained from the coupled equations

$$\frac{\partial^2 \phi}{\partial r^2} + \frac{1}{r}\frac{\partial \phi}{\partial r} + \frac{\partial^2 \phi}{\partial z^2} = \frac{1}{2}\frac{\partial V}{\partial \phi} \tag{4.31}$$

$$\frac{\partial^2 f}{\partial r^2} + \frac{1}{r}\frac{\partial f}{\partial r} - \frac{f}{r^2} + \frac{\partial^2 f}{\partial z^2} = \frac{1}{2}\frac{\partial V}{\partial f}, \quad (f = f_1, f_2). \tag{4.32}$$

The following ansatzen are assumed

$$\psi_1 = f_1(r,z)e^{i\theta_1(x,y)} \tag{4.33}$$

$$\psi_2 = f_2(r,z)e^{i\theta_2(x,y)} \tag{4.34}$$

$$\phi = \phi(r,z), \tag{4.35}$$

where $f_1(r,z)$ is the magnitude of ψ_1, $f_2(r,z)$ is the magnitude of ψ_2, and $\theta_1(x,y)$ and $\theta_2(x,y)$ are the phase angles around the vacuum minima of ψ_1 and ψ_2, respectively. The magnitude of ψ_1 vanishes at the center of the string ($r = 0$) and below the wall ($z < 0$), otherwise its value is w. Similarly the magnitude of ψ_2 vanishes at the center of the string and above the wall ($z > 0$), otherwise its value is also w. The phase angles around the vacua depend only on the x and y coordinates.

Since Eqs. (4.31) and (4.32) are non-linear, the solutions that define the D-wall are found using an iterative finite difference scheme whose convergence is sensitive to the choice of spatial step. To ensure that the solution converges, we employed a spatial step $\Delta h = 0.055$. Once the vortex solutions have been obtained they are transformed into Cartesian coordinates using Eqs. (4.33), (4.34) and (4.35), and evolved according to Eq. (4.30). Causality dictates that the time step must be smaller than the spatial step, hence we chose $\Delta t = 0.02$. The simulation uses free boundary conditions and a lattice (grid) consisting of 200^3 points. The D-wall is evolved up to $t = 20$, corresponding to 1000 iterations. This time scale is long enough to ensure that any disturbance (e.g., noise) from the boundary is able to affect the stability of the D-wall.

The numerical solution to Eqs. (4.31) and (4.32) uses a fixed point method (see Sec. 2.2). Trial initial conditions were used for the scalar fields, $f_1(r,z)$, $f_2(r,z)$ and

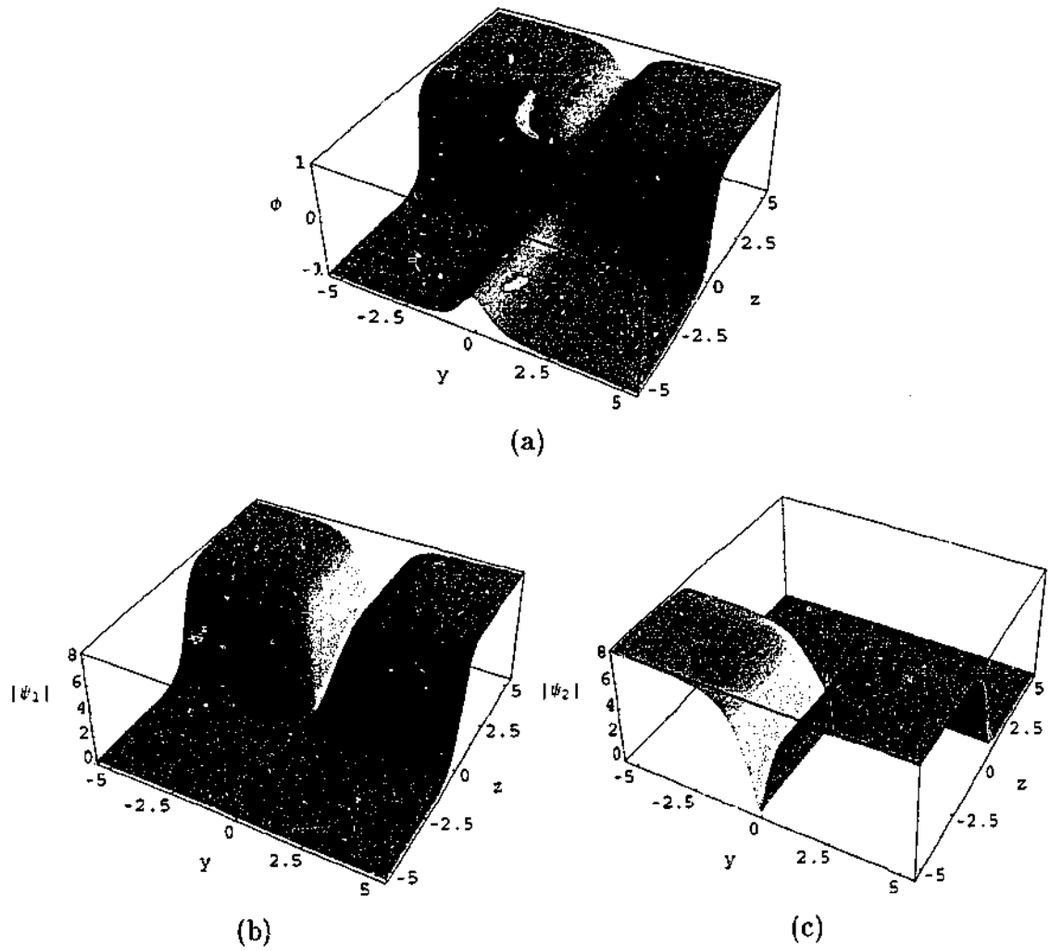

Figure 4.7: Cross-sections ($x = 0$) of the Higgs fields showing the D-wall located at $z = 0$ ($\mu = 6$). (a) ϕ, (b) $|\psi_1|$, and (c) $|\psi_2|$. String-one (characterized by ψ_1) is oriented along $+z$ and string-two (characterized by ψ_2) is oriented along $-z$. The magnitude of ϕ in the vicinity of the strings is lower than in the vacuum state. The value of $|\psi_1|$ falls to zero below the wall (b), whereas $|\psi_2|$ falls to zero above the wall (c). There is little interaction between string-one and string-two, and the term $h|\psi_1||\psi_2|$ in the potential is approximately zero everywhere.

$\phi(r,z)$, and a finite difference scheme was employed to iterate the scalar fields until they converged.[10] The initial conditions exploit our knowledge of the boundary values and vacuum state of the scalar fields. For example, consider a D-wall located at $z=0$, with string-one terminating on the wall from above and string-two from below. In this case we set $f_1(r, z<0)=0$, $f_1(0, z\geq 0)=0$, and $f_1(r\neq 0, z\geq 0)=w$. Similarly $f_2(r, z>0)=0$, $f_2(0, z\leq 0)=0$, and $f_2(r\neq 0, z\leq 0)=w$. Finally, the value of ϕ is set to v for $z>0$ and $-v$ for $z<0$. Since the stability of the D-wall depends on the parameter μ, the convergence of the numerical algorithm has been explored for various values of μ.

As $\mu\to\mu_c$ the numerical algorithm does not converge to a solution since $\lambda_\psi\to\infty$. To ensure that the simulations can be completed in a reasonable time frame we have restricted $\mu\geq 2.5$. The numerical solution for a D-wall configuration with two strings terminating on the wall is plotted in Fig. 4.7. This figure shows that the behaviour of ϕ, $|\psi_1|$ and $|\psi_2|$ is consistent with the previous analysis based on the D-wall potential (see Sec. 4.3.1). Various configurations of a D-wall (e.g., one string terminating on the wall) can also be obtained by modifying the boundary values and vacuum states of the scalar fields. In the following sections we describe the evolution of these D-wall configurations.

4.3.5 Two strings terminating on a wall

We first consider the stability of a D-wall with two strings terminating on the wall. The evolution of the D-wall uses a discretization of Eq. (4.30); the initial condition for this D-wall configuration has been discussed in Sec. 4.3.4. Because of computational constraints our numerical simulations are performed in the range $2.5\leq\mu\leq 10$, in steps of $\Delta\mu=0.5$. Cross-sections of the total energy density of the D-wall at the end of the simulation ($t=20$) were plotted and compared to the initial D-wall configuration (see Figs. 4.9 (a) and (b)). For the range of μ-values explored here, the D-wall did not show any instability.

Figure 4.8 shows the energy density of the D-wall for four different values of μ. As μ increases, the gradient of the ϕ- and ψ-fields also increases, however, this only changes the energy density of the D-wall. There is no evidence to suggest that higher energy densities result in unstable topological defects. If the D-wall is stable in the range $2.5\leq\mu\leq 10$, it is plausible to assume stability for larger values of μ. Figure 4.8 also shows that the energy density of the wall decreases where the two strings terminate. At lower values of μ the

[10] For an iterative finite difference scheme to converge we require that the difference in the norm of the scalar fields, at two successive iterations, is small, i.e., $||\chi||_k - ||\chi||_{k-1} < 10^{-10} \ll ||\chi||_k$ ($\chi=\phi, f_1, f_2$), where k denotes the iteration number.

energy density of the defects is smaller. As the value of μ approaches $\mu_c \approx 1.89$ ($\lambda \to \infty$), the energy density of the D-wall vanishes. This confirms that a D-wall is unstable for $\mu = \mu_c$ ($\lambda_\psi = \pm\infty$) and no D-wall forms for $\mu < \mu_c$ ($\lambda_\psi < 0$).

Figure 4.9 shows a typical simulation for $\mu = 6$. Comparing the energy density of the D-wall in Figs. 4.9 (a) and (b) we see no difference between the D-wall at the start and end of the simulation. For all values of μ studied, our numerical simulations suggest that the D-wall is a stable topological defect. In Sec. 4.3.6 we examine the stability of the D-wall in the presence of perturbations imposed on the wall.

4.3.6 Perturbations on the D-wall

We have explored the stability of the D-wall when it is perturbed by harmonic perturbations of the form

$$z = A\cos\left(\frac{\pi n y}{L}\right), \tag{4.36}$$

where A is the perturbation amplitude, n is a positive integer and $-5.5 \leq L \leq 5.5$ is the extent of the domain wall in the y direction. Simulations were carried out for $n = 1, 2$ and 3, and for amplitudes in the range $0 \leq A \leq 1$. A perturbation amplitude $A = 1$ is large compared to the thickness of the wall, $\delta = 1/\sqrt{\lambda_\phi} v \sim 0.1$ (for $\mu = 6$). It is observed that the perturbations decay, with energy partly transferred to the strings. No instabilities are observed when A is varied in the range $0 \leq A \leq 1$. Figures 4.10 and 4.11 show a D-wall at the beginning and end of a typical simulation for $A = 1$ and $n = 1$. The perturbation amplitude on the wall at the end of the simulation is smaller than that at the start, which is a consequence of the wall transferring kinetic energy to the strings.

Figure 4.12 shows the oscillations of the wall in the z direction. The effect of the strings on the wall is evident in Figs. 4.12 (b), (c) and (d), where the oscillating wall pulls on the strings. String-one and string-two terminate on the wall (at $z = 1$). As the wall oscillates, that part in contact with the strings accelerates more slowly than the rest of the wall, and lags behind. This results in a kink in the wall, which is evident in Figs. 4.12 (b) and (d). The wall imparts kinetic energy to the strings and the amplitude of the oscillations decays with time. However, throughout the oscillations the strings are still firmly attached to the wall. This indicates that the D-wall is stable in the presence of perturbations. Wall perturbations are also transferred to the strings and the D-wall is also stable in the presence of these string perturbations.

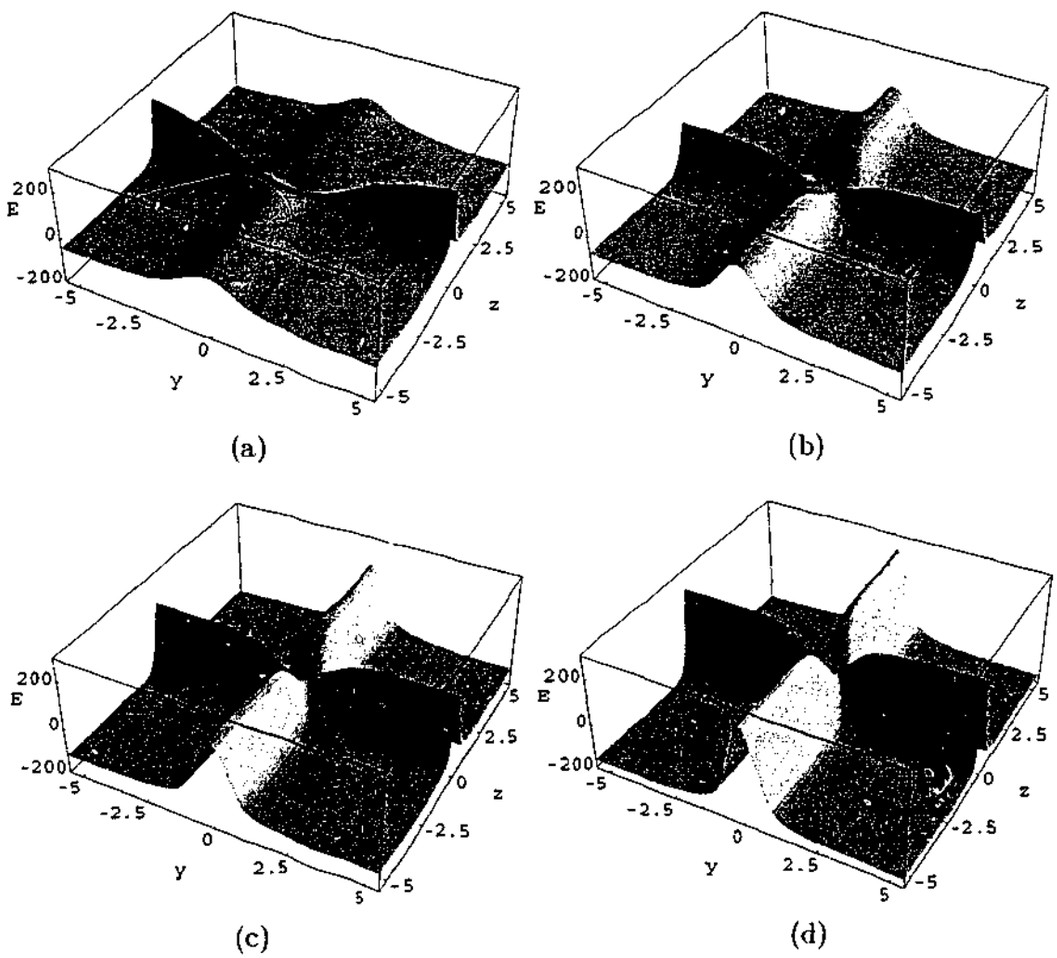

Figure 4.8: Cross-sections ($x = 0$) of the total energy density of the D-wall. (a) $\mu = 2.5$, (b) $\mu = 5$, (c) $\mu = 7.5$, and (d) $\mu = 10$. The energy density of the D-wall is higher for larger values of μ. The wall is located at $z = 0$ and the strings are located at $y = 0$. String-one (characterized by ψ_1) is defined for $z > 0$ and string-two (ψ_2) is defined for $z < 0$. The energy density of string-one decreases as we approach the wall from "above", whereas the energy density of string-two decreases as we approach the wall from "below". The energy density of the wall also decreases in the region where the two strings terminate.

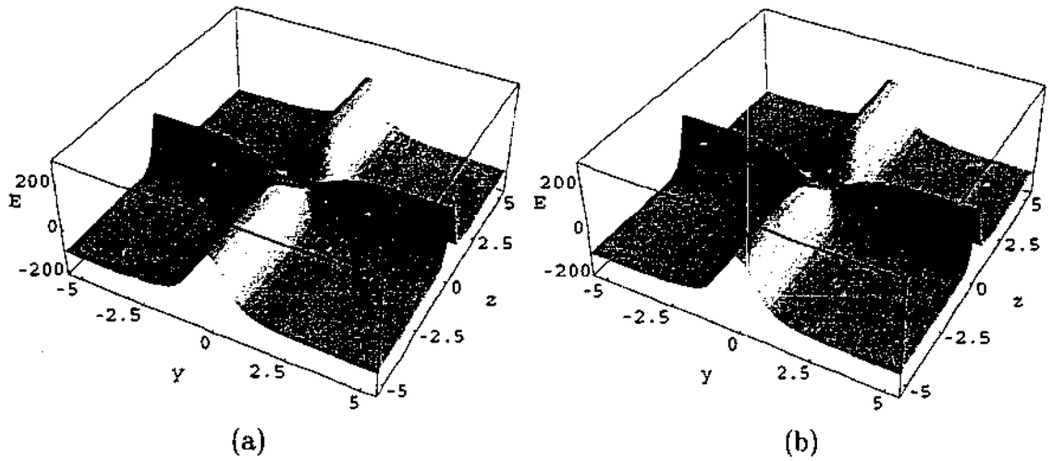

Figure 4.9: Cross-sections ($x = 0$) of the total energy density of the D-wall for $\mu = 6$. (a) $t = 0$ and (b) $t = 20$, corresponding to the end of the simulation. These figures show no difference between the D-wall at the start and end of the simulation. This provides evidence for the stability of the D-wall.

4.3.7 A single string terminating on a wall

An interesting scenario occurs when a single string terminates on the wall. Figure 4.13 shows a semi-infinite string oriented in the z direction, terminating on the wall from above. Since the second string is absent there is no non-contractable phase winding in the ψ_2-field. The static initial condition for ψ_2 is obtained using an iterative finite difference scheme, based on the time-independent field equations (4.31) and (4.32). In this case ψ_2 is set to w below the wall and zero above the wall. A typical numerical solution for the ϕ- and ψ_2-fields is shown in Figs. 4.14 (a) and (b). Without string-two the field configuration of ϕ adopts the VEV everywhere below the wall.

The results of a numerical simulation of a D-wall with a single string terminating on the wall are displayed in Fig. 4.15. Figures 4.15 (a) and (b) show the D-wall at the start of the simulation and at $t = 13$, respectively. The wall was initially located at $z = -2.5$, however, it is pulled up by the string due to string tension. As the wall gains kinetic energy and stretches, its energy density also increases, but the string is still firmly attached to the wall. No fluctuations are observed in the energy density that could lead to the destruction of the D-wall. This suggests that a D-wall with a single string is a stable hybrid defect.

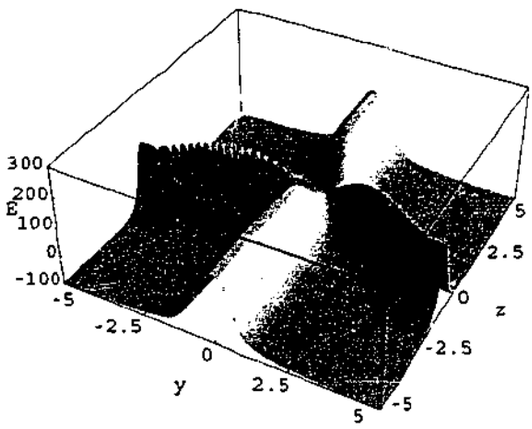

Figure 4.10: Cross-section ($x = 0$) of the total energy density of the D-wall. The domain wall is located at $z = 0$, with the locus of the strings along the z-axis at $y = 0$. The cross-section corresponds to $t = 0$. A perturbation has been introduced on the wall, with amplitude $A = 1$ and "harmonic number" $n = 1$.

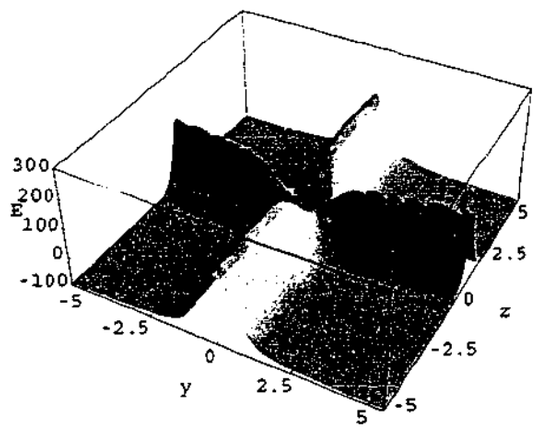

Figure 4.11: Cross-section ($x = 0$) of the total energy density of the D-wall at $t = 20$. This was evolved from the initial configuration shown in Fig. 4.10. The amplitude of the perturbation (in the z direction) has decayed, indicating that the D-wall is stable with respect to perturbations on the wall.

4.3.8 Domain walls connected by a string segment

When a single string terminates on a wall it pulls the wall in the direction of the string tension (see Fig. 4.15 (b)). This phenomenon has some interesting consequences if the other end of the string terminates on a second wall (see Fig. 4.16). The string is expected to exert tension on the walls, pulling them toward each other.

Simulations were performed to confirm this conjecture. Figure 4.16 shows the initial condition for the D-wall configuration. The string is characterized by ψ_1, vanishing below wall-one and above wall-two. Since there is no second string, there is no non-contractable phase winding in ψ_2; the ψ_2-field adopts a value w below wall-one and above wall-two, vanishing between the walls. The ϕ-field approaches $-v$ below wall-one and above wall-two; it adopts a value v between the walls.

Figure 4.17 (a) shows two walls connected by a string segment (the string is not shown). The system is initially stationary. Due to string tension the two walls are pulled toward each other (see Fig. 4.17 (b)), which results in the walls colliding. As noted previously two overlapping walls form a wall-anti-wall pair (see Sec. 4.2.2). It is expected that when the two walls collide they will annihilate. This is confirmed by our numerical simulations.

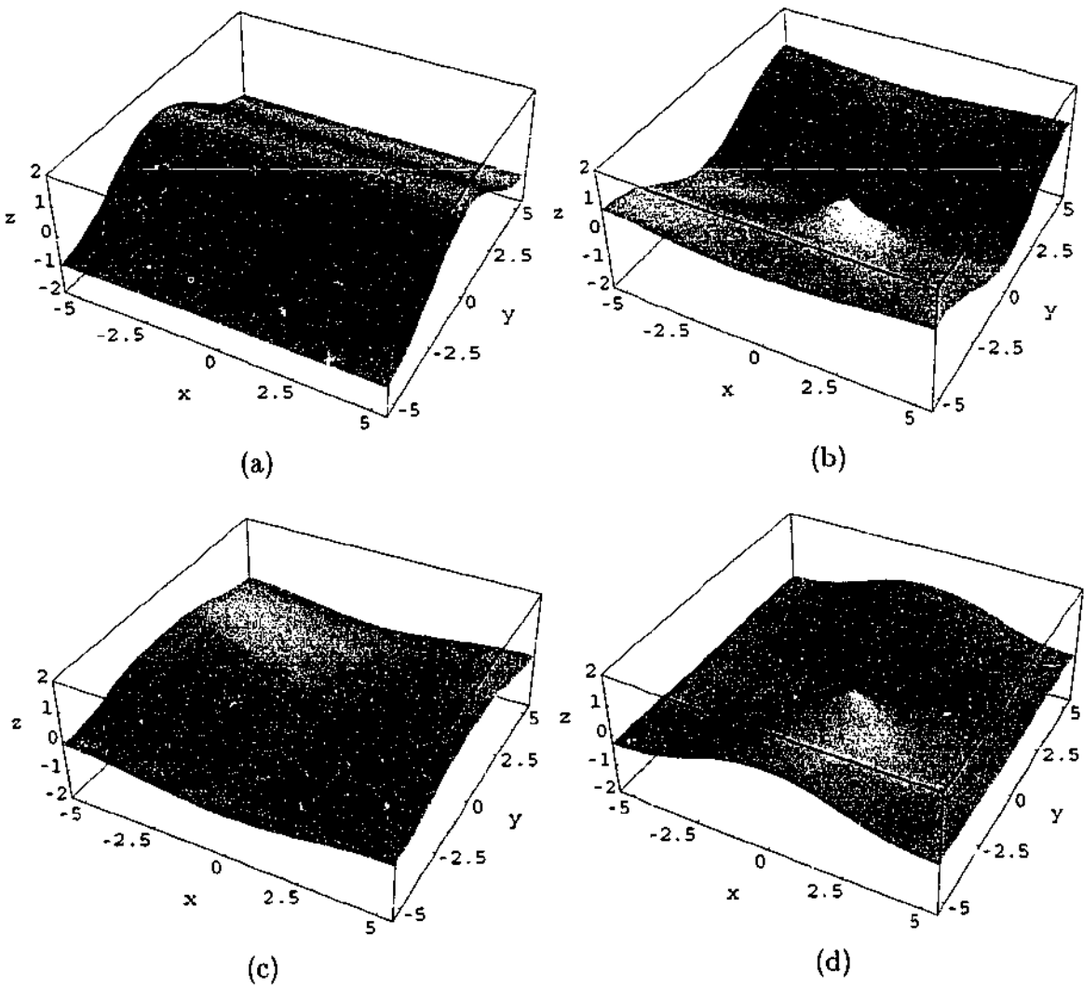

Figure 4.12: Cross-sections ($\phi = 0$) showing oscillations of the wall. (a) $t = 0$, (b) $t = 7$, (c) $t = 14$, and (d) $t = 20$. These are based on the simulation shown in Figs. 4.10 and 4.11. (a) Initial condition in which the wall has amplitude $A = 1$ and "harmonic number" $n = 1$. (b) A kink develops on the wall as the wall moves down. This is due to the wall pulling on the strings. In (c) and (d) we see the wall moving up and down. As the wall oscillates the attached strings follow, indicating that the perturbed D-wall is stable.

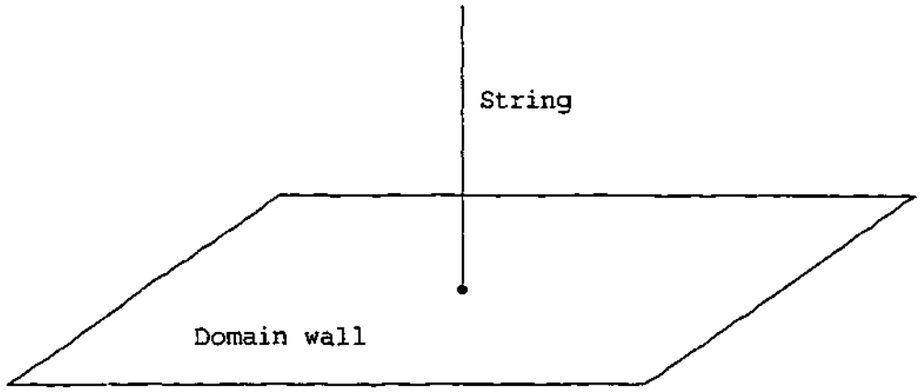

Figure 4.13: Schematic representation of a D-wall with a single string (characterized by the ψ_1-field) terminating on the wall from above.

Figure 4.18 shows cross-sections of the total energy density of the D-wall ($x = 0$) at four different times. Those parts of the wall that are in contact with the string move toward each other first. Consequently, the ends of the string come into contact, in which case the string unwinds and annihilates, thereby nucleating a hole in each wall. This hole expands outward at almost the speed of light[11], resulting in the annihilation of the walls.

The annihilation of a D-wall in this manner is analogous to the Langacker-Pi mechanism for monopoles (Langacker and Pi 1980). In this scenario a monopole is drawn to an anti-monopole by string tension. When the string connecting the monopole and anti-monopole shrinks to a point it unwinds, and the monopole annihilates with the anti-monopole. A similar annihilation mechanism is observed for the D-wall.

This observation may have relevance to cosmology, since a network of strings and walls is expected to form in the early Universe (via a series of symmetry breaking phase transitions). For example, a D-wall may arise for $U(1) \times U(1) \times Z_2 \times H \rightarrow U(1) \times U(1) \times H \rightarrow H$, with walls forming in the first phase transition and strings in the second phase transition. This can result in a hybrid defect in which walls are connected by strings. The speed at which the walls are pulled together will depend on the string tension. The larger the tension the faster the walls are pulled together, which increases the annihilation rate of D-walls. The string tension is proportional to η^2, where η is the symmetry breaking

[11] The speed at which the hole expands can be inferred from Figs. 4.18 (c) and (d). In Fig. 4.18 (c) (at $t = 5$) the two domain walls have just collided. The radius of the hole is $h_r \sim 0.35$ (determined from the peak-to-peak distance in the y direction at $z = 0$). In Fig. 4.18 (d) (at $t = 6$) the radius of the hole is $h_r \sim 1.25$, which is consistent with a hole expanding at ~90% the speed of light.

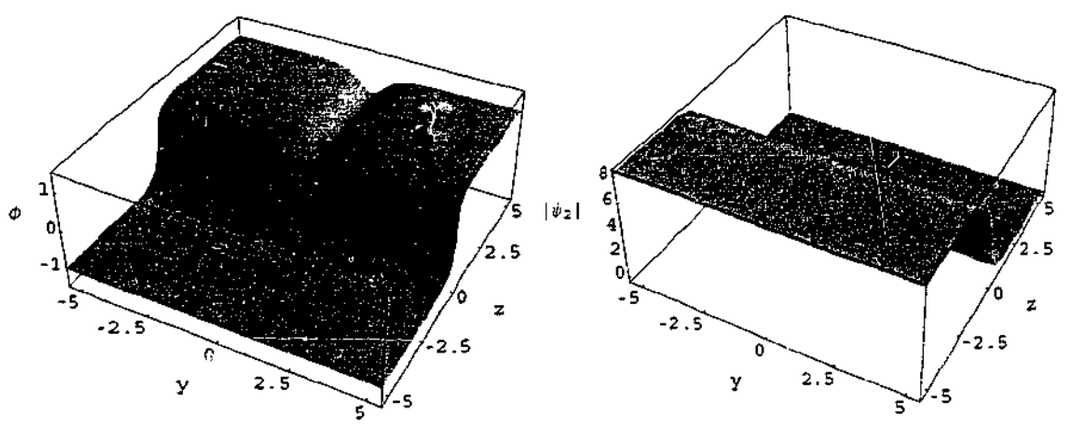

(a) (b)

Figure 4.14: Cross-sections ($x = 0$) through the D-wall with a single string terminating on the wall. (a) ϕ and (b) $|\psi_2|$. The ψ_1-field is the same as the case for two strings terminating on the wall. Since there is no second string, ψ_2 adopts its VEV below the wall and vanishes above the wall.

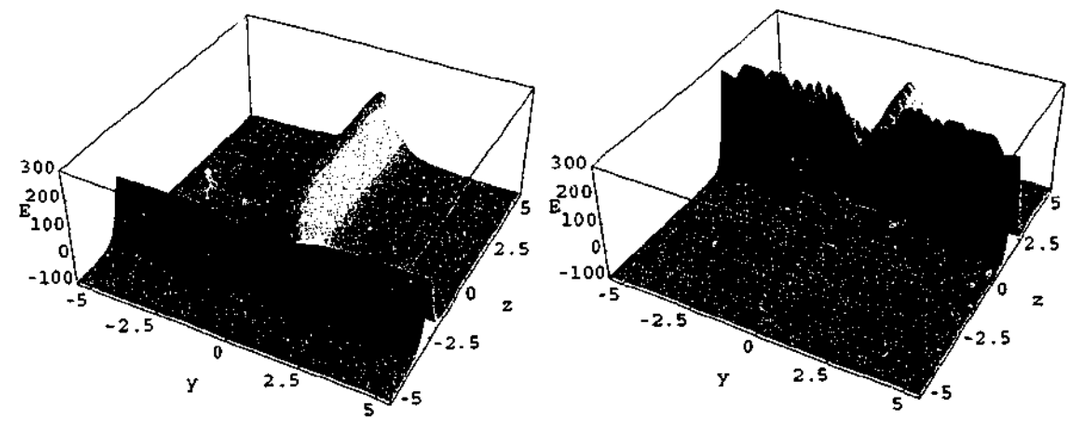

(a) (b)

Figure 4.15: Cross-sections ($x = 0$) of the total energy density of the D-wall, with a single string terminating on the wall. (a) $t = 0$ and (b) $t = 13$. The wall is located at $z = -2.5$ and the string locus is in the z direction (at $y = 0$). Comparing (a) and (b) shows that the wall is pulled in the z direction due to string tension. The energy density of the wall in (b) is higher than in (a) due to stretching of the wall under string tension. No fluctuations are observed in the energy density of the D-wall that could lead to the destruction of the hybrid defect.

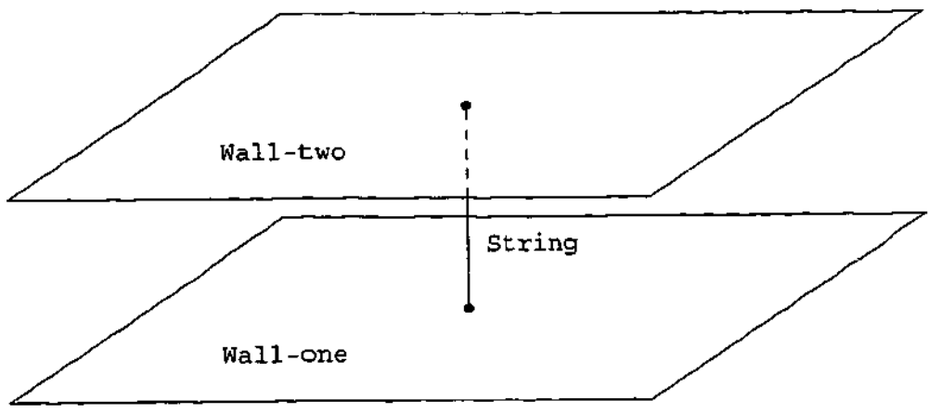

Figure 4.16: Schematic representation of a Dirichlet defect, in which two walls are connected by a string.

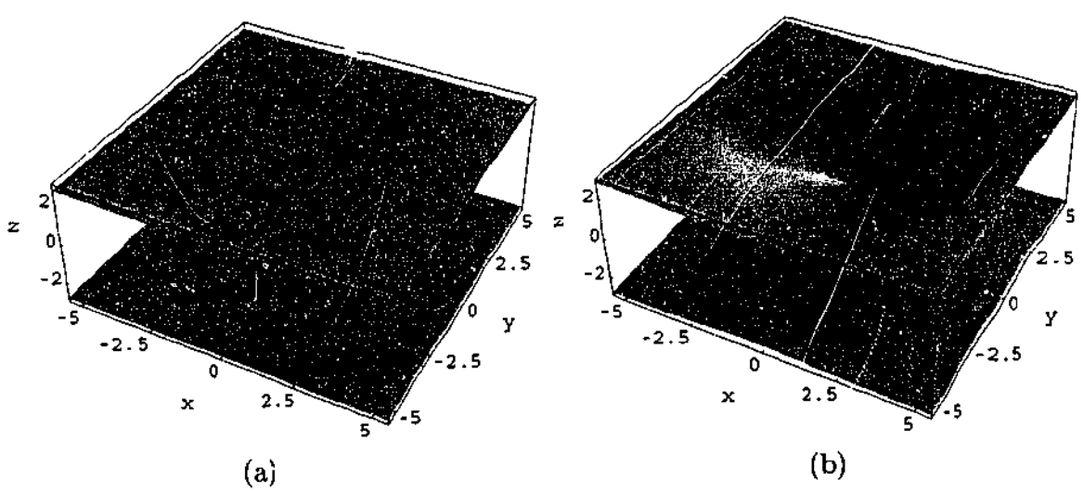

Figure 4.17: Cross-sections ($\phi = 0$) through two walls connected by a string (not shown). (a) $t = 0$ and (b) $t = 4$. The locus of the string is along the z direction. In (a) the hybrid defect is initially stationary, while in (b) the two walls are pulled toward each other.

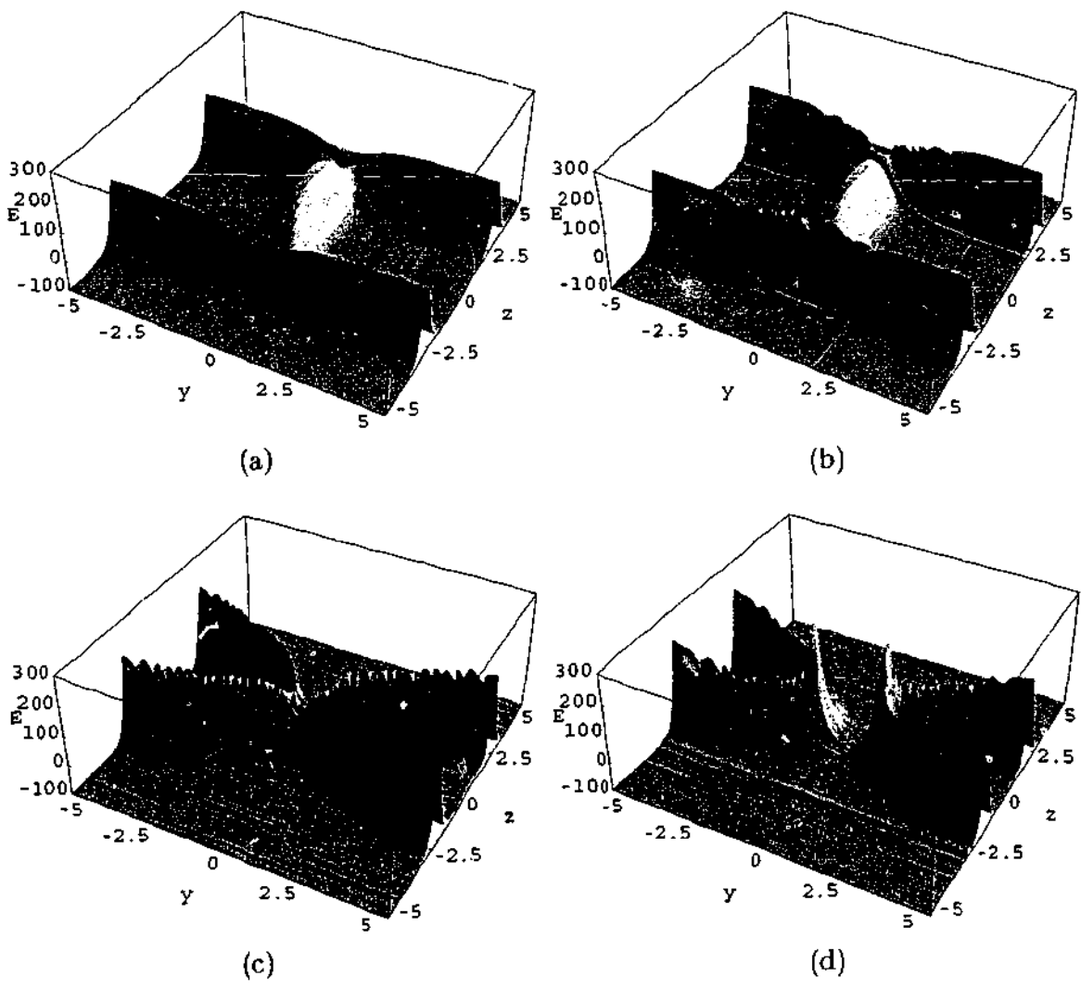

Figure 4.18: Cross-sections ($x = 0$) of the total energy density of the D-wall consisting of two walls connected by a string. (a) $t = 0$, (b) $t = 1$, (c) $t = 5$, and (d) $t = 6$. Initially the walls (located at $z = \pm 2.5$) are undeformed. The string locus is along the z direction (at $y = 0$). In (b) the walls are pulled toward each other under string tension, and in (c) the string unwinds, annihilates and nucleates a hole. The hole expands outward as is evident in (c) and (d). This results in the annihilation of the walls.

scale of the strings. Provided that strings form immediately after the walls, the symmetry breaking scale of the string is comparable to the wall. Under these circumstances, string tension will play a significant role in the evolution and annihilation of D-walls. The annihilation of these D-walls may also have implications for monopoles that form between the walls.

4.4 D-walls and the monopole problem

Monopoles form in GUT models as an unavoidable consequence of $SU(2) \to U(1)$ symmetry breaking. This poses a problem for GUTs and must be addressed in realistic scenarios of symmetry breaking. In this section we briefly discuss how the evolution of a D-wall may resolve the monopole problem.[12]

Dvali *et al.* (1998) proposed that monopoles can be "swept" away by domain walls. As the wall "sweeps" out a volume in space, monopoles collide with the wall. The collision between monopoles and the wall results in the annihilation of the monopoles, with the energy transferred to the wall. This scenario is analogous to the way skyrmions collide and annihilate with a domain wall (see e.g., Dvali *et al.* 1998). In order for the wall to sweep out monopoles it is assumed that the wall forms as a consequence of approximate Z_2 symmetry breaking. That is, the magnitude of the Higgs field of the domain wall at one side of the wall is different from the other side. Since the energy density on one side of the wall is higher there will be a pressure difference between the two sides. The wall moves toward the region with lower pressure, thereby "sweeping" out monopoles. If the wall moves outside our Hubble horizon, this provides a mechanism for avoiding the domain wall problem.

D-walls can also "sweep" away monopoles without requiring an approximate Z_2 symmetry. Consider a hybrid model in which monopoles form between two walls, which in turn are connected by a string (see Fig. 4.19). Such hybrid defects may form in a model with $SU(2) \times SU(2) \times U(1) \times U(1) \times Z_2 \to U(1) \times U(1)$ symmetry breaking. For simplicity we assume a global model (i.e., no gauge field). The $SU(2) \times SU(2) \times U(1) \times U(1) \times Z_2$ D-wall model can be constructed in a manner similar to the $U(1) \times U(1) \times Z_2$ D-wall, i.e.,

$$\mathcal{L} = \partial_\mu \Phi \partial^\mu \Phi + \overline{\partial_\mu \psi_1} \partial^\mu \psi_1 + \overline{\partial_\mu \psi_2} \partial^\mu \psi_2 + \overline{\partial_\mu \Psi_1} \partial^\mu \Psi_1 + \overline{\partial_\mu \Psi_2} \partial^\mu \Psi_2 - V(\Phi, \psi_1, \psi_2, \Psi_1, \Psi_2), \tag{4.37}$$

[12] In Chapter 5 we discuss topological defects in $\mathcal{R}^{4+1}$ spacetime, and address the monopole problem from a different perspective.

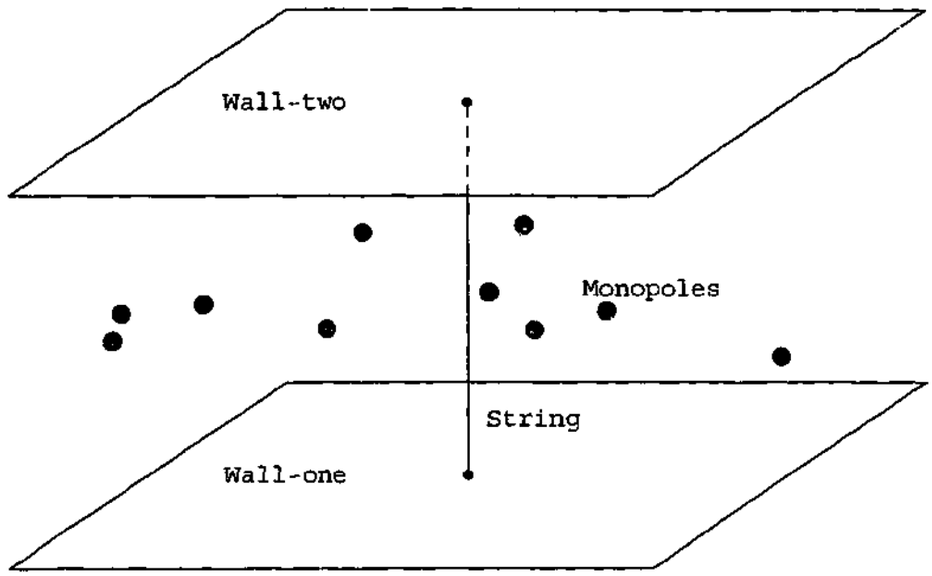

Figure 4.19: Schematic representation of a Dirichlet defect, in which monopoles form between two walls, which are connected by a string.

where $\Phi = \phi_1\phi_2$ describes the domain walls, ψ_1 and ψ_2 describe the cosmic strings and Ψ_1 and Ψ_2 describe the monopoles. The potential, $V(\Phi, \psi_1, \psi_2, \Psi_1, \Psi_2)$, is generalized from Eq. (4.17) for the D-wall, i.e.,

$$\begin{aligned} V(\Phi,\psi_1,\psi_2,\Psi_1,\Psi_2) &= \lambda_\Phi\left(\Phi^2-\widetilde{v}^2-\widetilde{v}_m^2\right)^2+\lambda_\psi\left[|\psi_1|^2+|\psi_2|^2-\widetilde{w}^2+g\left(\Phi^2-\widetilde{v}^2\right)\right]^2 \\ &\quad +h|\psi_1|^2|\psi_2|^2-\mu\Phi\left(|\psi_1|^2-|\psi_2|^2\right) \\ &\quad +\lambda_m\left[|\Psi_1|^2+|\Psi_2|^2-\widetilde{w}_m^2+g_m\left(\Phi^2-\widetilde{v}_m^2\right)\right]^2 \\ &\quad +h_m|\Psi_1|^2|\Psi_2|^2-\mu_m\Phi\left(|\Psi_1|^2-|\Psi_2|^2\right), \end{aligned} \tag{4.38}$$

where λ_m, g_m, h_m and μ_m are additional coupling parameters. Since we are not concerned with how a monopole interacts with the strings, we ignore the coupling between monopoles and strings in the potential. As the values of μ and μ_m increase from zero (see the earlier discussion of D-walls in Sec. 4.3.1), the VEVs of the fields Φ, ψ_1, ψ_2, Ψ_1 and Ψ_2 adopt the following values:

$$\langle\Phi\rangle = v, \quad \langle|\psi_1|\rangle = w, \quad \langle|\psi_2|\rangle = 0, \quad \langle|\Psi_1|\rangle = w_m, \quad \langle|\Psi_2|\rangle = 0 \tag{4.39}$$

and

$$\langle\Phi\rangle = -v, \quad \langle|\psi_1|\rangle = 0, \quad \langle|\psi_2|\rangle = w, \quad \langle|\Psi_1|\rangle = 0, \quad \langle|\Psi_2|\rangle = w_m, \tag{4.40}$$

where v, w and w_m are obtained by minimizing the potential (4.38) with respect to Φ, $|\psi_1|$ or $|\psi_2|$, and $|\Psi_1|$ or $|\Psi_2|$. The behaviour of Ψ_1 and Ψ_2 is analogous to ψ_1 and ψ_2, respectively. For example, Ψ_1 possesses monopole solutions between the walls, however, it vanishes below wall-one and above wall-two; whereas Ψ_2 has monopole solutions below wall-one and above wall-two, and vanishes between the walls.

The dynamics of the D-wall are governed by an equation of motion derived from the Lagrangian (4.37). The behaviour of the D-wall, with monopoles located between the walls, can be understood by considering the evolution of the $U(1) \times U(1) \times Z_2$ D-wall. In Sec. 4.3 we showed that two walls connected by a string are pulled toward each other due to string tension. As the two walls move toward each other they collide with monopoles located between the walls. The fate of a monopole upon collision with a wall is governed by the VEV of the Ψ_1-field. Between the walls $\langle\Phi\rangle = v$ and $\langle|\Psi_1|\rangle = w_m$ (see Eq. (4.39)). Regions between the walls exhibit symmetry breaking in the Ψ_1-field. However, as a wall moves past a monopole, the VEV of the wall changes from v to $-v$ at the location of the monopole; consequently, $\langle|\Psi_1|\rangle$ decreases to zero (see Eq. (4.40)). This results in the restoration of symmetry in the Ψ_1-field, and the monopole must unwind and annihilate. As the walls approach each other they remove the monopoles located between the walls.

Once all monopoles are removed, the two walls collide and annihilate. Since hybrid defects are expected to form in realistic GUT symmetry breaking schemes, our D-wall model provides a scenario for resolving the overabundance of monopoles and domain walls in the early Universe.

4.5 Conclusion

It is found that D-walls are stable for a wide range of coupling parameters and under perturbations imposed on the wall. Our numerical study supports earlier work by Carroll and Trodden (1998) suggesting that D-walls are stable defects. However, these stable D-walls would eventually dominate the energy density of the Universe, and would appear to be ruled out on the basis of observation. When two walls are connected by a string they are pulled toward each other, and in this case the string unwinds, annihilates and nucleates a hole in the walls. The hole expands outward at almost the speed of light and annihilate the walls. A network of such D-walls will quickly annihilate, rapidly diluting the energy density of the network, thereby obviating a domain wall dominated Universe.

A D-wall may also be invoked to resolve the monopole problem in the early Universe. As the walls are pulled together, monopoles located between the walls collide with the walls, unwind and annihilate. The walls subsequently collide and annihilate (after removing the monopoles), thereby providing a mechanism for avoiding both domain walls and monopoles in the early Universe.

Chapter 5

Monopoles and Strings in $\mathcal{R}^{3+1}$ and $\mathcal{R}^{4+1}$ Spacetime

5.1 Introduction

Grand Unified theories (GUTs) that exhibit $G \to U(1) \times H$ symmetry breaking predict the formation of large numbers of monopoles in the early Universe (Zeldovich and Khlopov 1978 and Preskill 1979). In the present epoch the predicted monopole number density is estimated to be $\sim 10^{-19}$ cm^{-3}, which is incompatible with the upper limit of $\sim 10^{-30}$ cm^{-3} inferred from magnetic monopole fluxes on Earth, and proton decay processes in the Sun (Zeldovich and Khlopov 1978, Preskill 1979, Kolb *et al.* 1982, Dimopoulos *et al.* 1982, Freese *et al.* 1983 and Dvali *et al.* 1998). This large discrepancy presents a problem for a GUT model that predicts the formation of monopoles. The monopole problem was examined briefly in Chapter 4 in the context of hybrid (Dirichlet) topological defects. In this chapter we examine the monopole problem in higher dimensional spacetime.

It is speculated that the Universe may have dimensions greater than the observed three spatial dimensions. In 1921 Kaluza showed that Einstein's theory of gravitation and Maxwell's theory of electromagnetism can be formulated within a unified framework by utilizing an extra dimension[1] (see e.g., Appelquist *et al.* 1987). Kaluza theory assumes that the extra dimension does not affect the physical processes in the known $(3 + 1)$-dimensional spacetime. Klein proposed that this extra dimension is compactified, i.e., curled up and small compared to the observed three spatial dimensions (see e.g., Overduin and Wesson 1997). Experimental observations (such as high-energy particle experiments) constrain the upper limit on the size of the Kaluza-Klein compactified dimension to be $\sim 10^{-18}$ m (Kostelecký and Samuel 1991). The successful construction of gauge invariant field theories of the electromagnetic and weak nuclear forces has provided the impetus to formulate a "theory of everything" that unifies the fundamental forces. Candidates for the "theory of everything" include superstring theory and M-theory, formulated in $9 + 1$

[1] Einstein's field equations in $3 + 1$ dimensions (i.e., ${}^4G_{\mu\nu} = {}^4T^{EM}_{\mu\nu}$) and Maxwell's equations can be derived from the vacuum equations in $(4 + 1)$-dimensional spacetime, i.e., ${}^5G_{\mu\nu} = 0$.

and $10+1$ dimensions, respectively (see e.g., Kaku 1999). These theories[2] are currently in early stages of development. In the absence of a "theory of everything" we consider a simple model of monopoles in $(4+1)$-dimensional spacetime.

According to the homotopy classification of topological defects (see Sec. 1.4), a monopole in $\mathcal{R}^{4+1}$ is a one-dimensional object and may exhibit string-like behaviour. It is known that a string network in $\mathcal{R}^{3+1}$ does not dominate the energy density of the Universe (Albrecht and Turok 1989, Allen and Shellard 1990 and Bennett and Bouchet 1990). The evolution of strings in $\mathcal{R}^{4+1}$ may provide insight into the monopole problem. In this chapter we discuss the evolution of monopoles in uncompactified and compactified $\mathcal{R}^{4+1}$ spacetime. The results are then generalized to topological defects in $\mathcal{R}^{d+1}$ spacetime, with $d-3$ compactified dimensions.

5.2 Monopole topological defects

5.2.1 Monopoles in $\mathcal{R}^{3+1}$ spacetime

The simplest monopole is the 't Hooft-Polyakov monopole ('t Hooft 1974 and Polyakov 1974), where the gauge field configuration possesses an $SO(3)$ symmetry with the Higgs field having a triplet representation, $\Phi = (\Phi_1, \Phi_2, \Phi_3)$. The 't Hooft-Polyakov monopole is described by the Lagrangian

$$\mathcal{L} = \frac{1}{2}\mathcal{D}_\mu\Phi_a\mathcal{D}^\mu\Phi_a - \frac{1}{4}F^a_{\mu\nu}F^{a\mu\nu} - \frac{\lambda}{4}(\Phi_a\Phi_a - \eta^2)^2, \quad (a=1,2,3), \tag{5.1}$$

where $\mathcal{D}_\mu$ denotes the non-abelian covariant derivative defined by

$$\mathcal{D}_\mu\Phi_a = \partial_\mu\Phi_a - e\epsilon_{abc}A^b_\mu\Phi_c, \quad (a,b,c=1,2,3), \tag{5.2}$$

and $F^a_{\mu\nu}$ is the Yang-Mills field strength

$$F^a_{\mu\nu} = \partial_\mu A^a_\nu - \partial_\nu A^a_\mu + 2e\epsilon_{abc}A^b_\mu A^c_\nu, \tag{5.3}$$

in which A^a_μ is the a-th component of the gauge field, and ϵ_{abc} is the Levi-Civita completely skew-symmetric tensor. The equations of motion follow from the Lagrangian (5.1), i.e.,

$$\mathcal{D}_\mu\mathcal{D}^\mu\Phi_a + \lambda\Phi_a\left(\Phi_b\Phi_b - \eta^2\right) = 0, \tag{5.4}$$

$$\partial_\mu F^{a\mu\nu} - 2e\epsilon_{abc}A^b_\nu F^{c\mu\nu} + 2e\epsilon_{abc}\Phi_b\mathcal{D}_\mu\Phi_c = 0. \tag{5.5}$$

[2] An alternative theory referred to as loop quantum gravity attempts a synthesis of general relativity and quantum mechanics without purporting to unify the forces of nature (see e.g., Smolin 2003).

In the absence of a gauge field the Lagrangian (5.1) describes a global model, in which monopoles exhibit long-range interactions.[3] The field equation describing global monopoles is

$$\Box\Phi_a + \lambda\Phi_a(\Phi_1^2 + \Phi_2^2 + \Phi_3^2 - \eta^2) = 0. \tag{5.6}$$

This comprises three equations, one for each field component Φ_a ($a = 1,2,3$). It can be shown that (Polyakov 1974)

$$\Phi_a = \frac{x_a}{r}u(r) \tag{5.7}$$

is the static monopole solution to the field equation (5.6), where $u(r)$ is a radial real scalar field. Substituting Eq. (5.7) into the static solution to Eq. (5.6) gives (for each component of the Higgs field):

$$\nabla^2 u + 2\left(\frac{1}{x} - \frac{x}{r^2}\right)\frac{\partial u}{\partial x} - \frac{2y}{r^2}\frac{\partial u}{\partial y} - \frac{2z}{r^2}\frac{\partial u}{\partial z} - \frac{2}{r^2}u - \lambda u(u^2 - \eta^2) = 0, \tag{5.8}$$

$$\nabla^2 u - \frac{2x}{r^2}\frac{\partial u}{\partial x} + 2\left(\frac{1}{y} - \frac{y}{r^2}\right)\frac{\partial u}{\partial y} - \frac{2z}{r^2}\frac{\partial u}{\partial z} - \frac{2}{r^2}u - \lambda u(u^2 - \eta^2) = 0, \tag{5.9}$$

$$\nabla^2 u - \frac{2x}{r^2}\frac{\partial u}{\partial x} - \frac{2y}{r^2}\frac{\partial u}{\partial y} + 2\left(\frac{1}{z} - \frac{z}{r^2}\right)\frac{\partial u}{\partial z} - \frac{2}{r^2}u - \lambda u(u^2 - \eta^2) = 0. \tag{5.10}$$

These equations are re-written in spherical coordinates as

$$u'' + \frac{2}{r}u' + \left(\lambda\eta^2 - \frac{2}{r^2}\right)u - \lambda u^3 = 0, \tag{5.11}$$

where a dash denotes a derivative with respect to the radial coordinate. Since u is only a function of r, the Higgs field of a monopole "points" along the radial direction and describes a "hedgehog" with spherically symmetric uniform phase winding. The magnitude of the Higgs field vanishes at the origin and approaches η at spatial infinity.

In the presence of a gauge field the static solutions to the field equations (5.4) and (5.5) are ('t Hooft 1974)

$$\Phi_a(x) = \frac{x_a}{r}u(r), \tag{5.12}$$

$$A_\mu^a(x) = \epsilon_{\mu ab}x_b\left(a(r) - \frac{1}{er^2}\right), \tag{5.13}$$

where $a(r)$ is a real, radially dependent scalar field.[4] The real scalar fields $u(r)$ and $a(r)$ satisfy the equations (Polyakov 1975)

$$u'' + \frac{2}{r}u' + \left(\lambda\eta^2 - 2e^2a^2\right)u - \lambda u^3 = 0, \tag{5.14}$$

$$a'' + \frac{4}{r}a' - \frac{3}{r^2}a - e^2r^2a^3 - e^2u^2a = 0. \tag{5.15}$$

[3]The distinction between local and global models was discussed in Sec. 1.2.

[4]Here we utilize the convention $\epsilon_{4ab} = 0$.

These equations are non-linear and have no known analytic solutions, however, the asymptotic and near field solutions give useful insight into the behaviour of the scalar fields. The magnitude of the vacuum expectation value of the Higgs field is η at spatial infinity, hence Eq. (5.14) implies that $a(r \to \infty) = 0$; at the origin $A^a_\mu = 0$, therefore $a(r \to 0) = 1/er^2$.

To explore monopole formation we perform numerical simulations based on the Kibble mechanism. The simulations use the equations of motion (5.4) and (5.5), recast in dimensionless form with the following transformations:

$$\Phi \to \eta\Phi, \tag{5.16}$$

$$A^a_\mu \to \eta A^a_\mu, \tag{5.17}$$

$$x_\mu \to (e\eta)^{-1}\, x_\mu. \tag{5.18}$$

Consequently the equations of motion (5.4) and (5.5) depend only on one coupling parameter, $\alpha = \lambda/e^2$. For simplicity we assume that the self-coupling of the Higgs field is identical to its coupling to the gauge field, i.e., $\alpha = 1$. With this assumption the coordinates are measured in units of the Compton length $(1/\sqrt{\lambda}\eta)$ and the energy density in units of $\lambda\eta^4$. The initial condition is constructed by assigning a random value (between -1 and 1) to Φ_a at each grid point, with the magnitude of the vacuum expectation value constrained to unity, i.e., $\Phi_1^2 + \Phi_2^2 + \Phi_3^2 = 1$. A gauge field arises naturally via a local gauge transformation, for simplicity we set the initial value of the gauge field to zero (see e.g., Moore *et al.* 2001). Because the Higgs field is assigned a random value, there will be fluctuations in the Higgs and gauge fields as they evolve. These fluctuations do not decay, and since energy is conserved we add a damping term, $b\partial\Phi_a/\partial t$, to the evolution equation for the Φ_a-field. Similarly a term, $b\partial A^a_\mu/\partial t$, is added to the evolution equation for the A^a_μ-field. Here b denotes a constant, whose value is chosen to ensure that fluctuations in the fields are significantly damped during the simulation. For $b \ll 10\Delta t$ (where Δt is the time step) it is impossible to distinguish between monopoles and noise, however, for $b \gg 10\Delta t$ the Higgs and gauge fields are heavily damped and monopoles do not have time to form over the duration of the simulation. For expedience we set $b = 10\Delta t$, with spatial step $\Delta h = 0.5$ and time step $\Delta t = 0.1$; $\Delta t < \Delta h$ ensures the stability of the numerical integration scheme.[5] The duration and size of the simulations are such that noise from the boundary does not have time to propagate into the visualization frame (see Sec. 3.4).

[5]See Appendix A for a discussion of numerical techniques, including an analysis of the stability criterion.

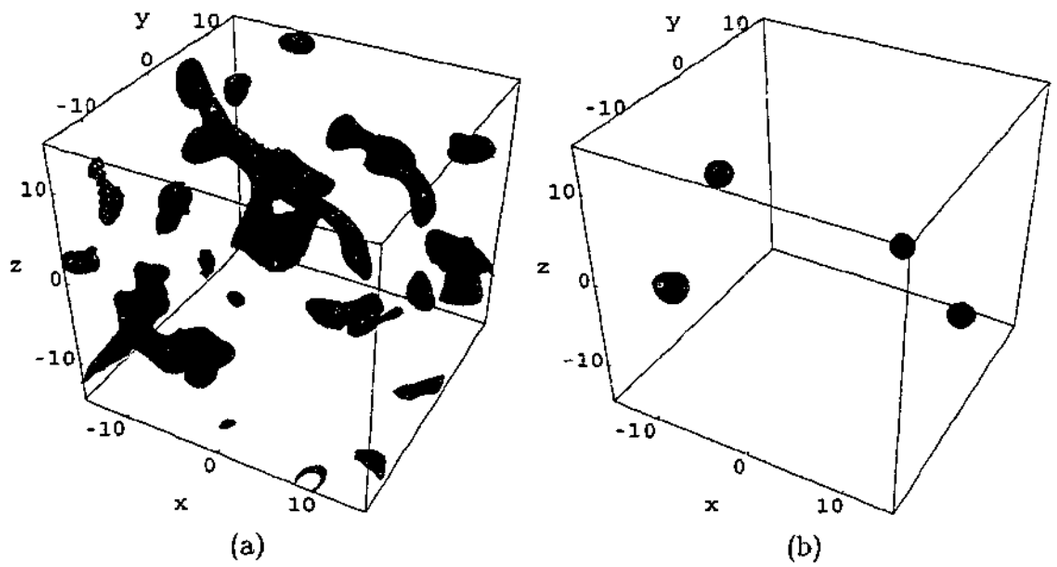

Figure 5.1: Isocontour plots of the energy density ($E/\lambda\eta^4 = 0.5$) for a typical simulation in $\mathcal{R}^{3+1}$. (a) Formation of monopoles (at $t = 10$) via the Kibble mechanism, and (b) monopoles at $t = 50$.

The results are displayed using contour plots of the energy density (in units of $\lambda\eta^4$)

$$E = \frac{1}{2}\left|\left(\partial_\mu\Phi_a - \epsilon_{abc}A^b_\mu\Phi_c\right)\left(\partial^\mu\Phi_a - \epsilon_{abc}A^\mu_b\Phi_c\right)\right| + \frac{1}{4}F^a_{\mu\nu}F^a_{\mu\nu} + \frac{1}{4}\left(\Phi_a\Phi_a - 1\right)^2, \quad (5.19)$$

where $(a = 1, 2, 3)$. Figure 5.1 displays contour plots of the energy density ($E/\lambda\eta^4 = 0.5$) obtained in a typical simulation. Figure 5.1 (a) shows the formation of monopoles as a consequence of the Kibble mechanism. In Fig. 5.1 (b) monopoles are seen as localized objects. At a spatial scale much larger than the Compton length of the Higgs field monopoles are point-like objects.

Immediately following their formation, monopoles were strongly scattered by the surrounding plasma.[6] This is expected to have a damping (frictional) effect on the motion of monopoles. As the Universe evolves, the random velocity of monopoles and anti-monopoles decreases due to interactions with the surrounding plasma, allowing monopoles to be captured by anti-monopoles (or vice versa). This is known as the diffusive capture mechanism (Zeldovich and Khlopov 1978 and Preskill 1979), and is effective as long as the mean free path $l_M = m\gamma/T^{3/2}$ (where m is the mass of a monopole, γ is a damping constant and T

[6]Before the quark-hadron phase transition ($t \sim 10^{-6}$ s) the Universe was filled with a quark-gluon plasma. 't Hooft-Polyakov monopoles possess a gauge field and are strongly scattered by quarks.

is the absolute temperature) of the monopoles and anti-monopoles is less than the capture radius $r_c \sim g^2/T$ (where g is the magnetic charge). A monopole-antimonopole pair forms a bound state before eventually annihilating. As the Universe expanded, its temperature decreased; at $t \sim 10^{-5}$ s after the Big Bang the mean free path was larger than the capture radius, and monopole-anti-monopole annihilation ceased (Zeldovich and Khlopov 1978).

Without an efficient energy loss mechanism the evolution of monopoles is quite different from a string network. 't Hooft-Polyakov monopoles (which possess a gauge field) exhibit short-range interactions (see Sec. 1.2.3). At large spatial separations they are very weakly interacting and their point-like structure suggests that they rarely collide with each other. In the present epoch the monopole number density is estimated to be $\sim 10^{-19}$ cm^{-3}. This is many orders of magnitude greater than observational upper limits (10^{-30} cm^{-3}) inferred from cosmic monopole fluxes and cosmic magnetic fields (see e.g., Zeldovich and Khlopov 1978). Similar constraints on the monopole number density are set by the rate of proton decay in stars (Kolb *et al.* 1982, Dimopoulos *et al.* 1982 and Freese *et al.* 1983). This large discrepancy presents a problem for GUTs that predict the formation of large numbers of monopoles in the early Universe.

There are at least four known solutions to the monopole problem. One solution invokes the Langacker-Pi mechanism (Langacker and Pi 1980) (see also Secs. 4.3 and 4.4). This is based on the Georgi-Glashow $SU(5)$ model (Georgi and Glashow 1974) of symmetry breaking

$$SU(5) \rightarrow SU(3) \times SU(2) \times U(1) \rightarrow SU(3) \times U(1), \tag{5.20}$$

where the first phase transition produces strings and the second produces monopoles. This scenario presents two possibilities - one in which the phase transition that led to the formation of monopoles occurs very late so that there is no monopole problem. The second possibility is that monopoles and anti-monopoles are connected by strings, which draw the pair together leading to their annihilation, thereby avoiding the problem. A second solution to the monopole problem is the inflationary scenario (see Sec. 4.2.3), where the monopole number density is diluted due to exponential expansion of the early Universe. A third solution to the monopole problem relies on GUTs that avoid symmetry restoration at high temperature (Salomonson *et al.* 1985 and Dvali *et al.* 1995). This approach is predicated on the assumption that there was no GUT phase transition in the early Universe, and therefore monopoles (or anti-monopoles) never formed. Finally, a

fourth solution to the monopole problem relies on the symmetry breaking phase transition (Dvali *et al.* 1998)

$$SU(5) \times Z_2 \rightarrow [SU(3) \times SU(2) \times U(1)]/Z_6, \tag{5.21}$$

which leads to the formation of monopoles and Z_2 domain walls (hybrid defects). When the wall moves, monopoles scatter off the wall and are annihilated. Therefore monopoles created in this GUT phase transition are "swept away" by domain walls (see Sec. 4.4).

The Langacker-Pi mechanism requires a series of GUT symmetry breaking phase transitions that have to be fine tuned. Consequently this mechanism is not favored to resolve the monopole problem. Symmetry non-restoration in the early Universe is also unappealing, since condensed matter systems provide compelling evidence for symmetry restoration at high temperatures (see e.g., Kirzhnits 1972, Kirzhnits and Linde 1972 and Dolan and Jackiw 1974). Further, if there were no symmetry breaking phase transitions in the early Universe it is not clear how the fundamental forces became distinguishable. A symmetry breaking phase transition that leads to the simultaneous formation of walls and monopoles may resolve the monopole problem, however, this model also has to be fine tuned to "sweep" away monopoles. In any case domain walls have problems of their own, inducing temperature anisotropy in the CMBR that is inconsistent with observations (see Chapter 4 for a detailed discussion of domain walls). Currently, inflation is considered the most satisfactory solution to the monopole problem. However, recent speculation that the Universe may have higher dimensions leads us to investigate an alternative solution to the monopole problem in $\mathcal{R}^{4+1}$ spacetime.

5.2.2 Monopoles in $\mathcal{R}^{4+1}$ spacetime

A topological defect is constructed from a non-trivial mapping between the vacuum manifold, $\mathcal{M}$, and an n-surface, S^n, embedded in d-dimensional physical space. A p-dimensional defect in $\mathcal{R}^{d+1}$ is given by the non-trivial homotopy group

$$\pi_{n=d-p-1}(\mathcal{M}) \neq 0. \tag{5.22}$$

A monopole forms when the vacuum manifold has a non-trivial second homotopy group, $\pi_2(\mathcal{M}) \neq I$. In $\mathcal{R}^{3+1}$, the 2-surface encloses a point and the monopole is a zero dimensional object (i.e., $p = d-n-1 = 0$). However, in $\mathcal{R}^{4+1}$ spacetime, the 2-surface does not enclose a point. For S^2 to be non-contractable, the monopole must form a closed loop or an infinitely

long one-dimensional object (see Sec. 1.4). Therefore a monopole in $\mathcal{R}^{4+1}$ is a "string" (i.e., $p = d - n - 1 = 1$). Since monopoles in $\mathcal{R}^{4+1}$ are one-dimensional objects, they may be expected to exhibit string-like behaviour. To investigate the evolution of monopoles in $\mathcal{R}^{4+1}$ spacetime, it is necessary to carry out numerical simulations of a string network in $4+1$ dimensions. We begin by examining the simpler case of strings in $\mathcal{R}^{3+1}$ spacetime.

5.3 Abelian cosmic strings

5.3.1 The abelian-Higgs model

Abelian cosmic strings are the simplest gauge strings. They are described by the abelian-Higgs model, which exhibits local $U(1) \rightarrow I$ symmetry breaking (see Sec. 1.2). The Lagrangian for the abelian-Higgs model is

$$\mathcal{L} = \overline{D_\mu \Phi} D^\mu \Phi - \frac{1}{4} F_{\mu\nu} F^{\mu\nu} - \frac{\lambda}{4} \left(|\Phi|^2 - \eta^2 \right)^2 , \tag{5.23}$$

where Φ is a complex $U(1)$ Higgs field, D_μ and $F_{\mu\nu}$ are the gauge covariant derivative and electromagnetic field tensor, respectively. These are defined in terms of the $U(1)$ gauge field, A_μ:

$$D_\mu = \partial_\mu - ieA_\mu \tag{5.24}$$

$$F_{\mu\nu} = \partial_\mu A_\nu - \partial_\nu A_\mu . \tag{5.25}$$

There are three important parameters in the model; namely, two coupling parameters λ and e, and the symmetry breaking scale, η. The number of parameters can be reduced using the transformations:

$$\Phi \rightarrow \eta \Phi , \tag{5.26}$$

$$A_\mu \rightarrow \eta A_\mu , \tag{5.27}$$

$$x_\mu \rightarrow (e\eta)^{-1} x_\mu . \tag{5.28}$$

The equations of motion, derived from the Lagrangian (5.23), are given by

$$(\partial_\mu - iA_\mu)(\partial^\mu - iA^\mu)\Phi + \alpha\Phi \left(|\Phi|^2 - 1 \right) = 0, \tag{5.29}$$

$$\Box A_\mu - 2Im \left[\bar{\Phi} (\partial_\mu - iA_\mu) \Phi \right] = 0, \tag{5.30}$$

where $\alpha = \lambda / 2e^2$.

Interactions between topological defects are mediated by exchanging Goldstone bosons. In the absence of a gauge field, Goldstone bosons are massless, and the interactions are long-range. When the gauge field is introduced however, the Goldstone boson becomes massive and the interactions are short-range (see Sec. 1.2). The type of interaction depends on the value of α. In the abelian-Higgs model, interactions are classified as type I for $\alpha < 1$ (attractive interaction), type II for $\alpha > 1$ (repulsive interaction), and critically coupled for $\alpha = 1$ (no long-range interaction).

Topological defects can be studied by numerically solving Eqs. (5.29) and (5.30). We utilize a second-order leapfrog finite difference scheme (see Appendix A), with initial conditions obtained by numerically solving for the static vortex in cylindrical coordinates (see Sec. 2.3).

5.3.2 Static vortex solution

To obtain the static vortex solution we consider a string located at $r = \sqrt{x^2 + y^2} = 0$, oriented in the z direction. For this orientation there is no variation of the gauge field, $A_\mu(r)$, in the z direction (i.e., $A_z = 0$). A static string has the following ansatzen for the Higgs and gauge fields (Nielsen and Olesen 1973):

$$\phi(r) = f(r)e^{-i\theta(r)}, \tag{5.31}$$

$$\mathbf{a}(r) = \frac{\hat{\mathbf{e}}_r \times \hat{\mathbf{e}}_z}{r} b(r), \tag{5.32}$$

where $\hat{\mathbf{e}}_r$ is a unit radial vector, $\hat{\mathbf{e}}_z$ is a unit vector in the z direction, $b(r)$ is a real scalar field, and $\mathbf{a}(r)$ is a 2-vector gauge field with components a_x and a_y. For a vortex located at the origin, the phase of the Higgs field is given by

$$\theta(x, y) = \tan^{-1}\left(\frac{y}{x}\right). \tag{5.33}$$

In component form the gauge fields are

$$a_x(x, y) = -\frac{y}{r^2} b(r), \tag{5.34}$$

$$a_y(x, y) = \frac{x}{r^2} b(r). \tag{5.35}$$

Using Eqs. (5.31) and (5.32), the time-independent equations for the abelian-Higgs model are written as (in cylindrical coordinates):

$$f''(r) + \frac{1}{r} f'(r) - \frac{f(r)}{r^2} \left(b(r) - 1\right)^2 - \alpha f(r) \left(f^2(r) - 1\right) = 0, \tag{5.36}$$

$$b''(r) - \frac{1}{r} b'(r) - 2f^2(r) \left(b(r) - 1\right) = 0, \tag{5.37}$$

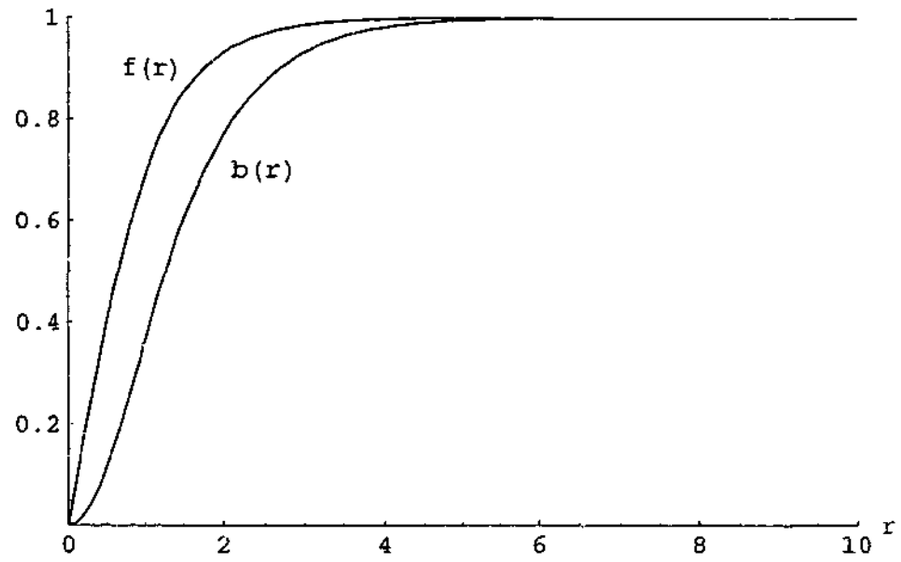

Figure 5.2: Magnitude of the Higgs field, $f(r)$, and gauge field, $b(r)$, for a critically coupled vortex ($\alpha = 1$) in the abelian-Higgs model.

where a dash denotes differentiation with respect to the radial coordinate. The numerical solutions to Eqs. (5.36) and (5.37) are obtained using a fixed point method (see Sec. 2.3). This involves guessing the magnitude of the scalar field and gauge field, and then employing a finite difference scheme to iterate the fields. To determine the magnitude of the fields requires knowledge of their "boundary" behaviour. Equations (5.36) and (5.37) require $f(r \to \infty) = b(r \to \infty) = 1$. At the center ($r = 0$) of the vortex the vacuum state is symmetric, and $f(0) = b(0) = 0$. We adopt $f(r \neq 0) = b(r \neq 0) = 1$ and $f(0) = b(0) = 0$ as an initial guess. The solution for a critically coupled vortex ($\alpha = 1$) is plotted in Fig. 5.2. This shows that both $f(r)$ and $b(r)$ increase quickly as we move out from the origin. The gradient of the Higgs field, $f'(r)$, does not vanish at the origin, unlike $b'(r)$.

Once the static solutions for $f(r)$ and $b(r)$ are obtained, the ϕ- and a-fields are constructed from the Nielsen-Olesen vortex solutions (5.31) and (5.32). String dynamics requires us to superpose multiple vortex-lines (i.e., strings). This is achieved by employing the Abrikosov ansatz (Abrikosov 1957):

$$\Phi(\mathbf{r}) = \prod_i \phi(\mathbf{r} - \mathbf{r}_i), \tag{5.38}$$

$$A_\mu(\mathbf{r}) = \sum_i a_\mu(\mathbf{r} - \mathbf{r}_i), \tag{5.39}$$

where $\mathbf{r}_i$ denotes the displacement vector of the i-th vortex and $|\mathbf{r}| = \sqrt{x^2 + y^2 + z^2}$.

5.3.3 String interactions

There are two important string interactions: string intercommutation (where two strings exchange ends when they intersect) and loop collapse (where a string loop shrinks to a point under string tension and annihilates). These string interactions provide an effective energy loss mechanism for a string network (see Sec. 5.4.2).

Numerical simulations of intercommutation and loop collapse are shown in Figs. 5.3 and 5.4. In these figures strings are represented using isocontour plots of the energy density. In units of $\eta^4\lambda/2$ the energy density is given by ($\alpha = 1$),

$$E = |(\partial_\mu + iA_\mu)\tilde{\Phi}(\partial^\mu - iA^\mu)\Phi| + \frac{1}{4}F_{\mu\nu}F^{\mu\nu} + \frac{1}{2}\left(|\Phi|^2 - 1\right)^2. \tag{5.40}$$

For the purpose of visualization we have set $E = 1$ in these figures. Figure 5.3 shows two strings moving toward each other in the x direction. When the two strings intersect they exchange ends (intercommute). Intercommutation occurs as a consequence of orthogonal vortex scattering in the x-y plane ($z = 0$) (see e.g., Vilenkin and Shellard 1994).

Following self-intersection of a long string, intercommutation allows a loop to break off from the string. The dynamics of a loop are governed by string tension along the loop, which is determined by the energy density of the string (Vilenkin 1981). String tension guarantees that a loop will collapse (see Fig. 5.4). To understand loop annihilation, consider the phase winding at opposite points on a loop (see e.g., Fig. 5.4 (a)). The orientation of a plane through a loop containing the z-axis is specified by $\hat{\mathbf{e}}_z \times (x\hat{\mathbf{e}}_x + y\hat{\mathbf{e}}_y)$. Diametrically opposite points on the loop have opposite phase winding, and constitute a vortex-anti-vortex pair. Once the loop collapses to a point, the phase unwinds and the loop annihilates. After annihilation, energy is radiated away in the form of vector bosons and Higgs particles (see e.g., Vilenkin and Shellard 1994). For a string network in an expanding Universe, loop collapse provides the network with an important energy loss mechanism, which works in concert with intercommutation to prevent cosmic stings from dominating the energy of the Universe (Albrecht and Turok 1989, Allen and Shellard 1990 and Bennett and Bouchet 1990). In the following section we discuss string network evolution in more detail.

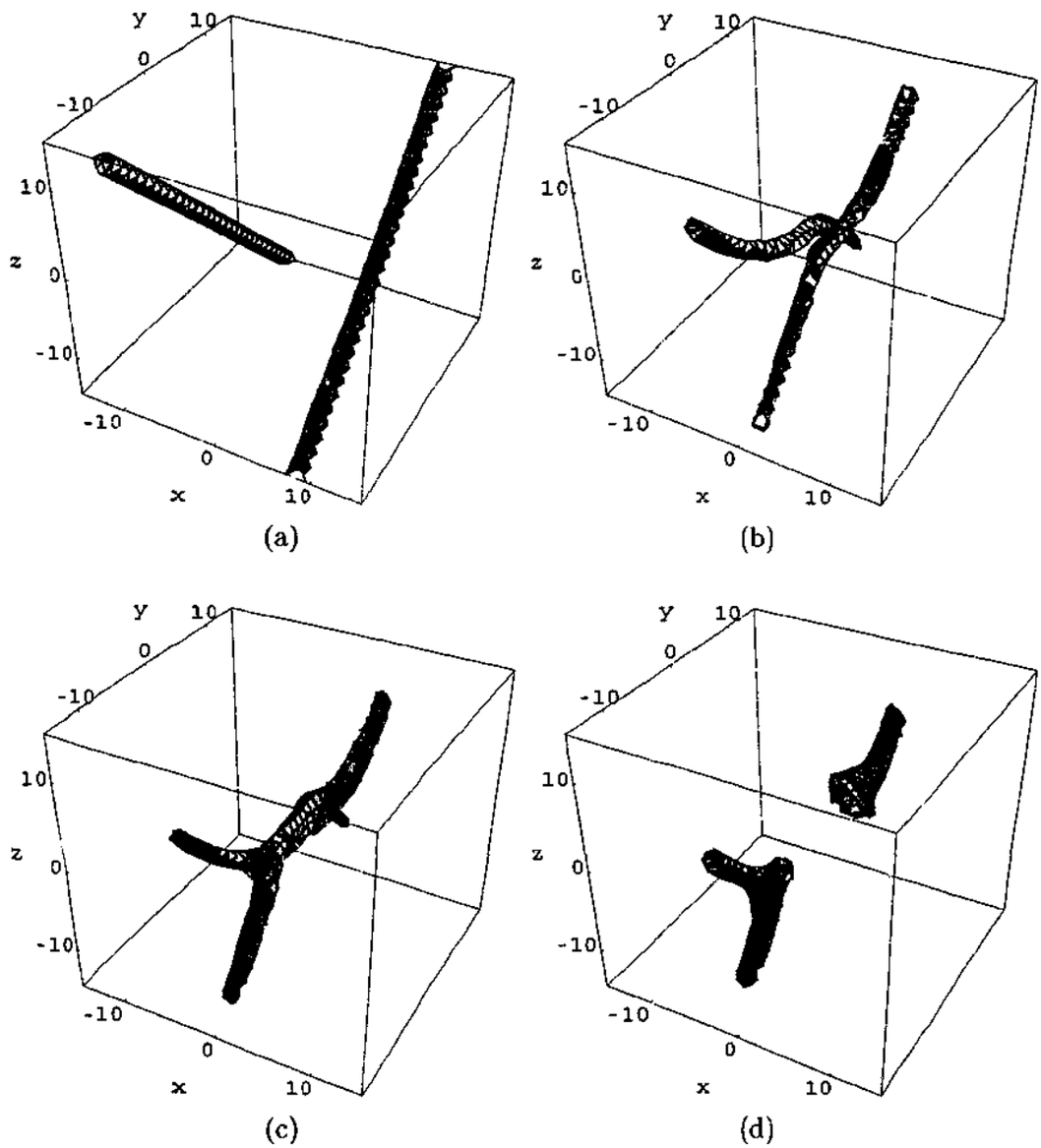

Figure 5.3: Isocontour plots of the energy density ($E = 1$) of two critically coupled strings ($\alpha = 1$) showing string intercommutation. The initial velocity $v_0 = 0.5$ ($c = 1$). The strings are shown at: (a) $t = 0$, (b) $t = 12.5$, (c) $t = 15$, and (d) $t = 17.5$. In (a) and (b) the strings are moving toward each other, whereas (c) and (d) show the strings exchanging ends (i.e., intercommutation), and subsequently moving away from each other. Note the formation of kinks after intercommutation that propagate along the strings.

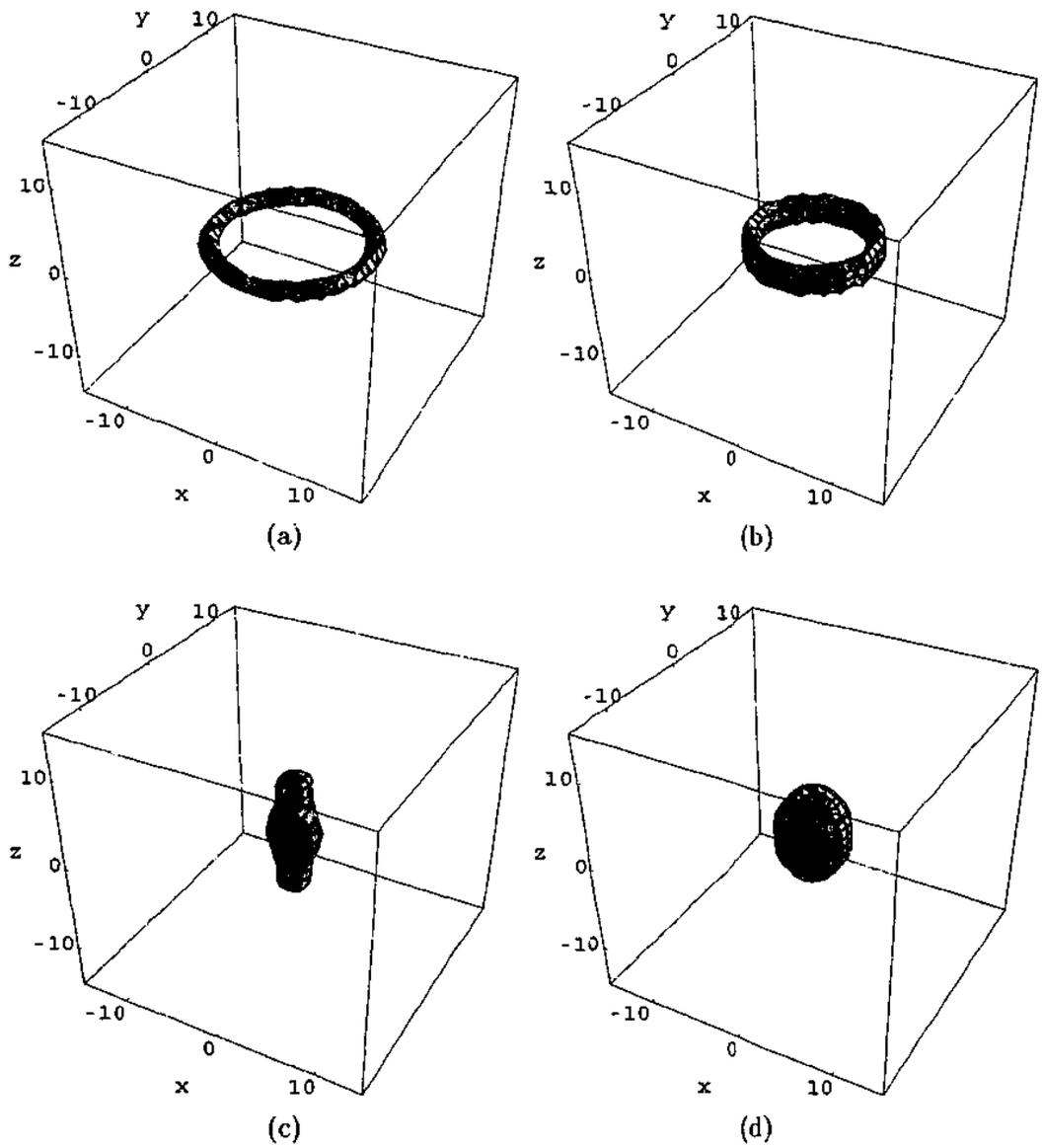

Figure 5.4: Isocontour plots of the energy density ($E = 1$) of a collapsing string loop ($\alpha = 1$). The loop is shown at: (a) $t = 5$, (b) $t = 7.5$, (c) $t = 15$, and (d) $t = 17.5$. Note that in (c) and (d) the loop has collapsed to a point and annihilated. The energy density in (d) appears larger than that in (c), because the collapsed loop radiates energy in the form of Higgs particles and vector bosons.

5.4 Numerical simulations of a string network in $\mathcal{R}^{3+1}$ spacetime

5.4.1 Friedmann equations

The simulation of a string network must account for the expansion of the Universe and the evolution of its energy density. We start with the Friedmann-Robertson-Walker (FRW) metric in a homogeneous isotropic Universe:

$$g_{\mu\nu} = \mathrm{diag}(1, -a^2(t), -a^2(t), -a^2(t)). \tag{5.41}$$

The line element is given by

$$ds^2 = dt^2 - a^2(t)(dx^2 + dy^2 + dz^2), \tag{5.42}$$

where $a(t)$ is the scale factor that dictates the expansion of the Universe. The Einstein field equations for a flat ($k = 0$) spacetime with vanishing cosmological constant ($\Lambda = 0$) are written as

$$G_{\mu\nu} = 8\pi T_{\mu\nu}, \tag{5.43}$$

where $G_{\mu\nu}$ is the Einstein tensor and $T_{\mu\nu}$ is the energy-momentum tensor. For a perfect fluid model of the Universe

$$T_{\mu\nu} = (\rho(t) + p(t))\, u_\mu u_\nu - p(t) g_{\mu\nu}, \tag{5.44}$$

where ρ is the energy density, p is the pressure, and u_μ is the four-velocity of the co-moving fluid, with $u_0 = 1$ and $u_i = 0$. Utilizing the Einstein field equations for a perfect fluid model, we obtain the Friedmann equations

$$3\frac{\dot{a}^2}{a^2} = 8\pi\rho, \tag{5.45}$$

$$\frac{2a\ddot{a} + \dot{a}^2}{a^2} = -8\pi p, \tag{5.46}$$

where a dot denotes differentiation with respect to time. If we assume $a(t) \propto t^n$ (where n is a real number), then $\dot{a}/a = nt^{-1}$, and Eq. (5.45) specifies the evolution of the energy density of the Universe, i.e.,

$$\rho = \frac{3n^2}{8\pi} t^{-2} \propto t^{-2}. \tag{5.47}$$

Equations (5.45) and (5.46) give

$$\dot{\rho} + 3\frac{\dot{a}}{a}(p + \rho) = 0. \tag{5.48}$$

Equation (5.48) governs the evolution of the energy density of the Universe in $\mathcal{R}^{3+1}$ space-time. In the radiation era $p = \frac{1}{3}\rho$, whereas $p = 0$ in the matter era. Using Eqs. (5.47) and (5.48), the scale factor (expansion) of the Universe is $a(t) \propto t^{1/2}$ in the radiation era, and $a(t) \propto t^{2/3}$ in the matter era.

5.4.2 Kibble's scaling model

Numerical simulations allow us to determine how fast the energy density of a string network decreases. Before performing these simulations it is important to understand qualitatively the behaviour of the string network. A scaling model due to Kibble (Kibble 1985) predicts that the decrease in the energy density of long strings in the network is proportional to the decrease in the energy density of the Universe.

Cosmic strings are made up of false vacuum energy and in an expanding Universe the strings are stretched. As a string is stretched, its length increases, however, the energy per unit length remains constant and the total energy of the string increases. It is therefore expected that the energy density of a string network does not dilute as fast as the matter density in the Universe. As we have shown in Sec. 5.3, string dynamics are governed by intercommutation and loop collapse, which decrease the energy density of the string network. To appreciate how the energy density of the network evolves as the Universe expands, consider a string segment of length L in a Hubble volume $V = L^3$. The energy, E, and energy density, $\rho_\infty = E/V$, of the string segment (within V) is given by

$$E = \mu L, \tag{5.49}$$

$$\rho_\infty = \frac{\mu}{L^2}, \tag{5.50}$$

where μ is the mass per unit length of the string. If we assume that at a given time t_0, the string has length L_0, then the expansion of the Universe results in the length of the string increasing according to

$$L = \frac{a(t)}{a(t_0)} L_0, \tag{5.51}$$

where $a(t)/a(t_0)$ is the expansion factor of the Universe relative to time t_0. Using Eqs. (5.49) and (5.51), the evolution of total energy of the long string network is governed by

$$\dot{E} = \frac{\dot{a}}{a} E. \tag{5.52}$$

Equation (5.52) indicates that, unlike the total energy of the Universe, which does not change during expansion, the total energy of long strings increases as the Universe expands.

Without an efficient energy loss mechanism (i.e., intercommutation and loop collapse), the string network will soon come to dominate the energy of the Universe.

Since there is only one string of length L in a volume V, the separation between strings is L. The string is expected to travel a distance L in time Δt before encountering another string, so the number of collisions (or intercommutations) is proportional to $L^{-1}\Delta t$. The number of collisions per volume is $L^{-4}\Delta t$. Every time a long string intersects it loses a segment of length L, and consequently loses energy[7] μL. The total energy loss, ΔE_L, in the time interval Δt (inside the Hubble volume) is

$$\Delta E_L = -\frac{\Delta t}{L^4}\mu L V = -\frac{E}{L}\Delta t. \tag{5.53}$$

In the limit $\Delta t \to 0$, Eq. (5.53) gives the energy loss rate $\dot{E}_L = -E/L$, whence the total energy loss rate becomes

$$\dot{E} = \frac{\dot{a}}{a}E - \frac{E}{L}, \tag{5.54}$$

with energy density

$$\dot{\rho}_\infty = -2\frac{\dot{a}}{a}\rho_\infty - \frac{\rho_\infty}{L}. \tag{5.55}$$

Using Eq. (5.55), and assuming $a(t) \propto t^n$, the evolution equation is

$$\dot{L} = \frac{nL}{t} + \frac{1}{2}. \tag{5.56}$$

Equation (5.56) can be readily solved using a change of variable. Defining $u = L/t$, we obtain the general solution

$$L = c_1 t^n + \frac{t}{2(1-n)}, \tag{5.57}$$

where c_1 is an integration constant. For $n < 1$ (e.g., in the radiation era $n = 1/2$ and in the matter era $n = 2/3$) the linear term in Eq. (5.57) dominates, and the length scale will approach the linear regime over large time scales. Using only the linear term, the long string energy density is

$$\rho_\infty \sim 4(1-n)^2\frac{\mu}{t^2}. \tag{5.58}$$

This indicates that the evolution of the energy density of the long string network is proportional to t^{-2}, which is commensurate with the rate at which the energy density of the Universe decreases. This simple scaling argument shows that the energy of the Universe is not dominated by the cosmic string network.

[7]When a string self-intersects, intercommutation results in a loop breaking off from the string. Since loops collapse and annihilate, a long string loses energy every time self-intersection occurs.

Although Eq. (5.58) provides a simple model for the energy density of a string network, we have ignored the subtleties of string dynamics, e.g., the model does not take into account small scale structure of the string.[8] Therefore, the scaling model can only provide a qualitative description of the evolution of a string network. To confirm the scaling behaviour of long strings, it is necessary to carry out detailed numerical simulations.

Numerical simulations of a string network can be performed by utilizing a field theoretic model (e.g., based on the equations of motion (5.29) and (5.30)). However, a full field simulation is inefficient for long term evolution of the string network and very computationally intensive. As the network evolves, the string number density decreases, but a full field simulation uses the same amount of memory regardless of the evolution stage. A more efficient approach is to exploit the Nambu-Goto action, which describes the dynamics of relativistic strings (Goddard *et al.* 1973). This approach is commonly adopted in the literature (see e.g., Albrecht and Turok 1989, Allen and Shellard 1990 and Bennett and Bouchet 1990).

5.4.3 Dynamics of relativistic strings

The Nambu-Goto action for a string is given by

$$\mathcal{S} = -\mu \int dA, \tag{5.59}$$

where A is the area of the world-sheet swept out by the string and μ is the string tension. For simplicity we assume the string network evolves in an isotropic and homogeneous Universe, so that the line element is given by Eq. (5.42). The equations of motion of the string are parameterized by conformal coordinates, defined by

$$d\tau = a^{-1} dt, \tag{5.60}$$

where τ is the conformal time. The line element in conformal coordinates is

$$ds^2 = a^2(\tau)(d\tau^2 - dx^2 - dy^2 - dz^2). \tag{5.61}$$

Variation of the Nambu-Goto action yields the evolution equations of the string

$$\ddot{\mathbf{x}} + 2h(1 - \dot{\mathbf{x}}^2)\dot{\mathbf{x}} = \epsilon^{-1} \left(\frac{\mathbf{x}'}{\epsilon} \right)' \tag{5.62}$$

[8] Small scale structure includes kinks in the string smaller than the horizon (see Fig. 5.3). These small scale structures frequently self-intersect and break off from the string. This results in a significant increase in the intercommutation rate, which may result in the energy density of the string network decreasing faster than predicted by Kibble's scaling model.

$$\dot{\epsilon} = -2h\epsilon\dot{\mathbf{x}}^2 \tag{5.63}$$

$$\epsilon \equiv \left(\frac{\mathbf{x}'^2}{1-\dot{\mathbf{x}}^2}\right)^{1/2}, \tag{5.64}$$

where a dash denotes differentiation with respect to the spatial parameter along the string σ, a dot denotes differentiation with respect to conformal time τ, the 3-vector $\mathbf{x} = \mathbf{x}(\tau, \sigma)$, ϵ is the energy per unit σ, and h is Hubble's constant defined as

$$h = \frac{\dot{a}}{a}. \tag{5.65}$$

The dynamics of the string are described by Eq. (5.62), whereas Eq. (5.63) determines the evolution of the energy density of the string (i.e., the energy per unit σ). In this formalism $d\sigma$ is the separation between points on the string in parameter space σ, rather than the separation, dl, in physical space. There is a simple relationship between the two. If the string segment is stationary ($\dot{\mathbf{x}} = 0$), Eq. (5.64) relates $d\sigma$ to dl, i.e.,

$$\epsilon = \frac{dl}{d\sigma}, \tag{5.66}$$

where $dl = |d\mathbf{x}|$.

Equations (5.62) and (5.63) are non-linear and the evolution of a cosmic string network can only be determined from numerical simulations. In non-expanding (Minkowski) spacetime, Hubble's constant vanishes, and initially we can set dl equal to $d\sigma$, so that $\epsilon = 1$. In the conformal gauge the equations of motion of the string are written in terms of the 3-vector, $\mathbf{x} = \mathbf{x}(t, l)$ (see e.g., Vilenkin and Shellard 1994). These equations have the form

$$\ddot{\mathbf{x}} - \mathbf{x}'' = 0 \tag{5.67}$$

$$\dot{\mathbf{x}} \cdot \mathbf{x}' = 0 \tag{5.68}$$

$$\dot{\mathbf{x}}^2 + \mathbf{x}'^2 = 1. \tag{5.69}$$

The constraint equation (5.68) means that $\dot{\mathbf{x}}$ is always perpendicular to $\mathbf{x}'$, where $\dot{\mathbf{x}}$ is the velocity of the string and $\mathbf{x}'$ is proportional to the tangent vector, $d\mathbf{x}/dl$, along the string,

$$\mathbf{x}' = \frac{d\mathbf{x}}{dl}\frac{dl}{d\sigma}. \tag{5.70}$$

The equation of motion (5.67) shows that the string acceleration is proportional to the local curvature of the string. The direction of $\ddot{\mathbf{x}}$ is such that a curved string tends to

straighten. In doing so it develops a velocity and begins to oscillate. In an expanding Universe these oscillations are damped due a velocity term (see Eq. (5.62)).

We now consider numerical simulations of a string network in expanding spacetime. Although simulations can be performed by discretising Eqs. (5.62) and (5.63) using a leap-frog method, this technique is prone to numerical instabilities. A better approach is to introduce left movers, $\mathbf{l}$, and right movers, $\mathbf{r}$, defined as (Bennett and Bouchet 1990 and Albrecht and Turok 1989)

$$\mathbf{l} = \dot{\mathbf{x}} + \frac{\mathbf{x}'}{\epsilon}, \tag{5.71}$$

$$\mathbf{r} = \dot{\mathbf{x}} - \frac{\mathbf{x}'}{\epsilon}. \tag{5.72}$$

The equations of motion of the string are now written in the form

$$\dot{\mathbf{l}} = h[(\mathbf{l}\cdot\mathbf{r})\mathbf{l} - \mathbf{r}], \tag{5.73}$$

$$\dot{\mathbf{r}} = h[(\mathbf{l}\cdot\mathbf{r})\mathbf{r} - \mathbf{l}], \tag{5.74}$$

$$\dot{\epsilon} = -h\epsilon(\mathbf{l}\cdot\mathbf{r} + \mathbf{1}), \tag{5.75}$$

with the constraint $\mathbf{l}^2 = \mathbf{r}^2 = 1$. Equations (5.73) - (5.75) arise when we evolve the left mover, $\mathbf{l}$, on the characteristic curve $\sigma - \Delta\tau/\epsilon$ (where $\Delta\tau$ is the conformal time step), and the right mover, $\mathbf{r}$, on $\sigma + \Delta\tau/\epsilon$ (see Appendix A). The evolution of the left and right movers on their characteristic curves proceeds according to

$$\mathbf{l}(\sigma - \Delta\tau/\epsilon, \tau + \Delta\tau) = \mathbf{l}(\sigma,\tau) + \Delta\tau\dot{\mathbf{l}}(\sigma,\tau) \tag{5.76}$$

$$\mathbf{r}(\sigma + \Delta\tau/\epsilon, \tau + \Delta\tau) = \mathbf{r}(\sigma,\tau) + \Delta\tau\dot{\mathbf{r}}(\sigma,\tau), \tag{5.77}$$

where $\mathbf{l}$ has moved to the "left" by an amount $\Delta\tau/\epsilon$, and $\mathbf{r}$ has moved to the "right" by an amount $\Delta\tau/\epsilon$.

The initial condition of the Nambu-Goto action is different from the initial condition used in a field theoretic simulation. This is because the Nambu-Goto action describes the string as a structureless one-dimensional object. To generate the initial condition for the Nambu-Goto action we exploit a method proposed by Vachaspati and Vilenkin (1984).

5.4.4 Vachaspati-Vilenkin initial condition

To emulate the Kibble mechanism, the Vachaspati-Vilenkin (VV) method divides space into unit cells whose lattice spacing is equal to the coherence length (i.e., $\xi = 1$). Periodic

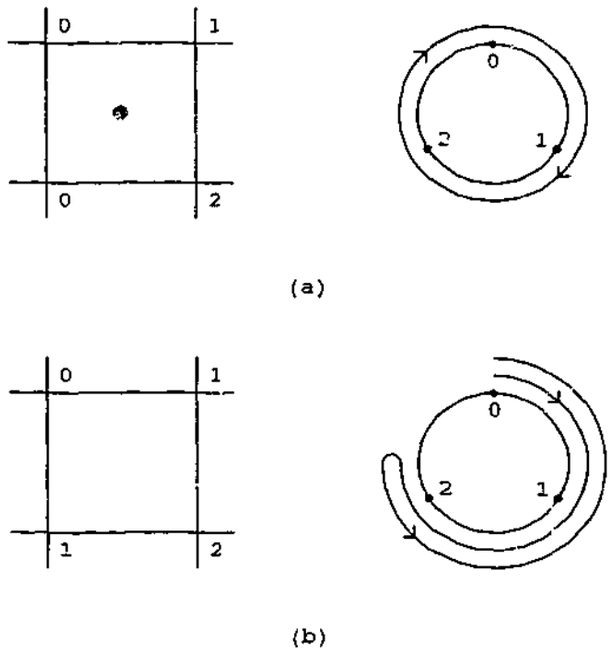

Figure 5.5: As we move around the face of the unit cell in real space (schematic on left), the Higgs field describes a trajectory in phase space (right). (a) A string segment pierces the face if the trajectory has non-trivial phase winding. (b) No string pierces the face if the trajectory has a trivial phase winding (adapted from Vachaspati and Vilenkin 1984).

boundary conditions are assumed. A discrete phase (i.e., 0, $2\pi/3$ or $4\pi/3$) is randomly assigned to each lattice point (unit cell). These phases are denoted by 0, 1 and 2, respectively. We step through the faces of each unit cell and determine whether a string enters the cell. This occurs if any of the six faces of the cell are pierced by a string segment, i.e., if the phase winding on the four edges is non trivial (see Fig. 5.5). Numerical simulations show that the probability that no string enters a cell is 0.23; the probability that one string enters a cell is 0.66, and the probability that two strings enter a cell is 0.11

Figure 5.6 shows a typical Vachaspati-Vilenkin initial condition, with spatial step $\Delta x = 1$. One of the features of the VV initial condition is that, due to connections between unit cells, the network is dominated by 90° kinks.[9] These kink "artifacts" are smoothed by utilizing a suitable interpolation scheme. Figure 5.7 shows the VV initial condition obtained from Fig. 5.6 by applying a cubic spline interpolation. Comparing Fig. 5.7 with

[9]When one face of a unit cell is pierced by a string, the probability that it pierces the opposite face is 1/5, while the probability that it pierces the orthogonal faces is 4/5. The initial string network is dominated by 90° kinks.

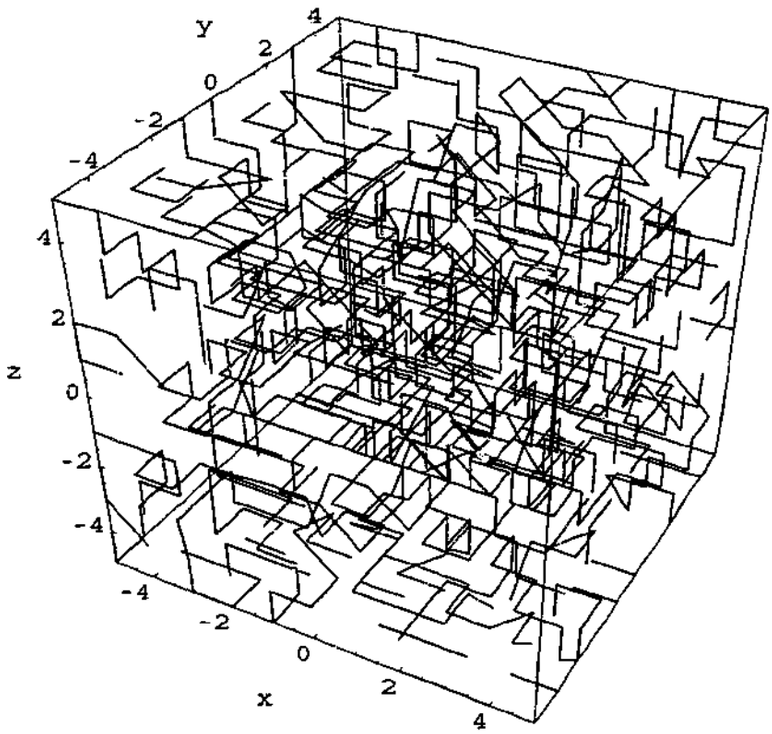

Figure 5.6: Initial condition for a string network generated using the Vachaspati-Vilenkin method. The initial condition resembles a random walk with the network dominated by 90° kinks.

5.6 we see that the kinks are smoothed significantly.

Figure 5.8 shows a logarithmic plot of the string number density versus string length. This shows that, at formation, there are more short strings (loops) than long strings.[10] Since small loops quickly collapse and annihilate (see Sec. 5.3), it is expected that long strings will dominate the evolution of the string network.

5.4.5 String network evolution

To evolve a string network using the Nambu-Goto action, detailed string interactions must be accurately reproduced. This is achieved by manually implementing string intercommutation and removing loops when they collapse. The evolution of Nambu-Goto loops is different from abelian cosmic string loops (see Fig. 5.4). The former do not annihilate and disappear from the network, but collapse and re-expand in a series of oscillations (see

[10]Strings are classified as long or short (i.e., loops) according to whether they are larger or smaller than the horizon (Hubble distance), which is the inverse of Hubble's constant (see Eq. (5.65)).

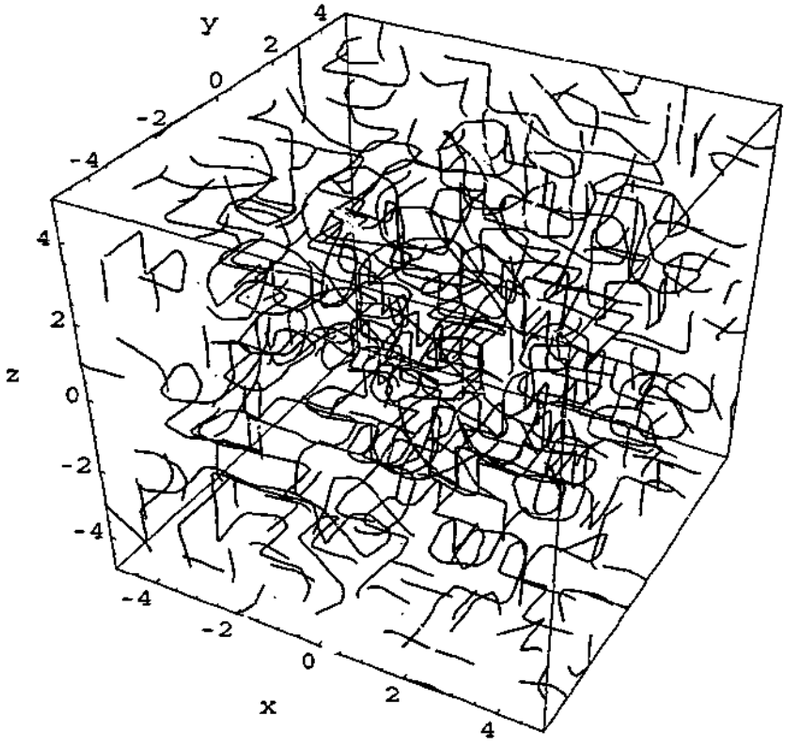

Figure 5.7: The initial condition in Fig. 5.6 after cubic spline interpolation, which smooths the 90° kinks.

e.g., Vilenkin and Shellard 1994). To account for the collapse and annihilation of cosmic string loops, the numerical scheme removes the Nambu-Goto loops when the number of points that are used to represent a loop is less than a cut-off.[11] Numerical simulations show that a loop is not evolved accurately when fewer than 16 points are used (Allen and Shellard 1990); therefore we adopt a minimum of 16 points as the cut-off.

Intercommutation has been implemented by detecting if two string segments cross each other, in which case we exchange ends. To detect string crossings we divide space (i.e., the simulation volume) into cells.[12] A list of all points in a cell is then constructed. Each string segment is checked for crossing with all other segments in the same cell and its 26 nearest-neighbor cells. Two string segments cross each other if the scalar triple product $(\mathbf{a} \times \mathbf{b}) \cdot \mathbf{c}$ changes sign in a given time step (see e.g., Bennett and Bouchet (1990) and

[11] Strings and loops are represented in terms of points. The cut-off here refers to the smallest number of points that make up the loop. Loops are removed from the network when the number of points is smaller than the cut-off.

[12] In order not to miss detecting string crossings when the strings move at relativistic speeds, the cell is chosen to have a size larger than the conformal time step $\Delta\tau$.

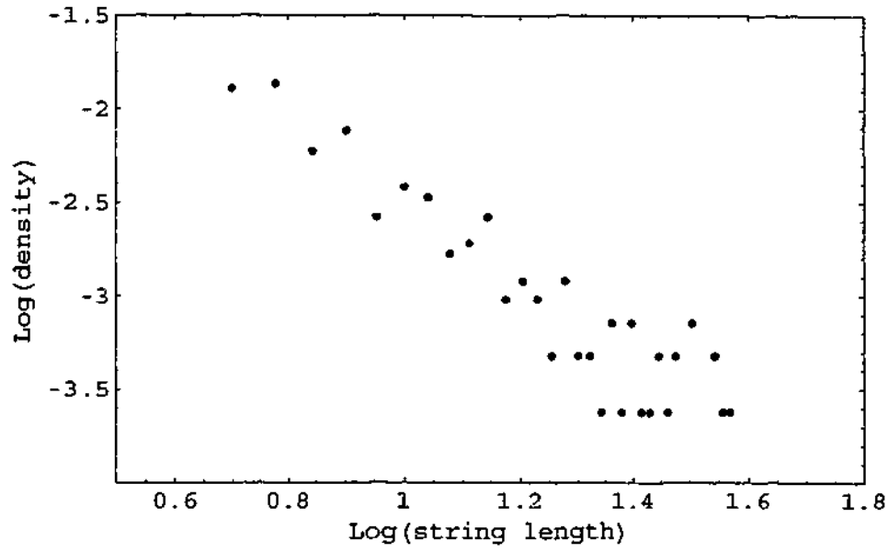

Figure 5.8: Logarithmic plot of string number density versus string length for a typical VV initial condition. As the string length increases, the number density decreases exponentially. Although there is a large number of short strings (loops) compared to the number of long strings, most segments in the network are associated with long strings.

Allen and Shellard 1990); here **a** denotes the separation vector of the two ends of a string segment, **b** is the separation vector of the two ends of the other segment, and **c** is the separation vector from the center of one string segment to the center of the other segment. In addition, Albrecht and Turok (1989) transform one string segment into the Galilean rest frame of the other segment and check if any part of the string segment intersects the world-sheet of the other segment. While these methods are easy to implement in $\mathcal{R}^{3+1}$ spacetime, it is not obvious how to generalize them to $\mathcal{R}^{4+1}$. Since our main aim is to simulate a string network in $4+1$ dimensions, we have chosen to implement an alternative method for detecting string crossings.

This method is illustrated in Fig. 5.9. The points P_0, P_1, P_2, P_3, P_4, and P_5 denote the ends of the string segments at two conformal times (τ_0 and τ_1). Each point is specified by a vector with three components. For example, the vector to point P has components P^x, P^y and P^z. To detect if two string segments, $S1$ and $S2$, cross each other in a conformal time step, we transform $S1$ to the Galilean rest frame of $S2$. In a given conformal time step ($\Delta\tau = \tau_1 - \tau_0$), $S1$ will sweep out a plane and $S2$ will be a line segment (see Fig. 5.9). Crossing of $S1$ and $S2$ occurs if the plane containing $S1$ intersects the line $S2$ (at

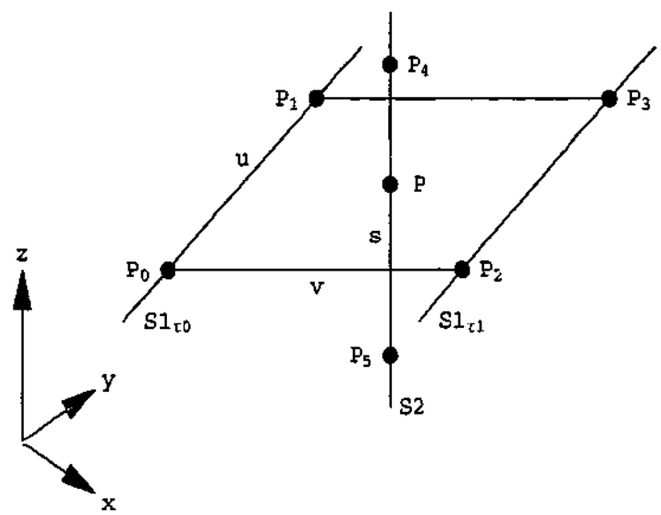

Figure 5.9: Crossing detection method used in the $\mathcal{R}^{3+1}$ simulations. Here $S1_{\tau 0}$ and $S1_{\tau 1}$ are segments of a string at two different conformal times, τ_0 and τ_1. The string segment $S1$ is in the Galilean rest frame of the other string segment (denoted by $S2$). Here u parameterizes the string segment $\overline{P_0P_1}$, while v parameterizes the line segment $\overline{P_0P_2}$, and s parameterizes the string segment $\overline{P_4P_5}$. The string segment $S1$ (in the rest frame of $S2$) sweeps out a plane (world-sheet) that intersects the line segment $S2$ at point P. This point can be found by solving three linear equations as discussed in the text.

a point). The intersection point is anywhere inside the plane containing $S1$ and along the line segment $S2$. The plane containing $S1$ is parameterized by u and v, with any point on the plane determined by $P_0 + u(P_1 - P_0) + v(P_2 - P_0)$, where u and v are real-valued parameters. The line segment $S2$ is parameterized by s, with any point on the line determined by $P_4 + s(P_5 - P_4)$. In general, the intersection point P (see Fig. 5.9), between an infinite plane containing $S1$ and an infinitely long line $S2$, can be obtained from the solution to three linear equations

$$P_0^i + u(P_1^i - P_0^i) + v(P_2^i - P_0^i) = P_4^i + s(P_5^i - P_4^i),\ (i = x, y, z), \tag{5.78}$$

where the two string segments ($S1$ and $S2$) intersect in a given conformal time step if $0 \leq u, v, s < 1$. This method is easily generalized to $\mathcal{R}^{4+1}$ since it only involves solving linear equations.

When two string segments cross, intercommutation is implemented by exchanging the ends of the strings. This is done by redirecting pointers along the string. Following intercommutation, the equations of motion (5.73), (5.74) and (5.75) are no longer satisfied for

the two string segments that have exchanged ends. Numerous methods have been reported in the literature to resolve this problem. For example, Bennett and Bouchet (1990) invoke a numerical diffusion scheme. From Eq. (5.64) we note that the quantity $\dot{\mathbf{x}}^2 + (\mathbf{x}'/\epsilon)^2$ is conserved for any string segment. The numerical diffusion scheme involves smoothing points where $\dot{\mathbf{x}}^2 + (\mathbf{x}'/\epsilon)^2$ is 5% larger than unity. In our numerical simulations, whenever two string segments exchange ends, we re-parameterize the string by recalculating the left and right movers using Eqs. (5.71) and (5.72). The quantities ϵ and $\Delta\sigma$ are preserved, so that the network satisfies the Courant-Friedrichs-Lewy (CFL) condition ($\Delta\tau \leq \epsilon\Delta\sigma$) for long term evolution (see Appendix A). Since $\Delta\tau$ is kept constant throughout the simulation, to satisfy the definition of ϵ in Eq. (5.64) we must modify the velocity of each string segment according to

$$\dot{\mathbf{x}} = \left(1 - \frac{\mathbf{x}'^2}{\epsilon^2}\right)^{1/2} \frac{\dot{\mathbf{x}}_0}{|\dot{\mathbf{x}}_0|}, \tag{5.79}$$

where $\dot{\mathbf{x}}_0$ is the original velocity of the string before intercommutation. The modification of the velocity during intercommutation does not change the velocity distribution of the string network. We have tested our simulation code in both the radiation and matter eras. The scaling solution and root mean squared velocity, $\dot{\mathbf{x}}_{rms}$, of the string network are in good agreement with results based on alternative approaches reported in the literature (see e.g., Bennett and Bouchet 1990, Allen and Shellard 1990 and Albrecht and Turok 1989).

When the VV initial condition is generated, each point along the string is separated from another point by a distance $\Delta l = \xi = 1$. An interpolation scheme is implemented to increase the resolution of each string segment.[13] The initial string number density can be changed by varying the coherence length, ξ, of the string network. For example, the initial condition with $\xi = 0.5$ has a string number density eight times that of $\xi = 1$.[14] Once the initial string network has been obtained, we initialize the left and right movers using Eqs. (5.71) and (5.72). By assuming a stationary initial condition (in which strings in the network are initially at rest), $\Delta\sigma$ can be replaced by Δl by setting $\epsilon = 1$ (see Eq. (5.64)). As the string network evolves, the left and right movers are defined on the

[13]Two points on a string segment (in the VV initial condition) are separated by a distance $\Delta l = 1$. To increase the resolution to $\Delta l = 0.1$, nine more points are added in-between the original points. The positions of the new points are obtained by a cubic spline interpolation, or more simply by linear interpolation. As noted previously cubic spline interpolation smooths 90° kinks on the string, however, it is hard to make Δl exactly equal 0.1 for all points along the string. For this reason it is expedient to use linear interpolation.

[14]To obtain the initial condition (with coherence length ξ) for a simulation of size L, we first generate the VV initial condition with size L' and then scale according to $L' \to L = \xi L'$.

characteristic curves $\sigma \pm \Delta\tau/\epsilon$. After $\Delta\tau$ the the left mover has moved to $\sigma - \Delta\tau/\epsilon$, and the right mover to $\sigma + \Delta\tau/\epsilon$ (see Fig. A.1). To find $\mathbf{l}$ and $\mathbf{r}$ at σ, a linear interpolation scheme is implemented.[15] The left and right movers are re-scaled to satisfy the constraint $\mathbf{l}^2 = \mathbf{r}^2 = 1$. The energy density, ϵ, is determined using Eq. (5.75), with periodic boundary conditions imposed on the string network.

The energy density of the Universe evolves according to $\rho \propto t^{-2}$, which implies that ρt^2 is a constant quantity. The energy density of a long string network (within the Hubble volume V) is given by

$$\rho_\infty = \frac{a\mu}{V} \int_V \epsilon d\sigma \tag{5.80}$$

If a string network possesses a scaling solution (as predicted by Kibble's scaling model), then the quantity $\rho_\infty t^2/\mu$ will not change with time (in the scaling regime). If $\rho_\infty t^2/\mu$ is much larger than the scaling solution, high intercommutation rates guarantee that it decreases toward the scaling solution. Similarly, if $\rho_\infty t^2/\mu$ is smaller than the scaling solution it will increase. Since the string network energy density depends on the initial coherence length, ξ, the evolution of $\rho_\infty t^2/\mu$ can be explored by changing ξ. Alternatively, since t is defined in terms of τ, the initial value of $\rho_\infty t^2/\mu$ can be determined from the initial conformal time, τ_i. The scaling behaviour of the string network is investigated for various expansion factors, X, where

$$X = \frac{a(t)}{a(t_i)}. \tag{5.81}$$

In the radiation era $X = \tau/\tau_i$, since $a(t) \propto t^{1/2} \propto \tau$.

A typical cosmic string network simulation (in the radiation era) is shown in Fig. 5.10. The size of the simulation is 10^3, with $\xi = 0.5$, $\Delta\sigma = 0.025$ and $\Delta\tau = 0.005$, where $\Delta\tau < \epsilon\Delta\sigma$ guarantees numerical stability (see Appendix A). The simulation was run for 4000 conformal time steps. The size and duration of the simulation guarantees that periodic boundary conditions do not affect the scaling behaviour of the network. Figure 5.10 shows a visualization volume[16] of size 5^3. Figure 5.10 (a) displays the VV initial condition using cubic spline interpolation. Figures 5.10 (a) and (b) show that a significant number of strings disappear (due to intercommutation and loop collapse) when

[15]Interpolation can be performed along the great circle in $\mathcal{R}^{3+1}$, however, it is not obvious how to generalize this procedure to $\mathcal{R}^{4+1}$. A simpler method is to utilize linear interpolation and re-scaling.

[16]Since the string number density depends on the initial coherence length ξ, the size of the visualization volume also depends on ξ. With $\xi = 0.5$ and $\Delta\sigma = 0.025$, the visualization volume 5^3 is equivalent to a full field theory simulation with lattice size $(5/0.025\xi)^3 = 400^3$.

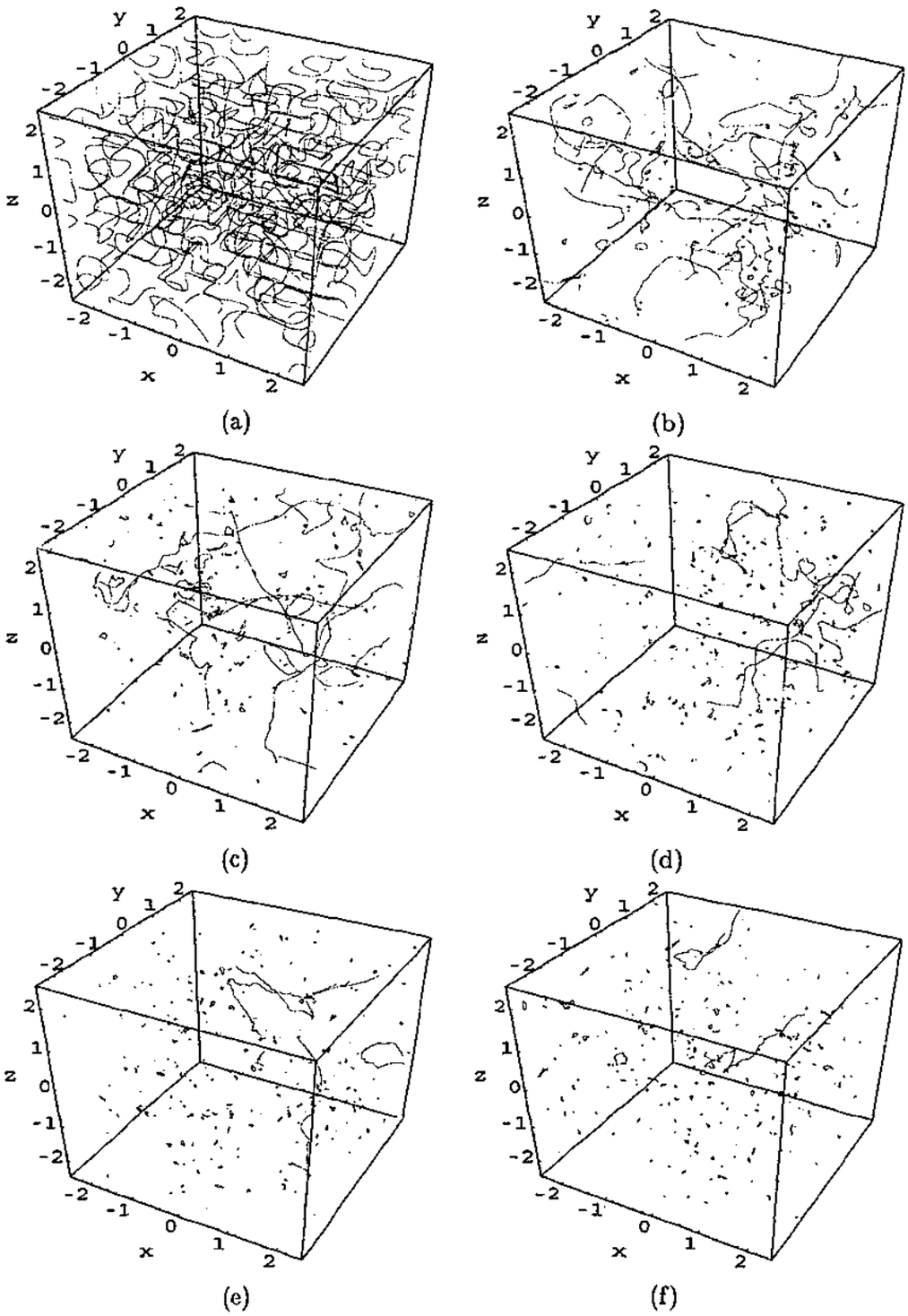

Figure 5.10: String network evolved for 4000 conformal time steps in the radiation era. (a) $X = 1$ (the VV initial condition uses a cubic spline interpolation), (b) $X = 1.2$, (c) $X = 2.4$, (d) $X = 3.6$, (e) $X = 4.8$, and (f) $X = 6$. Dilution of the string network results in it exhibiting scaling behaviour.

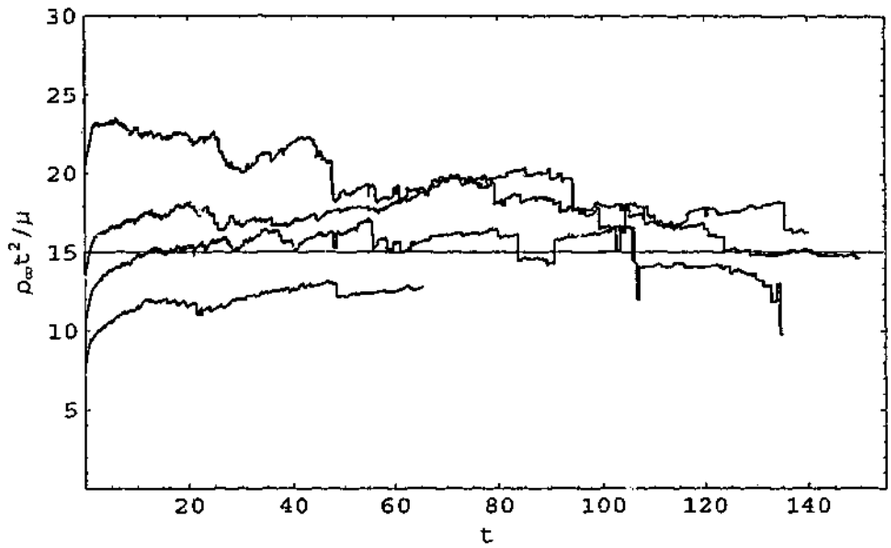

Figure 5.11: Scaling behaviour of long strings for various initial values of $\rho_\infty t^2/\mu$, with $\xi = 0.5$ and $2 \leq \tau_i \leq 5$. For a network with $\rho_\infty t^2/\mu < 15$, the solution increases toward 15 as the network evolves, whereas for $\rho_\infty t^2/\mu > 15$ the solution decreases toward 15. This implies the existence of a scaling solution for the network ($\rho_\infty t^2/\mu \approx 15$), in which strings do not dominate the energy of the Universe (see text).

the expansion factor is 1.2. Long strings fragment into small loops, as can be seen in Figs. 5.10 (c) - (f). Figures 5.10 (e) and (f) show that when the expansion factors are 4.8 and 6, the rate of dilution of long strings is such that there are only a few left at the end of the simulation. The rate of dilution of these long strings gives rise to a scaling solution for the string network (see Fig. 5.11).

Figure 5.11 shows the scaling behaviour of a long string network for four initial values of $t^2\rho_\infty/\mu$, which were obtained with different values of the initial conformal time, τ_i. It is evident that there is a scaling solution[17] $t^2\rho_\infty/\mu = 15 \pm 3$. If the initial value of $t^2\rho_\infty/\mu$ is much higher (lower) than 15 it will decrease (increase), eventually approaching 15. The value of 15 is consistent with results reported in the literature (see Albrecht and Turok 1985, Bennett and Bouchet 1988, Allen and Shellard 1990 and Bennett and Bouchet 1990). Our analysis gives us confidence in the linear interpolation scheme and string crossing detection method. This is a critical test, since we will extend the methodology

[17]The exact scaling value is not important. However, measurements of the anisotropy of the Cosmic Microwave Background Radiation (CMBR) from the Cosmic Background Explorer (COBE), and theories of large scale structure formation constrain $\mu = 1.5 \pm 0.5 \times 10^{-6} c^2/G_N$, where c is the speed of light and G_N is the Newtonian gravitational constant (see e.g., Bennett *et al.* 1992 and Allen *et al.* 1996).

to numerical simulations of a string network in $\mathcal{R}^{4+1}$ (see Sec. 5.5).

Various other statistical quantities, such as the mean squared velocity

$$\langle \dot{\mathbf{x}}^2 \rangle = \frac{\int d\sigma \epsilon \dot{\mathbf{x}}^2}{\int d\sigma \epsilon}, \tag{5.82}$$

are readily determined from the numerical simulations, and these are also consistent with the literature values (Allen and Shellard 1990 and Bennett and Bouchet 1990). Our simulations show that most strings have a velocity in the range 0.40 to 0.95 ($c = 1$). Such highly relativistic strings increase the rate of string crossing (intercommutation) and loop collapse.

A relativistic string network in the early Universe would quickly evolve toward a scaling regime. However, the scaling behaviour of the long string network is expected to depend on the number of spacetime dimensions. In the remainder of this chapter we examine the evolution of a string network in $\mathcal{R}^{4+1}$ spacetime.

5.5 Numerical simulations of a string network in $\mathcal{R}^{4+1}$ spacetime

To understand the evolution of a string network in $4 + 1$ dimensions, we examine the Friedmann equations in $\mathcal{R}^{4+1}$. The Kibble scaling model is extended to investigate the evolution of long strings in $\mathcal{R}^{4+1}$; detailed numerical simulations are carried out to elucidate the behaviour of the string network.

5.5.1 Friedmann equations in $\mathcal{R}^{4+1}$ spacetime

To derive the Friedmann equations in $\mathcal{R}^{4+1}$, consider the metric line element in $4 + 1$ dimensions. Introducing a scale factor, $a_w(t)$, which governs the expansion of the extra w-dimension, and utilizing the generalized FRW metric,

$$g_{\mu\nu} = \mathrm{diag}(1, -a^2(t), -a^2(t), -a^2(t), -a_w^2(t)), \tag{5.83}$$

we write the line element in $\mathcal{R}^{4+1}$ as

$$ds^2 = dt^2 - a^2(t)(dx^2 + dy^2 + dz^2) - a_w^2(t)dw^2. \tag{5.84}$$

Using a perfect fluid model of the Universe, the Einstein field equations lead to the generalized Friedmann equations:

$$3\frac{\dot{a}(\dot{a}a_w + a\dot{a}_w)}{a^2 a_w} = 8\pi\rho, \tag{5.85}$$

$$\frac{\dot{a}^2 a_w + 2a\ddot{a}a_w + a(a\ddot{a}_w + 2\dot{a}\dot{a}_w)}{a^2 a_w} = -8\pi p, \tag{5.86}$$

$$3\frac{\dot{a}^2 + a\ddot{a}}{a^2} = -8\pi p, \tag{5.87}$$

where ρ is the energy density of the Universe and p is the pressure. For the case of a non-expanding extra spatial dimension ($a_w = 1$), the evolution of the energy density is determined by

$$\dot{\rho} + 3\frac{\dot{a}}{a}(p + \rho) = 0, \tag{5.88}$$

$$\dot{\rho} + 2\frac{\dot{a}}{a}(p + 2\rho) = 0. \tag{5.89}$$

The energy density of the Universe in $\mathcal{R}^{4+1}$ is governed by the same equation as in $\mathcal{R}^{3+1}$. However, the existence of a flat extra dimension results in an additional constraint equation (5.89). Equations (5.88) and (5.89) can be satisfied if and only if the pressure equals the energy density ($p = \rho$), unless the Universe is empty, in which case the pressure and density adopt trivial values, $p = \rho = 0$. For a non empty Universe these equations do not satisfy the equation of state in the radiation era[18] ($p = \rho/4$), and $p = 0$ in the matter era. We therefore conclude that the Einstein field equations do not allow a non-expanding extra dimension.

Consider the case where the extra dimension expands at a different rate to the other three dimensions. If we assume that the extra dimension expands as $a_w(t) \propto t^m$, and the other three dimensions expand according to $a(t) \propto t^n$ (where m and n are real numbers), then Eqs. (5.86) and (5.87) give

$$-3n^2 + 2nm + m^2 + n - m = 0. \tag{5.90}$$

Equation (5.90) has two solutions $n = m$ and $n = \frac{1}{3}(1 - m)$. In the radiation era ($p = \rho/4$) Eqs. (5.85) and (5.87) require that $m = 4 - 9n$. To satisfy these equations we require $m = \pm n$. Likewise in the matter era ($p = 0$) we also obtain $m = \pm n$. Therefore in both the radiation and matter eras, the extra dimension either expands at the same rate as the other three spatial dimensions, or contracts at the same rate as these dimensions. This suggests two possible expansion scenarios for the Universe. In the first scenario the extra dimension expands at the same rate as the other three spatial dimensions. In the second

[18] See Appendix C for a detailed discussion of the relationship between pressure and density in $\mathcal{R}^{4+1}$ spacetime.

scenario the Universe expands at the same rate initially, however, the expansion slows down and eventually stops. At a later time the three spatial dimensions re-expand and the extra dimension contracts. This latter scenario requires fine tuning of the expansion rate, and demands non-vanishing vacuum energy, or a cosmological constant term (see e.g., Carroll 2001). In what follows we assume the first scenario.

When the expansion rate of the extra dimension is identical to the other three dimensions ($a_w(t) = a(t)$), the Friedmann equations reduce to

$$6\left(\frac{\dot{a}}{a}\right)^2 = 8\pi\rho, \tag{5.91}$$

$$3\frac{\dot{a}^2 + a\ddot{a}}{a^2} = -8\pi p, \tag{5.92}$$

for which the evolution equation for the energy density is

$$\dot{\rho} + 4\frac{\dot{a}}{a}(\rho + p) = 0. \tag{5.93}$$

Using $a \propto t^n$, Eq. (5.91) gives $\rho \propto t^{-2}$. In the radiation era ($p = \rho/4$) the evolution of the energy density is determined by

$$\dot{\rho} + 5\frac{\dot{a}}{a}\rho = 0. \tag{5.94}$$

The solution to Eq. (5.94) is of the form $\rho \propto a^{-5}$, which gives $a \propto t^{2/5}$. In the matter era ($p = 0$) we have

$$\dot{\rho} + 4\frac{\dot{a}}{a}\rho = 0. \tag{5.95}$$

Equation (5.95) has a solution of the form $\rho \propto a^{-4}$, which results in $a \propto t^{1/2}$.

A string network in $\mathcal{R}^{4+1}$ has a scaling solution if its energy density also evolves as $\rho_\infty \propto t^{-2}$. Our investigations of the scaling behaviour of a string network in $\mathcal{R}^{3+1}$, show that the qualitative scaling behaviour of the network can be obtained from Kibble's scaling model. In Sec. 5.5.2 we extend the scaling model to $\mathcal{R}^{4+1}$.

5.5.2 Kibble's scaling model in $\mathcal{R}^{4+1}$ spacetime

In expanding spacetime the energy of a string network is $E = a\mu\int\epsilon d\sigma$. Differentiating E with respect to t, and using $\dot{\epsilon} = -2\frac{\dot{a}}{a}\epsilon\mathbf{v}^2$ (where a dot denotes differentiation with respect to t and $\mathbf{v} = d\mathbf{x}/d\tau = ad\mathbf{x}/dt$), we obtain an expression for the evolution of the energy of the string network:

$$\dot{E} = \frac{\dot{a}}{a}E(1 - 2\langle\mathbf{v}^2\rangle). \tag{5.96}$$

To incorporate intercommutation and loop collapse, consider a string of length L in a four-dimensional volume, $V = L^4$. In $\mathcal{R}^{4+1}$ a string is expected to move a distance L^2 before encountering another string. The collision (intersection) probability in time Δt is $L^{-6}\Delta t$. Every time the string intersects it loses energy μL. The energy loss, ΔE_L, in a time interval Δt and volume V is

$$\Delta E_L = -\frac{\Delta t}{L^6}\mu L V. \tag{5.97}$$

In the limit $\Delta t \to 0$, the energy loss rate is $\dot{E}_L = \mu V L^{-5}$, so that net energy loss rate of the string network is given by

$$\dot{E} = \frac{\dot{a}}{a}E(1 - 2\langle \mathbf{v}^2 \rangle) - \frac{\mu V}{L^5}. \tag{5.98}$$

The energy and energy density in $\mathcal{R}^{4+1}$ are

$$E = \frac{\mu V}{L^3}, \tag{5.99}$$

$$\rho_\infty = \frac{\mu}{L^3}. \tag{5.100}$$

Consequently, the length of a string changes according to

$$\dot{L} = n(1 + \frac{2}{3}\langle \mathbf{v}^2 \rangle)\frac{L}{t} + \frac{1}{3L}. \tag{5.101}$$

Equation (5.101) can be solved with a change of variable $u = L^2/t$, in which case the differential equation (5.101) is separable. The general solution to Eq. (5.101) is given by

$$L^2 = c_1 t^{2n(1+\frac{2}{3}\langle \mathbf{v}^2 \rangle)} + c_2 t, \tag{5.102}$$

where c_1 is an integration constant and c_2 is defined by

$$c_2 = \frac{2}{3 - 6n - 4n\langle \mathbf{v}^2 \rangle}, \tag{5.103}$$

where $\langle \mathbf{v}^2 \rangle$ is constant in the matter and radiation eras. Since the velocity of a string segment can range from zero to almost unity, it is assumed that on average the velocity of each string segment is $|\mathbf{v}| \sim 1/2$ (or $\langle \mathbf{v}^2 \rangle \sim 1/4$). Using $n = 2/5$ for the radiation era, Eq. (5.102) implies that intercommutation dominates in the long term evolution of the network, i.e., $L^2 \propto t$. Since $\rho_\infty \propto L^{-3}$, the evolution of the energy density of a string network in $\mathcal{R}^{4+1}$ is

$$\rho_\infty(t) \propto t^{-1.5}. \tag{5.104}$$

To see how string intercommutation in $\mathcal{R}^{4+1}$ affects the evolution of the energy density of long strings, consider the case where there is no string intercommutation. In this situation Eq. (5.102) gives $L^2 \propto t^{14/15}$. Consequently, the energy density of the long string network in $\mathcal{R}^{4+1}$ dilutes as

$$\rho_\infty(t) \propto t^{-1.4}. \tag{5.105}$$

Comparing Eq. (5.104) with Eq. (5.105) we see that string intercommutation does not play a significant role in determining the evolution of the energy density of long strings in $\mathcal{R}^{4+1}$. Furthermore, Eq. (5.104) suggests that a string network in $\mathcal{R}^{4+1}$ does not have a scaling solution, and consequently the evolution of strings in $4+1$ dimensions does not provide a mechanism for resolving the monopole problem in $\mathcal{R}^{3+1}$ spacetime.

Our simple model of long string evolution is based on various assumptions. In particular, the model does not take into account detailed string dynamics or the small scale structure of the strings. To describe accurately string network evolution in $\mathcal{R}^{4+1}$, it is necessary to perform detailed numerical simulations, where these assumptions can be relaxed. We start with the Vachaspati-Vilenkin initial condition in $\mathcal{R}^{4+1}$.

5.5.3 Extended Vachaspati-Vilenkin initial condition

The method of generating the initial condition for a string network in four-dimensional (4D) space is similar to the technique used in three dimensions. To proceed we label the 4D space in terms of the spatial coordinates (x, y, z, w). Three-dimensional space can be thought of as three orthogonal planes: $[x, y]$, $[x, z]$, and $[y, z]$. Analogously the 4D space is constructed from four orthogonal three-dimensional volumes: $[w, x, y]$, $[x, y, z]$, $[y, z, w]$, and $[z, w, x]$. We divide the three-dimensional volumes into unit cells of size $\xi = 1$, where ξ is the coherence length of the Higgs field. The total size of each three-dimensional volume is specified by $N\xi$, where N is the number of divisions. Each unit cell has six faces in three dimensions, whereas the total number of faces in 4D is 24. We assign each corner of the unit cell a random phase denoted by 0, 1 or 2, and determine if a string segment pierces any of the 24 faces. By stepping through all unit cells, we generate a string network configuration in the form of a random walk in four spatial dimensions.

Four-dimensional space can be considered as being constructed from four orthogonal three-dimensional spaces, hence each 4D unit cell can contain up to eight string segments. The probability of a string segment entering a cell in 4D is shown in Fig. 5.12. The

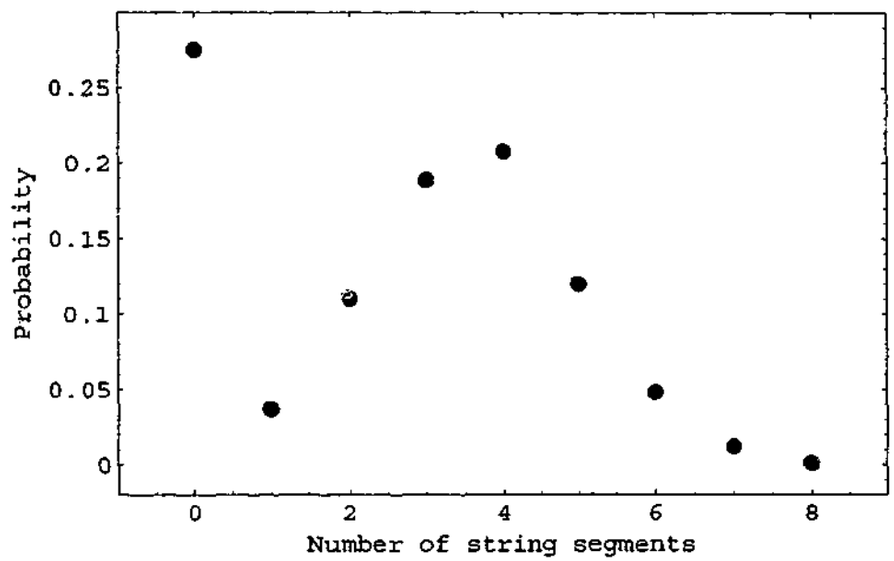

Figure 5.12: Probability of a string segment entering a unit cell in 4D. Up to eight string segments can enter a cell, however, for a cell containing strings the probability is highest for three or four strings.

probability that no string segment enters a cell is similar to its value in three dimensions, however, there is a high probability that three or four string segments enter a cell (see Fig. 5.12). This is in contrast to the 3D case, where most cells contain only one string segment.

Figures 5.13 and 5.14 show typical three-dimensional plots of the VV initial condition at $w = 0$ and $w = 0.1$, respectively. Four-dimensional space is divided into unit cells, and strings are aligned along integer values of x, y, z and w. Therefore strings are observed when a slice through the string network is plotted at $w = 0$ (see Fig. 5.13). A slice through the string network at non integer values of w (e.g., $w = 0.1$), shows points which are interpreted as monopoles in our model. Monopoles in three dimensions are strings in 4D, which are oriented along the direction orthogonal to the w-axis.

Figure 5.15 shows a logarithmic plot of the string number density versus string length for a typical 4D VV initial condition. The figure shows that, as the string length increases, the number density decreases exponentially. This indicates that there are more short strings than long strings. Since short strings are primarily associated with loops, this means there are significantly more loops than long strings, however, the network is still dominated by long strings. As was evident in the VV initial condition in three dimensions,

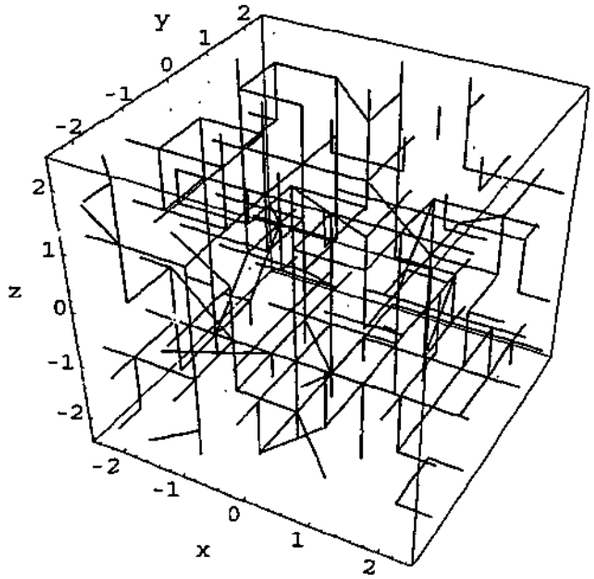

Figure 5.13: Three-dimensional slice (at $w = 0$) of the VV initial condition. The slice is through the center of the 4D cells and shows string segments. Many string segments have branches, since up to eight segments can enter a cell. Strings that are oriented in a direction orthogonal to (and intersect at) $w = 0$ are points in $\mathcal{R}^{3+1}$ (see Fig. 5.14).

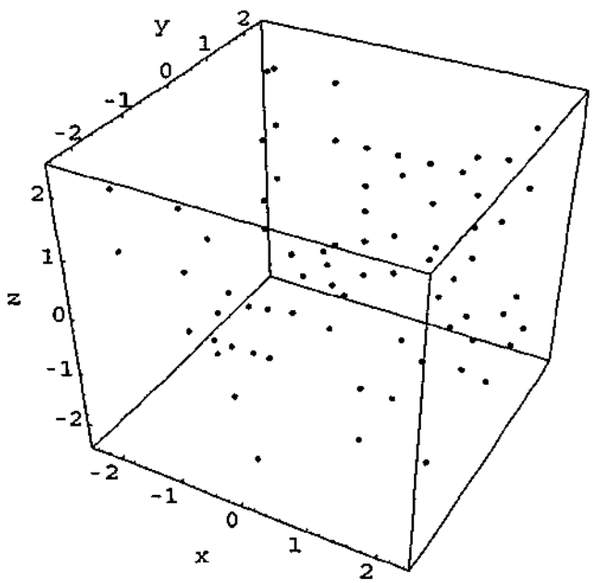

Figure 5.14: Three-dimensional slice (at $w = 0.1$) of the VV initial condition showing that strings in $\mathcal{R}^{4+1}$ can be interpreted as monopoles in $\mathcal{R}^{3+1}$.

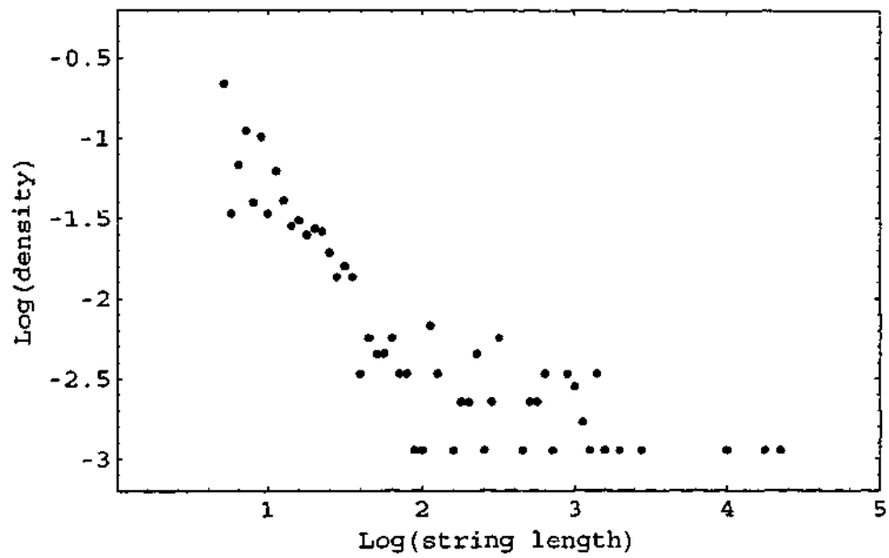

Figure 5.15: Logarithmic plot of the string number density versus string length for a typical 4D VV initial condition. This shows that there are more short strings (loops) than long strings, however, most string segments in the network are associated with long strings.

most string segments in a network are associated with long strings. It is expected that the evolution of the string network in $\mathcal{R}^{4+1}$ is also dominated by long strings.

5.5.4 String network evolution in $\mathcal{R}^{4+1}$ spacetime

The scale factor, $a(t)$, evolves differently in $\mathcal{R}^{4+1}$ than in $\mathcal{R}^{3+1}$, however, Hubble's constant remains unchanged (i.e., $h = \dot{a}/a \propto t^{-1}$). This implies that the equations of motion for strings in $\mathcal{R}^{4+1}$ are the same as those in $\mathcal{R}^{3+1}$ (see e.g., Eqs. (5.73), (5.74) and (5.75)). Evolving a string network in $\mathcal{R}^{4+1}$ involves solving for the left movers, l, and right movers, r, on their characteristic curves, $\sigma \pm \Delta\tau/\epsilon$ (see Sec. 5.4). To find l and r along σ, it is necessary to exploit an interpolation scheme. The constraint $\mathbf{l}^2 = \mathbf{r}^2 = 1$ is also valid in $\mathcal{R}^{4+1}$. To see this consider the defining relationship for l:

$$\mathbf{l}^2 = \dot{\mathbf{x}}^2 + 2\dot{\mathbf{x}} \cdot \mathbf{x}' + \frac{\mathbf{x}'^2}{\epsilon^2}, \tag{5.106}$$

where $\mathbf{x} = (x, y, z, w)$. Since $\mathbf{x}'^2/\epsilon^2 = 1 - \dot{\mathbf{x}}^2$ (see Eq. (5.64)) and $\dot{\mathbf{x}} \cdot \mathbf{x}' = 0$, Eq. (5.106) gives $\mathbf{l}^2 = 1$, independent of the number of spatial dimensions. Likewise the constraint $\mathbf{r}^2 = 1$ is independent of the number of spatial dimensions. Our numerical simulations use linear interpolation and re-scaling to satisfy the constraint $\mathbf{l}^2 = \mathbf{r}^2 = 1$.

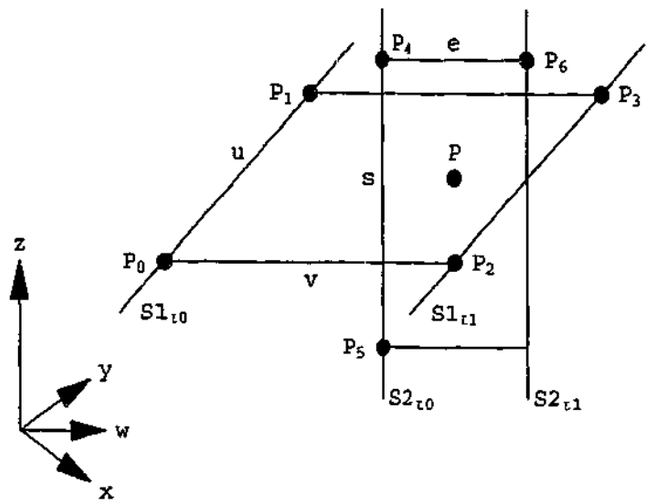

Figure 5.16: Crossing detection method used in the $(4+1)$-dimensional simulations. $S1_{\tau 0}$ and $S1_{\tau 1}$ are segments of a string $(S1)$ at two different conformal times, τ_0 and τ_1; $S2_{\tau 0}$ and $S2_{\tau 1}$ are segments of a string $(S2)$ at τ_0 and τ_1. Here u parameterizes the string segment $\overline{P_0P_1}$, while v parameterizes the line segment $\overline{P_0P_2}$; s parameterizes the string segment $\overline{P_4P_5}$, while e parameterizes the line segment $\overline{P_4P_6}$. $S1$ and $S2$ both sweep out planes (world-sheets) that intersect at a point P (in $\mathcal{R}^{4+1}$). This point can be found by solving four linear equations (see text).

As strings evolve they intercommute, which is modeled by detecting if two string segments cross. The crossing detection method in $\mathcal{R}^{4+1}$ is an extension of the scheme used in $\mathcal{R}^{3+1}$ (see Sec. 5.4.5). Figure 5.16 shows the method used to detect if two string segments, $S1$ and $S2$, cross in a given conformal time step $\Delta\tau = \tau_1 - \tau_0$. The ends of the string segments at two conformal times are denoted by P_0, P_1, P_2, P_3, P_4, P_5 and P_6. In $\mathcal{R}^{4+1}$ spacetime each point ($P, P_0, P_1, P_2, P_3, P_4$, P_5 and P_6) is specified by a vector with four components. For example, the vector to point P has components P^x, P^y, P^z and P^w. In a given conformal time step, the string segments $S1$ and $S2$ sweep out two planes (world-sheets). The plane containing $S1$ is parameterized by u and v. The plane containing $S2$ is parameterized by s and e. The crossing detection method checks if the two planes intersect in $\mathcal{R}^{4+1}$. The intersection point, P, between two planes containing $S1$ and $S2$ is obtained from the solution to four linear equations (cp. Eq. (5.78)):

$$P_0^i + u(P_1^i - P_0^i) + v(P_2^i - P_0^i) = P_4^i + s(P_5^i - P_4^i) + e(P_6^i - P_4^i), \ (i = x, y, z, w), \quad (5.107)$$

where the two string segments intersect in a given conformal time step if $0 \leq u, v, s, e < 1$.

For two non-parallel planes there is a unique solution for the parameters v, u, s and e, which implies that, in $4+1$ dimensions, the two planes intersect at a point. Once two string segments cross, intercommutation is implemented by exchanging the ends of the strings.

Numerical simulations were conducted to study the scaling behaviour of a string network in $\mathcal{R}^{4+1}$ spacetime. It is found that string intersections in $\mathcal{R}^{4+1}$ are rare (and therefore the intercommutation rate is very low) compared to $\mathcal{R}^{3+1}$. To fully investigate the effect of intercommutation on the scaling behaviour of long strings in $\mathcal{R}^{4+1}$ requires numerical simulations to be conducted at a much higher energy density than in $\mathcal{R}^{3+1}$. This also necessitates a much higher string number density. Consequently, a string network simulation in $4+1$ dimensions has to be performed with a smaller value of the coherence length, ξ. Numerical simulations show that a sufficiently high string number density can be obtained with $\xi = [0.1, 0.2]$. We have performed numerical simulations with $\Delta\sigma = 0.05$, which is comparable[19] to a full field theory simulation of size 40^4. For simplicity we fix the initial conformal time $\tau_i = 1$, for which the expansion factor $X = a(\tau)/a(\tau_i) = a(\tau)$. Furthermore, to guarantee that the numerical simulation is stable, the conformal time step ($\Delta\tau = 0.0025$) has been chosen to be much smaller than $\Delta\sigma$. Since the CFL condition for the stability of the numerical scheme requires $\epsilon\Delta\sigma \geq \Delta\tau$ (see Appendix A), the evolution of the energy density obeys the constraint $\epsilon \geq \Delta\tau/\Delta\sigma$. According to Eq. (5.63) the fastest rate of decay of the energy density is $\dot{\epsilon} = -2h\epsilon$. In the radiation era ($h = 2/3\tau$), the energy density evolves as

$$\epsilon(\tau) = \left(\frac{\tau}{\tau_i}\right)^{-4/3}. \tag{5.108}$$

To ensure stability of the numerical simulation, the string network can only be evolved to $\lesssim 10$ (with $\tau_i = 1$ and $\Delta\tau = 0.0025$). Since the expansion factor of the Universe is given by $a(\tau)/a(\tau_i) = (\tau/\tau_i)^{2/3}$, our simulations are implemented for $X \lesssim 4.5$. The behaviour of the string network in $\mathcal{R}^{3+1}$ indicates that an expansion factor of 4.5 is sufficient to study and quantify the scaling behaviour of the string network.

A typical string network simulation (in the radiation era) is plotted in Fig. 5.17. This shows the evolution of strings (one-dimensional objects in $\mathcal{R}^{4+1}$) and monopoles

[19]The size of the string network depends on the coherence length ξ, which determines the string number density, and $\Delta\sigma$, which determines the spatial resolution of the string.

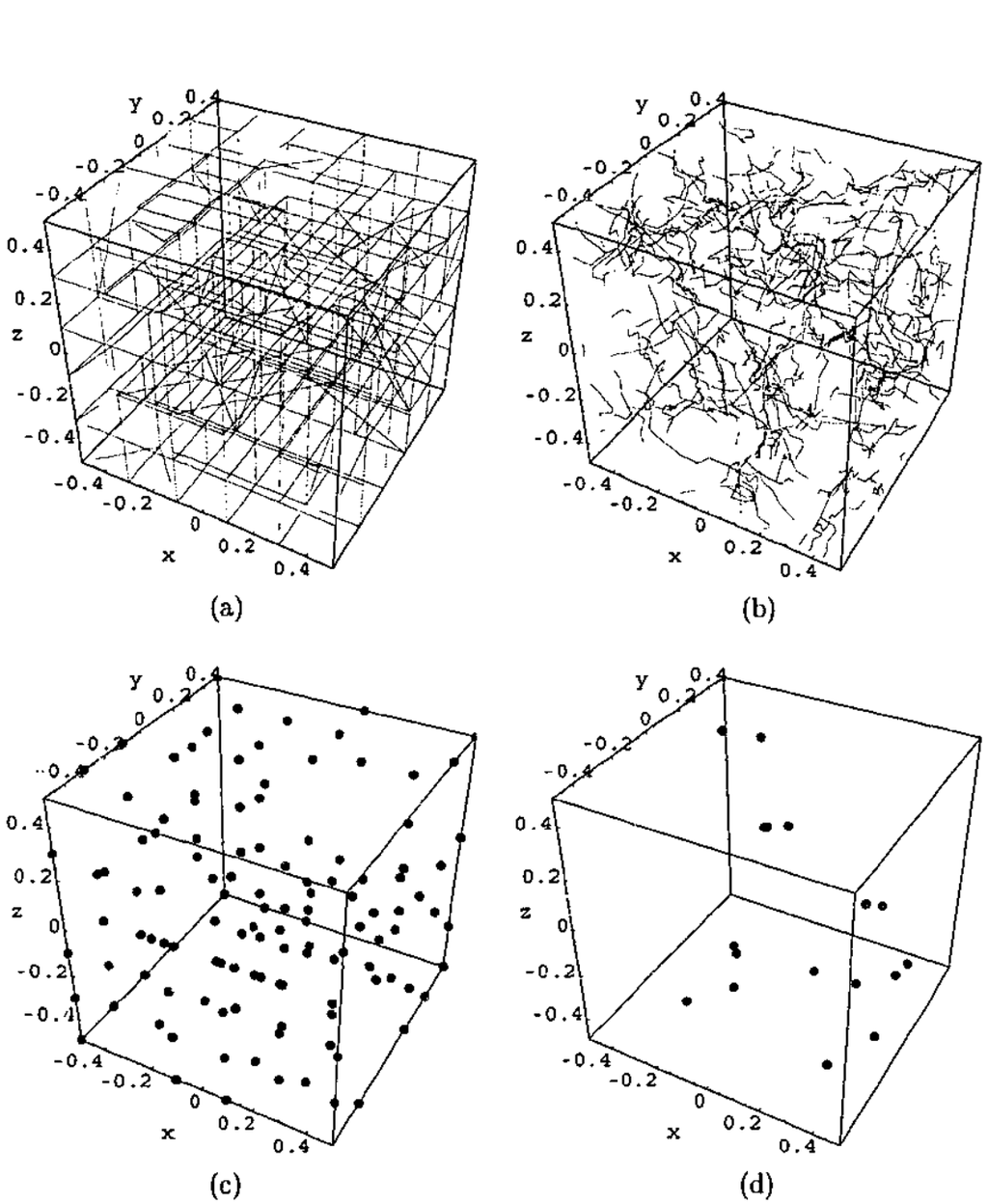

Figure 5.17: Evolution of a typical string network in $\mathcal{R}^{4+1}$ (in the radiation era). (a) and (c) are plots at the beginning of the simulation; (b) and (d) show the network at the end of the simulation, after the Universe has expanded by a factor of 4.5. In (a) and (b) the string network is plotted for w in the range $[-0.2, 0.2]$. (c) and (d) are plots of a slice through the network showing the evolution of monopoles. Intercommutation is rare in $\mathcal{R}^{4+1}$, and evolution of the network shows no significant dilution of strings.

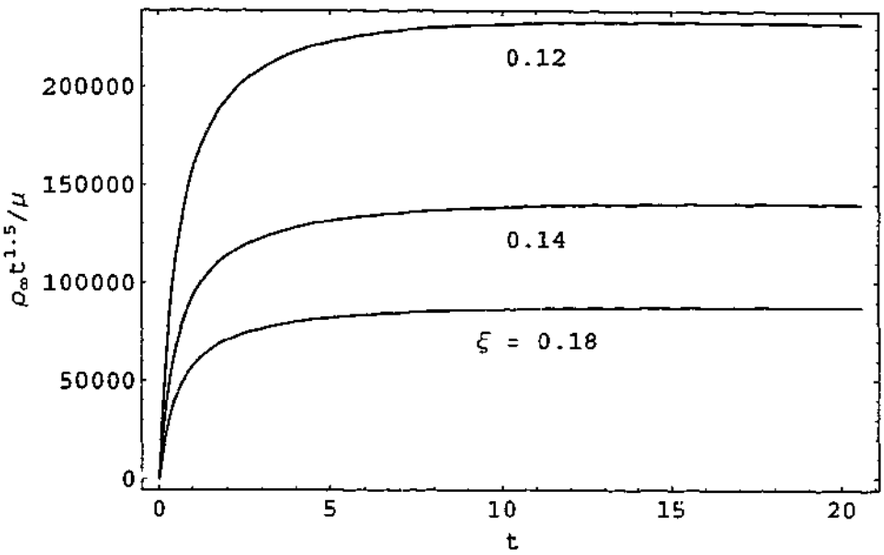

Figure 5.18: Evolution of the energy density (in the radiation era) of a string network in $\mathcal{R}^{4+1}$ ($\xi = 0.12, 0.14$, and 0.18). Note that a smaller value of ξ gives a larger energy density. These curves show little structure because intercommutation is rare in $\mathcal{R}^{4+1}$. All curves approach a constant value, with the energy density of the string network evolving as $t^{-1.5}$.

(zero-dimensional objects in $\mathcal{R}^{3+1}$). To visualize strings, we plot the network with a non-vanishing thickness in the w dimension, i.e., for $w = [-0.2, 0.2]$. Figure 5.17 (a) shows the string network in $\mathcal{R}^{4+1}$ at the beginning of the simulation, and Fig. 5.17 (b) shows the network at the conclusion of the simulation. Comparing Figs. 5.17 (a) and (b) we see no sign of dilution in the number of strings in the visualization volume. This indicates that in $\mathcal{R}^{4+1}$ (unlike $\mathcal{R}^{3+1}$) string crossings are rare. Figures 5.17 (c) and (d) show a slice through the 4D string network. Since a slice of the 4D space is a three-dimensional volume, Figs. 5.17 (c) and (d) show the evolution of monopoles in $\mathcal{R}^{3+1}$. Comparing Fig. 5.17 (c) with Fig. 5.17 (d), we see that some of the monopoles disappear. This indicates that although intercommutation is rare in $\mathcal{R}^{4+1}$, some monopoles are indeed removed from the network via string intercommutation. This may affect the long term evolution of the energy density of the monopoles. However, since intercommutation is rare in $\mathcal{R}^{4+1}$, the decrease in the energy density of a string network in $\mathcal{R}^{4+1}$ is expected to be slower than for a string network in $\mathcal{R}^{3+1}$. The behaviour of the string network in $\mathcal{R}^{4+1}$ is characterized by plotting $t^m \rho_\infty/\mu$ as a function of time, where m is a real (scaling) parameter (see e.g., Fig. 5.18). A value $m = 2$ implies that the energy density of the string network dilutes in

proportion to the energy density of the Universe. However, for $m < 2$ the energy density of the network dilutes more slowly than the energy density of the Universe.

The behaviour of the string network has also been explored by varying the coherence length, ξ, of the network. Figure 5.18 shows the behaviour of $\rho_\infty t^m/\mu$ ($m = 1.5$) for the range $0.12 \leq \xi \leq 0.18$. For $t \gtrsim 13$, the top curve ($\xi = 0.12$) decreases slightly as a function of t, whereas the bottom curve ($\xi = 0.18$) increases slightly. This is consistent with the energy density of a string network evolving as $\rho_\infty \propto t^{-1.5}$, which is in accord with Kibble's scaling model (see Sec. 5.5.2). Our numerical simulations in $\mathcal{R}^{4+1}$ give us confidence in the validity of the analytical results based on Kibble's scaling model. If we adopt the form $\rho_\infty \propto t^{-1.5}$, the evolution of the energy density of the string network in $\mathcal{R}^{4+1}$ is specified by

$$\rho_\infty(t) = \rho_s t_s^{1.5} t^{-1.5}, \tag{5.109}$$

where t_s is the time at formation (or when the phase transition occurred), and ρ_s is the string network energy density at t_s. The evolution of the energy density of the Universe, ρ, is given by

$$\rho(t) = \rho_0 t_s^2 t^{-2}, \tag{5.110}$$

where ρ_0 is the energy density of the Universe at the time of the phase transition. Equations (5.109) and (5.110) indicate that the ratio of the energy density of string network to the energy density of the Universe evolves according to

$$\frac{\rho_\infty}{\rho} = \frac{\rho_s}{\rho_0} t_s^{-0.5} t^{0.5}. \tag{5.111}$$

From Eq. (5.111) we obtain $\rho_\infty/\rho \propto t^{1/2}$, which indicates that the energy density of the string network in $\mathcal{R}^{4+1}$ increases with respect to the energy density of the Universe. This is in marked contrast to the evolution of a string network in $\mathcal{R}^{3+1}$. We conclude that a string network in $\mathcal{R}^{4+1}$ spacetime does not exhibit scaling behaviour.

The absence of a scaling solution for strings in $\mathcal{R}^{4+1}$ appears to rule out an extra spatial dimension as a way of resolving the monopole problem. However, an interesting situation arises if the extra dimension is smaller than the other spatial dimensions. In what follows we consider the evolution of a string network in a compactified dimension.[20]

[20] In Sec. 5.5.1 we showed that the generalized Friedmann equations in $\mathcal{R}^{4+1}$ lead to two possible scenarios for the evolution of the Universe. In the first scenario the extra dimension expands at the same rate as the other spatial dimensions. If all the spatial dimensions were created simultaneously (at the Big Bang), we expect each of the dimensions to have the same size. However, if the extra dimension was created at a later

5.5.5 Evolution of a string network in a compactified dimension

A naive model for the evolution of the Universe, with a compactified dimension, is based on interpolating the Friedmann equation between $\mathcal{R}^{3+1}$ and $\mathcal{R}^{4+1}$, i.e.,

$$\dot{\rho} + \left(3 + \frac{L_w}{L_x}\right)\frac{\dot{a}}{a}(p+\rho) = 0, \tag{5.112}$$

where L_w/L_x is the ratio of the size of the compactified dimension to the three uncompactified dimensions. As $L_w \to 0$, Eq. (5.112) describes the evolution of the energy density in $\mathcal{R}^{3+1}$, whereas for $L_w \to L_x$, Eq. (5.112) describes the evolution in $\mathcal{R}^{4+1}$. In the radiation era the equation of state also has to be interpolated between $\mathcal{R}^{3+1}$ and $\mathcal{R}^{4+1}$ spacetime, i.e.,

$$p = \frac{\rho}{3 + \frac{L_w}{L_x}}. \tag{5.113}$$

The energy density in the radiation and matter eras is found by solving Eq. (5.112), i.e.,

$$\rho_r \propto a_r^{-(4+L_w/L_x)}, \tag{5.114}$$

$$\rho_m \propto a_m^{-(3+L_w/L_x)}, \tag{5.115}$$

Using the fact that ρ is proportional to t^{-2}, we obtain the evolution equations for the scale factor in the radiation and matter eras as

$$a_r \propto t^{\frac{2}{4+L_w/L_x}}, \tag{5.116}$$

$$a_m \propto t^{\frac{2}{3+L_w/L_x}}, \tag{5.117}$$

For $a \propto t^{\alpha}$, where $\alpha = \frac{2}{4+L_w/L_x}$ in the radiation era and $\alpha = \frac{2}{3+L_w/L_x}$ in the matter era, the relationship between time, t, and conformal time, τ, is

$$\tau = \frac{1}{1-\alpha} t^{1-\alpha}. \tag{5.118}$$

Equations (5.114) - (5.117) show that the energy density of the Universe decreases as $\rho \propto t^{-2}$, independent of the dimensionality of the Universe. Therefore a string network in $\mathcal{R}^{4+1}$ will only have a scaling solution if the energy density of the network dilutes in the same way as in $\mathcal{R}^{3+1}$. This is possible if the size of the extra dimension approaches zero. The extent to which the scaling solution deviates from its behaviour in $\mathcal{R}^{3+1}$ is expected to

time, it would be smaller than the other spatial dimensions. Consequently, a compactified dimension is possible provided it was created at a different time to the three spatial dimensions. In the second scenario the extra dimension contracts, and a compactified dimension can arise naturally.

depend on the size of the extra (compactified) dimension. Without performing a detailed numerical simulation in compactified (4+1)-dimensional spacetime, we can infer the scaling behaviour as a function of L_w/L_x. Interpolating between $\mathcal{R}^{3+1}$ and $\mathcal{R}^{4+1}$, it is plausible to write

$$\rho_\infty(t) \propto t^{-2+L_w/2L_x}. \tag{5.119}$$

The behaviour of the energy density of the string network will depend on the upper limit imposed on the size of the compactified dimension; current experiments place this at 10^{-18} m (Kostelecky and Samuel 1991). A GUT scale string has a thickness $\sim 10^{-18}$ m (see Sec. 1.1), which is comparable to the upper bound on the compactified dimension. Consequently, the evolution of the energy density of monopoles in a compactified dimension can not be described by Eq. (5.119). To investigate the evolution of monopoles in a compactified dimension we must consider their formation in a symmetry breaking phase transition.

5.6 Monopoles in a compactified dimension

When a cosmological phase transition occurs, the vacuum expectation value of the monopole Higgs field adopts a non-zero value in the vacuum manifold (see Chapter 1). The value of $\langle\Phi\rangle$ depends on fluctuations of the Higgs field at $T = T_c$. The spatial scale over which Φ fluctuates is determined by its correlation length ξ, which is of the order of the Compton length of the Higgs field (see Sec. 5.5.5). Since the compactified dimension is comparable to ξ, the Higgs field is correlated over the size of the compactified dimension, i.e., Φ is considered to vary smoothly in the w direction.

Following a phase transition, space is causally connected in the w dimension, and therefore no "domain" structure forms in w-space. The size of the x, y and z dimensions is much larger than ξ. A $[x, y, z]$ volume can be obtained from the four-dimensional space by taking a slice at constant w. Below the critical temperature, Φ is causally uncorrelated over distances larger than ξ in each of the $[x, y, z]$ volumes. The $[x, y, z]$ volumes are divided into "domains" of size ξ, with the Higgs field in each of these "domains" adopting a random orientation; however, Φ is assumed to vary smoothly over ξ. A monopole forms when there is a non-trivial mapping between the 2-surface and the vacuum manifold of the monopole (see Sec. 1.4).

Figure (5.19) shows the formation of a "domain" structure following a cosmological

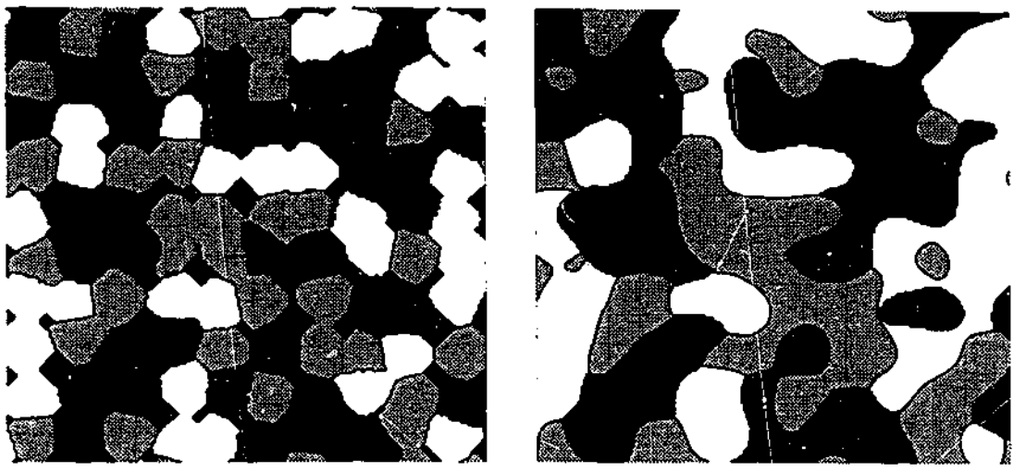

(a) (b)

Figure 5.19: (a) "Domain" structure following a cosmological phase transition. (b) Formation of monopoles in a $[x, y, z]$ volume (the w dimension is suppressed). Black denotes a phase of 0 and white denotes a phase of 2π. In (a) each region (of size ξ) is causally disconnected, and in (b) a monopole forms where the two-dimensional surface is non-contractable in the S^2 vacuum manifold.

phase transition. Figure 5.19 (a) is a slice through the four-dimensional space (at constant w). Since Φ is causally connected in the w dimension, this slice is identical to other slices at different w. Figure 5.19 (b) shows monopoles in the $[x, y, z]$ volume. A monopole becomes a line defect in four dimensional space, with the defect extending in the extra dimension. Because the extra dimension is curled up, this line defect forms a closed loop whose size corresponds to the compactified (Kaluza-Klein) dimension.

Figure 5.20 shows two possible configurations of a monopole that can arise in compactified $\mathcal{R}^{4+1}$ spacetime. In Fig. 5.20 (a) the monopole has a linear extension in the w direction, with the two ends of the monopole identified. Figure 5.20 (b) shows a monopole with its linear extension in the x direction. For a slice at constant x we would observe a discontinuous Higgs field in the w dimension. It is therefore unlikely for a monopole to form in this configuration. If the w dimension is much larger than the correlation length, the Higgs field becomes uncorrelated. In this situation a monopole may form, as shown in Fig. 5.20 (b), adopting the same configuration as it would in uncompactified $\mathcal{R}^{4+1}$ spacetime.

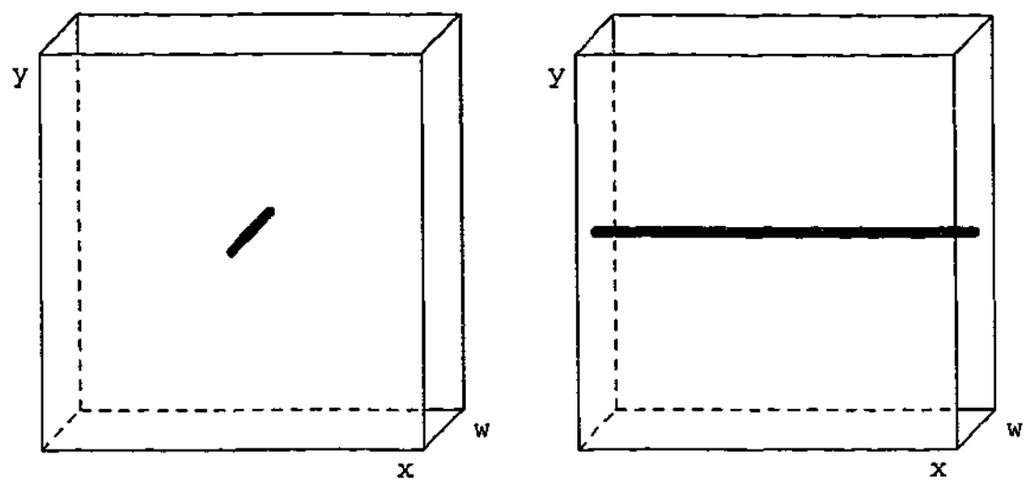

Figure 5.20: Two possible configurations of a monopole in $\mathcal{R}^{4+1}$ spacetime, with compactified dimension w. (a) The monopole is "oriented" in the w direction, and (b) the monopole is "oriented" in the x direction. The $[x, y, z]$ volume is causally disconnected, allowing the monopole to "orient" itself in the w direction as shown in configuration (a). However, the w dimension is causally connected and a monopole never forms in configuration (b). Since the extra dimension is curled up, the monopole forms a closed loop around the compactified (Kaluza-Klein) dimension.

The formation of monopoles in the compactified dimension is investigated using numerical simulations based on the Lagrangian (5.1) (with $\mu, \nu = 0, 1, 2, 3, 4$). The equations of motion are recast in dimensionless form (see Eqs. (5.16) - (5.18)). We assume that compactification occurs when the w dimension is smaller than the observed spatial dimensions (x, y and z). Our simulations use periodic boundary conditions on a lattice of size 30^4, with spatial step $\Delta h = 1$ in the x, y and z dimensions. Compactification of the w dimension is achieved by making the spatial step in the w dimension, Δh_w, smaller than the spatial steps in the x, y and z dimensions. For example, a compactified dimension with size $L_w = 6$ is obtained with $\Delta h_w = 0.2$ (i.e., $L_w = 30\Delta h_w = 6$). We performed numerical simulations in the range $0.1 \leq \Delta h_w \leq 1$, corresponding to $3 \leq L_w \leq 30$. To ensure numerical stability, we choose a small time step, $\Delta t = 0.05$ (see Appendix A). The initial condition is constructed by assigning a random value to Φ_a ($a = 1, 3, 3$) at each lattice point, with $\Phi_1^2 + \Phi_2^2 + \Phi_3^2 = \eta^2$. This assignment ensures that the Higgs field is correlated over ξ. A gauge field is introduced via a local gauge transformation, as discussed in Sec. 5.2.1. Damping terms $b\partial\Phi/\partial t$ and $b\partial A_\mu^a/\partial t$ (with $b = 10\Delta t$) are added to the equations

of motion (see Sec. 5.2.1).

A typical simulation is shown in Fig. 5.21. In this example the extra dimension is not compactified ($L_w = 30$). Monopoles exhibit string-like behaviour, however, they may appear as localized objects in cross-sectional plots. The results of a simulation with a compactified dimension ($L_w = 6$) are shown in Fig. 5.22. The compactified dimension is six times the size of the correlation length of the Higgs field; on comparing the slices at $w = -1.5$, 0 and 1.5, we see that the Higgs field is correlated. Following the symmetry breaking phase transition, monopoles form as loops around the compactified dimension, with the size of the loops corresponding to the size of the compactified dimension. A monopole adopts a loop configuration even though the size of the compactified dimension is larger than the correlation length of the Higgs field.

If the size of the compactified dimension is much smaller than the correlation length of the Higgs field, monopoles cannot fit into the compactified dimension. To understand what happens in this situation, consider the phase winding of a monopole when it forms a closed loop around the compactified dimension. The orientation of the phase winding at each point on the loop is tangent to the loop (see Sec. 5.3.3). Diametrically opposite points on the loop have opposite phase winding. For a compactified dimension much smaller than the correlation length of the Higgs field, two diametrically opposite points on the loop overlap. In this case a monopole either forms and instantly annihilates, or never forms.

If we assume that the compactified dimension is much smaller than the Hubble horizon, monopoles are small loops (which form around the compactified dimension). A loop which is very small compared to the Hubble horizon will collapse to a point, and can be treated as though it is in non-expanding spacetime. In this situation, the equations of motion for the loop (based on the Nambu-Goto action) are

$$\ddot{\mathbf{x}}(t,l) - \mathbf{x}''(t,l) = 0 \tag{5.120}$$

$$\dot{\mathbf{x}}(t,l) \cdot \mathbf{x}'(t,l) = 0 \tag{5.121}$$

$$\dot{\mathbf{x}}^2(t,l) + \mathbf{x}'^2(t,l) = 1, \tag{5.122}$$

where $\mathbf{x} = (x, y, z, w)$, a dot denotes differentiation with respect to time, t, and a dash denotes differentiation with respect to length, l. The dynamics of a loop in $\mathcal{R}^{4+1}$ can be understood by considering the evolution of a loop in $\mathcal{R}^{3+1}$. For a circular loop in the x-y

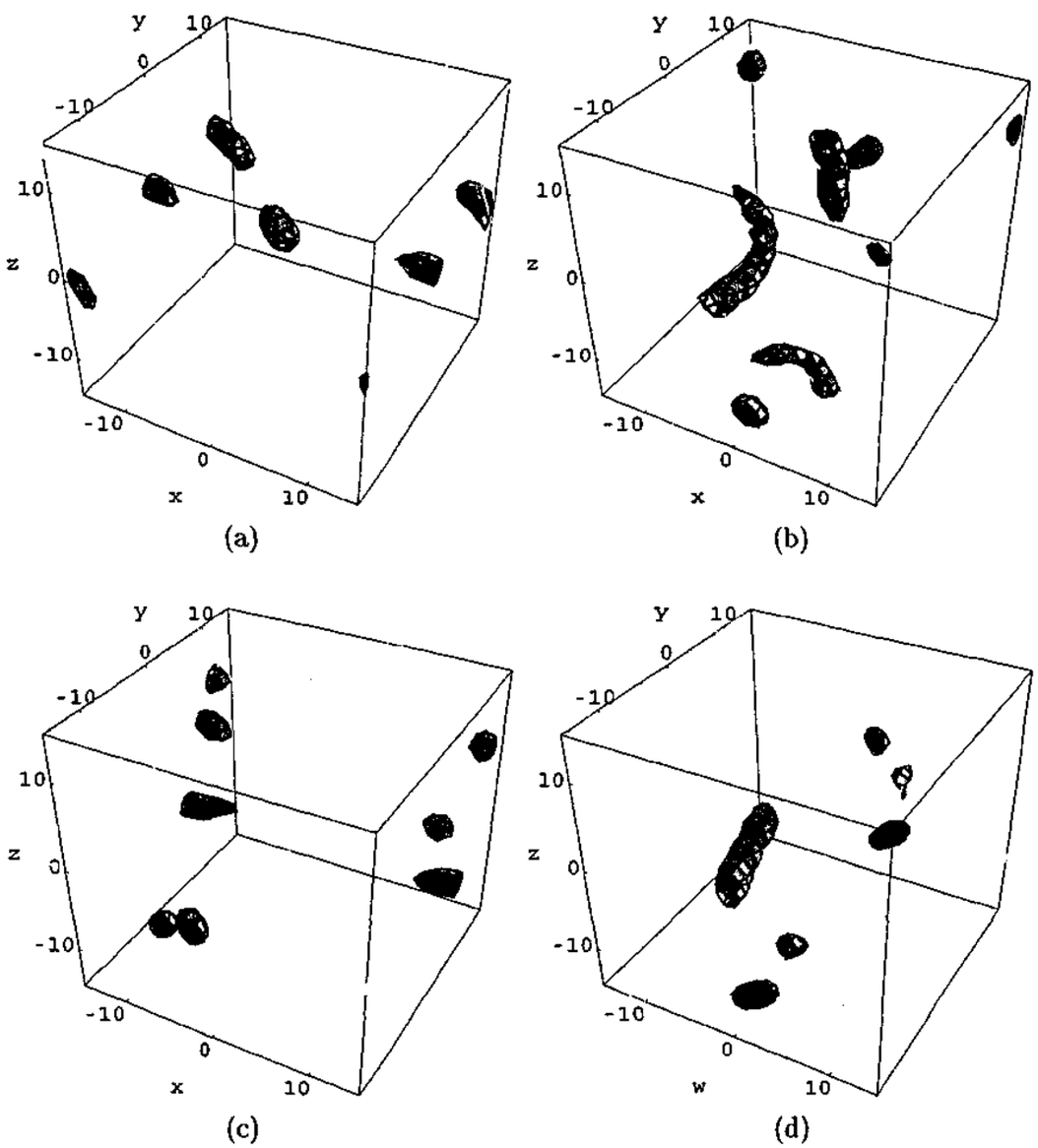

Figure 5.21: Isocontour plots of the energy density ($E/\lambda\eta^4 = 0.1$), showing the formation of monopoles in uncompactified $\mathcal{R}^{4+1}$ spacetime ($t = 25$, $\xi = 1$). (a), (b), and (c) are cross-sections at $w = -7.5$, 0, and 7.5, respectively. These figures show that the Higgs field is not correlated in the w dimension. (d) Cross-section ($x = 0$) showing that monopoles can appear as localized objects.

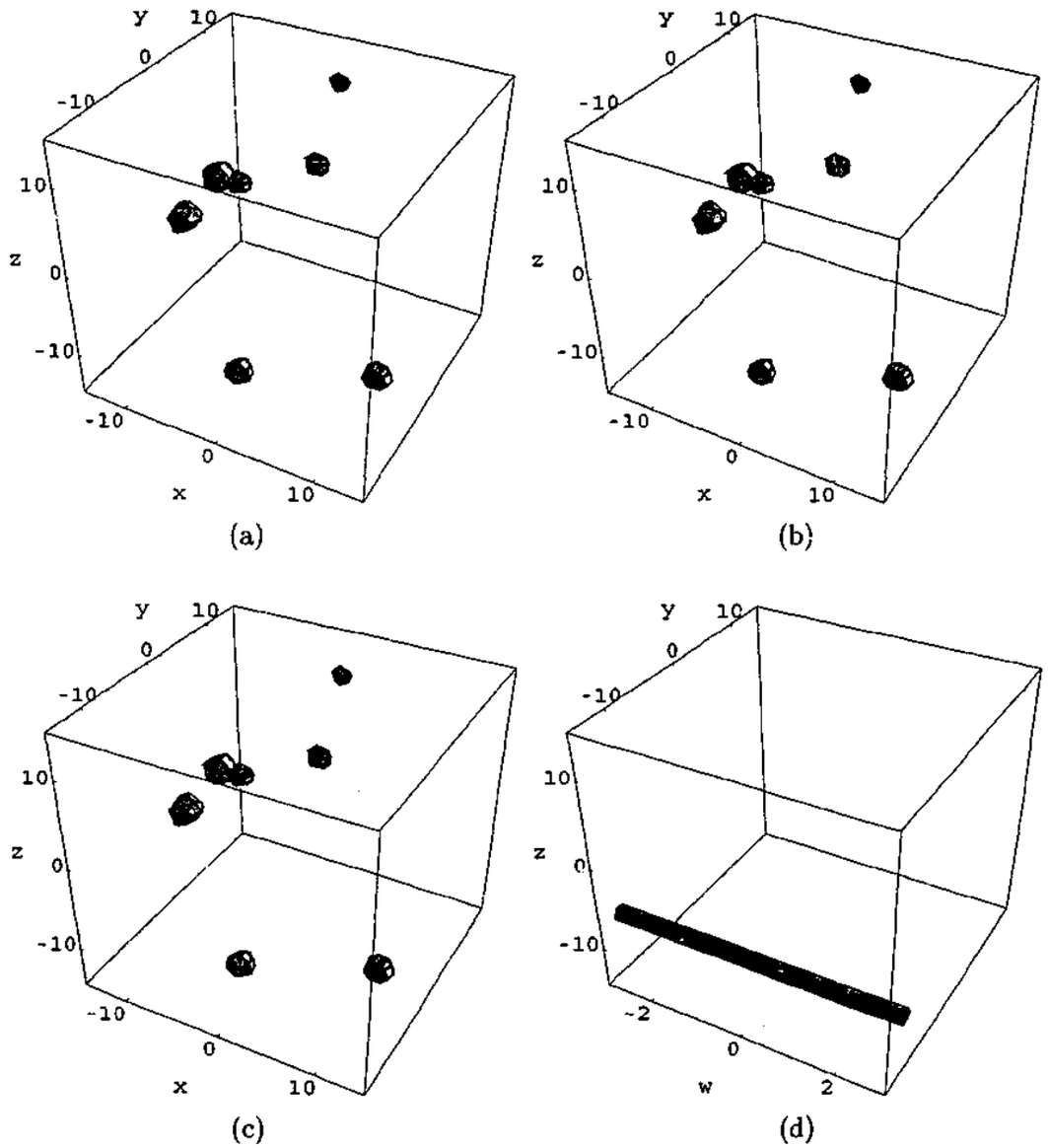

Figure 5.22: Isocontour plots of the energy density ($E/\lambda\eta^4 = 0.1$), showing the formation of monopoles in compactified $\mathcal{R}^{4+1}$ spacetime ($t = 25$, $\xi = 1$). (a), (b), and (c) are cross-sections at $w = -1.5$, 0, and 1.5, respectively. These figures show that the Higgs field is correlated in the compactified dimension. (d) Cross-section ($x = 0$) showing the monopole as an extended object (i.e., a string). Since the two ends of the string are identified, this corresponds to a loop in compactified Kaluza-Klein space, $S^1 \times \mathcal{R}^3$.

plane at $z = 0$, we have (see e.g., Kibble and Turok 1982)

$$x(t,l) = \frac{L}{4\pi}\left[\cos\left(\frac{2\pi(l-t)}{L}\right) + \cos\left(\frac{2\pi(l+t)}{L}\right)\right] \quad (5.123)$$

$$y(t,l) = -\frac{L}{4\pi}\left[\sin\left(\frac{2\pi(l-t)}{L}\right) + \sin\left(\frac{2\pi(l+t)}{L}\right)\right] \quad (5.124)$$

$$z(t,l) = 0, \quad (5.125)$$

where L is the maximum length of the loop. Equations (5.123) - (5.125) describe the collapse and expansion of the Nambu-Goto loop. The length of the loop at $t = 0$ is L. The loop collapses and expands in a series of oscillations with period $L/2$ ($c = 1$). However, cosmic strings intercommute when they self-intersect, and the loop will fragment into smaller loops that eventually annihilate. A cosmic string loop of length L (at $t = 0$) will collapse and annihilate at time $t = L/4$.

The equations describing a loop in compactified Kaluza-Klein spacetime ($S^1 \times \mathcal{R}^{3+1}$) are obtained by noting that the w dimension is periodic in L_w, whence

$$w = \frac{L_w}{2\pi} e^{-2\pi i l/L_w}, \quad (5.126)$$

where l/L_w is a path parameter along the w direction, with $0 \leq l/L_w \leq 1$. Equation (5.126) is re-written as

$$w = w_1 + i w_2, \quad (5.127)$$

where

$$w_1 = \frac{L_w}{2\pi}\cos\left(\frac{2\pi l}{L_w}\right) \quad (5.128)$$

$$w_2 = -\frac{L_w}{2\pi}\sin\left(\frac{2\pi l}{L_w}\right). \quad (5.129)$$

For an oscillating loop, w is expected to depend on l and t, i.e.,

$$w(l,t) = w_1(l,t) + i w_2(l,t), \quad (5.130)$$

The equations of motion of the loop in the w dimension are:

$$\ddot{w}(t,l) - w''(t,l) = 0 \quad (5.131)$$

$$\dot{w}(t,l) \cdot w'(t,l) = 0 \quad (5.132)$$

$$\dot{w}^2(t,l) + w'^2(t,l) = 1, \quad (5.133)$$

The solutions to Eqs. (5.131)-(5.133) are

$$w_1(t,l) = \frac{L_w}{4\pi}\left[\cos\left(\frac{2\pi(l-t)}{L_w}\right)+\cos\left(\frac{2\pi(l+t)}{L_w}\right)\right] \quad (5.134)$$

$$w_2(t,l) = -\frac{L_w}{4\pi}\left[\sin\left(\frac{2\pi(l-t)}{L_w}\right)+\sin\left(\frac{2\pi(l+t)}{L_w}\right)\right]. \quad (5.135)$$

Equations (5.134) and (5.135) describe an oscillating loop in the w dimension. At $t = 0$ Eqs. (5.134) and (5.135) reduce to Eqs. (5.128) and (5.129), respectively. A loop at $t = 0$ has a length corresponding to the size of the compactified dimension. When the loop collapses the Higgs field unwinds and annihilates, and the monopole is removed from the $[x, y, z]$ volume.[21]

Following a cosmological phase transition, monopoles in compactified $\mathcal{R}^{4+1}$ spacetime collapse and annihilate in a time scale comparable to the size of the compactified dimension. For a compactified Kaluza-Klein dimension ($\sim 10^{-18}$ m), monopoles will be removed at approximately 10^{-27} seconds after the phase transition.

These results can be generalized to other topological defects. Of particular interest are domain walls (see Chapter 4). Domain walls form when $\pi_{0=d-p-1}(\mathcal{M}) \neq 0$. In $3+1$ dimensions a domain wall is a two-dimensional object, however, in $4+1$ dimensions it is a three-dimensional object. The dynamics of the wall (in a plane perpendicular to the wall) can be described by the same equations of motion as a string (see e.g., Vilenkin and Shellard 1994). The dynamics of a wall in the compactified Kaluza-Klein space are described by the equations of motion (5.131) - (5.133). A wall with length L_w (at $t = 0$) in the compactified dimension, will collapse and annihilate at time $t = L_w/4$.

We can extend this mechanism to defects in $d+1$ dimensions, with $d-3$ compactified dimensions. For a defect described by the nth-homotopy group, the defect dimension is $p = d - n - 1$. These defects will form "loops" around each compactified dimension $(1, ..., d-3)$, whose length corresponds to the size of the compactified dimension. By extending our results for the collapse and annihilation of a cosmic string loop in $\mathcal{R}^{3+1}$ spacetime (see Sec. 5.3.3), it can be shown that all self-intersecting defect "loops" will annihilate upon collapsing to a point. Diametrically opposite points on the "loop" have opposite phase winding. Once the "loop" collapses to a point the phase unwinds and the "loop" annihilates. Therefore defect " loops" in $\mathcal{R}^{d+1}$ spacetime will quickly collapse and

[21] We assume that spacetime is simply connected, since an investigation of the topology of multiply connected spacetime is beyond the scope of this thesis (see Chapter 6).

annihilate. This leads to the interesting conclusion that, with at least one compactified dimension, defects may not pose a problem for GUT models of the early Universe.

5.7 Concluding remarks

Monopoles are one-dimensional objects in $4+1$ dimensions and their dynamics can be described by the Nambu-Goto action for strings. In homogeneous isotropic $\mathcal{R}^{4+1}$ spacetime, where the extra dimension is large, the evolution of the energy density of monopoles was found to vary as $t^{-1.5}$, while the energy density of the Universe varies as t^{-2}. This implies that monopoles in uncompactified $\mathcal{R}^{4+1}$ spacetime do not have a scaling solution, and invoking an extra dimension does not solve the monopole problem as had been initially anticipated.

The evolution of the energy density of monopoles in $\mathcal{R}^{4+1}$ should reproduce the behaviour of a string network in $\mathcal{R}^{3+1}$, when the size of the compactified dimension is significantly smaller than the observed spatial dimensions. If the size of the compactified dimension is comparable to the correlation length of the Higgs field, a monopole forms a closed loop in the Kaluza-Klein space $S^1 \times \mathcal{R}^3$, whose length is equal to the size of the compactified dimension. In this situation the loop collapses and annihilates in a time scale corresponding to the size of the compactified dimension.

This result was generalized to topological defects in $\mathcal{R}^{d+1}$ spacetime, with $d-3$ compactified dimensions. A topological defect forms a "loop" in each of the compactified dimensions. This "loop" collapses and annihilates in a manner analogous to the collapse of a monopole in a single compactified dimension. In a spacetime with at least one compactified dimension, topological defects collapse and annihilate quickly following their formation, and may not pose a problem for GUTs.

CHAPTER 6

Conclusions and Future Work

Particle cosmology predicts the formation of topological defects in the early Universe, such as cosmic strings, domain walls and monopoles. These cosmic defects can initiate density perturbations, resulting in large scale structure, and imprint anisotropy on the Cosmic Microwave Background Radiation (CMBR) (see e.g., Vilenkin and Shellard 1994). However, recent observations of the CMBR, based on the Wilkinson Microwave Anisotropy Probe (WMAP), found no evidence of topological defects in the early Universe (Bennett *et al.* 2003). This is puzzling, since topological defects are observed in many condensed matter systems (see e.g., Hendry *et al.* 1994 and Zurek 1996), and the underlying principle of symmetry breaking would appear to be ubiquitous in nature. This thesis is devoted to understanding the formation and evolution of topological defects arising in symmetry breaking phase transitions. Numerical simulations were carried out to elucidate the behaviour of vortices in two-dimensional condensates, domain walls in $\mathcal{R}^{3+1}$ spacetime and monopoles in $\mathcal{R}^{4+1}$ spacetime.

In Chapter 2 we examined vortices in a rotating Bose-Einstein condensate (BEC). Rotation of the condensate leads to the formation of a triangular vortex lattice, whose structure follows from minimizing the energy functional for the rotating condensate (see e.g., Castin and Dum 1999). Although the appearance of a vortex lattice follows from the minimization procedure, this approach does not give insight into how vortices are nucleated in a BEC, or the dynamics of vortices once they form. We provide a new perspective on the formation of vortices in a rotating BEC. Rotation of the condensate imprints a background phase gradient on the condensate, leading to a confining potential for vortices. Perturbations at the boundary of the condensate, or anisotropy in the atomic trap, can nucleate vortices (at the boundary) which move into the rotating condensate. Vortices also experience mutually repulsive interactions in the BEC, which arise from the phase gradient of other vortices. The competition between mutually repulsive inter-vortex forces, and the confining potential (due to rotation), results in a stable triangular vortex configuration.

We also considered the formation of vortices via the Kibble-Zurek mechanism (Kibble 1980 and Zurek 1985). Following a symmetry breaking phase transition to the BEC state, conservation of topological charge produces vortex-anti-vortex pairs, whose positions are randomly distributed in the condensate. Rotation of the BEC expels anti-vortices from the condensate, leaving vortices to evolve toward a stable lattice.

Vortex dynamics in a BEC is explained by invoking the inviscid (frictionless) nature of a quantum fluid. In the absence of viscosity, vortices in a rotating quantum fluid do not "feel" the background fluid-flow. However, fluid-flow modifies the velocity profile of the circulating fluid around a vortex, resulting in a pressure difference in the quantum fluid. In this situation, vortices deflect perpendicular to the background fluid-flow. The behaviour of vortices in a BEC is in marked contrast to vortices in a classical fluid. In Sec. 2.3 we investigated an unusual condensate, comprising liquid light, which arises when a high power laser beam enters a material with non-linear (cubic-quintic) refractive index (see Michinel *et al.* 2002). In this situation the electric field in the medium exhibits "self-interactions", analogous to 2- and 3-body interactions in a liquid BEC[1]. The equation of motion describing the LLC contains both first and second order time derivatives. The former endows the condensate with internal "friction" (or "viscosity"). In the LLC, vortices deflect in the direction of the background fluid-flow, and consequently, rotate about each other. This is in contrast to vortices in a BEC, which exhibit mutually repulsive interactions.

In principle, vortices in a LLC may be observed[2] by directing a high power laser beam into a non-linear optical material (e.g., chalcogenide glass). When laser light enters the non-linear medium, a symmetry breaking phase transition to the LLC state occurs at the boundary between vacuum and the medium. Following the phase transition, the scalar field of the condensate will settle down quickly to its ground state. The correlation length of the LLC is expected to be much less than the size of the condensate, and consequently vortices will form.

Exploring vortex dynamics in exotic condensates provides insight into systems for

[1] A liquid BEC may be obtained by exploiting Feshbach resonances to change the two-body interactions of the condensate atoms from repulsive to attractive. In this case the (gaseous) BEC becomes unstable and collapses. As it collapses the condensate number density increases, and three-body repulsive interactions become significant. These stop the BEC from further collapse, and under suitable conditions may allow the BEC to exist in a liquid state.

[2] The existence of the LLC state has not been confirmed by experiment. A preprint outlining a method for imaging vortices in two-dimensional condensates is included at the end of the thesis.

which direct observation is not possible. In Chapter 3 we considered a scalar dark matter condensate, which arises from a weakly interacting degenerate "ether" (WIDGET) (see Silverman and Mallett 2001a). The dark matter condensate is characterized by a self-interacting scalar field, Φ. In the presence of gravity, the symmetry breaking potential for the dark matter condensate is obtained using a stationarity ansatz (see Sec. 3.5.1). It is found that the symmetry breaking potential, in the weak field limit, can be written as $\frac{1}{2}\left(|\Phi|^2 - 1/(1+2V)\right)^2$, where V is the gravitational potential. This symmetry breaking potential gives rise to vortices in the dark matter condensate (see Sec. 3.5). Rotation of the condensate induces a confining potential for vortices. Numerical simulations show that an initially Keplerian vortex number density, $n_v \propto r^{-1.5}$, evolves toward an equilibrium configuration with vortex number density $n_v \propto r^{-1}$; this corresponds to a flat velocity profile for the dark matter condensate. To understand how the observed flat velocity profile for luminous (baryonic) matter arises, we incorporated gravitational interactions between dark matter and baryonic matter. N-body simulations show that dark matter exerts gravitational "drag" on baryonic matter, resulting in the latter quickly adopting the same velocity as the dark matter condensate.

Our numerical simulations highlight an unexpected role for vortices in understanding the rotation curves of spiral galaxies. However, a quantitative understanding of galactic dynamics must include hierarchical mass clustering and gravitational instabilities based on the cold dark matter WIDGET model. This will require a large N-body simulation of structure formation and a three-dimensional model of vortex dynamics. Future work will be directed at performing numerical simulations of gravitationally interacting baryonic matter coupled to the self-interacting dark matter condensate.

Symmetry breaking is pivotal to models of particle cosmology. Grand unified theories (GUTs) predict that the early Universe underwent a series of symmetry breaking phase transitions, resulting in topological defects (Kibble 1976). Monopoles are predicted to form in numbers that conflict with observations inferred from cosmic magnetic fields and proton decay processes in the Sun (Zeldovich and Khlopov 1978, Preskill 1979, Kolb *et al.* 1982, Dimopoulos *et al.* 1982, Freese *et al.* 1983 and Dvali *et al.* 1998). Furthermore, domain walls induce a temperature anisotropy in the CMBR that is inconsistent with observations based on the COBE data and the more recent WMAP data. The overabundance of topological defects, predicted by GUTs, must be reconciled with the absence of

cosmic topological defects in the present epoch. The accepted paradigm for resolving the overabundance problem is inflation (Guth 1981). However, it is worth emphasizing that the physical origin of inflation is unknown (see e.g., Kolb and Turner 1990). A major theme of the thesis was the exploration of alternative scenarios for resolving the cosmic defect problem.

Chapter 4 investigated hybrid defects (i.e., Dirichlet walls), in which cosmic strings terminate on a domain wall (Carroll and Trodden 1998). D-walls are found to be stable for a wide range of parameters, and when perturbations are imposed on the wall. Since stable walls are inconsistent with temperature anisotropy in the CMBR, this would seem to rule out D-walls in the early Universe.

For a D-wall with one string attached to it, numerical simulations show that the string exerts tension on the wall, pulling it in the direction of string tension. An interesting situation arises when two domain walls are connected by a string. Since the string exerts tension on the walls, they are pulled toward each other. As the walls collide, the ends of the string come into contact, and the string unwinds and annihilates. This nucleates a hole in the walls, which propagates outward at almost the speed of light, resulting in the annihilation of the domain walls. This process is analogous to the Langacker-Pi mechanism for monopoles. Hybrid defects consisting of strings terminating on domain walls will quickly annihilate, rapidly decreasing the energy density of the D-wall network. The annihilation of D-walls has implications for monopoles located between the walls. As the walls are pulled toward each other, monopoles located between the two domain walls collide with the walls. Upon collision, symmetry restoration occurs in the Higgs field of the monopole, and the monopole annihilates. Once the monopoles are removed, the walls collide and annihilate. This scenario provides a viable mechanism to obviate both the monopole and domain wall problem in particle cosmology. However, the D-wall model requires fine tuning of the coupling parameters and symmetry breaking scale. Quantitative understanding of D-wall dynamics will require a numerical simulation of a complex D-wall network, in which multiple cosmic strings terminate on domain walls. Future work will be directed at elucidating the cosmological implications of a D-wall network in an expanding Universe.

In Chapter 5 we considered alternative scenarios for resolving the cosmic defect problem. Specifically we investigated the formation and evolution of monopoles in $4+1$ dimensions. In $\mathcal{R}^{4+1}$ spacetime, monopoles are one-dimensional objects, which exhibit string-like behaviour. It is well known that a cosmic string network in $3+1$ dimensions has a scaling solution, i.e., the energy of the network decreases at the same rate as the energy of the expanding Universe (Albrecht and Turok 1989, Allen and Shellard 1990, Bennett and Bouchet 1990). We examined the evolution of a string network in $\mathcal{R}^{4+1}$ spacetime, where the extra dimension was uncompactified, i.e., comparable to the other three spatial dimensions. It is found that strings in uncompactified $(4+1)$-dimensional spacetime rarely collide with each other. The energy density of the string network decreases more slowly than the energy density of the Universe; consequently, a string network in $\mathcal{R}^{4+1}$ does not have a scaling solution, and the monopole problem persists in higher dimensions. On this basis we can rule out an uncompactified (extra) dimension as a way of resolving the monopole problem in the early Universe.

Chapter 5 also considered the situation where the size of the extra dimension is much smaller than the three spatial dimensions, i.e., compactified Kaluza-Klein space. Experimental observations constrain the size of the compactified Kaluza-Klein dimension to less than 10^{-18} m (Kostelecký and Samuel 1991), which is of the order of the correlation length of the Higgs field (following a GUT scale symmetry breaking phase transition). In this case it is found that monopoles form loops around the compactified dimension, with the length of the loop corresponding to the size of the compactified dimension. The dynamics of the loop can be described by the Nambu-Goto action, which predicts that a loop will collapse to a point in a time corresponding to $t = L/2$, where L is the length of the compactified dimension. When a loop collapses to a point, it self-intersects and the phase unwinds. This results in the annihilation of the loop. If we set the size of the compactified dimension to $\sim 10^{-18}$ m, monopoles will collapse and annihilate in $\sim 10^{-27}$ seconds following a cosmological phase transition.

This result was generalized to topological defects in $\mathcal{R}^{d+1}$ spacetime, with $d-3$ compactified dimensions (see Sec. 5.6). The Kibble mechanism predicts that for compactified dimensions of size less than (or comparable to) the correlation length of the Higgs field, the defect will form a "loop" in each of the compactified dimensions. A topological defect

"loop" will collapse and annihilate. This suggests that introducing at least one compactified (extra) dimension provides a mechanism for avoiding the overabundance of topological defects in the early Universe.

In arriving at this conclusion we have implicitly assumed that the compactified dimension is simply connected. However, neither Einstein's theory of general relativity, nor particle physics, prescribes the topology of spacetime. A detailed investigation of multiply connected spacetime is beyond the scope of this thesis; nevertheless, it is interesting to speculate on the topology of the compactified dimension and the mechanism by which it can arise.

If we assume a compactified Kaluza-Klein space, with topology $S^1 \times \mathcal{R}^{3+1}$, the compactified dimension may be written as

$$w = |w|e^{i\theta}, \tag{6.1}$$

where $2\pi|w|$ is the compactification size and θ is the "phase angle" around the compactified dimension. A slice at constant "phase angle" gives $\mathcal{R}^{3+1}$ spacetime. Equation (6.1) is trivially decomposed into

$$w = w_1 + iw_2 \quad (w_1, w_2 \in \mathbb{R}). \tag{6.2}$$

To construct a simply connected compactified dimension, we postulate that the Universe is endowed with two extra spatial dimensions, w_1 and w_2. In this case the Universe is described by (5+1)-dimensional spacetime. The compactified Kaluza-Klein space, $S^1 \times \mathcal{R}^3$, can be "constructed" from an $\mathcal{R}^5$ manifold by ascribing a potential energy[3] to the two extra dimensions. If the potential energy density has $U(1)$ symmetry, with minima lying on a circle S^1, then we may consider compactified Kaluza-Klein space, $S^1 \times \mathcal{R}^3$, as the vacuum manifold of $\mathcal{R}^5$.

Consider the expansion rate of compactified Kaluza-Klein space. The expansion velocity, v, of the three observable spatial dimensions is given by

$$v = \frac{\dot{a}}{a} L = hL, \tag{6.3}$$

where a is the scale factor, h is Hubble's constant and L is the spatial size of the three uncompactified dimensions. The expansion velocity, v_w, of the compactified dimension

[3]The energy associated with the extra dimensions is analogous to vacuum energy, which is a fundamental prediction of quantum field theory. Vacuum energy is incorporated in Einstein's theory of general relativity by invoking a cosmological constant term; this is required to explain the accelerated rate of expansion of the Universe (see e.g., Carroll 2001).

may be written as

$$v_w = \frac{\dot{a}_w}{a_w} = 2\pi h_w |w|, \tag{6.4}$$

where a_w is the scale factor, h_w is Hubble's constant and $2\pi|w|$ is the spatial extent of the compactified dimension. Assuming $a \propto t^n$ and $a_w \propto t^m$ (where n and m are real numbers), the Friedmann equations predict that $h_w/h = \pm 1$ (see Sec. 5.5.1). Therefore we obtain $v_w = \pm 2\pi v|w|/L$, and for $|w| \ll L$ we have $v_w \ll v$. As a first approximation we assume that the compactified dimension is static compared to the three uncompactified spatial dimensions. The simplest potential for a static compactified dimension, with $U(1)$ symmetry, is given by

$$V(|w|) = \frac{\lambda_w}{4}\left(|w|^2 - \eta_w^2\right)^2, \tag{6.5}$$

where η_w is the symmetry breaking scale, and $\lambda_w \eta_w^4/4$ is the energy density difference between the symmetric and non-symmetric ground states of the compactified dimension. Figure 6.1 shows the shape of the symmetry breaking potential (6.5), with the compactified dimension "located" on the ring of minima, S^1. Figure 6.1 (b) shows a schematic representation of the compactified four-dimensional Kaluza-Klein space, $S^1 \times \mathcal{R}^3$. The topology of the simply connected compactified dimension is S^1. Simply "connectedness" is evident in Fig. 6.1 (a), where a loop around the compactified dimension can be contracted to a point by leaving the vacuum state $\langle|w|\rangle = \eta_w$. However, since the energy density difference between the "false vacuum" (located at $\langle|w|\rangle = 0$) and the "true vacuum" ($\langle|w|\rangle = \eta_w$) is $\lambda_w \eta_w^4/4$, and the length of the compactified dimension is $2\pi|w|$, there is an energy cost of $2\pi|w|\lambda_w\eta_w^4/4$ in contracting the loop.

Without performing detailed numerical simulations, we can appreciate the dynamics of a defect in the compactified dimension by considering the behaviour of the Higgs field. The potential of the Higgs field in the compactified dimension can be written as

$$V(|w|, |\Phi|) = \frac{\lambda}{4}(\Phi_a\Phi_a - \eta^2)^2 + \frac{\lambda_w}{4}\left(|w|^2 - \eta_w^2\right)^2 \Phi_a\Phi_a, \tag{6.6}$$

where Φ_a is the scalar field of the topological defect ($\Phi_a\Phi_a = \Phi_1^2 + \Phi_2^2 + ... = |\Phi|^2$), λ is the self-coupling strength and η is the symmetry breaking scale of the Φ-field. Minimizing the potential (6.6) with respect to $|\Phi|$ we obtain

$$|\Phi|^2 = \eta^2 - \frac{\lambda_w}{2\lambda}\left(|w|^2 - \eta_w^2\right)^2. \tag{6.7}$$

Plots of $|\Phi|^2$ as a function of $|w|$ are shown in Fig. 6.2. For $\eta^2 > \lambda_w\eta^2/2\lambda$, the Φ-field is non zero at $w = 0$; however, for $\eta^2 \leq \lambda_w\eta^2/2\lambda$, the Φ-field vanishes at $w = 0$. This suggests that the non-vanishing Φ-field is confined to the compactified dimension.

In general, topological defects form loops around the compactified dimension, where the magnitude of the Higgs field is non zero, i.e., $|\Phi| \neq 0$. For regions where $|w| \neq \eta_w$, the defects are unstable and move in the direction of decreasing magnitude of the Higgs field.[4] Topological defects will form when $|w| \sim \eta_w$, with length $2\pi|w|$ around the compactified dimension. Due to string tension $\sim\mu/|w|$, where μ is the linear mass density, the loop will collapse inwards. For $\eta^2 < \lambda_w\eta^2/2\lambda$, the Φ-field vanishes before the loop collapses to a point. As the loop shrinks, $|\Phi| \to 0$, and symmetry restoration occurs in the Φ-field. In this case, the loop annihilates before collapsing to a point. For $\eta^2 \geq \lambda_w\eta^2/2\lambda$, the loop collapses to a point, the phase unwinds and it annihilates. Thus topological defects will be removed in a time comparable to, or less than, the size of the compactified dimension.

A numerical simulation of topological defects in compactified $S^1 \times \mathcal{R}^{3+1}$ spacetime will be computationally intensive. Consider the simpler situation in which cosmic strings wrap around a compactified dimension in $S^1 \times \mathcal{R}^{1+1}$ spacetime. The Lagrangian for the string is written as

$$\mathcal{L} = \overline{D_\mu\Phi}D^\mu\Phi - \frac{1}{4}F_{\mu\nu}F^{\mu\nu} - \frac{\lambda}{4}\left(|\Phi|^2 - \eta^2\right)^2 - \frac{\lambda_w}{4}\left(|w|^2 - \eta_w^2\right)^2|\Phi|^2, \qquad (6.8)$$

where Φ is a complex scalar field describing the string, $F_{\mu\nu}$ is the electromagnetic field tensor, λ is the self coupling strength and η is the symmetry breaking scale of the Φ-field. In the absence of a gauge field, Eq. (6.8) is analogous to the model of a BEC with an atomic trap potential given by $\lambda_w\left(|w|^2 - \eta_w^2\right)^2/4$. In principle, experiments can be performed with a BEC to confirm the collapse and annihilation of a topological defect loop in the "compactified" dimension. This may be accomplished by replacing the harmonic trap potential of the BEC, $\frac{1}{2}m\omega^2(x^2+y^2)|\Psi|^2$, with the modified trap potential $\frac{1}{4}\lambda_w(x^2+y^2-\eta_w^2)^2|\Psi|^2$, where λ_w and η_w are parameters used to adjust the location, shape and size of the condensate. With this trap potential, the BEC will be confined to the "compactified" dimeusion, i.e., it has the shape of a ring oriented in the z direction with radius η_w. Once the condensate is obtained, a vortex loop is constructed in the condensate by rotating the

[4]This is analogous to the behaviour of vortices in a non-rotating Bose-Einstein condensate. A vortex located outside the center of the condensate will move in the direction of decreasing condensate number density (see Sec. 2.2.1).

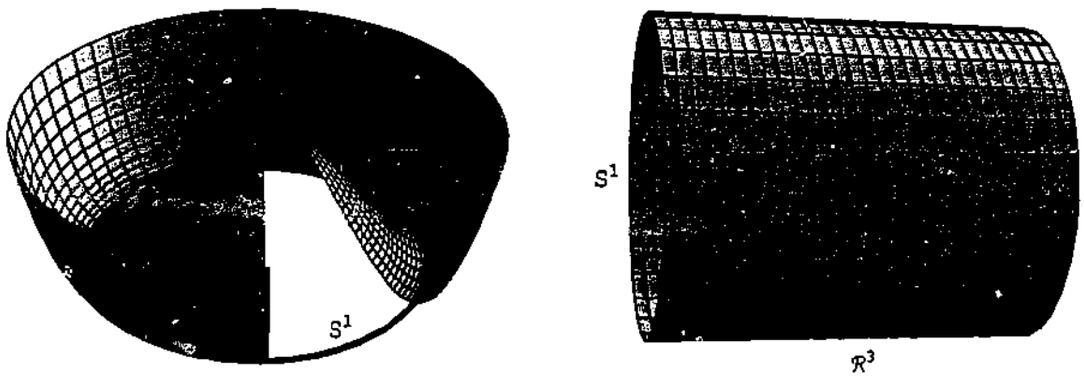

Figure 6.1: (a) Potential for the compactified dimension S^1. The compactified Kaluza-Klein dimension is simply connected, since a loop around the compactified dimension can be contracted to a point. (b) Schematic representation of compactified Kaluza-Klein space, $S^1 \times \mathcal{R}^3$.

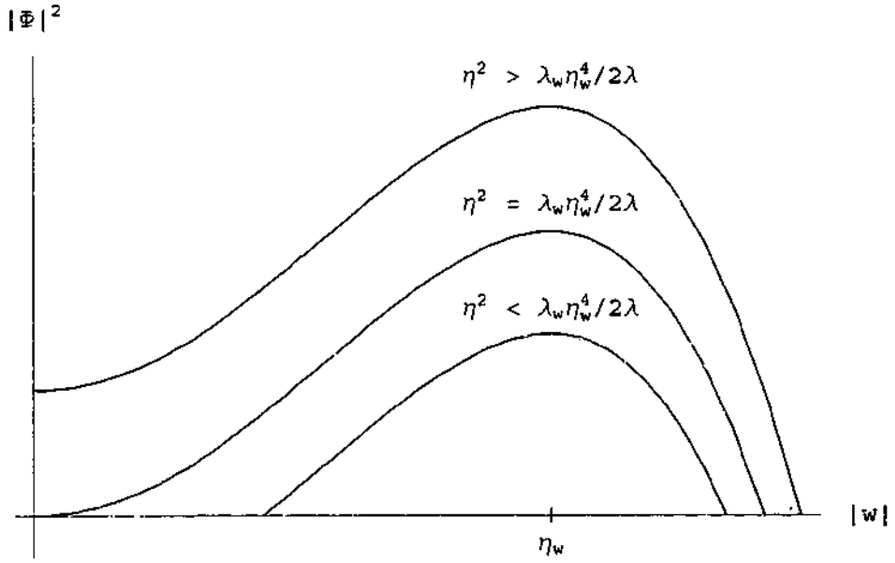

Figure 6.2: Plots of $|\Phi|^2$ as a function of $|w|$, showing confinement of the Higgs field in the compactified Kaluza-Klein space, $S^1 \times \mathcal{R}^3$. For $\eta^2 \leq \lambda_w \eta_w^4/2\lambda$ the non-vanishing Φ-field is confined to the compactified dimension, with its maximum value at $|w| = \eta_w$, whereas for $\eta^2 > \lambda_w \eta_w^4/2\lambda$, the Φ-field is non zero at $|w| = 0$.

condensate about its center. The behaviour of the loop can be investigated by turning off the rotation, and observing its collapse and annihilation. The collapse and annihilation of a vortex loop in a BEC may provide insight into the behaviour of topological defects in "compactified" dimensions.

In summary, the formation of topological defects in the early Universe is a major prediction of particle cosmology. However, defects are predicted to form in numbers that conflict with observation. Various scenarios have been proposed in this thesis to resolve the overabundance problem. A promising avenue utilizes a simply connected compactified Kaluza-Klein space. Understanding the formation and evolution of topological defects in compactified dimensions is a major challenge for future work.

APPENDIX A

Numerical Techniques

This appendix describes the numerical techniques used for modeling the dynamics of topological defects, including vortices in two-dimensional condensates (Chapter 2), vortices in the dark matter condensate (Chapter 3), Dirichlet defects (Chapter 4), and cosmic string networks in $\mathcal{R}^{3+1}$ and $\mathcal{R}^{4+1}$ spacetime (Chapter 5).

A.1 Finite difference approximation

For the models considered in this thesis we replace the equations of motion with a finite difference approximation. For example, in $1+1$ dimensions a continuous function $f(t,x)$ is discretized on a lattice, in which case $f(t,x)$ is replaced by $f_{m,n}$, defined as

$$f_{m,n} = f(m\Delta t, n\Delta x), \tag{A.1}$$

where Δt is the temporal step, Δx is the spatial step, and m and n are integers representing the lattice coordinates in $1+1$ dimensions. Derivatives of $f(t,x)$, with respective to x, are described by the central difference approximation (see e.g., Smith 1985)

$$\frac{\partial f}{\partial x} \simeq \frac{f_{m,n+1} - f_{m,n-1}}{2\Delta x} + \mathcal{O}(\Delta x^2), \tag{A.2}$$

$$\frac{\partial^2 f}{\partial x^2} \simeq \frac{f_{m,n+1} - 2f_{m,n} + f_{m,n-1}}{\Delta x^2} + \mathcal{O}(\Delta x^4). \tag{A.3}$$

Clearly the accuracy of the finite different scheme is limited to $\mathcal{O}(\Delta x^2)$. We can apply the numerical discretization scheme to the equation of motion for the Goldstone model (1.27).[1] Utilizing the central differences (A.2) and (A.3), the evolution of the equation of motion (1.12) in the absence of a gauge field is obtained by finding the Higgs field at the next time step, $\Phi_{m+1,n}$, based on the Higgs field at the present time step and the previous time, $\Phi_{m-1,n}$. Utilizing a leap-frog method, the equation of motion for the Goldstone model is given by

[1] The Goldstone model is the abelian Higgs model (1.9) in the absence of a gauge field. The equation of motion for the Goldstone model is determined from Eq. (1.12) by setting the gauge field to zero.

$$\Phi_{m+1,n} = 2\Phi_{m,n} - \Phi_{m-1,n} + \left(\frac{\Delta t}{\Delta x}\right)^2 (\Phi_{m,n-1} - 2\Phi_{m,n} + \Phi_{m,n+1}) - \Delta t^2 \Phi_{m,n} \left(|\Phi_{m,n}|^2 - 1\right). \quad \text{(A.4)}$$

The coordinates are measured in units of the Compton length $1/\sqrt{\lambda}\eta$ of the Higgs field (λ is the self-coupling strength of the Higgs field and η is the symmetry breaking scale). Equation (A.4) is easily generalized to higher spatial dimensions.

Numerical simulations of a BEC are based on the Gross-Pitaevskii (GP) equation, or non-linear Schödinger equation, evolved in imaginary time, $\tau = it$. Evolution of the GP equation, based on a leap-frog (Euler) method, is only accurate to $\mathcal{O}(\Delta\tau)$. To improve the accuracy we use Runge-Kutta integration, which is accurate to $\mathcal{O}(\Delta\tau^4)$.

An alternative approach to modeling cosmic strings is to exploit lattice gauge theory, where the gauge symmetry is preserved by the discretized fields (Kogut 1983 and Creutz *et al.* 1983). However, the finite difference scheme used in this thesis is sufficient to understand the formation and evolution of topological defects (see Chapters 4 and 5). Numerical simulations of abelian string dynamics based on finite difference approximations are consistent with the results obtained using lattice gauge techniques (see e.g., Moriarty *et al.* 1988 and Myers *et al.* 1992). Our numerical schemes utilize the Lorentz condition $\partial^\mu A_\mu = 0$, in contrast to lattice gauge techniques, which necessitate the use of the temporal gauge, $A_t = 0$.

The equations of motion are re-scaled by performing transformations of the coordinates and fields to eliminate free parameters. The re-scaling schemes are discussed in Secs. 2.2.1 and 2.2.4 for the GP equation, Sec. 2.3.1 for the LLC, Secs. 3.4.1 and 3.5.1 for the dark matter condensate, Sec. 4.2 for the Z_2 domain wall, and in Secs. 5.2.1 and 5.3.1 for $SO(3)$ monopole formation and the abelian-Higgs model. Tables A.1 - A.8 summarize the numerical simulations performed in this thesis.

A.2 Initial and boundary conditions

To construct the initial conditions involving vortices and strings, we numerically solve for a static vortex (see Secs. 2.3.2, 3.4.1, 4.3.4 and 5.3.2). Once the static vortex solution is obtained, the initial conditions are constructed by utilizing the Abrikosov ansatz

Type	Grid size	Lattice spacing	Section
2D $U(1)$ vortex formation	$400^2 \times 30$	$\Delta h = 0.3$, $\Delta t = 0.1$	1.4.2

Table A.1: Parameters used to simulate vortex formation based on the Kibble mechanism.

Type	Grid size	Lattice spacing	Section
BEC number density	500	$\Delta h = 0.05$	2.2.1
BEC vortex solution	500	$\Delta h = 0.05$	2.2.1
BEC vortex dynamics	$600^2 \times 50,000$	$\Delta h = 0.1$, $\Delta \tau = 0.001$	2.2.4
BEC vortex formation	$600^2 \times 100,000$	$\Delta h = 0.1$, $\Delta \tau = 0.001$	2.2.5
LLC vortex solution	3,000	$\Delta h = 0.5$	2.3.2
Two LLC vortices	$3,000^2 \times 7,000$	$\Delta h = 0.5$, $\Delta t = 0.1$	2.3.2
Multiple LLC vortices	$3,000^2 \times 6,000$	$\Delta h = 0.5$, $\Delta t = 0.1$	2.3.2

Table A.2: Parameters used to simulate vortices in a Bose-Einstein condensate (BEC) (τ denotes imaginary time), and vortices in a liquid light condensate (LLC) (t denotes real time).

Type	Grid size	Lattice spacing	Section
DMC vortex solution	4,000	$\Delta h = 0.1$	3.4.1
Vortex dynamics	$1,400^2 \times 6,000$	$\Delta h = 0.1$, $\Delta t = 0.01$	3.4.1
Vortex configuration	$2,400^2 \times 9,000$	$\Delta h = 1.0$, $\Delta t = 0.1$	3.4.2
DMC distribution	3,000	$\Delta h = 1.0$	3.5.1
Vortices in a DMC	$4,600^2 \times 2,500$	$\Delta h = 1.0$, $\Delta t = 0.2$	3.5.4

Table A.3: Parameters used to simulate vortices in a rotating dark matter condensate (DMC).

Type	Particles	Simulation frame	Time step	Section
Gravitational drag of DMC	10^4	$32,000^2 \times 10,000$	$\Delta t = 0.1$	3.6

Table A.4: Parameters used in the N-body simulation of gravitational drag between dark matter and baryonic matter.

Type	Grid size	Lattice spacing	Section
Domain wall formation	$200^3 \times 500$	$\Delta h = 0.5$, $\Delta t = 0.1$	4.2.1
D-wall dynamics	$200^3 \times 1,000$	$\Delta h = 0.055$, $\Delta t = 0.02$	4.3

Table A.5: Parameters used to investigate the stability and dynamics of a Dirichlet domain wall (D-wall).

Type	Grid size	Lattice spacing	Section
3D $SO(3)$ monopole formation	$140^3 \times 500$	$\Delta h = 0.5$, $\Delta t = 0.1$	5.2.1
Abelian-Higgs vortex solution	300	$\Delta h = 0.1$	5.3.2
Intercommutation and loop collapse	$140^3 \times 250$	$\Delta h = 0.5$, $\Delta t = 0.1$	5.3.3

Table A.6: Parameters used to simulate monopoles and strings in $3+1$ dimensions.

Type	Simulation frame	Length parameters	Section
3D Cosmic strings	$(20\xi)^3 \times (4{,}000\Delta\tau)$	$\Delta\sigma = 0.05$, $\Delta\tau = 0.005$	5.4
4D Cosmic strings	$(10\xi)^4 \times (3{,}500\Delta\tau)$	$\Delta\sigma = 0.05$, $\Delta\tau = 0.0025$	5.5

Table A.7: Parameters used to simulate a cosmic string network in $\mathcal{R}^{3+1}$ and $\mathcal{R}^{4+1}$ spacetime. ξ is the correlation length, τ is the conformal time and σ is a length parameter (see Sec. 5.4.3). In $3+1$ dimensions $\xi = 0.5$ and the initial conformal time lies in the range $2 \leq \tau_i \leq 5$, whereas in $4+1$ dimensions $0.1 \leq \xi \leq 0.2$ and $\tau_i = 1$.

Type	Grid size	Lattice spacing	Section
4D $SO(3)$ monopoles	$30^4 \times 500$	$\Delta h = 1.0$, $0.1 \leq \Delta h_w \leq 1$, $\Delta t = 0.05$	5.6

Table A.8: Parameters used to simulate monopole formation in compactified $\mathcal{R}^{4+1}$ spacetime. Δh is the spatial step in the x, y and z dimensions, whereas Δh_w is the spatial step in the compactified dimension.

(Abrikosov 1957)

$$\Phi(\mathbf{r}) = \prod_{i=1}^{n_s} \phi(\mathbf{r} - \mathbf{r}_i), \tag{A.5}$$

$$A_\mu(\mathbf{r}) = \sum_{i=1}^{n_s} a_\mu(\mathbf{r} - \mathbf{r}_i), \tag{A.6}$$

where n_s is the number of superposed vortices and $\mathbf{r}_i$ denotes the position of the i-th vortex.

Numerical simulation of the formation of topological defects following a phase transition exploits the Kibble-Zurek mechanism (Kibble 1976 and Zurek 1985). The initial conditions are obtained by assigning random values (between -1 and 1) to the Higgs field at each lattice point. The field is constrained to its ground (vacuum) state expectation value. A gauge field arises naturally via a local gauge transformation; the value of the gauge field is set to zero initially. For a cosmic string network simulation based on the

Nambu-Goto action (see Secs. 5.4 and 5.5), the initial condition is obtained by using the Vachaspati-Vilenkin method (Vachaspati and Vilenkin 1984). This method emulates the Kibble mechanism for the formation of cosmic strings in the early Universe (see Sec. 5.4.4). In $\mathcal{R}^{4+1}$ spacetime the initial condition is obtained by extending the Vachaspati-Vilenkin method to four spatial dimensions (see Sec. 5.5).

The boundary conditions in our numerical schemes depend on the nature of the scalar field (or wavefunction) on the boundary, or on the topological defect configuration. For example, the wavefunction of a BEC in a rotating trap vanishes on the boundary. Numerical simulations of vortices in the LLC, vortices in the rotating dark matter condensate and Dirichlet topological defects, all exploit free boundary conditions, where the gradient of the scalar field vanishes on the boundary. Periodic boundary conditions are employed for simulations of defect formation (Secs. 1.4.2, 4.2.1, 5.2.1 and 5.6), N-body simulations (Sec. 3.6), and numerical simulations of a cosmic string network in $\mathcal{R}^{3+1}$ and $\mathcal{R}^{4+1}$ spacetime (Secs. 5.4 and 5.5). In these situations the simulation domain has a T^2, T^3 or T^4 topology for two-, three- or four-dimensional simulations.

A.3 Stability criterion

Numerical finite difference schemes are prone to instability. To establish the stability criterion, we utilize the von Neumann method (see e.g., Smith 1985), writing $\Phi_{m,n}$ as

$$\Phi_{m,n} = e^{i\alpha n\Delta x}\xi^m, \tag{A.7}$$

where the wavevector α is a constant, and $\xi = e^{\alpha\Delta t}$ is called the amplification factor. Equation (A.7) implies that $\Phi_{m,n}$ converges for $m \to \infty$ (i.e., $\Delta t \to 0$) if and only if $|\xi| \leq 1$.

Substituting Eq. (A.7) into the equation of motion, Eq. (A.4), results in

$$\xi^2 - 2A\xi + 1 = 0, \tag{A.8}$$

where A is given by

$$A = 1 - 2\left(\frac{\Delta t}{\Delta x}\right)^2 \sin^2\left(\frac{\alpha\Delta x}{2}\right) - \frac{\Delta t^2}{2}\left(|\Phi_{m,n}|^2 - 1\right) \tag{A.9}$$

Equation (A.8) has the solution

$$\xi = A \pm \sqrt{A^2 - 1}. \tag{A.10}$$

The stability criterion requires

$$|A| \leq 1. \tag{A.11}$$

For the simulations reported in this thesis $0 \leq |\Phi_{m,n}| \leq 1$ at the start of each simulation and $(\Delta t)^2 \ll 1$. Consequently, $\Delta t^2 \left| |\Phi_{m,n}|^2 - 1 \right| \ll 1$. Based on these considerations, the stability criterion (A.11) becomes $\Delta t < \Delta x$. For a d-dimensional space, the stability criterion is generalized to the Courant-Friedrichs-Lewy (CFL) condition (see e.g., Courant *et al.* 1928), where

$$\sqrt{d}\left(\frac{\Delta t}{\Delta x}\right) < 1. \tag{A.12}$$

The CFL stability condition (A.12) for the wave equation (A.4) can be understood in terms of the accumulation of noise in the scalar field $\Phi_{m,n}$, which propagates over a distance $\Delta x = \Delta t$. Since the value of the field at the next time step, $\Phi_{m+1,n}$, utilizes $\Phi_{m,n+1}$, $\Phi_{m,n-1}$ and the field at the previous time step, $\Phi_{m-1,n}$, any noise induced in $\Phi_{m-1,n}$ will propagate to $\Phi_{m,n+1}$ and $\Phi_{m,n-1}$ if $\Delta t \geq \Delta x$. This results in a numerical instability when the equation of motion is evolved for a long time. However, for $\Delta t < \Delta x$ the noise induced in $\Phi_{m,n-1}$ can never propagate to $\Phi_{m,n+1}$ and $\Phi_{m,n-1}$, and therefore the numerical scheme is stable.[2]

The CFL condition in $1+1$ dimensions also applies to the equations of motion for the left mover, $\mathbf{l}$, and right mover, $\mathbf{r}$, that are used to evolve strings in an expanding spacetime (see Chapter 5). In the next section, we discuss the numerical techniques used to solve the equations of motion of relativistic strings and the concomitant CFL condition.

A.4 Left and right movers and the CFL condition

The dynamics of relativistic strings in an expanding spacetime are governed by Eqs. (5.62) and (5.63). A direct numerical solution to Eqs. (5.62) and (5.63) based on a finite difference scheme is prone to numerical errors, and does not accurately evolve small scale structure on the strings. The accuracy can be improved by numerically solving the equations of motion in terms of the left and right movers (see Sec. 5.4). Substituting Eqs. (5.71) and (5.72) into Eqs. (5.62) and (5.63), the equations of motion of relativistic strings are given by

$$\dot{\mathbf{l}} = \frac{\mathbf{l}'}{\epsilon} + h\left[(\mathbf{l}\cdot\mathbf{r})\mathbf{l} - \mathbf{r}\right], \tag{A.13}$$

[2]Noise propagates at the speed of light, so in a time step Δt (one iteration) it can never reach the neighboring points at the next time step (iteration).

$$\dot{\mathbf{r}} = \frac{\mathbf{r}'}{\epsilon} + h\left[(\mathbf{l}\cdot\mathbf{r})\mathbf{r} + \mathbf{l}\right], \tag{A.14}$$

$$\dot{\epsilon} = -h\epsilon(\mathbf{l}\cdot\mathbf{r} + \mathbf{1}). \tag{A.15}$$

The gradient terms in Eqs. (A.13) and (A.14) can be eliminated by considering the next time step of the left movers at position $\sigma - \Delta\tau/\epsilon$ and the right movers at position $\sigma + \Delta\tau/\epsilon$. Using a first order Taylor expansion, a left mover at position $\sigma - \Delta\tau/\epsilon$ may be written as

$$\begin{aligned}
\mathbf{l}(\sigma - \frac{\Delta\tau}{\epsilon}, \tau + \Delta\tau) &= \mathbf{l}(\sigma,\tau) + \Delta\tau\dot{\mathbf{l}}(\sigma,\tau) - \frac{\Delta\tau}{\epsilon}\mathbf{l}'(\sigma,\tau), \\
&= \mathbf{l} + \Delta\tau\left[\frac{\mathbf{l}'}{\epsilon} + h(\mathbf{l}\cdot\mathbf{r})\mathbf{l} - h\mathbf{r}\right] - \frac{\Delta\tau}{\epsilon}\mathbf{l}', \\
&= \mathbf{l} + h\Delta\tau\left[(\mathbf{l}\cdot\mathbf{r})\mathbf{l} - \mathbf{r}\right].
\end{aligned} \tag{A.16}$$

Likewise a right mover at position $\sigma + \Delta\tau/\epsilon$ is specified by

$$\mathbf{r}(\sigma + \frac{\Delta\tau}{\epsilon}, \tau + \Delta\tau) = \mathbf{r} + h\Delta\tau\left[(\mathbf{l}\cdot\mathbf{r})\mathbf{r} + \mathbf{l}\right]. \tag{A.17}$$

Equations (A.16) and (A.17) can be written as

$$\dot{\mathbf{l}} = h\left[(\mathbf{l}\cdot\mathbf{r})\mathbf{l} - \mathbf{r}\right], \tag{A.18}$$

$$\dot{\mathbf{r}} = h\left[(\mathbf{l}\cdot\mathbf{r})\mathbf{r} + \mathbf{l}\right], \tag{A.19}$$

with the left and right movers evolving on the characteristic curves $\sigma - \Delta\tau/\epsilon$ and $\sigma + \Delta\tau/\epsilon$, respectively.

Figure A.1 shows the evolution of the left and right movers at two different conformal time steps. Strings are represented by points (parameterized by σ), with each point separated from its nearest neighbor by $\Delta\sigma$. These points are marked by a cross in Fig. A.1. The left and right movers are stored at ... $n-1$, n, $n+1$, ..., which are half-way between two nearest neighbor points. The left movers evolve on the characteristic curve $\sigma - \Delta\tau/\epsilon$, with $\mathbf{l}(\sigma_n, \tau + \Delta\tau)$ found by interpolating between $\mathbf{l}(\sigma_n - \Delta\tau/\epsilon_n, \tau + \Delta\tau)$ and $\mathbf{l}(\sigma_{n+1} - \Delta\tau/\epsilon_{n+1}, \tau + \Delta\tau)$. Similarly the right movers evolve on the characteristic curve $\sigma + \Delta\tau/\epsilon$, with $\mathbf{r}(\sigma_n, \tau + \Delta\tau)$ found by interpolating between $\mathbf{r}(\sigma_{n-1} - \Delta\tau/\epsilon_{n-1}, \tau + \Delta\tau)$ and $\mathbf{r}(\sigma_n + \Delta\tau/\epsilon_n, \tau + \Delta\tau)$.

Figure A.1 indicates that if $\Delta\tau/\epsilon \geq \Delta\sigma$, the left mover $\mathbf{l}(\sigma_n - \Delta\tau/\epsilon_n, \tau + \Delta\tau)$ will adopt a value to the left of $n-1$, whereas $\mathbf{l}(\sigma_{n+1} - \Delta\tau/\epsilon_{n+1}, \tau + \Delta\tau)$ will adopt a value to the left of n. In this situation a left mover $\mathbf{l}(\sigma_n, \tau + \Delta\tau)$ is found by extrapolating $\mathbf{l}(\sigma_n - \Delta\tau/\epsilon_n, \tau + \Delta\tau)$ and $\mathbf{l}(\sigma_{n+1} - \Delta\tau/\epsilon_{n+1}, \tau + \Delta\tau)$. Likewise a right mover $\mathbf{r}(\sigma_n, \tau +$

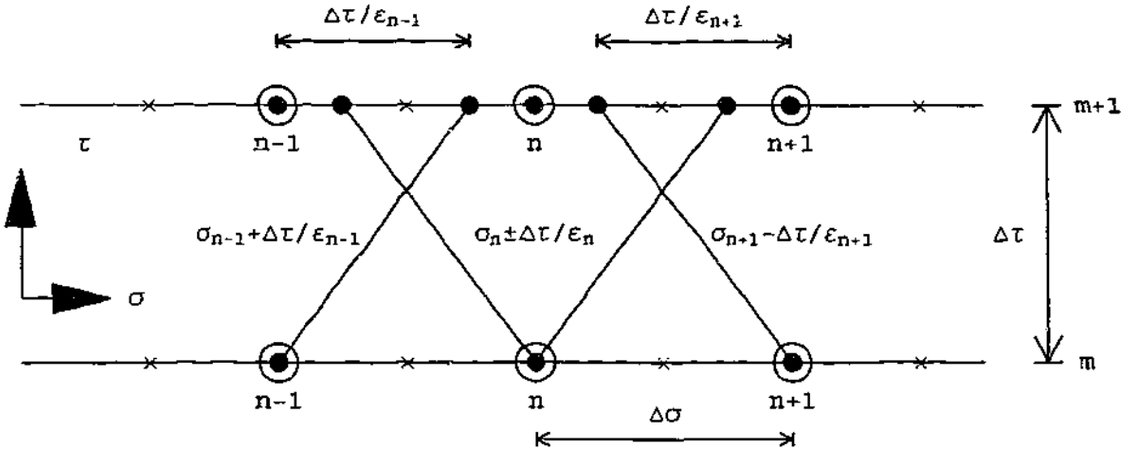

Figure A.1: String world-sheet showing the characteristic curves $\sigma + \Delta\tau/\epsilon_{n-1}$, $\sigma \pm \Delta\tau/\epsilon_n$ and $\sigma - \Delta\tau/\epsilon_{n+1}$ of the left and right movers (adapted from Albrecht and Turok 1989). The world-sheet is parameterized using conformal time, τ, and the spatial parameter σ. The positions of a string are stored at points designated by a cross ($\times$). The left and right movers are stored at the half-way points designated by a circle ($\bigcirc$). Neighboring points on the string are separated by $\Delta\sigma$.

$\Delta\tau$) is found by extrapolating $\mathbf{r}(\sigma_{n-1} - \Delta\tau/\epsilon_{n-1}, \tau + \Delta\tau)$ and $\mathbf{r}(\sigma_n + \Delta\tau/\epsilon_n, \tau + \Delta\tau)$. Numerical extrapolation schemes are prone to error, and may become unstable for long term evolution. To maintain stability in a numerical simulation we must constrain $\Delta\tau/\epsilon < \Delta\sigma$. The left and right movers at the next conformal time step are found by utilizing a numerical interpolation scheme. There was no evidence to suggest that our numerical interpolation scheme leads to instability in the long term evolution of the system. The CFL stability criterion for the evolution of the left and right movers is

$$\frac{1}{\epsilon}\frac{\Delta\tau}{\Delta\sigma} < 1. \tag{A.20}$$

This is consistent with Eq. (A.12) for $d = 1$, with τ playing the role of physical time t and $\epsilon\Delta\sigma = \Delta x$ (see Eq. (5.66)).

A.5 Accuracy of string network simulations

Where possible, our string network simulations employ methods that have been adopted in the literature (see e.g., Albrecht and Turok 1989, Bennett and Bouchet 1990 and Allen and Shellard 1990). In $\mathcal{R}^{4+1}$ spacetime the evolution of the left and right movers use linear interpolation and re-scaling (see Secs. 5.4.5 and 5.5.4), and the crossing detection method

is implemented by solving linear equations (see Secs. 5.4.5 and 5.5.4). A major source of inaccuracy is energy loss due to smoothing of the kinks after intercommution (see Allen and Shellard 1990). In our simulations, we update the velocity of the intercommuting string segments to satisfy the energy density relation (see Eqs. (5.64) and (5.79)). This guarantees that the energy of a string is conserved at each iteration. Our simulations of a cosmic string network in $\mathcal{R}^{3+1}$ are consistent with the results obtained in the literature (see Sec. 5.4).

APPENDIX B

Vortices in a Dark Matter Condensate

In Sec. 3.5 we discussed the nucleation of vortices in a dark matter condensate. Here we describe how vortices are "placed" in the condensate. The radial vortex number density, $n_v(r)$, and velocity, $v(r)$, of the condensate are given by Eqs. (3.68), (3.69) and (3.70). The method requires the total number of vortices, N, the size of the rigid-body region, R_0, and the size of the condensate that contains all vortices, R_1. Once N, R_0 and R_1 are known, we solve for c_0 and c_1 (see Eqs. (3.69) and (3.70)). We "place" N_0 vortices within R_0, according to

$$N_0 = 2\pi c_0 \int_0^{R_0} r dr = \pi c_0 R_0^2, \tag{B.1}$$

and N_1 vortices between R_0 and R_1, according to

$$N_1 = 2\pi c_1 \int_{R_0}^{R_1} r^{-\frac{3}{2}} r dr = 4\pi c_1 \left(R_1^{\frac{1}{2}} - R_0^{\frac{1}{2}} \right). \tag{B.2}$$

At $r = R_0$, continuity of the number density requires that $c_0 = c_1 R_0^{-3/2}$. Since $N = N_0 + N_1$, we have

$$c_0 = \frac{N}{\pi R_0^2 + 4\pi R_0^{\frac{3}{2}} \left(R_1^{\frac{1}{2}} - R_0^{\frac{1}{2}} \right)}, \tag{B.3}$$

and

$$c_1 = c_0 R_0^{\frac{3}{2}}. \tag{B.4}$$

Once c_0 and c_1 are known, the initial vortex configuration is constructed with radial dependence obeying Eqs. (3.69) and (3.70). Each vortex is "placed" in the condensate according to the following prescription:

$$2\pi c_0 \int_{r_i}^{r_f} r dr = 1, \tag{B.5}$$

for $r \leq R_0$ and

$$2\pi c_1 \int_{r_i}^{r_f} r^{-3/2} r dr = 1, \tag{B.6}$$

for $r > R_0$. For example, to "place" the first vortex in the condensate we solve Eq. (B.5) for r_f, with $r_i = 0$ (i.e., we start from the center of the condensate). The radial position

of the vortex is then given by $(r_i + r_f)/2$. After finding the radial position for the first vortex we set $r_i = r_f$, and find the radial position for the next vortex. The process is repeated until all N_0 vortices have been "placed" within the radial region R_0.

To "place" N_1 vortices within the radial region $R_0 < r \leq R_1$, we solve Eq. (B.6) for r_f, starting with $r_i = R_0$. Once a vortex position is obtained we set $r_i = r_f$, and find the radial position for the next vortex. The process is repeated until the positions of all N_1 vortices have been determined.

APPENDIX C

Density of States for a Photon Gas in $\mathcal{R}^{4+1}$ Spacetime

To describe the evolution of the Universe in $\mathcal{R}^{4+1}$ spacetime necessitates that we solve Eq. (5.93) for the scale factor. This requires knowledge of the equation of state of the photon gas (which relates radiation pressure and mass density). To derive the density of states of a photon gas in $\mathcal{R}^{4+1}$, we consider standing waves in a four-dimensional hypercube, i.e.,

$$\phi_{n_1,n_2,n_3,n_4}(x,y,z,w) = A \sin\left(\frac{n_1 \pi w}{L}\right) \sin\left(\frac{n_2 \pi x}{L}\right) \sin\left(\frac{n_3 \pi y}{L}\right) \sin\left(\frac{n_4 \pi z}{L}\right), \tag{C.1}$$

where A is a constant, n_1, n_2, n_3 and n_4 are positive integers and L is the edge length of the hypercube. The four-dimensional wavevector, k, is given by

$$k = \left(\frac{\pi}{L} n_1, \frac{\pi}{L} n_2, \frac{\pi}{L} n_3, \frac{\pi}{L} n_4\right), \tag{C.2}$$

with magnitude

$$|k| = \frac{\pi}{L} \sqrt{n_1^2 + n_2^2 + n_3^2 + n_4^2}. \tag{C.3}$$

The spacing between points in k-space is π/L, so the volume per cell is $(\pi/L)^4$. The surface area of an N-dimensional sphere of radius r is given by

$$S(r) = \frac{N r^{N-1} \pi^{\frac{N}{2}}}{\frac{N}{2}!}. \tag{C.4}$$

In $4+1$ dimensions the surface area of a sphere is therefore

$$S(r) = 2\pi^2 r^3. \tag{C.5}$$

The positive quadrant in k-space between k and $k + dk$ is $\frac{1}{16} 2\pi^2 k^3 dk$, and the number of standing wave modes is

$$\begin{aligned} f(k)dk &= \frac{1}{16} \left(2\pi^2 k^3 dk\right) \left(\frac{\pi}{L}\right)^{-4} \\ &= \frac{V k^3 dk}{8\pi^2}, \end{aligned} \tag{C.6}$$

where $V = L^4$ is the volume of the hypercube. Using the dispersion relation $\omega = ck$, where c is the speed of light, Eq. (C.6) becomes

$$f(\omega)d\omega = \frac{V \omega^3 d\omega}{8\pi^2 c^4}. \tag{C.7}$$

It can be shown that the partition function, $Z(T,V)$, for the photon gas is given by (see e.g., Mandl 1988),

$$\ln Z(T,V) = -2\int_0^\infty f(\omega)d\omega \ln\left[1-e^{-\beta\hbar\omega}\right], \tag{C.8}$$

where T is the absolute temperature, $\beta = 1/k_BT$. and k_B is Boltzmann's constant. The factor of 2 in Eq. (C.8) is due to the two polarization states of the photon. Substituting for $f(\omega)$ into Eq. (C.8), the partition function for a photon gas in $4+1$ dimensions becomes

$$\ln Z(T,V) = -\frac{V\omega^3}{4\pi^2c^4}\int_0^\infty d\omega \ln\left[1-e^{-\beta\hbar\omega}\right]. \tag{C.9}$$

The Helmholtz free energy, $F(T,V) = -k_BT\ln Z(T,V)$, is given by

$$F(T,V) = \frac{Vk_BT}{4\pi^2c^4}\int_0^\infty \omega^3 d\omega \ln\left[1-e^{-\beta\hbar\omega}\right]. \tag{C.10}$$

Introducing the variable $x = \beta\hbar\omega$, and integrating by parts, Eq. (C.10) becomes

$$\begin{aligned} F(T,V) &= -\frac{Vk_B^5T^5}{16\pi^2\hbar^4c^4}\int_0^\infty \frac{x^4}{e^x-1}dx, & \text{(C.11)}\\ &= -\frac{3Vk_B^5T^5}{2\pi^2\hbar^4c^4}\zeta(5), & \text{(C.12)} \end{aligned}$$

where $\zeta(5) = 1.03693...$ is the Riemann zeta function evaluated for $n = 5$. From the Helmholtz free energy we obtain other thermodynamical properties, e.g., the entropy, S, pressure, p, and energy density, ρ. These are defined as

$$\begin{aligned} S &= -\left(\frac{\partial F}{\partial T}\right)_V, \\ &= \frac{15Vk_B^5T^4}{2\pi^2\hbar^4c^4}\zeta(5), & \text{(C.13)}\\ p &= -\left(\frac{\partial F}{\partial V}\right)_T, \\ &= \frac{3k_B^5T^5}{2\pi^2\hbar^4c^4}\zeta(5), & \text{(C.14)}\\ \rho &= \frac{F+TS}{V}, \\ &= \frac{6k_B^5T^5}{\pi^2\hbar^4c^4}\zeta(5). & \text{(C.15)} \end{aligned}$$

From Eqs. (C.14) and (C.15) the equation of state[1] for a photon gas in $\mathcal{R}^{4+1}$ spacetime is given by

$$p = \frac{1}{4}\rho. \tag{C.16}$$

[1] The equation of state for a photon gas in $\mathcal{R}^{3+1}$ spacetime is $p = \rho/3$.

Utilizing Eq. (C.16) and the solution to the Friedmann equation (5.93), we deduce that the matter density of the Universe in $\mathcal{R}^{4+1}$ spacetime evolves as $\rho \propto a^{-5}$ (see Sec. 5.5), in contrast to $\rho \propto a^{-4}$ for $\mathcal{R}^{3+1}$ spacetime.

References

Abo-Shaeer, J.R., Raman, C., Vogels, J.M., and Ketterle, W. (2001), *Science* **292**, 476.

Abraham, E.R.I., McAlexander, W.I., Sackett, C.A., and Hulet, R.G. (1995), *Phys. Rev. Lett.* **74**, 1315.

Abrikosov, A.A. (1957), *Sov. Phys. JETP* **5**, 1174.

Acheson, D.J. (2000), *Eur. J. Phys.* **21**, 269.

Albrecht, A. and Turok, N. (1985), *Phys. Rev. Lett.* **54**, 1868.

Albrecht, A. and Turok, N. (1989), *Phys. Rev. D* **40**, 973.

Allen, B., Caldwell, R.R., Shellard, E.P.S., and Stebbins, A., *et al.* (1996), *Phys. Rev. Lett.* **77**, 3601.

Allen, B. and Shellard, E.P.S. (1990), *Phys. Rev. Lett.* **64**, 119.

Anderson, J.D., Laing, P.A., Lau, E.L., Liu, A.S., Nieto, M.M., and Turyshev, S.G. (2002), *Phys. Rev. D* **65**, 082004.

Anglin, J.R. and Ketterle, W. (2002), *Nature* **416**, 211.

Appelquist, T., Chodos, A., and Freund, P.G.O., *Modern Kaluza-Klein Theories* (Addison-Wesley, California, 1987).

Avelino, P.P. and Shellard, E.P.S. (1995), *Phys. Rev. D* **51**, 369.

Bahcall, N.A. (2000), *Phys. Rep.* **333-334**, 233.

Bahcall, N.A., Ostriker, J.P., Perlmutter, S., and Steinhardt, P.J. (1999), *Science* **284**, 1481.

Belavin, A.A., Poyakov, A.M., Schwartz, A.S., and Tyupkin, Y.S. (1975), *Phys. Lett. B* **59**, 85.

Bennett, C.L., Halpern, M., Hinshaw, G., and Jarosik, N., *et al.* (2003), *astro-ph/0302207* .

Bennett, D.P. and Bouchet, F.R. (1988), *Phys. Rev. Lett.* **60**, 257.

Bennett, D.P. and Bouchet, F.R. (1990), *Phys. Rev. D* **41**, 2408.

Bennett, D.P., Stebbins, A., and Bouchet, F.R. (1992), *Astrophys. J.* **399**, L5.

Bergström, L. (2000), *Rep. Prog. Phys.* **63**, 793.

Bergström, L. and Goodbar, A., *Cosmology and Particle Astrophysics* (Wiley, Chichester, 1999).

Bernardis, P.D., Ade, P.A.R., Bock, J.J., and Bond, J.R., *et al.* (2000), *Nature* **404**, 955.

Binney, J. and Tremaine, S., *Galactic Dynamics* (Princeton University, New Jersey, 1987).

Bosma, A. (1981), *Astron. J.* **86**, 1825.

Bouchet, F.R., Bennett, D.P., and Stebbins, A. (1988), *Nature* **335**, 410.

Bowick, M.J., Chandar, L., Schiff, E.A., and Srivastava, A.M. (1994), *Science* **263**, 943.

Burles, S., Nollett, K.M., Truran, J.W., and Turner, M.S. (1999), *Phys. Rev. Lett.* **82**, 4176.

Callan, C.G., Dashen, R.F., and Gross, D.J. (1976), *Phys. Lett. B* **63**, 334.

Carroll. B.W. and Ostlie, D.A., *An Introduction to Modern Astrophysics* (Addison-Wesley, Massachusetts, 1996).

Carroll, S.M. (2001), *astro-ph/0004075* .

Carroll, S.M. and Trodden, Mark (1998), *Phys. Rev. D* **57**, 5189.

Castin, Y. and Dum, R. (1999), *Eur. Phys. J. D* **7**, 399.

Cheng, H.Y. (1988), *Phys. Rep.* **158**, 1.

Chiao, R.Y., Garmire, E., and Townes, C.H. (1964), *Phys. Rev. Lett.* **13**, 479.

Chuang, I., Durrer, R., Turok, N., and Yurke, B. (1991), *Science* **251**, 1336.

Clemens, D.P. (1985), *Astrophys. J.* **295**, 422.

Copi, C.J., Schramm, D.N., and Turner, M.S. (1995), *Science* **267**, 192.

Courant, R., Friedrichs, K., and Lewy, H. (1928), *Math. Annalen* **100**, 32.

Covi, L., Kim, J.E., and Roszkowski, L. (1999), *Phys. Rev. Lett.* **82**, 4180.

Creutz, M., Jacobs, L., and Rebbi, C. (1983), *Phys. Rep.* **95**, 201.

Dalal, N., K. Abazajian, E. Jenkins, and Manohar, A.V. (2001), *Phys. Rev. Lett.* **87**, 141302.

Dalfovo, F., Giorgini, S., Pitaevskii, L.P., and Stringari, S. (1999), *Rev. Mod. Phys.* **71**, 463.

Dalfovo, F. and Stringari, S. (2001), *Phys. Rev. A* **63**, 011601.

Dimopoulos, S., Preskill, J., and Wilczek, F. (1982), *Phys. Lett. B* **119**, 320.

D'Inverno, R., *Introducing Einstein's Relativity* (Oxford University Press, New York, 1996).

Dolan, L. and Jackiw, R. (1974), *Phys. Rev. D* **9**, 3320.

Dvali, G., Liu, H., and Vachaspati, T. (1998), *Phys. Rev. Lett.* **80**, 2281.

Dvali, G., Melfo, A., and Senjanovic, G. (1995), *Phys. Rev. Lett.* **75**, 4559.

Feder, D.L. and Clark, C.W. (2001), *Phys. Rev. Lett.* **87**, 190401.

Feder, D.L., Svidzinsky, A.A., Fetter, A.L., and Clark, C.W. (2001), *Phys. Rev. Lett.* **86**, 564.

Forsbergh, P.W. (1949), *Phys. Rev.* **76**, 1187.

Freese, K., Turner, M.S., and Schramm, D.N. (1983), *Phys. Rev. Lett.* **51**, 1625.

Fukuda, Y., Hayakawa, T., Ichihara, E., and Inoue, E., *et al.* (1998), *Phys. Rev. Lett.* **81**, 1562.

Georgi, H. and Glashow, S.L. (1974), *Phys. Rev. Lett.* **32**, 438.

Gill, A.J. (1998), *Contemp. Phys.* **39**, 13.

Ginzburg, V.L. and Landau, L.D. (1950), *J. Exptl. Theoret. Phys. (U.S.S.R.)* **20**, 1064.

Ginzburg, V.L. and Pitaevskii, L.P. (1958), *Sov. Phys. JETP* **7**, 858.

Glashow, S. (1961), *Nucl. Phys.* **22**, 579.

Goddard, P., Goldstone, J., Rebbi, C., and Thorn, C.B. (1973), *Nucl. Phys. B* **56**, 109.

Goldstone, J. (1961), *Nuovo Cimento* **19**, 154.

Goldstone, J., Salam, A., and Weinberg, S. (1962), *Phys. Rev.* **127**, 965.

Goodman, J. (2000), *New Astron.* **5**, 103.

Gross, E.P. (1961), *Nuovo Cimento* **10**, 454.

Guth, A.H. (1981), *Phys. Rev. D* **23**, 347.

Guzman, F.S. and Matos, T. (2000), *Class. and Quantum Grav.* **17**, L9.

Harrison, E.R. (1970), *Phys. Rev. D* **1**, 2726.

Harvey, J.A., Kolb, E.W., Reiss, D.B., and Wolfram, S. (1982), *Nucl. Phys. B* **201**, 16.

Hendry, P.C., Lawson, N.S., Lee, R.A.M., and McClintock, P.V.E., *et al.* (1994), *Nature* **368**, 315.

Higgs, P.W. (1964), *Phys. Lett.* **12**, 132.

Higgs, P.W. (1966), *Phys. Rev.* **145**, 1156.

Holland, M. and Cooper, J. (1996), *Phys. Rev. A* **53**, R1954.

Hooton, J.A. and Merz, W.J. (1955), *Phys. Rev.* **98**, 409.

Inouye, S., Andrews, M.R., Stenger, J., and Miesner, H.J., *et al.* (1998), *Nature* **392**, 151.

Jackiw, R. (1974), *Phys. Rev. D* **9**, 1686.

Jackiw, R. and Rebbi, C. (1976), *Phys. Rev. Lett.* **37**, 172.

Kagan, Y., Muryshev, A.E., and Shlyapnikov, G.V. (1998), *Phys. Rev. A* **81**, 933.

Kagan, Y., Shlyapnikov, G.V., and Walraven, J.T.M. (1996), *Phys. Rev. Lett.* **76**, 2670.

Kaku, M., *Strings, Conformal Fields, and M Theory* (Springer-Verlag, New York, 1999).

Kibble, T.W.B. (1976), *J. Phys. A: Math. Gen.* **9**, 1387.

Kibble, T.W.B. (1980), *Phys. Rep.* **67**, 183.

Kibble, T.W.B. (1985), *Nucl. Phys. B* **252**, 227.

Kibble, T.W.B. (2002), *Physica C* **369**, 87.

Kibble, T.W.B., Lazarides, G., and Shafi, G. (1982), *Phys. Rev. D* **26**, 435.

Kibble, T.W.B. and Turok, N.G. (1982), *Phys. Lett. B* **116**, 141.

Kim, J.E. (1987), *Phys. Rep.* **150**, 1.

Kirillov, A.A. and Turaev, D. (2002), *Phys. Lett. B* **532**, 185.

Kirzhnits, D.A. (1972), *JETP Lett.* **15**, 745.

Kirzhnits, D.A. and Linde, A.D. (1972), *Phys. Lett. B* **42**, 471.

Kogut, J. (1983), *Rev. Mod. Phys.* **55**, 775.

Kolb, E.W., Colgate, S.A., and Harvey, J.A. (1982), *Phys. Rev. Lett.* **79**, 137.

Kolb, E.W. and Turner, M.S., *The Early Universe* (Addison-Wesley, California, 1990).

Kostelecký, V.A. and Samuel, S. (1991), *Phys. Lett. B* **270**, 21.

Kravtsov, A.V., Klypin, A.A., Bullock, J.S., and Primack, J.R. (1998), *Astrophys. J.* **502**, 48.

Langacker, P. and Pi, S.Y. (1980), *Phys. Rev. Lett.* **45**, 1.

Lange, A.E., Ade, P.A.R., Bock, J.J., and Bond, J.R., *et al.* (2001), *Phys. Rev. D* **63**, 042001.

Lazarides, G., Shafi, Q., and Walsh, T.F. (1982), *Nucl. Phys. B* **195**, 157.

Liddle, A.R. and Lyth, D.H., *Cosmological Inflation and Large-Scale Structure* (Cambridge University Press, Cambridge, 2000).

Madison, K.W., Chevy, F., Wohlleben, W., and Dalibard, J. (2000), *Phys. Rev. Lett.* **84**, 806.

Mandel, L. and Wolf, E., *Coherence and Quantum Optics* (Plenum Press, New York, 1973).

Mandl, F., *Statistical Physics.* 2nd edition (John Wiley & Sons, Chichester, 1988).

Martins, C.J.A.P. and Shellard, E.P.S. (1996), *Phys. Rev. D* **54**, 2535.

McDonald, J. (2002), *Phys. Rev. Lett.* **88**, 091304.

McGraw, P. (1998), *Phys. Rev. D* **57**, 3317.

McNamara, P.A. and Wu, S.L. (2002), *Rep. Prog. Phys.* **65**, 465.

Merz, W.J. (1952), *Phys. Rev.* **88**, 421.

Michinel, H., Taboas, J.C., Fernandez, R.G., and Slgueiro, J.R., *et al.* (2002), *Phys. Rev. A* **65**, 066604.

Milgrom, M. (2002), *New Astron. Rev.* **46**, 741.

Moore, J.N., Shellard, E.P.S., and Martins, C.J.A.P. (2001), *Phys. Rev. D* **65**, 023503.

Moriarty, K [illegible], E., and Rebbi, C. (1988), *Phys. Lett. B* **207**, 411.

Myers, E., Rebbi, C., and Strilka, R. (1992), *Phys. Rev. D* **45**, 1355.

Navarro, J.F., Frenk, C.S., and White, S.D.M. (1996), *Astrophys. J.* **462**, 563.

Nielsen, H.B. and Olesen, P. (1973), *Nucl. Phys. B* **61**, 45.

Nozières, P. and Pines, D., *The Theory of Quantum Liquids* (Addison-Wesley, Redwood City, 1990).

Ostriker, J.P. and Steinhardt, P.J. (1995), *Nature* **377**, 600.

Overduin, J.M. and Wesson, P.S. (1997), *Phys. Rep.* **283**, 303.

Parkins, A.S. and Walls, D.F. (1998). *Phys. Rep.* **303**, 1.

Peccei, R.D. and Quinn, H.R. (1977), *Phys. Rev. Lett.* **38**, 1440.

Perivolaropoulos, L. (1992), *Nucl. Phys. B* **375**, 665.

Perlmutter, S., Aldering, G., Goldhaber, G., and Knop, R.A., *et al.* (1999), *Astrophys. J.* **517**, 565.

Persic, M., Salucci, P., and Stel, F. (1996), *Mon. Not. R. Astron. Soc.* **281**, 27.

Pitaevskii, L.P. (1961), *Sov. Phys. JETP* **13**, 451.

Polyakov, A.M. (1974), *JETP Lett.* **20**, 194.

Polyakov, A.M. (1975), *JETP Lett.* **41**, 988.

Preskill, J.P. (1979), *Phys. Rev. Lett.* **43**, 1365.

Press, W.H., Ryden, B.S., and Spergel, D.N. (1989), *Astrophys. J.* **347**, 590.

Quigg, C., *Gauge Theories of the Strong, Weak, and Electromagnetic Interactions* (Benjamin-Cummings, Massachusetts, 1983).

Raman, C., Abo-Shaeer, J.R., Vogels, J.M., and Xu, K., *et al.* (2001), *Phys. Rev. Lett.* **87**, 210402.

Raman, C., Köhl, M., Onofrio, R., and Durfee, D.S., *et al.* (1999), *Phys. Rev. Lett.* **83**, 2502.

Rey, M.L. and Luminet, J.P. (1995), *Phys. Rep.* **254**, 135.

Riess, A.G., Filippenko, A.V., Challis, P., and Clocchiatti, A., *et al.* (1998), *Astrophys. J.* **502**, 48.

Riotto, A. and Tkachev, I. (2000), *Phys. Lett. B* **484**, 177.

Robinson, M.R., *The Cosmological Distance Ladder* (Freeman, New York, 1985).

Rokhsar, D.S. (1997), *Phys. Rev. Lett.* **79**, 2164.

Roszkowski, L. (2000), *Nucl. Phys. B (Proc. Suppl.)* **87**, 21.

Rubakov, V.A. (1981), *JETP Lett.* **33**, 644.

Rubakov, V.A. (1982), *Nucl. Phys. B* **203**, 311.

Rubin, V.C., Ford, W.K., and Thonnard, N. (1980), *Astrophys. J.* **238**, 471.

Ruffini, R. and Bonazzola, S. (1969), *Phys. Rev.* **187**, 1767.

Sackett, C.A., Stoof, H.T.C., and Hulet, R.G. (1998), *Phys. Rev. Lett.* **80**, 2031.

Salam, A., *Proceedings of the 8th Nobel Symposium.* Edited by N. Svartholm (Almqvist and Wiksell, Stockholm, 1968), 367; see also Salam, A. (1980), *Rev. Mod. Phys.* **52**, 525.

Salomonson, P., Skagerstam, B.S., and Stern, A. (1985), *Phys. Lett. B* **151**, 243.

Schunck, F.E. and Mielke, W.W. (1998), *Phys. Lett. A* **249**, 389.

Shellard, E.P.S. (1987), *Nucl. Phys. B* **283**, 624.

Shyryak, E.V. (1996), *Phys. Rev. A* **54**, 3151.

Silverman, M.P. and Mallett, R. L. (2001a), *Class. and Quantum Grav.* **18**, L37.

Silverman, M.P. and Mallett, R. L. (2001b), *Class. and Quantum Grav.* **18**, L103.

Sin, S.J. (1994), *Phys. Rev. D* **50**, 3650.

Smektala, F., Quemard, C., Couderc, V., and Barthelemy, A. (2000), *J. Non-Cryst. Solids* **274**, 232.

Smith, G., *Numerical Solutions of Partial Differential Equations: Finite Difference Methods.* 3rd edition (Oxford University Press, Oxford, 1985).

Smolin, L. (2003), *hep-th/0303185 v2* .

Smoot, G.F., Bennett, C.L., Kogut, A., and Wright, E.L., *et al.* (1992), *Astrophys. J. Lett.* **396**, L1.

Spergel, D.N. and Steinhardt, P.J. (2000), *Phys. Rev. Lett.* **84**, 3760.

Stauffer, D. (1979), *Phys. Rep.* **54**, 1.

Stebbins, A. (1988), *Astrophys. J.* **327**, 584.

Stebbins, A. and Turner, M.S. (1989), *Astrophys. J. Lett.* **339**, L13.

Stoof, H.T.C. (1997), *J. Stat. Phys.* **87**, 1353.

't Hooft, G. (1974), *Nucl. Phys. B* **79**, 276.

't Hooft, G. (1976), *Phys. Rev. Lett.* **37**, 8.

Thatcher, M.J. and Morgan, M.J. (1997), *Class. and Quantum Grav.* **14**, 3161.

Turner, M.S. (1999), *Nucl. Phys. B (Proc. Suppl.)* **72**, 69.

Turner, M.S. (2000), *Phys. Rep.* **333-334**, 619.

Turner, M.S. (2001), *Nucl. Phys. B (Proc. Suppl.)* **91**, 405.

Turok, N. (1989), *Phys. Rev. Lett.* **63**, 2629.

Ueda, M. and Leggett, A. (1998), *Phys. Rev. Lett.* **80**, 1576.

Vachaspati, T. (1986), *Nucl. Phys. B* **277**, 593.

Vachaspati, T. and Vilenkin, A. (1984), *Phys. Rev. D* **30**, 2036.

Vilenkin, A. (1980), *Phys. Rev. Lett.* **46**, 1169.

Vilenkin, A. (1981), *Phys. Rev. D* **23**, 852.

Vilenkin, A. (1985), *Phys. Rep.* **121**, 263.

Vilenkin, A. and Shellard, E.P.S., *Cosmic Strings and other Topological Defects* (Cambridge University Press, Cambridge, 1994).

Weinberg, S. (1967), *Phys. Rev. Lett.* **19**, 1264; see also Weinberg, S. (1974), *Phys. Rev. D* **9**, 3357.

Witten, E. (1997), *Nucl. Phys. B* **507**, 658.

Zel'dovich, Ya.B. (1972), *Mon. Not. R. Astron. Soc.* **160**, 1P.

Zel'dovich, Ya.B. and Khlopov, M.Yu. (1978), *Phys. Lett. B* **79**, 239.

Zel'dovich, Ya.B., Kobzarev, I.Yu., and Okun, L.B. (1975), *Sov. Phys. JETP* **40**, 1.

Zel'dovich, Y.B. (1980), *Mon. Not. R. Astron. Soc.* **192**, 663.

Zurek, W.H. (1985), *Nature* **317**, 505.

Zurek, W.H. (1994), *Nature* **368**, 292.

Zurek, W.H. (1996), *Phys. Rep.* **276**, 177.

Zwicky, F. (1933), *Helv. Phys. Acta* **6**, 110.

Supporting Publications

INSTITUTE OF PHYSICS PUBLISHING CLASSICAL AND QUANTUM GRAVITY

Class. Quantum Grav. 18 (2001) L163–L169 PII: S0264-9381(01)28451-2

LETTER TO THE EDITOR

Numerical study of the stability of $U(1) \times U(1) \times Z_2$ Dirichlet defects

Rotha P Yu[1], Nadia Adam[2], Marcus J Thatcher[1] and Michael J Morgan[1]

[1] School of Physics and Materials Engineering, Monash University, Victoria 3800, Australia
[2] Department of Physics, Cornell University, Ithaca, NY 14853, USA

E-mail: Rotha.Yu@spme.monash.edu.au

Received 28 August 2001
Published 21 November 2001
Online at stacks.iop.org/CQG/18/L163

Abstract

A numerical study of the stability of $U(1) \times U(1) \times Z_2$ Dirichlet topological defects (D-walls) has been carried out for a classical scalar field theory. It is found that the D-walls are stable for a wide range of coupling parameters and under perturbations to the wall. However, when two walls are connected by a string, they annihilate via a mechanism analogous to the Langacker–Pi mechanism for monopoles.

PACS number: 1127

(Some figures in this article are in colour only in the electronic version)

Topological defects are predicted by field theories with spontaneously broken symmetries [1]. These defects can be classified as monopoles, cosmic strings, domain walls, or textures, according to the homotopy group of the vacuum manifold. However, since domain walls and monopoles are associated with adverse cosmological consequences [2], these particular defects may never have formed, or formed and subsequently annihilated or were removed by inflation.

Dirichlet defects were originally discussed within the context of superstring theory (i.e., D-branes [3]), and a corresponding model for cosmic topological defects was introduced by Carroll and Trodden [4]. When cosmic strings terminate on a domain wall, it is known that the wall is unstable to the nucleation of holes bounded by string loops [5]. Such holes can result in the eventual decay of the wall defect; however, the time scale involved in hole formation is thought to be extraordinarily large [5], which would seem to exclude hybrid topological defects as a way of obviating problems with a domain-wall-dominated Universe. In this paper we examine the stability of a Dirichlet defect (or D-wall) [4], in which cosmic strings terminate on a domain wall.

Consider a simple abelian model based on $U(1) \times U(1) \times Z_2$ global symmetry breaking [4]. In this model the spontaneously broken Higgs fields consist of a real scalar field, ϕ, for

the domain wall defect and two complex scalar fields, (ψ_1, ψ_2), for the string windings. The model is defined by the Lagrangian (with $\hbar = c = 1$),

$$\mathcal{L} = \partial_\mu \phi \partial^\mu \phi + \overline{\partial_\mu \psi_1} \partial^\mu \psi_1 + \overline{\partial_\mu \psi_2} \partial^\mu \psi_2 - V(\phi, \psi_1, \psi_2) \tag{1}$$

where the potential is given by

$$V(\phi, \psi_1, \psi_2) = \lambda_\phi (\phi^2 - \tilde{v}^2)^2 + \lambda_\psi \left[|\psi_1|^2 + |\psi_2|^2 - \tilde{w}^2 + g(\phi^2 - \tilde{v}^2) \right]^2 + h|\psi_1|^2 |\psi_2|^2 - \mu\phi \left(|\psi_1|^2 - |\psi_2|^2 \right). \tag{2}$$

The form of the potential is governed by the coupling parameters, λ_ϕ, λ_ψ, g, h and μ. If the parameter μ is zero, i.e., the interaction between the different fields vanishes, then there are four degenerate sets of vacuum expectation values (VEVs) which minimize the potential, namely,

$$\langle \phi \rangle = \pm \tilde{v} \qquad \langle |\psi_1| \rangle = \tilde{w} \qquad \langle |\psi_2| \rangle = 0 \tag{3}$$

and

$$\langle \phi \rangle = \pm \tilde{v} \qquad \langle |\psi_1| \rangle = 0 \qquad \langle |\psi_2| \rangle = \tilde{w}. \tag{4}$$

As pointed out by Carroll and Trodden [4], for a $Z_2 \times Z_2 \times Z_2$ Dirichlet defect, once the value of μ is increased from zero this degeneracy is removed. In this case there remain only two sets of VEVs,

$$\langle \phi \rangle = v \qquad \langle |\psi_1| \rangle = w \qquad \langle |\psi_2| \rangle = 0 \tag{5}$$

and

$$\langle \phi \rangle = -v \qquad \langle |\psi_1| \rangle = 0 \qquad \langle |\psi_2| \rangle = w. \tag{6}$$

The boundary beetween regions with different VEVs defines a domain wall defect. String windings in either of the ψ-fields can terminate on a domain wall, producing a D-wall. When either of the ψ-fields terminate on the wall its VEV vanishes. In this case, the hybrid defect resembles a free wall and is expected to be stable, since the Higgs field corresponding to a Z_2 domain wall is stable. However, to establish the stability of the D-wall, it is necessary to show that the wall is stable for a wide range of coupling parameters and when perturbations are imposed on the wall.

The form of the potential is governed by a multi-dimensional parameter space. We can gain insight into the parameters that govern the stability of the D-wall by examining the minimum of the potential (2), which occurs at $\langle \phi \rangle = v$ and $\langle \psi \rangle = w$, i.e.

$$4\lambda_\phi v(v^2 - \tilde{v}^2) + 2g\mu v^2 - \mu w^2 = 0 \tag{7}$$

$$2\lambda_\psi (w^2 - \tilde{w}^2 + g(v^2 - \tilde{v}^2)) - \mu v = 0. \tag{8}$$

These equations indicate that the VEVs of the ϕ- and the ψ-fields do not depend on the parameter h, which governs the interaction between the two ψ-fields. Because ψ_1 terminates on the wall from 'above' and ψ_2 terminates on the same wall from 'below', $h|\psi_1|^2|\psi_2|^2$ will be approximately equal to zero everywhere. Using equations (7) and (8), we seek to establish constraints on the other parameters in the potential, i.e.

$$\lambda_\psi = \frac{\mu^2 v^3}{\beta\mu - \alpha} \tag{9}$$

$$g = \frac{1}{v^2 - \tilde{v}^2} \left[\frac{\mu v}{2\lambda_\psi} + \tilde{w}^2 - w^2 \right] \tag{10}$$

where, following [4], we have set $h = -1/12$ and α and β are defined by

$$\alpha \equiv 4\lambda_\phi v(v^2 - \bar{v}^2)^2 \tag{11}$$

$$\beta \equiv 2(w^2 - \bar{w}^2)v^2 + (v^2 - \bar{v}^2)w^2. \tag{12}$$

Equation (9) determines the conditions under which a D-wall forms. The stability of the wall is dictated by the sign of λ_ψ in the potential (2). We note that $\lambda_\psi \to \pm\infty$ if $\mu \to \alpha/\beta$, with $\mu = \alpha/\beta$ representing an unstable configuration. If $\lambda_\psi > 0$ we have a Mexican hat potential which characterizes a symmetry-breaking phase transition. However, if $\lambda_\psi < 0$ the potential does not exhibit symmetry breaking, i.e., the ψ-fields do not have non-zero VEVs. Thus, a D-wall is precluded from forming unless we constrain the parameter, μ, which couples the strings to the wall, i.e. $\mu > \alpha/\beta$. We know that a single domain wall is stable, therefore varying the self-coupling, λ_ϕ, is unlikely to cause an instability in the D-wall; consequently, we fix the value of λ_ϕ in our numerical simulations. To facilitate comparison with the work reported by Carroll and Trodden [4], we set $\bar{v}^2 = \frac{1}{24}$, $\bar{w}^2 = -3$, $v^2 = 1$, $w^2 = 69$ and $\lambda_\phi = 108$. For this choice of symmetry-breaking scale, equations (9) and (10), become

$$\lambda_\psi = \frac{8\mu^2}{1681\mu - 3174} \tag{13}$$

$$g = \frac{12}{23}\left(\frac{\mu}{\lambda_\psi} - 144\right) \tag{14}$$

which constrains $\mu > \mu_c$, where $\mu_c = 3174/1681 \approx 1.89$. Equations (13) and (14) show that the parameters λ_ψ and g are completely determined for a given value of μ. Thus, in our numerical simulations, the string-wall coupling parameter, μ, is the only independent variable and we can explore the stability of the D-wall by varying μ.

The equations of motion of the D-wall, derived from the Lagrangian (1), are

$$\Box\chi = -\frac{1}{2}\frac{\partial V}{\partial \bar{\chi}} \qquad (\chi = \phi, \psi_1, \psi_2). \tag{15}$$

The numerical solution to equation (15), utilized a second-order leapfrog difference scheme [6]. To obtain a complete picture of the hybrid defect, simulations were carried out for one and two strings terminating on the wall. The initial conditions invoked cylindrical symmetric vortex solutions. In three dimensions, with the wall located at $z = 0$ and the strings located at $r = \sqrt{x^2 + y^2} = 0$, the cylindrical symmetric vortex is described by the coupled equations

$$\frac{\partial^2\phi}{\partial r^2} + \frac{1}{r}\frac{\partial\phi}{\partial r} + \frac{\partial^2\phi}{\partial z^2} = \frac{1}{2}\frac{\partial V}{\partial\phi} \tag{16}$$

$$\frac{\partial^2 f}{\partial r^2} + \frac{1}{r}\frac{\partial f}{\partial r} - \frac{1}{r^2}f + \frac{\partial^2 f}{\partial z^2} = \frac{1}{2}\frac{\partial V}{\partial f} \qquad (f = f_1, f_2). \tag{17}$$

The following ansatzen are assumed:

$$\psi_1 = f_1(r, z)e^{i\theta_1} \tag{18}$$

$$\psi_2 = f_2(r, z)e^{i\theta_2} \tag{19}$$

$$\phi = \phi(r, z). \tag{20}$$

Since the resulting equations are non-linear, the solutions which define the D-wall are found using an iterative finite difference scheme, whose convergence is sensitive to the choice of spatial step. In order to ensure that the solution converges, our numerical simulations employed a spatial step $\delta k = 0.055$. Once the vortex solutions is obtained, they are transformed into cartesian coordinates and evolved using equation (15). Causality dictates that the time step must be smaller than the spatial step; hence we chose $\delta t = 0.02$. The size of our simulation is

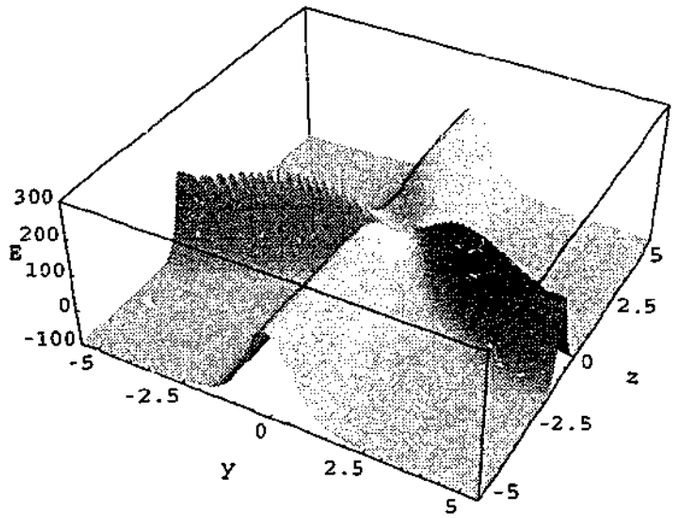

Figure 1. Cross-sectional plot of the total energy density of the D-wall. The domain wall is located at $z = 0$ and the locus of the strings is along the z-axis at $y = 0$. The cross-section corresponds to $x = 0, t = 0$. A perturbation is introduced on the wall, with amplitude $A = 1$ and $n = 1$.

200^3 lattice points and we evolve the D-wall up to $t = 20$ (corresponding to 1000 iterations). This time scale is long enough to ensure that any disturbance (noise) from the boundary is able to affect the stability of the D-wall.

As $\mu \to \mu_c$ the numerical algorithm does not converge to a solution, since $\lambda_\psi \to \infty$. To ensure that the simulations can be completed in a reasonable time frame, we have restricted $\mu \geqslant 2.5$. Numerical simulations were performed in the range $2.5 \leqslant \mu \leqslant 10$, in steps of $\delta\mu = 0.5$. Cross-sections of the total energy density of the D-wall (at $t = 20$), were plotted and compared to the initial D-wall configuration (see figures 1 and 2). For the range of μ-values explored here, the D-wall showed no signs of instability. As μ increases, the gradient of the ϕ- and ψ-fields also increases; however, this only changes the energy density of the D-wall (a similar effect can be achieved by increasing the value of λ_ϕ). Simulations involving one string terminating on the wall also show the D-wall to be stable (see figures 3 and 4).

We have explored the stability of the D-wall when it is perturbed by harmonic perturbations of the form

$$z = A\cos\left(\frac{\pi n y}{L}\right) \tag{21}$$

where A is the perturbation amplitude, n is a positive integer and $-5.5 \leqslant L \leqslant 5.5$ is the extent of the domain wall in the y-direction. Simulations were carried out for $n = 1$, 2 and 3 and for amplitudes $0 \leqslant A \leqslant 1.0$. A perturbation amplitude $A = 1.0$ is large compared to the thickness of the wall, $\delta = 1/\sqrt{\lambda_\phi}v \sim 0.1$ (for $\mu = 6$). It is observed that the perturbations decay with time, with energy partly transferred into the strings. No instabilities are observed when A is varied in the range $0 \leqslant A \leqslant 1$. Figures 1 and 2 show typical results (with $A = 1$ and $n = 1$).

When one string terminates on the wall, for example at $z = -2.75$ in figure 3, it exerts tension on the wall, pulling it up to $z = +2.75$ (see figure 4). This phenomenon has some interesting consequences if the other end of the string terminates on the second wall. Two such walls connected by a string are pulled towards each other (see figures 5 and 6). When the ends

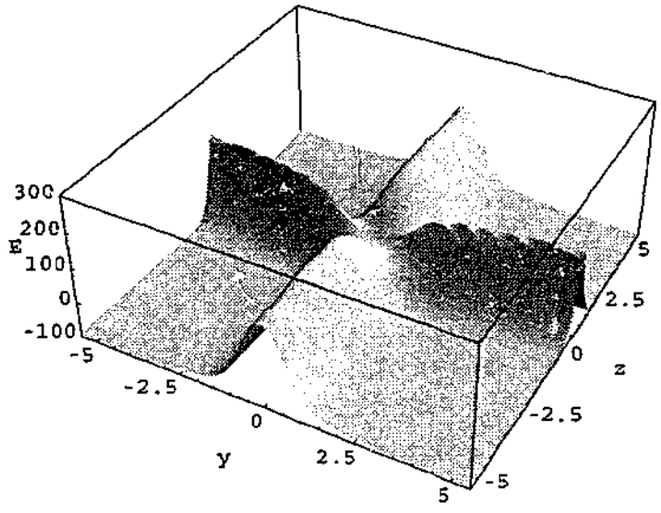

Figure 2. Cross-sectional plot of the total energy density of the D-wall at $t = 20$, evolved from the initial configuration shown in figure 1. The amplitude of the perturbation (in the z-direction) has been reduced, indicating that the D-wall is stable with respect to perturbations on the wall. The wall transfers energy to the strings as is evident from the small peaks on the strings.

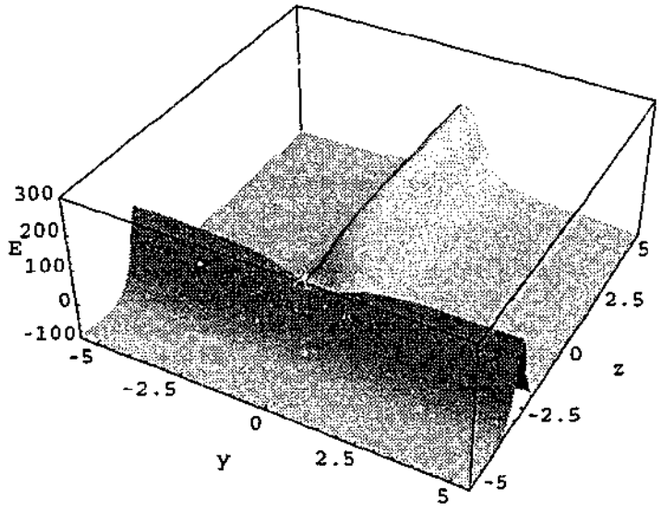

Figure 3. Cross-sectional plot of the total energy density of the D-wall (at $t = 0$), with one string terminating on a wall. The wall is located at $z = -2.5$ and the string locus is in the z-direction at $y = 0$.

of the string come into contact, the string unwinds and the section of the wall on which the string terminates nucleates a hole in the walls (see figure 6). The hole then expands outwards resulting in the annihilation of the walls. This is analogous to the Langacker–Pi mechanism [7], in which monopoles and anti-monopoles, connected by strings, are drawn together and annihilate.

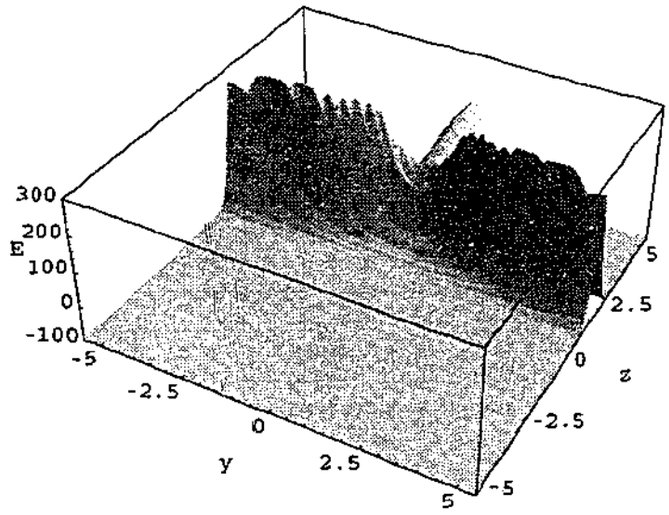

Figure 4. Cross-sectional plot of the D-wall at $t = 13$, evolved from the initial configuration shown in figure 3. Comparison with figure 3 shows that the wall is stable; it is pulled in the z-direction due to string tension. The energy density of the wall is higher than that in figure 3, due to stretching of the wall under string tension.

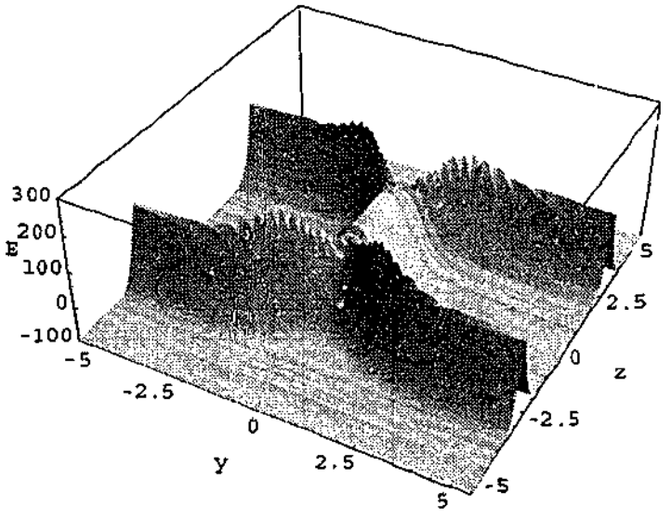

Figure 5. Cross-sectional plot of the total energy density of two walls connected by a string at $t = 2$. In this frame we see that the walls have been pulled towards each other under string tension. At $t = 0$ (not shown), the walls (located at $z = \pm 2.5$) are undeformed. The string locus is along the z-direction at $y = 0$.

In conclusion, it is found that D-walls are stable for a wide range of coupling parameters and under perturbations imposed on the wall. Our numerical study supports the earlier speculation that D-walls are stable defects. The present results may have cosmological implications, since a network of hybrid topological defects, such as D-walls, is expected to

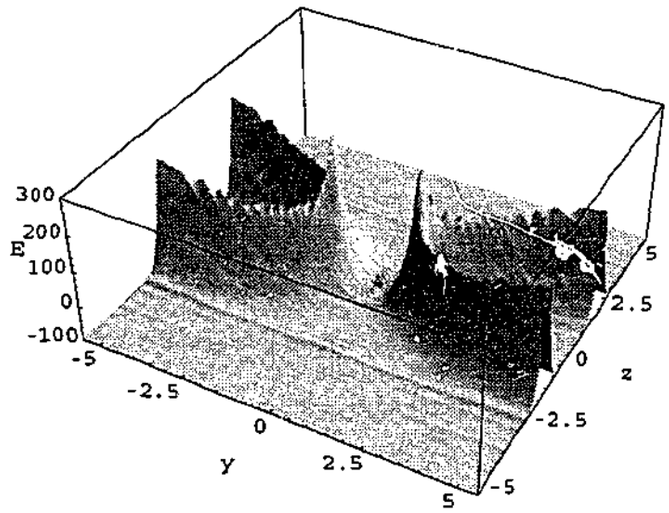

Figure 6. Cross-sectional plot of the total energy density of the D-wall at $t = 6$, evolved from the configuration shown in figure 5. As the two walls are pulled towards each other, the ends of the strings come into contact and unwind, thereby nucleating a hole in the walls. This hole expands outwards resulting in the annihilation of the walls.

form in the early Universe. Walls connected by strings will quickly annihilate, rapidly diluting the energy density of the network, thereby obviating a domain-wall-dominated Universe.

Acknowledgments

One of the authors, Rotha P Yu, acknowledges the support of an Australian Postgraduate Award.

References

[1] Kibble T 1976 *J. Phys. A: Math. Gen.* **9** 1387
[2] Zel'dovich Ya B, Kobzarev I Yu and Okun L B 1975 *Sov. Phys.–JETP* **40** 1
[3] Witten E 1997 *Nucl. Phys.* B **507** 658
[4] Carroll S M and Trodden M 1998 *Phys. Rev.* D **57** 5189
[5] Kibble T, Lazarides G and Shafi Q 1982 *Phys. Rev.* D **26** 435
[6] Moriarty K J M, Myers E and Rebbi C 1989 *Comput. Phys. Commun.* **54** 273
[7] Langacker P and Pi S Y 1980 *Phys. Rev. Lett.* **45** 1

INSTITUTE OF PHYSICS PUBLISHING CLASSICAL AND QUANTUM GRAVITY

Class. Quantum Grav. 19 (2002) L157–L166 PII: S0264-9381(02)37062-X

LETTER TO THE EDITOR

Vortices in a rotating dark matter condensate

Rotha P Yu and Michael J Morgan

School of Physics and Materials Engineering, Monash University, Victoria 3800, Australia

E-mail: Rotha.Yu@spme.monash.edu.au and Michael.Morgan@spme.monash.edu.au

Received 9 May 2002, in final form 24 July 2002
Published 16 August 2002
Online at stacks.iop.org/CQG/19/L157

Abstract

We examine vortices in a self-gravitating dark matter Bose–Einstein condensate (BEC), consisting of ultra-low mass scalar bosons that arise during a late-time cosmological phase transition. Rotation of the dark matter BEC imprints a background phase gradient on the condensate, which establishes a harmonic trap potential for vortices. A numerical simulation of vortex dynamics shows that the vortex number density, $n_v \propto r^{-1}$, resulting in a flat velocity profile for the dark matter condensate.

PACS numbers: 9535, 0530, 9880C

Observational evidence indicates that about 90% of the universe is composed of dark matter [1, 2]. Support for this hypothesis comes from the non-Keplerian fall-off in the rotation curves of spiral galaxies [3]. Numerous models have been proposed to explain the flat velocity profiles. One approach is to modify Newtonian gravity by adding terms to the gravitational potential. However, this is an *ad hoc* procedure, which requires a negative cosmological constant [4]. Alternative scenarios consider a spherical distribution of dark matter in the galactic halo, which acts as a self-attracting sphere of ideal gas at a uniform temperature (isothermal halo model [5]). Other phenomenological models have been developed to describe the asymptotic behaviour of galactic rotation curves [3, 6]. These models are not predicated on any particular dark matter candidate and assume an analytical form for the dark matter distribution, with adjustable parameters chosen to fit the observations.

The nature of non-baryonic dark matter has also been the subject of widespread discussion in the literature (see, e.g., [6] for a comprehensive review). Scalar matter fields have been considered as dark matter candidates [6, 7]. Following a late-time cosmological phase transition, pseudo-Nambu–Goldstone bosons [8] are produced and under certain conditions may condense as a Bose liquid. Fine tuning is required to ensure that this phase transition does not impact adversely on nucleosynthesis or the isotropy constraints imposed by the cosmic microwave background. Recently, Silverman and Mallett [9, 10] considered a neutral scalar field coupled to gravity. Spontaneous symmetry breaking of the scalar field gives rise to ultra-low mass bosons $\sim 2 \times 10^{-23}\,\mathrm{eV}\,c^{-2}$. It is conjectured that these particles constitute a weakly interacting degenerate 'ether' (WIDGET), that can form a Bose–Einstein condensate

(BEC), with number density $n \sim 6 \times 10^{34}\,\mathrm{m}^{-3}$. The temperature of the phase transition giving rise to these bosons is $T_c \sim 2 \times 10^9\,\mathrm{K}$, corresponding to the state of the universe about 1 s after formation. In the present epoch, a cosmic BEC behaves like non-relativistic cold dark matter (CDM), producing a spherical mass distribution which contributes to the Newtonian potential. An interesting consequence of galactic rotation is that it can give rise to vortices in the condensate with quantized circulation. This letter examines the ramifications of vortex formation in a cosmic BEC and shows that vortex dynamics leads to a flat velocity profile for a rotating dark matter condensate.

Our starting point is the Goldstone model, which is specified by a Lagrangian density with global $U(1)$ symmetry ($\hbar = c = 1$)

$$\mathcal{L} = \partial^\mu \bar{\Psi} \partial_\mu \Psi - \frac{\lambda}{4}(|\Psi|^2 - \eta^2)^2, \tag{1}$$

where Ψ is a self-coupled complex scalar field interacting only with gravity. The potential energy of the field is modelled by a Ginzburg–Landau potential of the form utilized in a phenomenological treatment of superfluidity [11]. The parameters λ and η determine the Compton mass of the scalar boson, i.e., $m^2 = \lambda\eta^2/2$. The equation of motion, derived from equation (1), is

$$\Box \Psi + \frac{\lambda}{2}\Psi(|\Psi|^2 - \eta^2) = 0. \tag{2}$$

An axisymmetric static solution to equation (2), for a string oriented along the z-axis, is given by the Nielsen–Olesen vortex of the form

$$\psi(r) = f(r)\mathrm{e}^{\mathrm{i}n\theta}, \tag{3}$$

where $f(r)$ is the magnitude of the field configuration, $r^2 = x^2 + y^2$, $\theta = \theta(x, y)$ is the phase of the field and n is the winding number around the degenerate vacuum manifold, S^1. In what follows we set $n = 1$. For a vortex located at the origin, the phase of the scalar field is given by $\theta(x, y) = \tan^{-1}(y/x)$. The magnitude of the field, $f(r)$, is obtained by numerically finding the static solution of equation (2) in cylindrical coordinates.

Consider a vortex embedded in a background scalar field, ϕ_0. The magnitude of the background field is assumed to be constant; however, its phase varies according to $\nabla\Theta \cdot \mathbf{r}$. If the phase gradient is a constant vector in the y-direction we can write ϕ_0 as

$$\phi_0(y) = \mathrm{e}^{\mathrm{i}\alpha y}, \tag{4}$$

where $\alpha = \partial\Theta/\partial y$. We will return to discuss how a phase gradient is established in a cosmic BEC. An Abrikosov ansatz is used to describe a vortex embedded in the background field, i.e.,

$$\Psi(t, x, y) = \Phi(t, x, y)\phi_0(y). \tag{5}$$

Substituting $\Psi(t, x, y)$ into the Lagrangian (1), we obtain

$$\mathcal{L} = \partial^\mu \bar{\Phi} \partial_\mu \Phi + \mathrm{i}\alpha\left(\bar{\Phi}\frac{\partial \Phi}{\partial y} - \Phi\frac{\partial \bar{\Phi}}{\partial y}\right) - \alpha^2|\Phi|^2 - \frac{\lambda}{4}(|\Phi|^2 - \eta^2)^2. \tag{6}$$

The scalar field can be represented by the quantum 'hydrodynamic' form, $\Phi(t, x, y) = |\Phi(t, x, y)|\mathrm{e}^{\mathrm{i}\theta}$. For a vortex located at the origin we have $\partial\theta/\partial y = x/r^2$, which enables us to write the potential energy term in equation (6) as

$$V(|\Phi|) = -2\alpha|\Phi|^2\frac{x}{r^2} + \alpha^2|\Phi|^2 + \frac{\lambda}{4}(|\Phi|^2 - \eta^2)^2. \tag{7}$$

The dynamics of a vortex in the background field is governed by the asymmetric potential $V_A = -2\alpha|\Phi|^2 x/r^2$. The form of V_A is determined from the numerical solution to the static vortex $f(r)$. The asymptotic vortex solution approaches the vacuum expectation value (VEV),

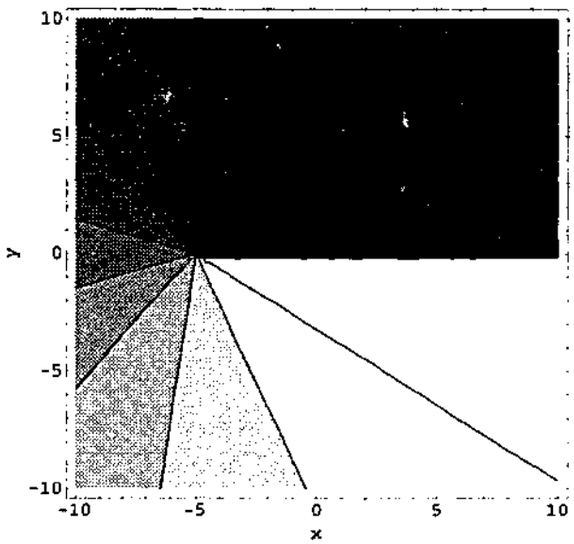

Figure 1. Grey scale plot of the initial phase winding of a vortex embedded in a constant background phase gradient oriented in the y-direction (with $\alpha = 0.01$). We have set $\lambda = 2\eta = 2$ (i.e., $m^2 = 1$). The phase winding of the vortex, initially at rest at $(-5, 0)$, is anticlockwise with black denoting a phase of 0 and white representing a phase of 2π.

for which $f(r \to \infty) = \eta$. However, the near-field solution is given by $f(r) \approx cr$, where $c = 0.58$, hence $V_A \approx -0.67\alpha x$. The resulting force on the vortex is therefore $\mathcal{F}_x = 0.67\alpha$, whence a vortex embedded in a phase gradient (in the y-direction) experiences a force in the x-direction that is proportional to the magnitude of the phase gradient α. Numerical simulations were performed to confirm this prediction. The equation of motion follows from the Lagrangian (6)

$$\Box\Phi - 2i\alpha\frac{\partial\Phi}{\partial y} + \alpha^2\Phi + \frac{\lambda}{2}\Phi(|\Phi|^2 - \eta^2) = 0. \tag{8}$$

Equation (8) is numerically solved using a second-order leapfrog difference scheme, with time step $\delta t = 0.01$ and spatial step $\delta h = 0.1$, where $\delta t < \delta h$ guarantees numerical stability. The size of the simulation frame is 140×140, with a subset of data (20×20) chosen for the purpose of visualization. The simulation was evolved for 6000 time steps. This procedure obviates problems associated with the propagation of noise from the boundary. Figures 1 and 2 show a typical numerical simulation for a vortex in a uniform background phase gradient. The phase gradient is oriented in the y-direction. The vortex, initially at rest, experiences an acceleration in the x-direction, whose magnitude depends on α. As the sign of α is changed the acceleration of the vortex reverses. At the end of each simulation the phase winding of the vortex reveals that the lines of constant phase are curved. This is a result of the vortex trying to accommodate the background phase. The long-term evolution of the vortex in the background phase gradient is towards a state of constant velocity. The vortex can be thought of as having non-uniform phase winding, giving rise to a self-force [12], which attempts to restore its initial phase winding.

An important example of a phase gradient is that due to the presence of a second vortex. Consider a vortex located at the origin, interacting with a second vortex at an arbitrary position (x, y). The background phase due to the first vortex is $\theta(x, y) = \tan^{-1}(y/x)$. The force acting on the second vortex has components $\mathcal{F}_x \propto \partial\theta/\partial y$ and $\mathcal{F}_y \propto \partial\theta/\partial x$. The vortex–vortex force

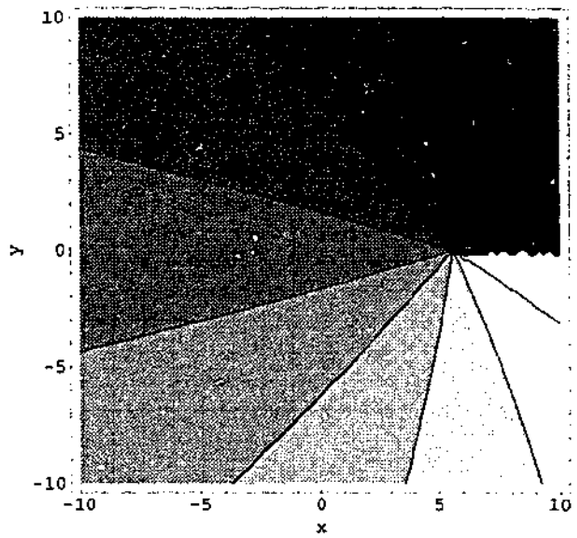

Figure 2. Grey scale plot of the phase winding at the end of the simulation ($t = 60$). The vortex shown in figure 1 experiences an acceleration in the x-direction and moves to (5.5, 0). The lines of constant phase are curved, indicating that the vortex attempts to accommodate the background phase gradient.

is long-range, falling off as $1/r$, in agreement with the predictions of alternative vortex models (see, e.g., [13]).

It is possible to arrange for a background phase gradient with components $\partial\Theta/\partial x = -\frac{1}{2}\Omega_x y$ and $\partial\Theta/\partial y = \frac{1}{2}\Omega_y x$. This provides a harmonic trap potential for the vortices. The strength of the trap is dictated by the values of Ω_x and Ω_y. For simplicity, we assume an isotropic trap with axisymmetric rotation, for which $\Omega_x = \Omega_y = \Omega$. With this background phase gradient, the equation of motion becomes

$$\Box\Phi + \frac{\lambda}{2}(|\Phi|^2 - \eta^2)\Phi - \Omega L_z\Phi + \frac{1}{4}\Omega^2 r^2\Phi = 0, \tag{9}$$

where $L_z = \mathrm{i}\left(y\frac{\partial}{\partial x} - x\frac{\partial}{\partial y}\right)$ is the angular momentum component and Ω is interpreted as an angular frequency. The last term in equation (9) represents a harmonic trap potential for the dark matter BEC. Equation (9) is the relativistic version of the mean field Gross–Pitaevskii equation, describing vortices in a stirred BEC [14]. In a frame rotating with angular velocity $\Omega\hat{\mathbf{e}}_z$, a background phase gradient is imprinted on the dark matter condensate. This is equivalent to an effective gauge field $(\Omega\hat{\mathbf{e}}_z \times \mathbf{r})/Q^*$, where Q^* is the bosonic 'charge'.

We now consider vortices in a self-gravitating dark matter condensate. Since galaxies are composed mainly of dark matter, we neglect the contribution to galactic dynamics from the baryonic matter component, and utilize the Lagrangian for a gravitationally coupled self-interacting complex scalar field (see, e.g., [15]), with a $|\Phi|^4$ potential,

$$\mathcal{L} = \frac{\sqrt{-g}}{2\kappa}\left\{R + \kappa\left[g^{\mu\nu}(\partial_\mu\bar{\Phi})(\partial_\nu\Phi) - \frac{\lambda}{4}|\Phi|^4\right]\right\}, \tag{10}$$

where $\kappa = 8\pi G_N$ is the gravitational constant in natural units, g is the determinant of the metric tensor $g_{\mu\nu}$ and R is the curvature scalar. Variation of equation (10) with respect to $\bar{\Phi}$ and $g_{\mu\nu}$ gives the coupled Einstein nonlinear Klein–Gordon equations,

$$G_{\mu\nu} = \kappa T_{\mu\nu}(\Phi) \tag{11}$$

$$\Box\Phi + \frac{\lambda}{2}|\Phi|^2\Phi = 0, \tag{12}$$

where $G_{\mu\nu} = R_{\mu\nu} - \frac{1}{2}g_{\mu\nu}R$ is the Einstein tensor and $T_{\mu\nu}(\Phi)$ is the energy–momentum tensor. In curved spacetime the energy–momentum tensor and d'Alembertian are given by

$$T_{\mu\nu}(\Phi) = \frac{1}{2}\left[(\partial_\mu\bar{\Phi})(\partial_\nu\Phi) + (\partial_\mu\Phi)(\partial_\nu\bar{\Phi})\right] - \frac{g_{\mu\nu}\mathcal{L}}{\sqrt{-g}} \tag{13}$$

$$\Box = \frac{\partial_\mu(\sqrt{-g}g^{\mu\nu}\partial_\nu)}{\sqrt{-g}}. \tag{14}$$

In the weak field limit the metric tensor has the form (see, e.g., [16])

$$g_{\mu\nu} = \mathrm{diag}(1 + 2V(x, y, z), -1, -1, -1), \tag{15}$$

where $V(x, y, z)$ is the gravitational potential. Using equation (15) the d'Alembertian is approximated by

$$\Box \approx \partial_\mu\partial^\mu\Phi = \frac{1}{1+2V}\ddot{\Phi} - \nabla^2\Phi, \tag{16}$$

where a dot denotes a time derivative. In arriving at equation (16) we have set $\partial_\mu g^{\mu\nu} = 0$, and assumed that the gravitational potential and scalar field are slowly varying spatial functions, so that the cross-term, $\nabla V \cdot \nabla\Phi$, can be neglected.

The self-interacting complex scalar field in the Lagrangian (10) does not break the global $U(1)$ symmetry. Symmetry breaking is induced by introducing a chemical potential, μ, via the stationarity ansatz

$$\Phi(t, x, y, z) = \mathrm{e}^{-\mathrm{i}\mu t}\phi(x, y, z). \tag{17}$$

Substituting equation (17) into equation (12) we obtain the nonlinear equation for the stationary state

$$-\nabla^2\phi + \frac{\lambda}{2}\left(|\phi|^2 - \frac{\eta^2}{1+2V}\right)\phi = 0, \tag{18}$$

where $\eta^2 = 2\mu^2/\lambda$. It is apparent from equation (18) that the symmetry-breaking potential, in the presence of gravity, is $\lambda(|\Phi|^2 - \eta^2/(1 + 2V))^2/4$. Replacing the $|\Phi|^4$ potential in equation (10) with this symmetry-breaking potential, the equation of motion for the scalar field is now given by

$$\frac{1}{1+2V}\ddot{\Phi} - \nabla^2\Phi + \frac{\lambda}{2}\left(|\Phi|^2 - \frac{\eta^2}{1+2V}\right)\Phi - \Omega L_z\Phi = 0, \tag{19}$$

where we have explicitly included the angular momentum term, $\Omega L_z\Phi$, which arises from assuming a background phase gradient due to axisymmetric rotation of the dark matter condensate as discussed earlier (see equation (9)). The trap potential for the dark matter condensate, $\frac{1}{4}\Omega^2r^2$, has been omitted from equation (19), since $\Omega r \approx 10^{-3}$ for a typical disc galaxy and the condensate is confined via gravitational interactions.

Clumping of the dark matter condensate arises because of the gravitational potential $\eta^2/(1+2V)$ in equation (19). Since particle number is conserved, there will be an increase in the field magnitude at the centre of the condensate. However, for convenience we set $\Phi = \eta$ at $r = 0$. For $V \ll 1$, we approach the flat space limit for which $(1+2V)^{-1} \simeq 1 - 2V$, whence the gravitational potential in equation (19) enters via a term of the form $\eta^2\lambda V\Phi$.

The equation governing the gravitational potential V is obtained from Einstein's field equation (11), with the source term specified by the energy–momentum tensor (13). Assuming a spherically symmetric dark matter halo, the line element is given by

$$\mathrm{d}s^2 = (1+2V)\mathrm{d}t^2 - \mathrm{d}r^2 - r^2(\sin^2\vartheta\,\mathrm{d}\varphi^2 + \mathrm{d}\vartheta^2). \tag{20}$$

Using equation (20), it is found that the time component of the Einstein tensor vanishes, i.e., $G_{00} = 0$. For a static spherically symmetric scalar field, $|\phi| = f(r)$, the T_{00}-component of the energy–momentum tensor is given by

$$T_{00} = \frac{\lambda}{8} f(r)^4 (1+2V) + \frac{1+2V}{2} f'(r)^2 - \frac{2V'}{\kappa r} + \frac{V'^2}{\kappa(1+2V)} - \frac{V''}{\kappa}, \tag{21}$$

where a prime denotes differentiation with respect to r. Setting $G_{00} = \kappa T_{00}$, the equation governing the gravitational potential, in the weak field limit, reduces to

$$V'' + \frac{2}{r} V' = \frac{\kappa}{2}(1+2V)\frac{\lambda}{4} f(r)^4, \tag{22}$$

where the terms $f'(r)^2$ and V'^2 have been neglected. Equation (22), governing the gravitational potential, reduces to the well-known Poisson equation in the Newtonian limit.

The coupled equations (19) and (22) are solved numerically using an iterative method. This approach is reminiscent of the Hartree method used in describing many-electron atoms. The parameters in the coupled equations are rendered dimensionless by rescaling according to $x_\mu \to \eta x_\mu$, $\Phi \to \eta^{-1}\Phi$, $\Omega \to \eta^{-2}\Omega$ and $\kappa \to \eta^2 \kappa$. This eliminates η, and for simplicity we have set $\lambda = 2$.

Vortices form in a rotating dark matter BEC when the angular frequency exceeds a critical value, Ω_c (see e.g., [10]). Immediately after formation, we conjecture that a disc protogalaxy has a Keplerian velocity profile outside its nucleus ($r > R_0$), whereas for $r \leqslant R_0$ the protogalaxy exhibits rigid body motion [5]. Rotation establishes a background phase gradient in the dark matter BEC, which is determined by the initial angular frequency profile, $\Omega(r)$, of the protogalaxy. When $\Omega(r) > \Omega_c$, vortices are nucleated in the condensate. The background phase gradient produces a harmonic trap for the vortices (expelling antivortices), with the trap force exhibiting a radial dependence, whose magnitude in the Keplerian regime ($r > R_0$) is given by

$$\mathcal{F}(r) \propto r\Omega(r) = \frac{\sqrt{G_N M_D(r)}}{r^{1/2}}, \tag{23}$$

where $M_D(r)$ is the mass of dark matter within radius r from the galactic centre. Each vortex has a quantized circulation, h/m, and a vortex lattice forms with number density, $n_v(r)$, determined from

$$\Omega(r) = \frac{\beta h}{m} n_v(r), \tag{24}$$

where the parameter β is introduced to modify the strength of the vortex trap. According to equation (23), the trapping force on a vortex (due to the rotation of the protogalaxy) has an $r^{-1/2}$ dependence. However, inter-vortex forces also establish a background phase gradient in the dark matter BEC, with each vortex experiencing an $r^{-1/2}$ repulsive force within its causal horizon d_H. Initially d_H is of the order of the coherence length of the BEC. The resultant force on a vortex is zero, since the trapping force due to rotation is balanced by the net repulsive force from all other vortices. As d_H increases, each vortex interacts with a larger number of vortices; consequently, a vortex experiences a non-zero force that causes it to move out in the radial direction. This results in an equilibrium vortex configuration with $n_v \propto r^{-1}$, which implies a flat velocity profile for the dark matter condensate (outside the galactic nucleus). In the vicinity of the nucleus, rigid body rotation produces a uniform vortex density with a concomitant zero net radial force on each vortex.

To confirm this conjecture, we have studied vortex dynamics in a harmonic trap using numerical simulations. We assume a spherically symmetric distribution of dark matter (in the galactic halo), and consider vortices in the two-dimensional transverse plane $\mathbf{r}_\perp = (x, y)$.

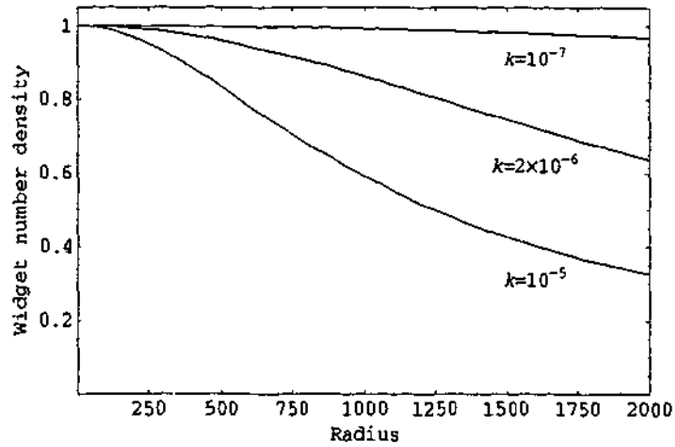

Figure 3. Radial plot of the WIDGET number density, $|\Phi|^2$, in the absence of rotation ($\Omega = 0$). As κ is increased, $|\Phi|^2$ changes from an approximately uniform number density to one where the dark matter condensate begins to 'clump' at the centre of the protogalaxy.

We exploit the static vortex solution of equation (19), in the absence of rotation ($\Omega = 0$). Once the static solution is found, it is wound onto a two-dimensional Cartesian grid. The initial multi-vortex configuration is constructed using an Abrikosov ansatz. A leapfrog method is then employed to evolve the equation of motion (19). The numerical simulation arrives at a final vortex lattice based on an initial Keplerian configuration for $r > R_0$, and rigid body motion for $r \leqslant R_0$. In order to maintain rigid body rotation, for $r < R_0$, it is necessary to 'tune' the strength of the trapping force by choosing a value for the parameter β. For $\beta < 1.4$, it is found that vortices are not confined to the galactic nucleus ($r < R_0$); consequently, we have set $\beta = 1.4$ in our simulations. The vortex configuration is initialized using a number density $n_v = c_0$ ($\leqslant R_0$), and $n_v = c_1 r^{-1.5}$ for the Keplerian regime ($r > R_0$), where c_0 and c_1 are constants. A grid of radius $R_1 = 1800$ is chosen with $R_0 = 100$. The number of vortices is determined by the rotational velocity of the protogalaxy, but is expected to be of the order of several hundred for a typical spiral galaxy [10]. The present simulation uses 500 vortices and a grid of size 4600×4600. The grid size is sufficiently large that, at the end of the simulation ($t = 500$), noise from the boundary does not propagate into the visualization frame (3300×3300). For these simulations we set the spatial step $\delta h = 1$ and the time step $\delta t = 0.2$. Although the initial vortex configuration is prescribed radially, its angular distribution is random. A pseudo-random number generator is used to establish the angular distribution (see figure 4). Since the initial separation of vortices can be small, the Abrikosov ansatz is expected to generate numerical noise as the simulation evolves. To remedy this we introduce a damping term, $b\partial\Phi/\partial t$, into equation (19), where b is a small positive constant ($b = 0.1\delta t$). The radial dependence of the vortex number density, $n_v(r)$, is calculated from the number of vortices inside an annular region, with $\delta r = 2$. However, with a small number of vortices this procedure leads to large variations in $n_v(r)$. To ameliorate this problem we smooth the number density using a Gaussian filter, centred on radial position r_0. The filter has the form $w(r) = \exp[-0.5s^2(r - r_0)^2]$, where $s = 4\sqrt{\ln 4}/3R_0$. This corresponds to a kernel with a full width at half maximum of $3R_0/2$. Although the vortex number density has been smoothed, this procedure does not modify the positions of vortices in the lattice.

Figure 3 shows a radial plot of the WIDGET number density, $|\Phi|^2$, for various values of κ in the absence of rotation ($\Omega = 0$). Rotation produces a centrifugal potential which modifies

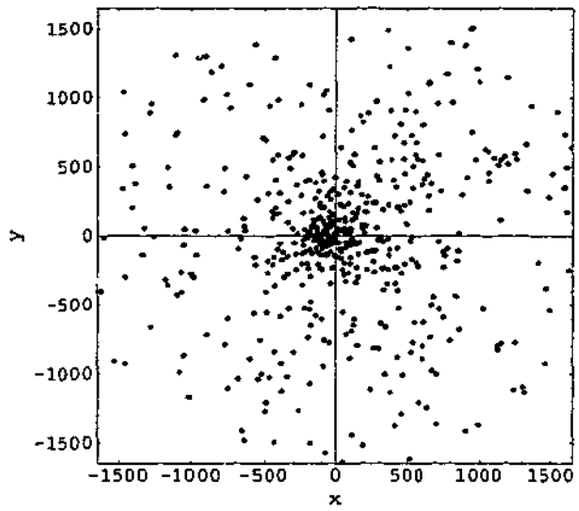

Figure 4. Initial configuration of 500 vortices located within $R_1 = 1800$, with $\kappa \approx 2 \times 10^{-6}$. The angular distribution of vortices is random. The vortex number density, $n_v(r)$, is constant for $r \leqslant R_0$ ($R_0 = 100$), characterizing rigid body rotation. The trap parameter $\beta = 1.4$ as discussed in the text. For $r > R_0$, the initial vortex configuration exhibits a Keplerian velocity profile, for which $\Omega(r) \propto r^{-1.5}$.

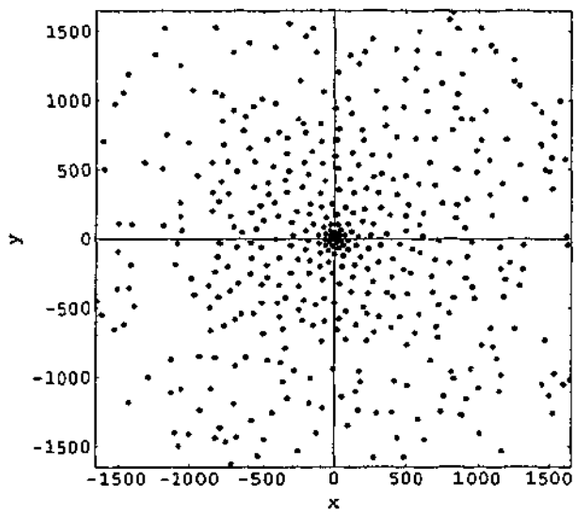

Figure 5. Final configuration obtained by evolving the vortices in figure 4. At the end of the simulation ($t = 500$), the vortex configuration (with 442 vortices remaining within the visualization frame) is characterized by a non-Keplerian profile ($r > R_0$), with $\Omega(r) \propto r^{-1}$.

the number density. A value of $\kappa \approx 2 \times 10^{-6}$ produces a dark matter profile consistent with that adopted in the literature (see, e.g., [6]). Our simulations indicate that the velocity profile of the rotating dark matter condensate is insensitive to the value of κ. Figures 4 and 5 show typical simulations for a rotating dark matter condensate, with $\kappa = 2 \times 10^{-6}$. It is observed that the initial vortex configuration evolves towards a triangular lattice, whose number density (outside the galactic nucleus, R_0) falls off as r^{-1}. Figure 6 is a plot of the rotational speed,

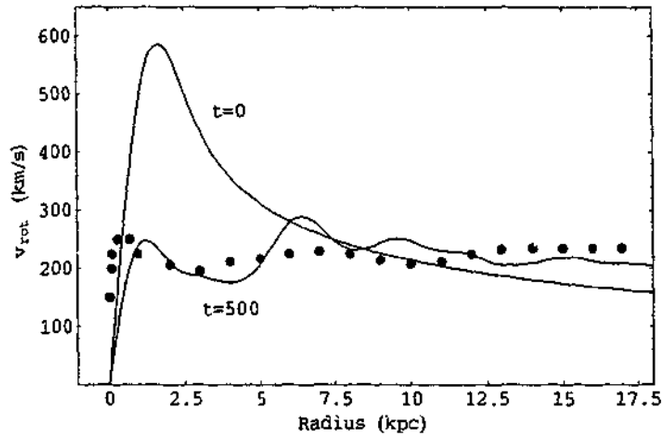

Figure 6. Velocity profiles based on the simulations shown in figures 4 and 5. Initially, the dark matter condensate has a Keplerian profile for $r > R_0$. At the end of the simulation ($t = 500$) we obtain a flat velocity profile, with oscillatory structure due to local variations in the vortex number density. The filled circles represent the rotation profile of the Milky Way galaxy (data derived from [17]). Our simulated rotation curve has been scaled to facilitate comparison with data for the Milky Way galaxy.

$v_{\rm rot}(r) = r\Omega(r)$, at the start and at the end of the simulation ($t = 500$). The velocity profile at $t = 500$ has been scaled in order to facilitate comparison with the rotation curve of the Milky Way galaxy [17]. We see that close to the galactic centre the velocity profile exhibits rigid body rotation, but has a flat velocity profile out to large distances from the galactic centre. It is noteworthy that the rotation curve shows oscillations. These arise because the angular frequency is determined from the local vortex number density, which is expected to show departures from the r^{-1} dependence. The asymptotically flat velocity profile of the dark matter component is found to be insensitive to specific values of the model parameters, such as R_0 and κ. To account for visible matter in the model of galactic dynamics, we include a baryonic mass density, ρ_B, in the energy–momentum tensor (13). Since the scalar bosons are uncharged they do not participate in electroweak interactions—the only coupling between baryonic and dark matter is via gravity. However, the inclusion of a baryonic mass density does not affect the qualitative predictions of our model.

In conclusion, scalar particles arising from a late-time cosmological phase may be a major component of dark matter, and under certain circumstances it is possible for these scalar particles to form a degenerate superfluid (BEC). Rotation of a self-gravitating dark matter condensate gives rise to quantized vortices, which evolve towards a vortex lattice whose number density, $n_v \propto r^{-1}$. This suggests that a rotating dark matter condensate will have a flat velocity profile. To provide a quantitative understanding of hierarchical clustering and gravitational instabilities we will require a large N-body simulation of structure formation, including a three-dimensional model of vortex dynamics. Nevertheless, the current paper has demonstrated a hitherto unexpected role for vortex dynamics in the evolution of disc galaxies.

Acknowledgments

One of the authors, RPY, acknowledges the support of an Australian Postgraduate Award. The constructive comments of a referee are gratefully acknowledged.

References

[1] Rowan-Robinson M 1985 *The Cosmological Distance Ladder* (New York: Freeman)
[2] Bahcall N, Ostriker J P, Perlmutter P S and Steinhardt P J 1999 *Science* **284** 1481
[3] Persic M, Salucci P and Stel F 1996 *Mon. Not. R. Astron. Soc.* **281** 27
[4] Bergstrom L and Goodbar A 1999 *Cosmology and Particle Astrophysics* (Chichester: Wiley)
[5] Binney J and Tremaine S 1987 *Galactic Dynamics* (Princeton, NJ: Princeton University Press)
[6] Bergström L 2000 *Rep. Prog. Phys.* **63** 793
[7] Guzmán F S and Matos T 2000 *Class. Quantum Grav.* **17** L9
[8] Sin S J 1994 *Phys. Rev.* D **50** 3650
[9] Silverman M P and Mallett R L 2001 *Class. Quantum Grav.* **18** L37
[10] Silverman M P and Mallett R L 2001 *Class. Quantum Grav.* **18** L103
[11] Zurek W H 1996 *Phys. Rep.* **276** 177
[12] Thatcher M J and Morgan M J 1997 *Class. Quantum Grav.* **14** 3161
[13] Perivolaropoulos L 1992 *Nucl. Phys.* B **375** 665
[14] Dalfovo F, Giorgini S, Pitaevskii L P and Stringari S 1999 *Rev. Mod. Phys.* **71** 463
[15] Schunck F E and Mielke W W 1998 *Phys. Lett.* A **249** 389
[16] D'Inverno R 1996 *Introducing Einstein's Relativity* (New York: Oxford University Press)
[17] Clemens D P 1985 *Astrophys. J.* **295** 422

Wavefunction reconstruction of complex fields obeying non-linear parabolic equations

Yaw-Ren E. Tan, David M. Paganin, Rotha P. Yu, and Michael J. Morgan
School of Physics and Materials Engineering, Monash University, Victoria 3800, Australia
(Dated: June 26, 2003)

We present a generalized Gerchberg-Saxton (GS) algorithm for reconstructing a (2+1)-dimensional complex scalar wave-field which obeys a known non-linear non-dissipative parabolic differential equation, given knowledge of the wave-field modulus at three or more values of an evolution parameter such as time. This algorithm is used to recover the complex wavefunction of a (2+1)-dimensional Bose-Einstein condensate (BEC) from simulated modulus data. The Gross-Pitaveskii equation is used to model the dynamics of the BEC, with the modulus information being provided by a temporal sequence of simulated absorption images of the condensate. The efficacy of the generalized GS algorithm is examined for a wide range of simulation conditions, including strong non-linearities, vortex states and Poisson noise. The general form of this algorithm, which allows one to reconstruct a time-dependent wavefunction, will be useful for studying the phase dynamics of topological defects in coherent quantum systems.

PACS numbers: 03.75.Lm, 03.75.Kk, 42.30.Rx

I. INTRODUCTION

The celebrated "phase problem" poses the question of determining the phase of a complex function using information about its modulus, supplemented by any relevant *a priori* knowledge. Solutions to particular phase problems (i.e., phase retrieval) have been studied in fields as diverse as astronomical imaging [1], crystallography [2], optical microscopy [3], electron microscopy [4], point projection imaging [5] and x-ray diffraction [6]. These examples deal with the problem of phase retrieval for matter or radiation wave-fields whose evolution is governed by linear partial differential equations. However, not all systems are governed by linear equations. For example, non-linear electromagnetic wave phenomena such as solitons [7] have long been studied by the non-linear optics community. Non-linear evolution also occurs for water waves [8], acoustic waves [9] and plasmas [10]. A topical example of non-linear wave-field evolution is Bose-Einstein condensation, the dynamics of which are modelled at zero temperature by a non-linear parabolic partial differential equation for the complex order parameter - the Gross-Pitaevskii equation [11–13].

There is emerging interest in the problem of phase retrieval for wave-fields which obey non-linear equations (see e.g. [14, 15]). Such studies have made first steps towards the goal of routinely determining phase for strongly non-linear systems. An important motivation for these studies is the fact that the canonical method of phase reconstruction, namely interferometry [16], is not applicable to strongly non-linear systems. Interferometric phase determination fails because the superposition principle does not hold for non-linear wave-fields: the superposition of the "reference wave" and the wave-field under study is not a valid solution to a given non-linear equation, even if the two wave-fields separately satisfy this equation.

The aim of this paper is to derive a phase-retrieval method, applicable to non-linear complex fields, which generalizes the Gerchberg-Saxton (GS) algorithm [17]. This is applied to the reconstruction of complex wave-fields that obey known (2+1)-dimensional non-dissipative non-linear parabolic partial differential equations, given as data the modulus of the wave-field at three or more values of a given evolution parameter. This evolution parameter is typically either time t or propagation distance z; we refer to the evolution parameter as "time" for the remainder of the paper. Solution to a given phase problem amounts to obtaining total knowledge of a quantum-mechanical complex wave-field (as encoded in the complex scalar wavefunction, macroscopic wavefunction or order parameter), or of a classical scalar radiation wave-field (as encoded in its complex analytic signal [16]), given as data the modulus of the wave over certain surfaces in space-time. We will refer to such modulus data as "holographic snapshots", since they constitute in-line holograms in the sense originally formulated by Gabor [18].

The outline of the paper is as follows. In Sec. II we describe the algorithm for the phase retrieval of waves obeying known non-linear parabolic equations, given a set of holographic snapshots. These snapshots may be supplemented by any relevant *a priori* knowledge which places constraints on the value of the wavefunction on the surfaces over which the holographic snapshots are taken. This algorithm is a generalization of the famous method of phase retrieval due to Gerchberg and Saxton [17, 19]. As an example of the application of these ideas to a strongly non-linear vortex-riddled system, Sec. III gives a robust means for recovering the wavefunction of a (2+1)-dimensional Bose-Einstein condensate which evolves according to the Gross-Pitaevskii equation, given simulated images of the modulus of the wavefunction at three or more times. We highlight the efficacy of the algorithm and discuss its applicability to experimental observations. We offer a discussion in Sec. IV, and conclude with Sec. V.

II. GENERALIZED GERCHBERG-SAXTON ALGORITHM

The Gerchberg-Saxton (GS) algorithm [17, 19] is a well-known solution to the following phase problem: given the modulus $|\Psi(\mathbf{r}_\perp)|$ of a complex scalar function of two space variables $\mathbf{r}_\perp \equiv (x, y)$, together with the modulus $|\hat{F}\{\Psi(\mathbf{r}_\perp)\}|$ of its Fourier transform with respect to $\mathbf{r}_\perp$, can one reconstruct the complex wavefunction $\Psi(\mathbf{r}_\perp)$? This phase problem, now known as the "Pauli problem", was first considered by Pauli in the context of quantum mechanics [20].

In its original and simplest form [17], the Gerchberg-Saxton algorithm claims the following iterative solution to the Pauli problem:

$$\Psi(\mathbf{r}_\perp) = \lim_{N\to\infty} \left(\hat{P}_1\hat{F}^{-1}\hat{P}_2\hat{F}\right)^N |\Psi(\mathbf{r}_\perp)|. \qquad (1)$$

Here, N is the number of iterations of the algorithm (taken to be sufficiently large for convergence to be attained), $\hat{F}$ denotes the operator for Fourier transformation with respect to $\mathbf{r}_\perp$, $\hat{F}^{-1}$ is the inverse Fourier transform, $\hat{P}_1$ is a projection operator which replaces the modulus of the function on which it acts by the known function $|\Psi(\mathbf{r}_\perp)|$, and $\hat{P}_2$ is a projection operator which replaces the modulus of the function on which it acts by the known function $|\hat{F}\Psi(\mathbf{r}_\perp)|$. Note that all operators in Eq. (1) act from right to left on the initial estimate $|\Psi(\mathbf{r}_\perp)|$ for the reconstructed wavefunction, which has the correct modulus and a constant phase.

Convergence of this algorithm is often problematic, with stagnation being a common problem [21]. Modifications such as those due to Fienup [21] may be used to achieve a more robust algorithm for attacking a given Pauli problem, although one might argue that such modifications lack the compelling simplicity of Gerchberg and Saxton's original proposal. For recent work employing the Gerchberg-Saxton-Fienup algorithm, see Weierstall *et al.* [22] and references therein.

In this article, we do not follow Fienup and others in seeking modified forms of the Gerchberg-Saxton algorithm which better solve the Pauli problem. Rather, we turn our attention to a class of related but different phase problems, which make use of slightly larger datasets of three or more images. With this in mind, note that the Fourier transform operator, which appears in Eq. (1), is unitary. This unitary operator may be replaced by a different unitary operator [23], such as the Fresnel transform [24](which evolves a solution to the linear parabolic equation forwards or backwards in time); note that the Fresnel transform is formally identical to the time evolution operator for the (2+1)-dimensional free-space time dependent Schrödinger equation. One is therefore led to a variant of the GS algorithm using a sequence of two-dimensional images related to one another by the Fresnel transform [25]. Superior results may be obtained when more than two images are incorporated into this algorithm [26]. In particular, Allen *et al.* [27, 28] used a through focal series (TFS) $\{|\Psi(\mathbf{r}_\perp, t_1)|, |\Psi(\mathbf{r}_\perp, t_2)|, |\Psi(\mathbf{r}_\perp, t_3)|, \cdots\}$ of three or more images to demonstrate the robustness of the GS algorithm in the presence of both noise and vortices; they did this for the case of a wavefunction obeying the linear Schrödinger equation:

$$(i\alpha\partial/\partial t + \nabla_\perp^2)\Psi(\mathbf{r}_\perp, t) = 0, \qquad (2)$$

where α is a constant, $\nabla_\perp^2$ is the Laplacian in the two-dimensional plane containing $\mathbf{r}_\perp$, and t is the propagation distance for a time-independent paraxial beam along a nominal optic axis [29]. When three images were employed, application of a modified GS algorithm with Fourier transforms replaced by Fresnel transforms, namely:

$$\Psi(\mathbf{r}_\perp, t_1) = \lim_{N\to\infty} \left(\hat{P}_1\hat{U}_{2,1}\hat{P}_2\hat{U}_{3,2}\hat{P}_3\hat{U}_{2,3}\hat{P}_2\hat{U}_{1,2}\right)^N |\Psi(\mathbf{r}_\perp, t_1)|, \qquad (3)$$

yielded extremely robust and stagnation-free convergence to the correct solution, for a wide variety of numerical experiments. Here, the Fresnel transform $\hat{U}_{m,n}$ (time-evolution operator) for Eq. (2) is defined by $\hat{U}_{m,n}\Psi(\mathbf{r}_\perp, t_m) = \Psi(\mathbf{r}_\perp, t_n)$, where $m, n = 1, 2, 3$, and $\hat{P}_m$ is a projection operator which replaces the modulus of the function on which it acts by the known function $|\Psi(\mathbf{r}_\perp, t_m)|$. The robustness of this algorithm, when applied to three or more images, was maintained even in the presence of spontaneously-generated wave-field vortices.

Both Eqs.(1) and (3) apply an iterated sequence of operators (projection operator, unitary operator, projection operator, unitary operator *etc.*) to an initial estimate for the reconstructed wavefunction which has the correct modulus and a constant phase. The three images employed in Eq. (3) were found to lead to considerably greater robustness in numerical experiments when compared to reconstructions based on two images. This robustness was maintained when the Fresnel transform in Eq. (3) was replaced with a more general class of linear unitary operators describing coherent shift-invariant linear imaging systems [30].

In the context of the present paper, we explore generalized forms of Eq. (3) which replace $\hat{U}$ with a unitary non-linear evolution operator. Consider the following class of non-linear non-dissipative parabolic equations (cf. [15]):

$$\left(i\alpha\partial/\partial t + \gamma\nabla_\perp^2 + \beta + V + f(|\Psi|)\right)\Psi = 0, \qquad (4)$$

where α, β, γ are real numbers, $V \equiv V(\mathbf{r}_\perp, t)$ is a real potential, f is a real function of a real variable, and $\Psi \equiv \Psi(\mathbf{r}_\perp, t)$ is a complex function of two space variables $\mathbf{r}_\perp \equiv (x, y)$ and one evolution parameter t. Special cases of our class of non-dissipative non-linear equations include the (2+1)-dimensional linear and non-linear Schrödinger equations [31], the paraxial equation of classical scalar

optics [29], the (2+1)-dimensional Gross-Pitaevskii equation [11–13], and the cubic-quintic parabolic equation for "liquid light" [32].

We address the following non-linear phase problem: Given a consecutive series $\{|\Psi(\mathbf{r}_\perp,t_1)|,|\Psi(\mathbf{r}_\perp,t_2)|,\cdots,|\Psi(\mathbf{r}_\perp,t_M)|\}$ of $M \geq 3$ holographic snapshots, where $\Psi(\mathbf{r}_\perp,t)$ obeys a known equation which is a special case of Eq. (4), can we reconstruct the full complex wavefunction $\Psi(\mathbf{r}_\perp,t)$? The wavefunction is to be reconstructed for all times lying in the time interval $t \in (t_1-\Delta_1, t_M+\Delta_2)$, where the positive real numbers Δ_1 and Δ_2 are sufficiently small that, at the numerical accuracy to which the wavefunction is approximated and the modulus data measured, the value of the wavefunction for any $t \in (t_1-\Delta_1,t_1)$ or $t \in (t_M,t_M+\Delta_2)$ may be accurately obtained from the boundary values $\Psi(\mathbf{r}_\perp,t_1)$ and $\Psi(\mathbf{r}_\perp,t_M)$, respectively. Similarly $|t_m - t_{m+1}|$, where $m = 1,2,\cdots,M-1$, must be sufficiently small that, at the numerical accuracy to which the wavefunction is approximated and the modulus data measured, $\Psi(\mathbf{r}_\perp,t)$ for any $t \in (t_m,t_{m+1})$ may be accurately obtained from either of the respective boundary values $\Psi(\mathbf{r}_\perp,t_m)$ or $\Psi(\mathbf{r}_\perp,t_{m+1})$.

We postulate that the following generalized Gerchberg-Saxton (GGS) algorithm gives a solution to our non-linear phase problem (cf. [30]):

$$\Psi(\mathbf{r}_\perp,t_1) = \lim_{N\to\infty}\left(\prod_{i=1}^{M-1}\hat{P}'_i\hat{U}_{i+1,i}\prod_{i=M}^{2}\hat{P}'_i\hat{U}_{i-1,i}\right)^N |\Psi(\mathbf{r}_\perp,t_1)|. \quad (5)$$

Since the class of equations (4) is non-dissipative, the associated non-linear time evolution operator $\hat{U}$ will be unitary: we define this operator via the equation $\hat{U}_{m,n}\Psi(\mathbf{r}_\perp,t_n) = \Psi(\mathbf{r}_\perp,t_n)$, with $\hat{U}$ being such that Ψ is a solution to Eq. (4). If no *a priori* knowledge is assumed, then $\hat{P}'_m = \hat{P}_m$. If, however, additional constraints on any or each of the wavefunctions $\Psi(\mathbf{r}_\perp,t_m)$ are given, then $\hat{P}'_m = \hat{P}''_m\hat{P}_m$, where $\hat{P}''_m$ is an operator which projects the wavefunction upon which it acts into the space of wavefunctions consistent with the given *a priori* knowledge. For example, $\hat{P}''_m$ might be used to impose such *a priori* knowledge as finite support for a given value of t.

Equation (5) contains as special cases the GS algorithm [17] of Eq. (1), Misell's algorithm [25], the TFS algorithm of Eq. (3), and variations of the TFS used in [30]. This algorithm retains the compelling simplicity of Gerchberg and Saxton's original proposal, as Eqs.(1) and (5) both comprise an iterated sequence of unitary evolution and projection operators, which is applied to an initial estimate of the reconstructed wavefunction that has the correct modulus and a constant phase.

III. RECOVERING THE WAVEFUNCTION OF A BOSE-EINSTEIN CONDENSATE

Bose-Einstein condensates [33, 34] give an interesting arena for retrieving the phase distribution of a wavefunction whose underlying dynamics are non-linear. Such condensates provide the opportunity to engineer a complex-valued macroscopic wavefunction (order parameter). For example, rotating a Bose-Einstein condensate (BEC) gives rise to quantized vortices [35, 36] which can be observed using absorption or dispersive imaging techniques [37]. In this context, phase retrieval gives a useful tool for studying the dynamics of topological phase defects [38]. In this section, we apply a special case of Eq. (5) to the problem of reconstructing the wavefunction of a (2+1)-dimensional Bose-Einstein condensate.

A. Modelling of a (2+1)-dimensional BEC

To simulate a BEC we employ a mean-field approach using the Gross-Pitaevskii (GP) equation [11–13], neglecting quantum and thermal fluctuations. We assume confinement of the BEC in the z direction, which allows us to describe the condensate in the two-dimensional transverse plane $\mathbf{r}_\perp \equiv (x,y)$. The simulated BEC is confined in a trap modelled by a harmonic oscillator potential [39]:

$$V_{trap}(\mathbf{r}_\perp) = \frac{1}{2}m\omega^2 r_\perp^2, \quad (6)$$

where m is the mass of the atomic species, $r_\perp^2 \equiv |\mathbf{r}_\perp|^2$, and ω_x,ω_y are oscillator frequencies which determine the trap frequency via $\omega = \sqrt{\omega_x^2+\omega_y^2}$. We now introduce dimensionless harmonic oscillator units [40] in which the unit of length, a_{ho}, corresponds to the average width of the Gaussian ground state wavefunction: $a_{ho} = \sqrt{\hbar/(m\omega_{ho})}$, where $\omega_{ho} = \sqrt{\omega_x\omega_y}$ is the geometric mean of the oscillator frequencies. Using re-scaled variables, for which ω_{ho}^{-1}, a_{ho} and $\hbar\omega_{ho}$ are the units of time, length and energy respectively, the time-dependent GP equation may be written as:

$$i\frac{\partial}{\partial t}\Psi = \left[-\frac{1}{2}\nabla_\perp^2 + \frac{1}{2}r_\perp^2 + V(|\Psi|)\right]\Psi, \quad (7)$$

where $\Psi \equiv \Psi(\mathbf{r}_\perp,t)$ is the condensate wavefunction normalized to unity, and $\nabla_\perp^2$ is the Laplacian in the $x-y$ plane. We identify the non-linear term $V(|\Psi|) = g|\Psi|^2$ with atomic interactions in the Bose gas, where g is the coupling constant (self-interaction coefficient). This constant is related to the s-wave scattering length, a_s, of a binary collision by $g = 4\pi N a_s/a_{ho}$, where N is the number of atoms in the condensate [40].

To simulate the BEC, Eq. (7) was evolved through time using a fourth order Runge-Kutta method with spatial step $\Delta h = 0.15$, and time step $\Delta t = 0.003$. These

parameters were chosen to ensure stability of the numerical integration scheme, and were used for all simulations in this paper. In these simulations, the initial condition used was the ground state wavefunction of the condensate in the given trapping potential. This ground state was calculated by using the time-independent GP equation that follows from substituting $\Psi(\mathbf{r}_\perp,t) = \Psi(\mathbf{r}_\perp)e^{-i\mu t}$ into Eq. (7), where μ is a real energy parameter (chemical potential). The time-independent GP equation is then given by:

$$\mu\Psi(\mathbf{r}_\perp) = \left[-\frac{1}{2}\nabla_\perp^2 + \frac{1}{2}r_\perp^2 + g|\Psi(\mathbf{r}_\perp)|^2\right]\Psi(\mathbf{r}_\perp). \quad (8)$$

Equation (8) was solved for the ground-state wavefunction using a diffusion Monte Carlo method [41], which finds the minimum energy configuration using a steepest descent approach. In the absence of interactions ($g = 0$), Eq. (8) reduces to that for the quantum harmonic oscillator, whose ground state is a Gaussian wavefunction. However, for $g > 0$ the condensate is broadened relative to the $g = 0$ case, as a result of repulsive atomic interactions.

B. Absorption imaging of a BEC

BECs can be imaged using absorption, fluorescence and dispersive techniques [39]. We shall consider simulated absorption images as input to the GGS algorithm in Eq. (5). However, we emphasize that dispersive imaging is equally well suited to the phase-retrieval methodology described here, provided that one is able to use a dispersive image to compute the probability density which forms the input to the GGS algorithm [37].

Here, we assume a thin lens approximation and consider the case where coherent laser probe light, propagating in the z direction, arrives perpendicular to the $x-y$ plane containing the condensate. The probe light field is assumed to be uniform immediately upstream of this plane, and the condensate is assumed to be well approximated by two-level atoms under the rotating-wave approximation. The intensity of the probe light at the exit surface of the BEC is then [39]:

$$I(\mathbf{r}_\perp) = I_0 \exp\left(-\frac{\sigma_0\tilde{n}}{1+\delta^2}\right), \quad (9)$$

where I_0 is the incident intensity of the probe beam, σ_0 is the resonant scattering cross-section, $\tilde{n} \equiv \int n(\mathbf{r}_\perp, z)dz$ is the integrated number density of atoms in the condensate, and δ is the detuning factor measured in half linewidths of the probe laser. This detuning factor is defined as $\delta = (\omega - \omega_0)/(\frac{1}{2}\Gamma)$, where ω_0 is the resonant frequency of the BEC, ω is the frequency of the probe light and Γ is the linewidth of the laser. Note that we identify $\tilde{n}(\mathbf{r}_\perp,t)$ with $N|\Psi(\mathbf{r}_\perp,t)|^2$.

In all simulations presented in this paper, Eq. (9) was used to model the process of forming an absorption image. Before being used as input into Eq. (5), each series of simulated absorption images was digitized to 16 bits. This was achieved by adjusting the detuning parameter δ, which appears in the normalized absorption coefficient $\sigma_0/(1+\delta^2)$, to ensure that the range of digitized transmitted intensity signals lies within the range 500 to 65000 counts.

C. Case I - Interference of two BECs

We first consider the situation where two spatially separated BECs are created in a double-well trapping potential, and then allowed to expand and overlap after the trap is turned off [42] ("Case I"). This double well potential was modelled by replacing the trap potential $\frac{1}{2}r_\perp^2$ in Eq. (7) with $\frac{1}{2}r_\perp^2 + V_{laser}$, where V_{laser} is the potential associated with a thin static sheet of laser light bisecting the trap. We modelled the potential of this sheet with the Gaussian:

$$V_{laser} = \alpha \exp[-\beta_x(x-x_0)^2 - \beta_y(y-y_0)^2], \quad (10)$$

where $\alpha = 100$ is the peak value of the potential, $\beta_x = 0.306$ and $\beta_y = 0.010$ are inversely proportional to the width of the laser beam in the x and y directions, and $(x_0, y_0) = (0,0)$ gives the centroid of the beam.

In this and all subsequent simulations, the Cartesian coordinate system (x,y) is mapped onto a square lattice of $2^m \times 2^m$ pixels, where m is a positive integer. The origin $(x,y) = (0,0)$ of Cartesian coordinates is identified with the "central" pixel, whose location is reached by first moving $2^{m-1}-1$ pixels to the right of the bottom-left pixel, and then moving $2^{m-1}-1$ pixels above the resulting lattice point. The physical width and height of each pixel was, in all simulations, equal to the spatial step $\Delta h = 0.15$; the time step was in all cases equal to $\Delta t = 0.003$.

Using the double-well potential $\frac{1}{2}r_\perp^2 + V_{laser}$, and $2^m = 256$ pixels, the BEC was modelled with three different self interaction coefficients: $g = 0$, $g = 100$ and $g = 1000$. The latter two values for g correspond to a high degree of non-linearity. The initial condition (ground state) of the BEC was generated for each value of g using the procedure described in section A. Figs. 1(a) and 1(b) respectively show the modulus and phase of the $g = 1000$ case of the interference of two spatially-separated BECs, $t = 300$ timesteps after the trap has been switched off, allowing the BEC pair to expand and overlap. Note that Fig. 1(c) will be discussed in Sec. III E.

D. Case II - Stirred condensate

We next consider stirring a BEC with a tightly focused blue-detuned laser beam [43, 44] ("Case II"). This blue-

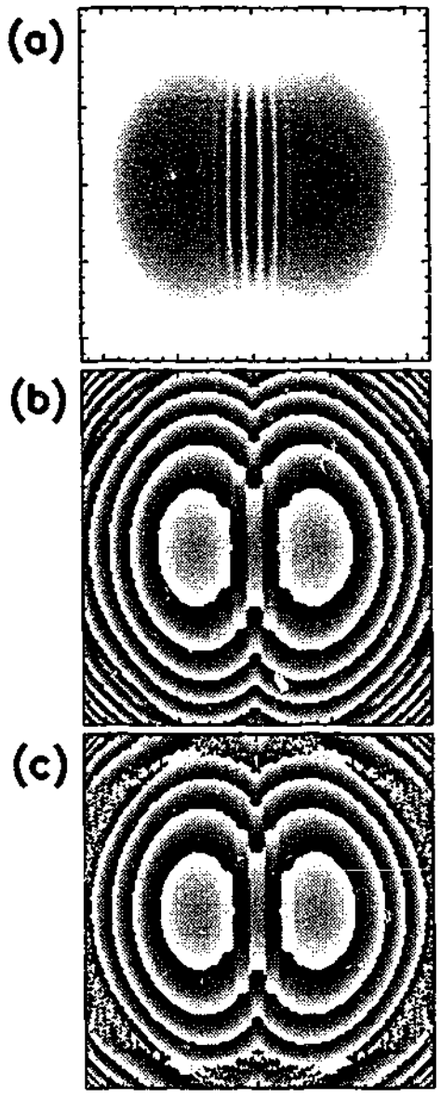

FIG. 1: Greyscale plots of (a) simulated modulus and (b) phase of two overlapping BECs, 300 timesteps after a double-well trap has been turned off and the condensate allowed to expand ($g = 1000$). (c) Phase retrieved with $N = 300$ iterations of Eq. (5), using as input data the five simulated absorption images at $t = 100, 150, 200, 250$ and 300 timesteps after the trap was turned off. In all phase maps, which are modulo 2π, black denotes a phase of 0 and white denotes 2π.

detuned laser light was modelled by a moving Gaussian potential:

$$V_{laser} = \alpha \exp[-\beta_x(x - x_0 - v_x t)^2 - \beta_y(y - y_0 - v_y t)^2]. \quad (11)$$

The centroid of this potential has initial coordinates (x_0, y_0), with this centroid being swept through the condensate with velocity (v_x, v_y). The Gaussian potential of the moving laser beam was again incorporated into the GP equation (7) by using the potential $\frac{1}{2}r_\perp^2 + V_{laser}$. The parameters used in Eq. (11) were $\alpha = 30$, $\beta_x = \beta_y = 3$, $(x_0, y_0) = (-1, -11)$, $(v_x, v_y) = (0, 2)$. The ground-state initial condition was generated over a 128×128 pixel grid without the laser beam, with $g = 100$. We then "switched on" the moving laser potential at $t = 0$. The parameters chosen for the potential in Eq. (11) are such that the stirring laser beam, which is initially outside the simulation frame, is passed through the condensate before leaving the simulation frame at $t = 2900$ timesteps. Figs. 2(a) and 2(b) respectively show the modulus and phase of the condensate wavefunction, 4600 timesteps after the stirring was completed. A number of counter-propagating quantized vortex pairs have been nucleated by the laser stirring, these being evident as screw dislocations in the multi-valued phase [38] of the wavefunction in Fig. 2(b). Fig. 2(c) will be discussed in the next sub-section.

E. Phase Retrieval of the BEC Wavefunction

Here, we model the phase retrieval of a BEC wavefunction using Eq. (5), in which the non-linear unitary time evolution operator $\hat{U}$ is determined by Eq. (7). The input to the GGS algorithm in Eq. (5) is obtained from three or more sequential absorption images of the BEC. To synthesize these absorption images the condensate is modelled according to either Case I or II, allowed to evolve for a fixed time, and then imaged according to Eq. (9). The natural logarithm of each of these absorption images is proportional to the modulus of the condensate wavefunction.

Since the condensate is disturbed by the absorptive imaging process, experimental recording of the multiple images used in Eq. (5) requires identical systems to be prepared and evolved for different times before being imaged. In this way it is possible to record the dynamics of an evolving BEC [45], and hence obtain the necessary data for wavefunction reconstruction using Eq. (5). Alternatively, one may use quantitative dispersive imaging techniques such as those described by Turner *et al.* [37], to non-destructively obtain such a series of images using a single condensate.

Fig. 1 shows the phase reconstruction for the non-linear double-well simulation described in section C. Here a sequence of five images, at $t = 100, 150, 200, 250$ and 300 timesteps after switching off the double-well trap, was used as input for Eq. (5). This noise-free simulation required 300 iterations of Eq. (5) to yield the reconstructed phase at $t = 300$, as shown in Fig. 1(c). Since the retrieved phase is only known up to an additive constant, the phase of both the true and reconstructed wavefunctions have both been set to π at the central pixel.

Qualitatively, the phase in Fig. 1(c) is well reconstructed over all parts of the image for which the probability density is non-negligible. However, to give a quantitative measure of the the closeness of the kth iterate $\tilde{\Psi}^{(k)}$ of the reconstructed wavefunction to the true wavefunction Ψ, we calculate the normalized root mean square

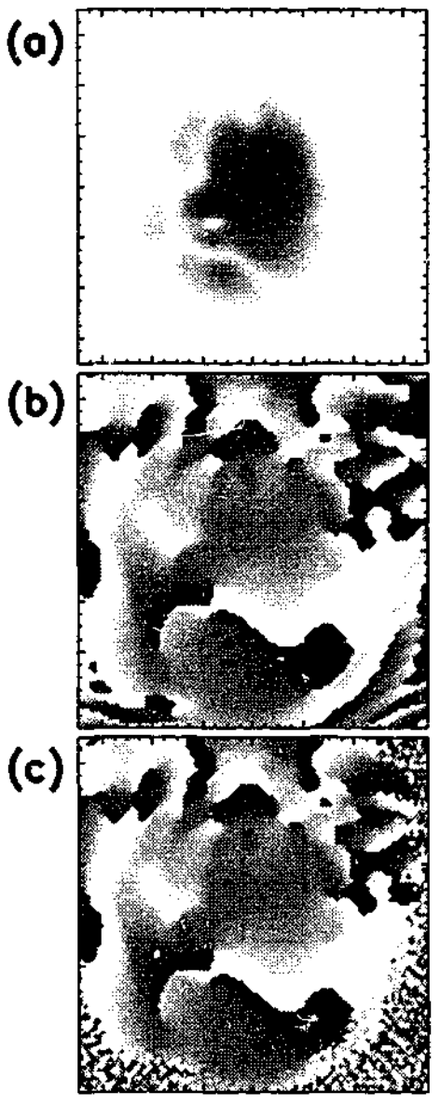

FIG. 2: Greyscale plots of (a) modulus and (b) phase of a simulated BEC, 4600 timesteps after completing stirring of the ground state of a harmonic trap with a moving laser spot ($g = 100$). (c) Phase retrieved with $N = 20$ iterations of Eq. (5), using as input data the nine simulated absorption images at $t = 3800, 3900, 4000, 4100, 4200, 4300, 4400, 4500$ and 4600 timesteps after stirring was commenced. In all phase maps, which are modulo 2π, black denotes a phase of 0 and white denotes 2π.

(RMS) error by:

$$\sigma_\Psi^{(k)} = \sqrt{\frac{\sum_{i=0}^{2^m-1}\sum_{j=0}^{2^m-1} |\Psi_{ij}(t) - \tilde{\Psi}_{ij}^{(k)}(t)|^2}{\sum_{i=0}^{2^m-1}\sum_{j=0}^{2^m-1} |\Psi_{ij}(t)|^2}} \qquad (12)$$

where i, j denote the grid coordinates in the $2^m \times 2^m$ pixel image. Using this error metric, the RMS error in the wavefunction reconstruction of Fig. 1 is 2.7×10^{-3}. Having completed the $g = 1000$ "Case I" reconstruction, the analysis was repeated for two further values of g, namely $g = 0$ and $g = 100$. The $g = 0$ version of Case I, with three images at $t = 400, 600$ and 800 timesteps after switching off the trap, required 498 iterations to yield an RMS reconstruction error of 6.9×10^{-3}. The $g = 100$ version of Case I, with five images at $t = 400, 500, 600, 700$ and 800 timesteps, required 498 iterations to yield an RMS reconstruction error of 5.5×10^{-3}. All of these RMS reconstruction errors compare favorably with the RMS error of approximately $1/\sqrt{2^{16}} \approx 4 \times 10^{-3}$ which was introduced by the 16-bit digitization of the simulated absorption images, as described at the end of section B.

Fig. 2 shows the phase reconstruction for the stirred BEC ("Case II"), in the presence of multiple vortices created using the procedure described in section D. A sequence of nine images, at $t = 3800, 3900, 4000, 4100, 4200, 4300, 4400, 4500$ and 4600 timesteps after commencing the stirring, was used as input for Eq. (5). This noise-free simulation required 20 iterations of Eq. (5) to yield the reconstructed phase at $t = 4600$ timesteps, as shown in Fig. 2(c). The phase of both the true and reconstructed wavefunctions was set to π at the central pixel. Using the error metric in Eq. (12), the error in the wavefunction reconstruction of Fig. 2 is 6.2×10^{-3}. Again, this compares favorably to the RMS error in the input data.

To give more insight into the convergence properties of wavefunction reconstruction using Eq. (5), Fig. 3 plots the RMS error $\sigma_\Psi^{(k)}$ versus iteration number k for the four scenarios described previously (i.e., Case I with $g = 0, 100, 1000$ and Case II with $g = 100$). We see that, in all cases, the RMS error exponentially approaches a value comparable to the RMS error ($\approx 4 \times 10^{-3}$) which was introduced into the input data by the 16-bit digitization of the simulated absorption images. Interestingly, the case with multiple vortices has a significantly more rapid convergence than the three vortex-free cases. Of the vortex free cases, it was the most strongly non-linear ($g = 1000$) that had the most rapid convergence.

Since the act of imaging a BEC perturbs the condensate, it is preferable to use as few probe photons as possible in forming an image of this quantum state: too many absorbed photons will destroy the condensate. In this context, we investigate the performance of Eq. (5) in the presence of significant amounts of noise in the simulated absorption-contrast images. This noise was added by taking the noise-free 16-bit absorption images described in section B, and then replacing the intensity at each pixel with a random number drawn from a Poisson distribution; this distribution had a mean given by the noise-free photon count at each particular pixel, with the photon count being proportional to the noise-free signal in each pixel. The noise added to a given image is fixed once and for all by specifying the RMS Poisson noise ξ on the the maximum intensity of the noise-free image; this corresponds to a ray of the laser probe beam which does not

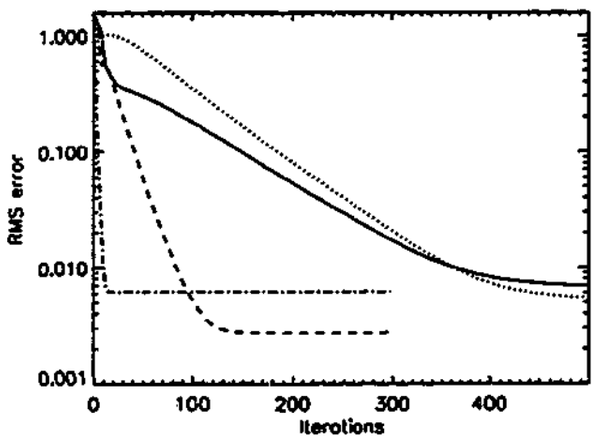

FIG. 3: RMS error $\sigma_\Psi^{(k)}$ in wavefunction reconstruction, calculated using Eq. (12), versus iteration number k. Case I, $g = 0$ (solid line); Case I, $g = 100$ (dotted line); Case I, $g = 1000$ (dashed line); Case II, $g = 100$ (dot-dashed line).

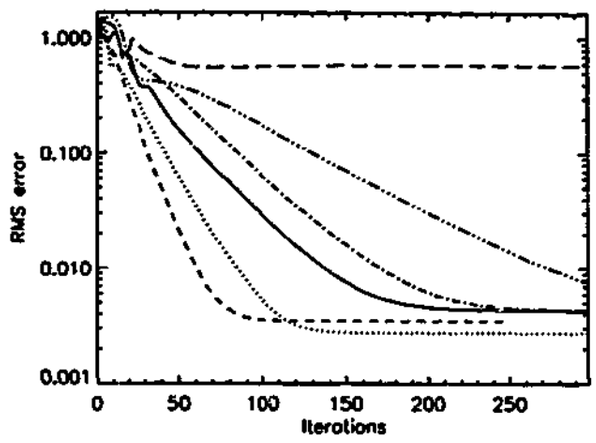

FIG. 4: RMS error $\sigma_\Psi^{(k)}$ of the reconstructed wavefunction, as a function of iteration number k. The different lines represent different retrieval parameters for Case I, with g=1000, using: 3 images with 100 timesteps between images (long dash); 5 images with 25 timesteps between images (dash ellipsis); 9 images with 25 timesteps (dash dot); 3 images with 50 timesteps (solid line); 5 images with 50 timesteps (dotted line); 9 images with 50 timesteps (short dash). In all cases, the first image corresponded to t=100 timesteps after turning off the double-well trap.

pass through the condensate. Evidently, the RMS noise level σ_ξ in the absorption image will be greater (possibly much greater) than ξ. Table I summarizes the RMS error $\sigma_\Psi^{(k)}$ in the reconstruction, with $\xi = 2.8 \times 10^{-2}$, for the four scenarios investigated in this paper (i.e., Case I with $g = 0, 100, 1000$ and Case II with $g = 100$). All of these RMS errors compare favorably with the RMS error σ_ξ introduced in simulating each of the noisy absorption images, with a maximum "noise amplification factor" of $\sigma_\Psi^{(k)}/\sigma_\xi \approx 1.36$.

TABLE I: RMS error $\sigma_\Psi^{(k)}$ of the wavefunction reconstruction in the presence of noise. The error was measured after k iterations, at which point the algorithm had converged. All simulations, with the exception of those indicated with an asterisk, were vortex free.

g	ξ	σ_ξ	k	$\sigma_\Psi^{(k)}$
0	0.028	0.32	498	0.38
100	0.028	0.22	498	0.30
1000	0.028	0.19	200	0.21
100*	0.028	0.21	20	0.25

We close this series of simulations by studying the influence, upon the rate of convergence of the wavefunction reconstruction, of changing both (i) the number of images used, and (ii) the number of timesteps allowed to elapse between consecutive images. For this final numerical study, we work with Case I, using $g = 1000$. The numerical results are shown in Fig. 4. We see that the algorithm converges exponentially rapidly to the "noise floor" for five out of the six studies presented there. We also note, from Fig. 4, that the algorithm's exponential rate of convergence is increased when one increases the number of images, while keeping constant the number of timesteps between each of these images. Convergence was not achieved for the study which had both the largest number of timesteps between images and the smallest number of images (3 images, 100 timesteps in between). For this non-convergent case, keeping the number of images fixed while decreasing the number of timesteps between images (from 100 to 50) led to convergence.

Why did the algorithm fail to converge when the number of timesteps between images was too large? This is a manifestation of the well-known "finite memory" of nonlinear systems: sensitive dependence on initial conditions implies that too great an elapsed time, between a pair of finite-precision numerically-evolved wavefunctions, precludes accurately tracing a direct causal link between the two. The presence of positive Lyapunov exponents in a volume-preserving phase-space flow implies that the ball of initial conditions, each consistent with the finite precision to which the wavefunction is specified, will be folded/mixed through the accessible phase space during the flow governed by the non-linear evolution equation [46]. Too great an evolution time between holographic snapshots will therefore imply that the reconstruction fails, since in evolving from snapshot to snapshot the result of applying the time-evolution operator is strongly perturbed by fluctuations below the noise level of the system.

IV. DISCUSSION

A. Wavefunction movies

The algorithm of Eq. (5) reconstructs the wavefunction $\Psi(\mathbf{r}_\perp, t_1)$ corresponding to the time t_1, given the moduli of the wavefunction at all times in the ordered set $\{t_1, t_2, \cdots, t_M\}$. Having obtained $\Psi(\mathbf{r}_\perp, t_1)$, one can obtain $\Psi(\mathbf{r}_\perp, t_2)$ via $\Psi(\mathbf{r}_\perp, t_2) = \hat{P}_2 \hat{U}_{1,2} \Psi(\mathbf{r}_\perp, t_1)$, a procedure that can be recursively applied to give:

$$\Psi(\mathbf{r}_\perp, t_j) = \prod_{i=j-1}^{1} \left(\hat{P}_{i+1} \hat{U}_{i,i+1} \right) \Psi(\mathbf{r}_\perp, t_1), 2 \leq j \leq M. \tag{13}$$

One therefore reconstructs the ordered wavefunction sequence $\Psi(\mathbf{r}_\perp, t_j), j = 1, \cdots, M$ corresponding to all times in the set $\{t_1, t_2, \cdots, t_M\}$. Moreover, one may also obtain a wavefunction "movie" by reconstructing the said wavefunction at any number of times t lying in the continuum $t \in (t_1 - \Delta_1, t_M + \Delta_2)$ (see Sec. II). To reconstruct the wavefunction $\Psi(\mathbf{r}_\perp, t_{i'})$ at any given time $t_{i'} \in (t_1 - \Delta_1, t_M + \Delta_2)$, first choose a member $t_{i''}$ of $\{t_1, t_2, \cdots, t_M\}$ which minimizes $|t_{i'} - t_{i''}|$, and then form $\hat{U}_{i'',i'} \Psi(\mathbf{r}_\perp, t_{i''}) = \Psi(\mathbf{r}_\perp, t_{i'})$. This allows one to reconstruct a temporal sequence of complex wavefunctions, which is useful in the context of studying both non-linear and linear wavefunction dynamics. This includes the topological phase dynamics associated with the nucleation and coalescence of quantized vortices [38].

B. Interference versus interferometry for non-linear fields

The GP equation is non-linear and therefore does not obey the superposition principle: if $\Psi_1(\mathbf{r}_\perp, t)$ and $\Psi_2(\mathbf{r}_\perp, t)$ are both solutions to Eq. (4), then $\Psi_1(\mathbf{r}_\perp, t) + \Psi_2(\mathbf{r}_\perp, t)$ will not in general be a solution. Therefore use of the term "interference" to describe the fringes of Fig. 1, while accurate, must not be visualized as arising from the linear superposition of two BEC wavefunctions that are separately valid solutions to Eq. (4). Notwithstanding this, we make the elementary remark that the concept of interference transcends the linearity assumption upon which the superposition principle is predicated.

The essence of interference is this: when two spatially-separated wavefunctions are allowed to come into contact with one another, the square modulus of the resulting disturbance is not equal to the sum of the squared moduli of each separate disturbance. The difference between the sum of the squared moduli of each separate disturbance, and the square modulus of the resulting disturbance, is the "interference term". In this context let us consider, as an initial condition, a pair of (2+1)-dimensional wavefunctions $\Psi_1(\mathbf{r}_\perp, t)$ and $\Psi_2(\mathbf{r}_\perp, t)$ which are spatially separated at $t = t_0$, i.e., $\int\int |\Psi_1(\mathbf{r}_\perp, t_0)\Psi_2(\mathbf{r}_\perp, t_0)| d\mathbf{r}_\perp \approx 0$.

Linear case: If the evolution of these initially-separated disturbances is governed by a linear equation, then interference effects occur if $|\Psi_1(t)|^2 + |\Psi_2(t)|^2 \neq |\Psi_1(t) + \Psi_2(t)|^2$ at some later time $t > t_0$. Here, $\Psi_1(t), \Psi_2(t)$ and $\Psi_1(t) + \Psi_2(t)$ are all solutions to the relevant linear equation, and functional dependence on $\mathbf{r}_\perp$ has been dropped for clarity. The associated linear interference term $I_L(t)$ is:

$$\begin{aligned} I_L(t) &\equiv |\Psi_1(t) + \Psi_2(t)|^2 - |\Psi_1(t)|^2 - |\Psi_2(t)|^2 \\ &= 2|\Psi_1(t)||\Psi_2(t)| \cos[\phi_1(t) - \phi_2(t)], \end{aligned} \tag{14}$$

where $\Psi_j(t) \equiv |\Psi_j(t)| \exp(i\phi_j(t))$ and $\phi_j(t) = \arg \Psi_j(t)$, with $j = 1, 2$. Linear interferometric phase determination aims to obtain the phase difference $\cos[\phi_1(t) - \phi_2(t)]$ from measurements of $I_L(t), |\Psi_1(t)|$ and $|\Psi_2(t)|$; typically, one of the wave phases (say, $\phi_1(t)$) is a known "reference" wavefront, and one seeks to determine $\phi_2(t)$.

Non-linear case: If, instead, our initially-separated disturbances are governed by a non-linear equation, then interference effects occur when $|\Psi_1(t)|^2 + |\Psi_2(t)|^2 \neq |\Psi_1(t) + \Psi_2(t) + \kappa[\Psi_1(t), \Psi_2(t)]|^2$, where $\Psi_1(t), \Psi_2(t)$ and $\Psi_1(t) + \Psi_2(t) + \kappa[\Psi_1(t), \Psi_2(t)]$ are all solutions to the relevant non-linear equation, with $\kappa[\Psi_1(t), \Psi_2(t)]$ being an appropriate interaction term which is generated when $\Psi_1(t)$ and $\Psi_2(t)$ are not spatially separated. The associated non-linear interference term $I_{NL}(t)$ is:

$$\begin{aligned} I_{NL}(t) &\equiv |\Psi_1(t) + \Psi_2(t) + \kappa[\Psi_1(t), \Psi_2(t)]|^2 \\ &\quad - |\Psi_1(t)|^2 - |\Psi_2(t)|^2 \\ &= I_L(t) + 2\mathrm{Re}(\kappa^*[\Psi_1(t), \Psi_2(t)](\Psi_1(t) + \Psi_2(t))) \\ &\quad + |\kappa[\Psi_1(t), \Psi_2(t)]|^2, \end{aligned} \tag{15}$$

which reduces to Eq. (14) when $\kappa = 0$. When $\kappa \neq 0$, Eq. (15) could, in principle, be used as a starting point for non-linear interferometric phase determination; however, the resulting non-linear equations are likely to be difficult to solve.

For both linear and non-linear interferometry, the measured interference term is sensitive to the phase of the wave-field, allowing one to consider the problem of inferring this phase from measurements of the wave-field modulus. This is the idea behind interferogram analysis, at least for the linear case, and it is motivated by the fact that it is probability density (or intensity) rather than phase which is measured by existing detectors of high-frequency fields.

Rather than seeking an interferometric solution to the problem of phase reconstruction, the phase-retrieval viewpoint of this paper eliminates the need for a reference wavefront. This can be done because the modulus of the wave-field at time t is a function of both the modulus and phase of the wave-field at earlier and later times. Measurement of the wave-field moduli at more than one time therefore yields information about both the modulus and phase of the wave-field, without the need for interference with a reference wave.

C. Some open questions

(a) A viable approach to the phase retrieval of both linear and non-linear multi-component wavefunctions may be of utility in the study of topological structures such as skyrmions [47, 48]. Can the methods of this paper be generalized to the case of multi-component wavefunctions, denoted by $\{\Psi_j(\mathbf{r}_d,t))\}$, which comprise a set of K complex scalar wavefunctions $\Psi_j \equiv \Psi_j(\mathbf{r}_d,t), j = 1,\cdots,K$, where $\mathbf{r}_d \in \Re^d$ and $d \geq 2$? This $(d+1)$-dimensional multi-component wavefunction might obey a system of coupled non-linear non-dissipative parabolic equations such as:

$$\left(i\alpha_j\partial/\partial t + \gamma_j\nabla_d^2 + \beta_j + V + \sum_{k=1}^{K} f_{kj}(|\Psi_k|)\right)\Psi_j = 0, \tag{16}$$

where $\alpha_j, \beta_j, \gamma_j$ are real numbers, ∇_d^2 is the d-dimensional Laplacian, f_{kj} is a real function of a real variable, k, j are integers lying between 1 and the number K of complex scalar components Ψ_j in the multi-component wavefunction, and $V \equiv V(\mathbf{r}_d,t)$ is a known real potential. In this context, the phase problem consists of reconstructing the multi-component wavefunction, given the modulus of each component at a number of given times.

For a first assault on this problem, one might try:

$$\{\Psi_j(\mathbf{r}_d,t_1)\} = \tag{17}$$
$$\lim_{N\to\infty}\left(\prod_{i=1}^{M-1}\hat{P}_i\hat{U}_{i+1,i}\prod_{i=M}^{2}\hat{P}_i\hat{U}_{i-1,i}\right)^N\{|\Psi_j(\mathbf{r}_d,t_1)|\}.$$

Here, $\{|\Psi_j(\mathbf{r}_d,t_1)|\}$ is an array of the known moduli at $t = t_1$, which forms the initial guess for the desired multi-component wavefunction $\{\Psi_j(\mathbf{r}_d,t_1)\}$. The non-linear multi-component time-evolution operator is defined by $\hat{U}_{m,n}\{\Psi_j(\mathbf{r}_d,t_m)\} = \{\Psi_j(\mathbf{r}_d,t_n)\}$, such that $\{\Psi_j(\mathbf{r}_d,t)\}$ is a solution to Eq. (16), and $\hat{P}_i$ is a projection operator defined by:

$$\hat{P}_i\{g_j(\mathbf{r}_d,t_i)\} \equiv \{|\Psi_j(\mathbf{r}_d,t_i)|\exp(i\arg g_j(\mathbf{r}_d,t_i))\}. \tag{18}$$

Additional *a priori* knowledge may be incorporated by appropriate generalization of the method given in Sec. II, where $\hat{P}_i$ is replaced by $\hat{P}_i''\hat{P}_i$.

(b) We have restricted ourselves to the problem of phase retrieval for non-dissipative non-linear fields, for which the time-evolution operator is unitary and therefore norm-preserving. If a field, whether it be linear or non-linear, obeys a *dissipative* equation - such as might be obtained by making α, β, γ, V or f complex in Eq. (4) - then the associated time-evolution operator will not be unitary. If such a non-unitary time-evolution operator is used in Eq. (5), under what circumstances will the resulting attempt at wavefunction reconstruction be successful? If the method is successful, how much dissipation can be tolerated before the method breaks down, for a given level of noise in the data?

V. CONCLUSION

We developed and demonstrated a robust non-interferometric algorithm for reconstructing the wavefunction of a complex field which obeys a known (2+1)-dimensional non-dissipative non-linear parabolic partial differential equation, given as input data the modulus of the wavefunction at three or more values of the specified evolution parameter (e.g., time). As a special case of this formalism we gave a numerical study of the reconstruction of the complex macroscopic wavefunction associated with a (2+1)-dimensional Bose-Einstein condensate, given a series of absorption images as input into the algorithm. In this numerical study, the algorithm converged exponentially quickly to the noise floor imposed by the input data: the root-mean-square error of the reconstructed wavefunction was in all cases similar to the RMS error in the input data. The presence of both strong non-linearities and quantized vortices was seen to increase the rate of convergence of the algorithm. The algorithm opens up the possibility of recovering a movie of the time-dependent macroscopic wavefunction of a BEC, and thus elucidating the phase dynamics of the condensate under experimental conditions. This includes situations where the wavefunction possesses topological defects. The method is also applicable to a number of other non-linear complex wave-fields, such as those encountered in paraxial non-linear optics using both radiation and matter waves.

Acknowledgments

Y-R.E.T. acknowledges financial support from the J.L. William Bequest and a Monash Vice Chancellor's Undergraduate Research Scholarship. D.M.P. acknowledges financial support from the Australian Research Council. We acknowledge useful conversations with Yvette Hancock.

[1] S.F. Gull and G.J. Daniell, Nature **272**, 686 (1978).
[2] H.A. Hauptman, Z. Kristallogr. **217**, 406 (2002).
[3] A.Barty, K.A.Nugent, D. Paganin, and A. Roberts, Opt. Lett. **23**, 817 (1998).
[4] S. Bajt, A. Barty, K.A. Nugent, M. McCartney, M. Wall, and D.Paganin, Ultramicroscopy **83**, 67 (2000).

[5] J. Miao, P. Charalambous, J. Kirz, and D. Sayre, Nature **400**, 342 (1999).

[6] D.K. Saldin, R.J. Harder, V.L. Shneerson, and W. Moritz, J. Phys: Condens. Matt. **13**, 10689 (2001).

[7] N.N. Akhmediev and A. Ankiewicz, *Solitons, Nonlinear Pulses and Beams* (Chapman and Hall, London, 1997).

[8] L. Debnath, *Nonlinear Water Waves* (Academic Press, Boston, 1994).

[9] R.T. Beyer, *Nonlinear Acoustics*, revised edition (US Naval Ship Systems Command, Washington, 1974).

[10] W. Horton and Y-H. Ichikawa, *Chaos and Structures in Nonlinear Plasmas* (World Scientific, Singapore, 1996).

[11] E.P. Gross, Nuovo Cimento **20**, 454 (1961).

[12] E.P. Gross, J. Math. Phys. **4**, 195 (1963).

[13] L.P. Pitaevskii, Zh. Eksp. Teor. Fiz. **40**, 646 (1961); trans. Sov. Phys. J.E.T.P. **13**, 451 (1961).

[14] P.J. Bardroff, U. Leonhardt, and W.P. Schleich, Opt. Comm. **147**, 121 (1998).

[15] D. Paganin and K.A. Nugent, Opt. Lett. **27**, 622 (2002).

[16] M.Born and E.Wolf, *Principles of Optics*, sixth corrected edition (Pergamon Press, Oxford, 1993).

[17] R.W. Gerchberg and W.O. Saxton, Optik **35**, 237 (1972).

[18] D. Gabor, Nature **161**, 777 (1948).

[19] W.O. Saxton, Computer Techniques for Image Processing in Electron Microscopy, Academic Press, New York, 1978.

[20] W. Pauli, Die allgemeinen Prinzipien der Wellenmechanik, in H. Geiger and K. Scheel (eds.), *Handbuch de. Physik* (Springer, Berlin, 1933).

[21] J.R. Fienup, Appl. Opt. **21**, 2758 (1982).

[22] U. Weierstall, Q. Chen, J.C.H. Spence, M.R. Howells, M. Isaacson, and R.R. Panepucci, Ultramicroscopy **90**, 171 (2002).

[23] R.W. Gerchberg and W.O. Saxton, Wave Phase from Image and Diffraction Plane Pictures, in P.W. Hawkes (ed.), *Image Processing and Computer-aided Design in Electron Optics* (Academic Press, London, 1973), p. 66.

[24] F.Gori, Why is the Fresnel Transform So Little Known?, in J.C. Dainty (ed.), *Current Trends in Optics* (Academic Press, London, 1994).

[25] D.L. Misell, J. Phys. D: Appl. Phys. **6**, 2200 (1973).

[26] P. Schiske, Wave Phase from Image and Diffraction Plane Pictures, in P. W. Hawkes (ed.), *Image Processing and Computer-Aided Design in Electron Optics* (Academic Press, London, 1973), p. 82.

[27] L.J. Allen, H.M.L. Faulkner, M.P. Oxley, and D. Paganin, D., Ultramicroscopy **88**, 85 (2001).

[28] L.J. Allen, H.M.L. Faulkner, K.A. Nugent, M.P. Oxley, and D. Paganin, Phys. Rev. E **63**, 037602 (2001).

[29] A. Papoulis, Scattering and Diffraction in Physical Optics, R.E. Krieger, Florida, 1981.

[30] L.J. Allen, M.P. Oxley, and D. Paganin, Phys. Rev. Lett. **87**, 123902 (2001).

[31] Y.S. Kivshar and B. Luther-Davies, Phys. Rep. **298**, 81 (1998).

[32] H. Michinel, J. Camo-Táboas, R.R. García-Fernández, J.R. Salgueiro, and M.L. Quiroga-Teizeiro, Phys. Rev. E. **65**, 066604 (2002).

[33] M.H. Anderson, J.R. Ensher, M.R. Matthews, C.E. Wieman, and E.A. Cornell, Science **269**, 198 (1995).

[34] J.R. Anglin and W. Ketterle, Nature **416**, 211 (2002).

[35] M.R. Matthews, B.P. Anderson, P.C. Haljan, D.S. Hall, C.E. Wieman, and E.A. Cornell, Phys. Rev. Lett. **83**, 2498 (1999).

[36] K.W. Madison, F. Chevy, W. Wohllenben, and J. Dalibard, Phys. Rev. Lett. **84**, 806 (2000).

[37] L.D. Turner, K.P. Weber, D. Paganin, and R.E. Scholten, Opt. Lett., submitted (2003).

[38] L.M. Pismen, *Vortices in Nonlinear Fields: From Liquid Crystal to Superfluids, From Non-Equilibrium Patterns to Cosmic Strings* (Oxford University Press, Oxford, 1999).

[39] W. Ketterle, D.S. Durfee, and D.M. Stamper-Kurn, Making, Probing and Understanding Bose-Einstein Condensates, in M. Inguscio, S. Stringari and C.E. Wieman (eds.), *Bose-Einstein Condensation in Atomic Gases, Proceedings of the International School of Physics "Enrico Fermi", Course CXL* (IOS Press, Amsterdam, 1999) p. 67.

[40] F. Dalfovo, S. Giorgini, L.P. Pitaevskii, and S. Stringari, Rev. Mod. Phys. **71**, 463 (1999).

[41] Y. Castin and R. Dum, Eur. Phys. Jour. D **7**, 399 (1999).

[42] M.R. Andrews, C.G. Townsend, H.J. Miesner, D.S. Durfee, D.M. Kurn, and W. Ketterle, Science **275**, 637 (1997).

[43] B. Jackson, J.F. McCann, and C.S. Adams, Phys. Rev. Lett. **80**, 3903 (1998).

[44] S. Inouye, S. Gupta, T. Rosenband, A.P. Chikkatur, A. Gorlitz, T.L. Gustavson, A.E. Leanhardt, D.E. Pritchard, and W. Ketterle, Phys. Rev. Lett. **87**, 080402 (2001).

[45] J. Denschlag, J.E. Simsarian, D.L. Feder, C.W. Clark, L.A. Collins, J. Cubizolles, L. Deng, E.W. Hagley, K. Helmerson, W.P. Reinhardt, S.L. Rolston, B.I. Schneider, and W.D. Phillips, Science **287**, 97 (2000).

[46] J.L. McCauley, *Chaos, Dynamics and Fractals: An Algorithmic Approach to Deterministic Chaos* (Cambridge University Press, Cambridge, 1993), ch. 1.

[47] J. Ruostekoski and J. R. Anglin, Phys. Rev. Lett. **86**, 3934 (2001).

[48] U. Al Khawaja and H. Stoof, Nature **411**, 918 (2001).